PHOTOCATALYTIC DEGRADATION OF DYES FROM MIXED DYE CONTAMINATED WATER USING VISIBLE LIGHT ACTIVE BISMUTH FERRITE@TiO$_2$ AND BISMUTH FERRITE@POLYANILINE HETEROSTRUCTURED NANOCOMPOSITES

Thesis

Submitted in partial fulfillment of the requirements for the degree of

DOCTOR OF PHILOSOPHY

by

SHANKRAMMA K

145056 CH14F04

DEPARTMENT OF CHEMICAL ENGINEERING

NATIONAL INSTITUTE OF TECHNOLOGY KARNATAKA

SURATHKAL, MANGALURU - 575025

February, 2021

DECLARATION

I hereby *declare* that the Research Thesis entitled "**Photocatalytic Degradation of Dyes from Mixed Dye Contaminated Water using Visible light active Bismuth ferrite@TiO$_2$ and Bismuth ferrite @Polyaniline Heterostructured Nanocomposites**" which is being submitted to the **National Institute of Technology Karnataka, Surathkal** in partial fulfillment of the requirements for the award of the Degree of **Doctor of Philosophy** in the Department of Chemical Engineering, is a *bonafide report of the research work carried out by me*. The material contained in this research thesis has not been submitted to any University or Institution for the award of any degree.

SHANKRAMMA K

145056 CH14F04

Department of Chemical Engineering

NITK, Surathkal

Place: NITK, Surathkal

Date: 18/02/2021

CERTIFICATE

This is to certify that the research thesis entitled "**Photocatalytic Degradation of Dyes from Mixed Dye Contaminated Water using Visible light active Bismuth ferrite@TiO₂ and Bismuth ferrite@Polyaniline Heterostructured Nanocomposites**" submitted by **SHANKRAMMA K** (Register Number: 145056 CH14F04) as the record of the research work carried out by her, is accepted as the Research thesis submission in partial fulfillment of the requirements for the award of degree of **Doctor of Philosophy**.

Research Supervisor
Prof. Vidya Shetty K
Dept. of Chemical Engineering
NITK, Surathkal

Chairman-DRPC
Dr. Prasanna B.D
Dept. of Chemical Engineering
NITK, Surathkal
HEAD OF THE DEPARTMENT
CHEMICAL ENGINEERING
National Institute of Technology Karnataka, Surathkal
P.O. Srinivasnagar - 575 025, D.K., Mangalore

ACKNOWLEDGEMENTS

My thesis is dedicated

to almighty God

to my parents for their encouragement, love and support

to my sister, brother, uncles, cousins, nieces and nephews for their affection

to my best friends for being with me always

to all my teachers and well-wishers for their encouragement

and to my guide for her moral support in all the way

ABSTRACT

The wastewater containing dye released from industries, when discharged to water bodies without any adequate prior treatment, ultimately leads to human health risk and threat to the environment. A proper wastewater treatment for Chemical Oxygen Demand (COD) and dye removal is essential. Photocatalysis with TiO_2 which utilizes ultraviolet light, is a well-known treatment method for dye wastewater. The development of visible light active photocatalysts is gaining importance to harness solar energy. The present study reports the synthesis of bismuth ferrite@ titanium dioxide (BFO@TiO_2), bismuth ferrite@polyaniline (BFO@PANI) heterostructured nanocomposites and their application in degradation of dyes from mixed dye contaminated water (MDCW) containing Methylene Blue (MB), Acid Yellow-17 (AY) and Rhodamine-B (Rh-B). The mixed phase BFO nanoparticles were synthesized by auto combustion method and were used in the synthesis of BFO@TiO_2 and BFO@PANI. The synthesis/calcination parameters were optimized based on maximum photocatalytic activity in terms of degradation of dyes from MDCW. BFO@TiO_2 particles synthesized with BFO:Ti molar ratio of 1:2, calcined at 400°C for 2 h (BFO@TiO_{2opt}) and BFO@PANI particles synthesized with BFO: aniline molar ratio of 1:0.0041 (BFO@$PANI_{opt}$) exhibited a maximum photocatalytic activity. The BFO@TiO_{2opt} and BFO@$PANI_{opt}$ nanocomposites exhibited superior visible light assisted photocatalytic activity than BFO, TiO_2 and PANI. BFO@TiO_{2opt} and BFO@$PANI_{opt}$ nanocomposites were found to form core-shell heterostructures and exhibited a band gap energy of 1.2 eV and 1.4 eV respectively. The parameters such as pH, catalyst loading and light intensity were optimized to maximize dye degradation. The COD removal of 96.7% and 97% were achieved with BFO@TiO_{2opt} and BFO@$PANI_{opt}$, respectively. These particles were found to be very effective even under solar light. The presence and increasing concentrations of other dyes were found to decrease the degradation of a target dye. The COD removal followed Langmuir–Hinshelwood (L-H) kinetics. BFO@TiO_{2opt} and BFO@$PANI_{opt}$ nanocomposites can be adopted for treatment of wastewater containing multiple dyes by harnessing solar energy for photocatalytic degradation.

Keywords: Bismuth ferrite; Mixed dye; Photocatalysis; Polyaniline; Solar energy; Visible light

TABLE OF CONTENTS

LIST OF FIGURES

iii

LIST OF TABLES

NOMENCLATURE AND ABBREVIATION

AB	Acid Black
AB113	Acid Blue 113
pKa	Acid Dissociation Constant
AO	Acid Orange
AO-7	Acid Orange 7
AR114	Acid Red 114
AR57	Acid red 57
AV-19	Acid violet 19
AY	Acid Yellow-17
ACG	Acidol grey
ACS	Acidol scarlet
ACY	Acidol yellow
AC	Activated Charcoal
AOP	Advanced oxidation process
APHA	American Public Health Association
Au-NaTNT	Au-functionalized sodium titanite nanotubes
AG	Azocarmine G
E_g	Bandgap
pKb	Base dissociation constant
BR46	Basic Red 46
BY28	Basic Yellow 28
BB3	Basic Blue 3
BOD	Biochemical Oxygen Demand
$BiFeO_3$/BFO	Bismuth ferrite
BFO@PANI	Bismuth ferrite@ polyaniline
BFO@TiO_2	Bismuth ferrite@ Titanium dioxide
$BiVO_4$	Bismuth vanadate
BR-19	Bright Blue Remazol
BG	Brilliant Green
Ca	Calcium

CMC-Na	Carboxymethylcellulose
CA	Cellulose acetate
CPCB	Central Pollution Control Board
COD	Chemical Oxygen Demand
CIZ	Cetirizine
CB	Conduction band
CR	Congo red
CO_2	Corban dioxide
CSNs	Core-shell nanoparticles
CV	Crystal Violet
CuO/NX	CuO/nano-zeolite X
DS	Derivative spectrophotometry
DO25	Disperse orange 25
DS	Derivative Spectrophotometry
TiO_2	Degussa P-25
EPD	Electrophoretic deposition
EDS	Energy Dispersive Spectroscopy
ESCA	Electron Spectroscopy for Chemical Analysis
EY	Eosin Yellow
EB	Evans Blue
FTIR	Fourier Transform Infrared spectroscopy
HOMO	Highest Occupied Molecular Orbital
HPEc	Hydrolysed pectin
^{o}OH	Hydroxyl radicals
HA	Humic Acid
IC	Indigo Carmine
ICP-OES	Inductive Coupled Plasma Optical Emission Spectroscopy
IBP	Ibuprofen
L-H	Langmuir-Hinshelwood
JG	Janus green
LUMO	Lowest Unoccupied Molecular Orbital

KM-LUX-100K	Lux meter
MAC	Magnetic Activated Carbon
MG	Malachite Green
MGO	Malachite Green Oxalate
λmax	Maximum Absorbance
MYR	Methyl green
MO	Methyl orange
MR	Methyl Red
MV	Methyl Violet
MB	Methylene Blue
MCNT	Multiwall Carbon nanotube
NCPs	Nanocomposites
NT	Nanotube
NPX	Naproxen
NIR	Near infrared
NiO	Nickel oxide
N-TiO$_2$	Nitrogen-doped TiO$_2$
R	Organic pollutant
•OH and •O$_2-$	Oxidative species
IO$_4$	Periodate ion
pHpzc	Point of Zero Charges
PANI	Polyaniline
PVP	Polyvinyl pyrrolidine
PANI–Gr	Polyaniline/graphene
KOH	Potassium Hydroxide
RB 5	Reactive Black 5
RB-19	Reactive Blue-19
RBB	Reactive Brilliant Blue KN-R
RO	Reactive Orange
RO 16	Reactive Orange 16
RO 84	Reactive Orange 84

RR-2	Reactive Red 2
RR-45	Reactive Red 45
RV5	Reactive Violet 5
RP H-7B	Red Porcin H-7B
RP MX-5B	Red porcin MX-5B
RB5	Remazol Black 5
RBB	Remazol brilliant blue
RR	Remazol-red
Rh-B	Rhodamine B
ROB	Rose Bengal
SEM	Scanning Electron microscopy
SiO_2	Silicon Dioxide Nanoparticles
STA	Silicatengstic acid
Ag NPs	Silver nanoparticles
SG	Sol-Gel
$^{\circ}O_2^-$	Superoxide radical
Tz	Tartrazine
$Ti(C_4H_9O)_4$	Tetra butyl titanite
TGS	Triglycine sulphate
$Ti\,(OBu)_4)$	Titanium butoxide
TNR	Titanium nanoribbon
TTIP	Titanium Tetra (IV) IsoPropoxide
TOC	Total organic carbon
TEM	Transmission Electron Microscopy
UV-C	UV light irradiation
VB	Valance band
W/cm^2	Watt per square centimetre
XRD	X-Ray Diffraction
XPS	X-Ray Photoelectron spectroscopy
ZACP	Zinc oxide activated charcoal polyaniline

CHAPTER 1

INTRODUCTION

1.1 Background of Research and Motivation

Environmental pollution is a threat to sustainable development of human civilization. Several synthetic dyes which are released with wastewater from various industries contribute majorly to water pollution. Synthetic dyes are being used in enormous quantities in several industries like food, leather, printing, textile, cosmetics and others. The estimated worldwide annual production of dyes and pigments would reach 9.0 million tons by the end of 2020 and nearly 280,000 tons (i.e. 20-50%) of textiles dyes are discharged into the effluents (Madamwar et al. 2019). India being the second biggest exporter of dyestuff in the global market, has a production capacity of more than 200,000 tonnes per annum and it shares around 12.5% of the global market in dyestuff industries (Madamwar et al. 2019). Synthetic dyes are of great environmental concern due to their widespread usage and non-biodegradable nature.

Approximately 1.6 million tons per year of synthetic dyes are consumed in industries globally (Homaeigohar 2020). In textile industries, 93% of the intake water comes out as colored wastewater due to the presence of dyes containing high concentration of organic compounds and heavy metals (Gupta et al. 2014; Wijannarong et al. 2013). The toxic effects of dyestuffs released from industrial establishments on the general public are widely reported.

Several synthetic dyes are used as food dyes, in textile, printing, tannery, paint, leather, paper manufacture, and photography industries. These dyes are inevitably discharged in industrial effluents. Many of the synthetic dyes have been reported to be non-biodegradable under aerobic conditions (Basibuyuk and Forster 1997; O'Neill et al. 2000). These dyes contribute to colour and Chemical Oxygen Demand (COD) in wastewater. They affect the ecosystem of streams, by either getting adsorbed or trapped in bioflocs. These dyestuffs affect the COD, Biochemical Oxygen Demand (BOD), toxicity, odour, and colour of wastewater (Vinu and Madras 2010). These dyes when released through industrial effluent and if discharged to water bodies without adequate treatment; affect the aquatic organisms and finally indulge in causing carcinogenic and mutagenic effect in human beings at the end of food chain. Thus, they ultimately lead

to health risk to the humans and threat to the environment. Government legislature on discharge standards in many countries has become progressively strict in order to protect the environment and to ensure sustainable growth. Though the removal of color from the wastewater is the first concern, the degradation of dyes to eliminate or reduce the toxicity has always been considered as the necessary action. Central Pollution Control Board (CPCB), India has prescribed discharge standard limit of less than 400 Hazen units and 250 mg/L COD for industrial effluents (Gage et al. 2014). In order to reduce the environmental risk and also to meet the discharge levels prescribed by the pollution regulatory authorities, proper wastewater treatment to degrade the dyes for reduction in COD level and colour removal is essential.

Several treatment methods and technologies have been intended and developed, thus dyes can be removed from wastewater by chemical coagulation or flocculation (Lin and Chen 1997), adsorption (Pala and Tokat 2002), ozonation (García-Montaño et al. 2008), membrane processes such as ultrafiltration or reverse osmosis (Sadr Ghayeni et al. 1998), electrochemical processes (Naumczyk et al. 1996) and biological treatment (Pala and Tokat 2002). The adsorption process mainly transfers the dye from water to the adsorbent, without mineralization of the dyes. The cost of adsorbent such as activated carbon is high. coagulation–flocculation treatments effectively eliminates insoluble dyes (Gahr et al. 1994), but have no effect on the elimination of soluble dyestuffs. Sludge generation leads to secondary pollution in coagulation–flocculation and disposal is a challenge. Electrochemical processes also lead to sludge formation (Lin and Chen 1997; Liu and Davis 1994). Decolorization of wastewater by ozonation alone does not lead to a significant reduction in COD (Adams et al. 1995; Marmagne and C. Coste 1996). Moreover, installation of ozonation plants can require additional costs (Scott and Ollis 1995). The reverse osmosis and other membrane techniques involve disadvantages like, the high cost of filters, the clogging of filters, associated maintenance difficulties or high energy requirement (Sadr Ghayeni et al. 1998; Tinghui et al. 1983; Treffry-Goatley et al. 1983), incomplete removal (Watters et al. 1991) and non-mineralization of the dyes with their accumulation in the retentate (Freger 2000; Kelly and Kelly 1995; Rossignol et al. 2000; Weber and Knauf 1998). Biological treatment by the activated sludge process does not achieve great success due to low

biodegradability of the dyes (Marmagne and C. Coste 1996; Pala and Tokat 2002; Specchia and Gianetto 1984) and a slower rate.

Advanced oxidation process (AOP) involving photocatalysis is cost-effective and green approach to degrade such toxic dyes into innocuous products (Gogate and Pandit 2004). Photocatalysis is an emerging treatment process gaining interest among the researchers owing to its potential in mineralization of the dyes (Chen et al. 2014; Khanna and Shetty K 2013, 2014; Nezamzadeh-Ejhieh and Karimi-Shamsabadi 2013; Soltani and Entezari 2013c). The conditions required for the photocatalytic process are very mild, the time required for the reaction is generally modest, and the chemical input is less (Kabra et al. 2004). Semiconductor photocatalysts have attracted a great deal of attention due to their potential application in environmental remediation. Among all the semiconductors, TiO_2 is the focus of numerous studies owing to its attractive characteristics as a photocatalyst, in the treatment of dye-contaminated water (Borges et al. 2016; Garg et al. 2016; Kalpaklı et al. 2014; Markad et al. 2017). Unfortunately, its weak photocatalytic activity under visible or solar irradiation (Khanna and Shetty K 2013, 2014; Ramírez-Aparicio et al. 2016; Xia and Yin 2013) along with its susceptibility to fast recombination of photogenerated electron-hole pairs (Chatterjee et al. 2008a; Wang et al. 2011d) limits its application. Many approaches have been developed to improve the photocatalytic activity of TiO_2 and to overcome the drawbacks mentioned above. The development of visible light active photocatalysts are gaining importance, to harness solar energy in photocatalysis. Fabrication of new highly active and visible-light-responsive photo-catalysts of small band-gap is critical, to improve the utilization of the solar spectrum. In this context, strategies should be deviced for (1) improvement of the separation rate of photogenerated electron-hole pairs, and (2) expansion of the absorption edge to visible light.

Bismuth ferrite ($BiFeO_3$ or BFO) is extensively known as multiferroic material with a rhombohedrally distorted perovskite structure. BFO has attracted enormous interest in solar applications due to its narrow band gap (2.1-2.7 eV) and the bulk photovoltaic effect (Li et al. 2009; Yang et al. 2010). It shows chemical stability during the photocatalytic process and visible light active (Gao et al. 2006a; Luo and Maggard 2006; Wu and Zhang 2011). However, a critical drawback of photo-corrosion (Li et al. 2009; Luo and Maggard 2006) and aggregation of the particles (Zhang et al. 2011c)

3

impairs their applications to a great extent. Hence, the surface of BFO nanoparticle may be protected by creating a shell of other semiconductor material, which not only prevents photo-corrosion but also creates a heterojunction to alter the band gap of BFO.

Nowadays a lot of effort has been made in the controlled synthesis of core-shell structured or other heterostructured nanocomposites such as $Bi_{12}TiO_{20}/g\text{-}C_3N_4$ (Sun et al. 2016), $BiFeO_3$@Ce-doped TiO_2 (Gong et al. 2013), (Ba, Sr)TiO_3/TiO_2 (Li et al. 2013a), $BiFeO_3$ coupled with nanocrystalline TiO_2 (Humayun et al. 2016), Bi_2S_3/TiO_2 (Brahimi et al. 2007), $CoFe_2O_4$-$BiFeO_3$ (Liu et al. 2005), BFO@TiO_2 (Liu et al. 2017), polymethyl methacrylate @BFO (Tamboli et al. 2014), BFO@ $SrTiO_3$ (Luo and Maggard 2006) and ZnO/TiO_2 (Marcì et al. 2001), which can improve the photocatalytic efficacy by decreasing the recombination rate of the photogenerated electron-hole pairs. These composite structures are gaining importance because of their conducive and versatile compositions and structures to serve such purposes (Pang et al. 2013; Tamboli et al. 2014). Core-shell nanoparticles (CSNs) are extremely functional materials with improved properties (Ghosh Chaudhuri and Paria 2012). CSNs may have properties that are synergistic amid the cores and shells, one or both offer new properties liable on the interactions between the cores and shells and also a useful tool to engineer their surface and functional properties (Adijanto et al. 2013; Cha et al. 2013; Kitchin et al. 2004; Liu et al. 2017b; Wang et al. 2005; Wang and Li 2011). Finally, the CSNs shows distinctive properties which improve their functionality as compared to their individual constituent materials due to combination of different materials that work together to gain an inherent capability to encounter a specific application requirement (Daniel and Astruc 2004; Ghosh Chaudhuri and Paria 2012).

The studies on photocatalysis using Bismuth ferrite-based nanocomposites are very scarce. Li et al. (2009) and Liu et al. (2017) have synthesised core shell structured BFO@TiO$_2$ to prevent photocorrosion; aggregation and have shown it to exhibit visible light activity in photocatalytic dye degradation.Chaturvedi et al. (2015) have reported that the agglomeration of BFO could be prevented by having a polyaniline (PANI) shell around BFO. PANI is a conducting polymer with excellent stability, corrosion protection property, nontoxicity, facile and less cost of synthesis, and excellent instinct redox properties (Chen and Liu 2011; Guimard et al. 2007; Hatchett and Josowicz 2008;

Huang et al. 2003; MacDiarmid 2001; Tan et al. 2004; Virji et al. 2006). PANI has shown great potential due to its high absorption coefficients in the visible-light (Shaheen et al. 2001) and high mobility of charge carriers.

Luo and Maggard (2006) and Sandhya et al.(2013) have shown the ability of PANI to photosensitize TiO_2 under visible light by having PANI as the shell. PANI coating may also serve to prevent photocorrosion and chemical corrosion (Sandhya et al. 2013). Additionally, on irradiation by light, PANI not only acts as an electron donor (Shirota and Kageyama 2007), but also as an outstanding hole acceptor. These distinct characteristics of PANI makes it a perfect material to achieve enhanced charge separation efficiency in the photocatalysis. Lately, many researchers have shown the visible light mediated photocatalytic enhancement by using PANI/TiO_2 nanocomposites (Kalikeri et al. 2018). Lately, many researchers have shown the visible light and solar light mediated photocatalytic enhancement by using PANI/semiconductor oxide nanocomposites (Chaturvedi et al. 2015; Kalikeri et al. 2018; Mirmohseni et al. 2019; Riaz et al. 2014).

The present research work was initiated on the basis of the hypothesis that BFO based nanocomposite with TiO_2 or PANI shell around the BFO core, can enhance the photocatalytic activity and prevent the corrosion and agglomeration of BFO.

To the best of our knowledge, studies on photocatalysis using Bismuth ferrite-based nanocomposites are very scarce. There are only a very few reports on the photocatalytic degradation of dyes such as Congo red (CR) (Li et al. 2009); CR, Methyl orange (MO) dye (Liu et al. 2017b); Rhodamine-B (Hengky 2013) and Methyl violet (MV) (Liu and Wu 2019) using BFO@TiO_2 core-shell nanoparticles under visible light irradiation. However, these studies reported the photocatalytic efficacy in degradation of a single dye with no detailed studies on optimization of process parameters for degradation. The synthesis strategy used in these reports did not yield the composites with good visible light mediated photocatalytic activity. There is no report showing the photocatalytic efficacy of BFO@PANI core-shell nanoparticles or heterostructures.

Industrial wastewaters may encompass a mixture of various dyes as contaminants. It is well known that when several components are present, there is interaction and competition between the different components for the adsorption sites

on the catalyst. Thus, the presence of other dyes in the mixed dye system may alter the degradation of the target dye by photocatalysis. According to literature, very few reports on photocatalytic degradation of dyes from mixed dye solutions using nanocomposites, viz. Core-Shell $Fe_3O_4/SiO_2/TiO_2$ (Alzahrani 2017), Ni-Oxide@TiO_2 (Lee et al. 2016b), $BiVO_4/CeO_2$ (Wetchakun et al. 2012a) and CuO/nano-zeolite (Nezamzadeh-Ejhieh and Karimi-Shamsabadi 2013) have been reported. There is no report on the application of bismuth ferrite-based nanocomposites in the dye degradation from mixed dyes containing water.

Acid yellow-17 (AY) is a mono azo dye containing N=N group, used in textiles and for the production of personal care, laundry and cleaning agents (Liu et al. 2015) It is mainly used for dyeing wool, silk and polyamide fibres. It is used in printing on wool fabric, dyeing leather, paper surface shading and for colouring anodized aluminium. It is used in paint, medicine, cosmetics, shampoo, detergent, soap and shower gel and as edible yellow pigment (Gao et al. 2010; National Center for Biotechnology Information 2020). AY dye is harmful to living organisms and it is highly toxic to humans and animals (Karthikeyan et al. 2014). This dye can cause dermatitis and eye irritation. These azo dyes have a serious environmental impact, because their precursors and degradation products (such as aromatic amines) are highly carcinogenic (Szymczyk et al. 2007). Rhodamine B (Rh-B) is a xanthene dye widely used in printing, textile, foodstuffs, paper and photographic industries (Ferrari et al. 2013; Guo et al. 2011; Kornbrust and Barfknecht 1985; Richardson et al. 2004). It is a cationic dye potentially both genotoxic and carcinogenic (European Food Safety Authority 2010). It causes irritation in skin, eyes and respiratory tract. It is reported as harmful to human beings and aquatic life because of its carcinogenicity, reproductive and developmental toxicity, neurotoxicity and chronic toxicity (Carneiro et al. 2016; Kornbrust and Barfknecht 1985). Rh-B is extensively used in the textile industry due to its high stability. Methylene blue (MB) is a synthetic cationic dye and it belongs to the phenothiazine family. It is used in textile, plastics, food industries and medicine (Acemioğlu 2004; Purkait et al. 2007; Sodeinde and Eboreime 2013). It is mainly used on soft vegetable fibres such as jute, flax, hemp, silk and wool (Àngels Olivella et al. 2012). These dyes are either carcinogenic, mutagenic or cause neurotoxicity and chronic toxicity in humans and animals (Jedynak et al. 2019; National Toxicology Program 2008). The

molecular structure of these three dyes are presented in Appendix I. Water contamination originating from the dyeing and finishing stages in textile industry has become a major concern (Teng Ong et al. 2017), as it contains a mixture of dyes.

The present research work reports the synthesis of Bismuth ferrite@TiO$_2$ (BFO@TiO$_2$) and Bismuth ferrite@Polyaniline (BFO@PANI) heterostructured nanocomposites and their application in the visible light mediated photocatalytic degradation of three textile dyes namely, Methylene Blue (MB), Acid Yellow-17 (AY), and Rh-B from the mixed dye contaminated water. Visible-light energy occupies about 48% of the total solar energy and this strategy may allow harnessing solar energy for wastewater treatment.

In this research work, bismuth ferrite nanoparticles have been synthesized by various methods and their visible light activity in terms of degradation of dyes from the mixed dye contaminated water have been assessed. The method for the synthesis of bismuth ferrite nanoparticles, that resulted in maximum visible light activity for degradation of the dyes was chosen, followed by synthesis of BFO@TiO$_2$ and BFO@PANI heterostructured nanocomposites in the core-shell form, and optimization of synthesis parameters to achieve maximum degradation of dyes from the mixed dye contaminated water. The studies on the effect of various parameters affecting the photocatalysis along with kinetics of dye degradation have also been reported.

CHAPTER 2

LITERATURE REVIEW

An extensive review of literature was undertaken, following the need for the study and the background of this research work as discussed in Chapter 1. Based on the review of literature, the scope of the study and objectives were formulated. The literature review is summarized in the following sections.

2.1 Photocatalysis

Heterogeneous photocatalysis is a process based on utilization of light energy by a photocatalyst for a chemical reaction. Photocatalysis has attracted a great deal of attention due to its potential application in environmental remediation, where an organic pollutant (R) is degraded. When a photocatalyst is irradiated with a light energy which is higher than its bandgap energy, it results in excitation related to charge separation and generation of high energy states of electron and hole pairs. The holes and electrons are powerful oxidizing and reducing agents, respectively. The excited electrons jump to the conduction band (CB) and positive holes are formed at the valence band (VB). The electrons from the CB react with oxygen and reduce it to superoxide radical ($^{\circ}O_2^-$), which in turn oxidizes the organic compound to CO_2 and H_2O. The holes react with water to generate hydroxyl radicals ($^{o\cdot}OH$) and the hydroxyl radicals further bring about the oxidation of organic compounds. Holes can react directly with the organic compound and oxidize it to CO_2 and H_2O (Boroski et al. 2009). The redox reactions occurring during photocatalysis is shown in Equation (2.1) to (2.6) respectively.

$$Photocatalyst + hv \rightarrow e^- + h^+ \dots\dots\dots\dots\dots\dots\dots\dots\dots\dots\dots(2.1)$$

$$h^+ + R \rightarrow intermediates \rightarrow CO_2 + H_2O \dots\dots\dots\dots\dots\dots\dots\dots\dots(2.2)$$

$$H_2O + h^+ \rightarrow \cdot OH + H^+ \dots\dots\dots\dots\dots\dots\dots\dots\dots\dots\dots(2.3)$$

$$\cdot OH + R \rightarrow intermediates \rightarrow CO_2 + H_2 \dots\dots\dots\dots\dots\dots\dots\dots\dots(2.4)$$

$$O_2 + e^- \rightarrow \cdot O_2^- \dots\dots\dots\dots\dots\dots\dots\dots\dots\dots\dots\dots(2.5)$$

$$\cdot O_2^- + R \rightarrow intermediates \rightarrow CO_2 + H_2O \dots\dots\dots\dots\dots\dots\dots(2.6)$$
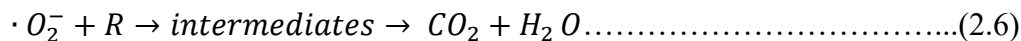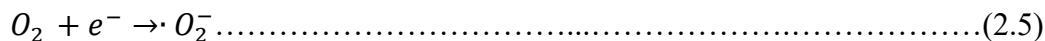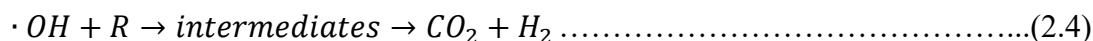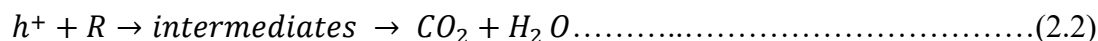
Particularly, photocatalysis in wastewater treatment has been considered a useful tool to remove harmful organic pollutants either by their complete mineralization (Chen et al. 2014; Khanna and Shetty K 2013, 2014; Nezamzadeh-Ejhieh and Karimi-Shamsabadi 2013; Soltani and Entezari 2013c), or partial degradation that permits successive biological, chemical and physical treatment (Lee et al. 2016). It is advantageous as it requires less time, mild chemical input, mild conditions of temperature and pressure. It does not produce waste (sludge) and avoids creation of toxic or harmful by-products. It involves the degradation of organic pollutants using various semiconductors as photocatalyst, in the presence of UV, visible or solar light. It opens up a possibility to utilize sunlight as an energy source.

Hence, the research and development in the field of photocatalysis is rising to improve photocatalysts and systems for several environmental applications. In this manner, it turns out to be a well-designed alternative for organic effluent treatment. Extensive studies and research conclude that an 'ideal photocatalyst' should possess the following attributes.

- ✓ Should have small size and high surface area
- ✓ Suitability towards visible or near UV light and good light absorption in the solar spectrum
- ✓ High conversion efficiency and high quantum yield
- ✓ Stability and sustained photoactivity.
- ✓ Biologically and chemically inert, non-toxic and low cost.

A photocatalyst reduced to a nanoscale can display properties that are different than that at macroscale size, facilitating unique applications in photocatalytic degradation of organic pollutants (Ansari et al. 2015; Chaturvedi et al. 2015). The increased surface area of the nanosized photocatalysts greatly influences their physiochemical properties (Kumari et al. 2010). In photocatalysis process, many semiconductor photocatalysts such as TiO_2, ZnO, ZnS, WO_3, CdS, Fe_2O_3 and $SrTiO_3$ (Chanathaworn et al. 2012; Fakhri and Behrouz 2015; Li et al. 2013a; Muhd Julkapli et al. 2014; Senthilvelan et al. 2013; Xue et al. 2015) are being used. Among them titanium dioxide (TiO_2) and zinc oxide (ZnO) have been widely applied as photocatalyst due to

their high activity, non-toxicity, chemical stability, lower costs, optical and electrical properties and environment friendly characteristics (Aslam et al. 2017; Bisen et al. 2013; Chen et al. 2011; Khataee and Zarei 2011; Senthilvelan et al. 2013; Shifu et al. 2009; Sobana and Swaminathan 2007). However, TiO_2 and ZnO have band gap energy of 3.2-3.5 eV and 3.3 eV respectively (Di Fonzo et al. 2009; Khan et al. 2014; Lu et al. 2008). These photocatalysts lack in efficiency due to their high band gap and low quantum yield. It cannot be used in sunlight, which consists only 4-5% of UV irradiations (Akhavan 2009; Nagaraja et al. 2012). The high rate of recombination of electrons and holes in these photocatalysts, reduce the rate of photocatalysis (Ikeda et al. 2001). This impairs the technological use of TiO_2 and ZnO (Sakthivel et al. 2002). Using UV irradiation for the treatment of industrial wastewater may be uneconomical and hazardous. Thus, there is a lot of interest in developing visible light active photocatalytic materials. Perovskite materials such as bismuth ferrite have attracted widespread attention due to their catalytic property, high multiferroicity and low band gap energy (Kalikeri and Shetty Kodialbail 2018a; Kim et al. 2005; Luo et al. 2010; Soram et al. 2012; Xue et al. 2015). BFO is one of the prime candidates for photocatalytic activity in a visible-light region, thus making it a potential catalyst for visible and solar photocatalysis.

2.2 Properties of Bismuth Ferrite (BFO)

BFO is one of the few single-phase materials that exhibit both ferroelectric and anti-ferromagnetic properties at room temperature. BFO material was first synthesized by Royen and Swars (1957). Under an ambient temperature, BFO has a highly distorted perovskite structure in rhombohedral symmetry. The BFO exhibits unique properties such as high multiferroic property, potentially high magnetoelectric property and superior electro dynamicity. Under its Curie temperature of about 1100 K, BFO shows simultaneous piezoelectricity, pyroelectricity and ferroelectricity along its polar axis (Li et al. 2009a). In addition to room-temperature magneto electric applications, due to these excellent properties, BFO-based materials could provide some opportunities for potential applications in many fields, such as photocatalysis, radio, television, microwave and satellite communication, bubble memory devices, audio video and

digital recording (Bucci et al. 1972; Kubel and Schmid 1990; Palkar et al. 2003; Wang et al. 2003).

2.3 BFO as a visible light driven photocatalyst

Recently, BFO has been examined as a photocatalyst in a visible-light region because of its small band gap value of 2.2 eV (Gao et al. 2006, 2007). Gao et al. (2007) further demonstrated that the BFO nanoparticles show significant degradation ability towards the photodegradation of some dyes upon irradiation with visible light due to its unique optical and multiferroic properties. In addition, due to the presence of internal dipole of the materials, it is being established that ferroelectric materials can be highly photoactive with some exceptional properties (Dunn et al. 2007; Tiwari and Dunn 2009). Recent research shows that the particle sizes greatly influence the Neel temperature and the lattice parameters of the BFO (Li et al. 2009a; Selbach et al. 2008; Shetty et al. 2002). BFO is a potential candidate for a valence band control element (Liu et al. 2005) and high chemical stability. Furthermore, according to recent studies, photocatalytic properties of BFO rely to a certain extent on the morphology of the sample. In the BFO nanocrystals, the recombination opportunities of the photogenerated electron and hole pairs in the volume will be reduced compared to the bulk BFO (Chen et al. 2017b), which can effectively move to the surface and degrade the adsorbed organic pollutant. Table 2.1 shows a brief summary of the application of BFO as a photocatalyst for degradation of various dyes, and it shows that BFO can be effectively used for photocatalysis under UV, visible and solar light.

2.3.1 Synthesis of BFO Nanoparticles

Initially, objectives of the synthesis approaches are for the search of monodispersed, high stability, crystallinity with controllable morphologies and significant progress has been made in the case of perovskite bismuth ferrite. Several techniques have been employed to produce BFO nanostructures. The main drive behind each technique was to obtain the highest purity at the lowest possible temperature with a process to make cost-effective materials for industrial applications. The traditional solid-state reactions method has the following drawbacks; they require a high sintering temperature (>800˚C) (Szafraniak et al. 2007; Wang et al. 2003), leaching in HNO_3 to

wash the secondary oxide phases and the residual Bi_2O_3 and did not yield the BFO particle in the nanoscale (Achenbach et al. 1967). Due to these drawbacks, new wet chemical approaches have gained interest and become the focus of the BFO materials development recently. The synthesis of various BFO micro and nano-structures using the wet chemical methods is highly controllable and tuneable.

A broad range of wet chemical methods have been applied to generate BFO nanoparticles in the past years (Chen et al. 2006; Hardy et al. 2009; Ke et al. 2011; Kim et al. 2005; Wei and Xue 2008). One among them is the sol-gel method, in which hydrated bismuth nitrate and iron nitrate salts are dissolved in 2-methoxyethanol and acetic acid to form a solution, followed by the addition of chelating agents to form a homogeneous polymeric precursor, ageing of the precursor to form dried gel and finally annealing at 600ºC in air or N_2 environment to yield nanoparticles (Kim et al. 2005). The sol-gel method exhibits a number of merits: (a) the procedures involved are simple, resulting in high reproducibility; (b) the method is cost effective due to the low sintering temperature with respect to the solid-state reaction (c) different particle sizes can be obtained by varying the sintering temperatures. However, the sol-gel process generally poses limitations such as a long synthetic duration (up to several days or even weeks) to form the dried gel and the toxicity of some emergent gases (such as NOx from the decomposition of metal nitrates) along with a large volume of shrinkage during the decomposition of the chelating compound. These limitations have led to the search for other wet chemical approaches towards the BFO nanoparticles synthesis. For instance, the hydrothermal method was commonly used to prepare sub-micron BFO particles or BFO nanoparticles. In this type of closed reaction system, the crystallization temperature will be effectively decreased due to autogenous pressure. Wei and Xue (2008) have reported the synthesis of BFO nanoparticles by a solution evaporation process. The resultant powder was collected and sintered for around 5 minutes at different temperatures (300–600°C) using the rapid thermal processor with a heating rate of up to 80°C/s to obtain BFO nanoparticles. Jiang et al. (2011c) have synthesized BFO powders with the Pechini method in which citric acid or EDTA are used as chelating agent. Chelation takes place in the solution to get desired nanomaterials (Galceran et al. 2007; Pathak and Pramanik 2001) and a very fine and homogeneous

multicomponent metal oxide materials are formed (Galceran et al. 2007; Pathak and Pramanik 2001).

Co-precipitation technique is a low cost and simple method in general. The method has the main advantage of a significantly lower synthesizing temperature. However, the disadvantage of this technique is the impurity phase's formation, which made this technique unpopular. Recently, Ke et al. (2011) and Kalikeri and Shetty Kodialbail (2018) investigated the synthesis of the BFO using a co-precipitation method with various parameters, but could not get rid of the formation of an impurity phase of BFO as $Bi_{25}FeO_{40}$.

One of the most widely used and useful methods of preparation of the BFO is the combustion synthesis route using a fuel. The fuel used may be glycine, citric acid, urea or sucrose (Farhadi and Zaidi 2009; Seema et al. 2010). Farhadi and Zaidi (2009) synthesized BFO using sol-gel auto combustion technique with sucrose as the fuel and it resulted in the formation of pure (single-phase) rhombohedral crystal structure and nano-size $BiFeO_3$ with the particle size observed to be around 40 nm. Combustion synthesis technique has become one of the most popular methods for the preparation of a wide variety of materials due to its simplicity, effectiveness, low cost, the broad applicability range, and the high-temperature self-purifying feature (Aruna and Mukasyan,2008). An aqueous solution of ions of metal nitrates acting as an oxidizer, and fuels such as glycine, urea or citric acid is heated up to moderate temperatures. Upon dehydration, the strongly exothermic redox reaction takes place and provides the energy for the formation of the oxide. BFO nanoparticles synthesized by ethylene glycol assisted, low temp (140°C) hydrothermal method have shown photocatalytic activity for degradation of Rh-B under visible-light illumination (Chen et al. 2014; Liu et al. 2013). The weak magnetic BFO nanoparticles synthesized by the sol-gel method have shown photocatalytic activity for degradation of MO dye under visible light irradiation (Gao et al., 2007).The pure BFO nanoparticles synthesized via ultrasound at low temperature was used for the degradation of MB dye under sunlight irradiation (Soltani and Entezari 2013c). Various synthesis methods and calcination conditions have been adopted to prepare BFO in the past few years for degradation of dyes (Table 2.1).

Table 2.1: Application of BFO synthesized by various methods, as a photocatalyst for degradation of dyes

Synthesis Method	Calcination conditions	Band gap (eV)	Dye	Light	Percentage degradation/Time (min)	Reference
Co-precipitation	600°C / 2 h	2.10	MO	UV	92% at 460 min	Liu et al. (2010b)
Solvothermal	160°C / 24 h	2.1	MB	Visible-light	86% as compared with TiO$_2$ P25	Huo et al. (2010)
Co-precipitation	600°C / 3 h	2.12	MO (10 mg/L)	UV and Visible	70% at 3 h	Xian et al. (2011b)
Modified polyacrylamide gel method	-	2.08	MO	Visible light	-	Zhang et al. (2011b)
Hydrothermal	200°C / 6 h	2.05	Rh-B	Visible-light	90.5%	Jiang et al. (2011b)
Aerosol- spraying 80%	500°C / 5 h	2.1	Rh-B	Visible-light	80%	Huo et al. (2011)

Method	Temp/Time	Band gap	Dye	Light	Degradation	Reference
Sol gel Method	80°C / 48 h	2.06	Rh-B	Visible light	-	Wang et al. (2011b)
Auto-combustion method	650°C / 48 h	2.1	Rh-B	Visible light	95%	Hengky et al. (2012)
Ultrasound	400°C + 500 °C / 0.5 h	2.00; 2.1; 2.07	Rh-B	Sunlight	100% 90 min	Soltani and Entezari (2013a; b; c)
			MB		100% at 90 min	
			Reactive Black5 (RB5)		60-95% at 65 min	
Electrospinning	550°C/ 2 h	2.19	Rh-B	Visible light	100%	Wang et al. (2013b)
Sol-gel	500°C / 2 h	2.05	MV, Rh-B and phenol	Visible light photo-Fenton-like catalyst	90% in the presence of H_2O_2	An et al. (2013)
Hydrothermal method	60°C / 12 h	-	MB	Visible light	64.9% at 20 min	Sun et al. (2013)
Hydrothermal	180°C / 72 h	-	MO	UV-light	52-61% at 180 min	Gheorghiu et al. (2013)

Hydrothermal	200°C / 5 h		MO	Visible light	72.5% at 350	Gao et al. (2015b)
Combustion reaction	500°C / 4 h	2.6	RB5	Visible-light	43% at 100 min	Kaur et al. (2015)
Co-precipitation method	950°C / 8 h	-	MB	Visible light	100% at 30 min	Shabbir et al. (2016)
Hydrothermal	200 °C / 3 h	-	Evans Blue (EB)	-	80% -	Paliwal et al. (2017)
Hydrothermal-	-	-	(CR)	Visible light	44%-	Fatima et al. (2017)
Thermal decomposition	500°C & 600°C / 2 h	2.1	MB	Visible light	61% at 90 min	Masoudpanah et al. (2017)
Bio templating method	550^{0}C / 2 h	-	MB	Visible light	96% at 180 min	Mohd Azmy et al. (2017)
Co-precipitation Method	400°C / 2 h	2.2	Acid yellow-17 (AY-17)	UV	90%, 85% 100% at 135 min	Kalikeri and Shetty

			and Reactive blue-19 (RB-19)	Visible and Solar light	86%, 84% 100% at 135 min	Kodialbail (2018)
Sol-gel technique	500°C / 4 h	≈2.1	Rh- B	Visible light	94% at 180 min	Siddique et al. (2019)
Sol-gel technique	-	2.0-2.77	Rh- B	Visible light	-	Haruna et al. (2020)

2.3.2. Limitations of BFO as a photocatalyst

Jones et al. (2008) have shown that perovskite ferroelectric materials can photo corrode. Li et al. (2009a) and Luo and Maggard (2006) have reported that as a visible light photocatalyst, BFO lacks stability due to photo-corrosion on the surface of the particle. Zhang et al. (2011b) have also reported that BFO has a tendency to aggregate. Thus, the catalyst modifications and new developments are required in order to improve photocatalytic efficiency, prevent photocorrosion, complete degradation of organic pollutants, improve visible light absorption, improve stability and reproducibility, and to improve recycle and reuse abilities of nanoparticles.

Though noble metal doped catalysts have shown improved visible light photocatalytic activity by prevention of electron–hole recombination, the cost of noble metals and the possible corrosion of these during photocatalysis are the noted disadvantages (Bumajdad and Madkour 2014). The review of literature suggests that bismuth ferrite nanoparticles have band gap energy of 2.2 eV (Soltani and Entezari 2013b) and they exhibit good visible light photocatalytic activity. The syntheses of these nanoparticles are simpler and cost effective. Hence, the surface of BFO nanoparticle may be protected by creating a shell of other semiconductor material which not only prevent photo-corrosion but also create a heterojunction to alter the band gap of BFO along with prevention of electron-hole recombination.

Recently researchers are making efforts in the controlled synthesis of core-shell structured or other heterostructure bismuth based nanocomposites such as $Bi_{12}TiO_{20}$/g-C_3N_4 (Sun et al. 2016), $BiFeO_3$@ Ce-doped TiO_2 (Gong et al. 2013), (Ba, Sr)TiO_3/TiO_2 (Li et al. 2013a), $BiFeO_3$ coupled with nanocrystalline TiO_2 (Humayun et al. 2016), Bi_2S_3/TiO_2 (Brahimi et al. 2007), CoO_4O_4-$BiFeO_3$ (Liu et al. 2005), $BiVO_4$/ TiO_2 (Zalfani et al. 2015), $BiFeO_3$-TiO_2 (Humayun et al. 2016; Liu and Wu 2019), BFO@TiO_2 (Hengky 2013; Li et al. 2009b; Liu et al. 2017b; Zhu et al. 2014),n-$SrTiO_3$/p-BiOI (Xia et al. 2018), polymethyl methacrylate @BFO (Tamboli et al. 2014), BFO@ $SrTiO_3$ (Luo and Maggard 2006), ZnO/TiO_2 (Marcì et al., 2001), and $BiFeO_3$/$ZnFe_2O_4$ (Safizade et al. 2018) which can improve the photocatalytic efficacy

by decreasing the recombination rate of the photogenerated electron-hole pairs. These composite structures are gaining importance because of their conducive and versatile compositions and structures to serve such purposes (Pang et al. 2013; Tamboli et al. 2014). The studies on photocatalysis using bismuth ferrite-based nanocomposites are very few. Li et al.(2009a) and Liu et al.(2017b) have synthesised core shell structured BFO@ TiO_2 to prevent photocorrosion, aggregation and have shown it to exhibit visible light activity in photocatalytic dye degradation.

2.4 BFO@TiO_2 nanocomposites

The photo-corrosion and aggregation of BFO can be prevented by having a shell around the BFO core. Such a shell can prevent aggregation of BFO nanoparticles and the photo-corrosion by UV radiation in sunlight. The protection of the surface of the BFO nanoparticles by creating a heterojunction of BFO with TiO_2 forming BFO core - TiO_2 shell nanoparticles Li et al.(2009a) and BFO with $SrTiO_3$ forming BFO core $SrTiO_3$ shell nanoparticles Luo and Maggard (2006) to alter the band gap of the BFO have been reported.
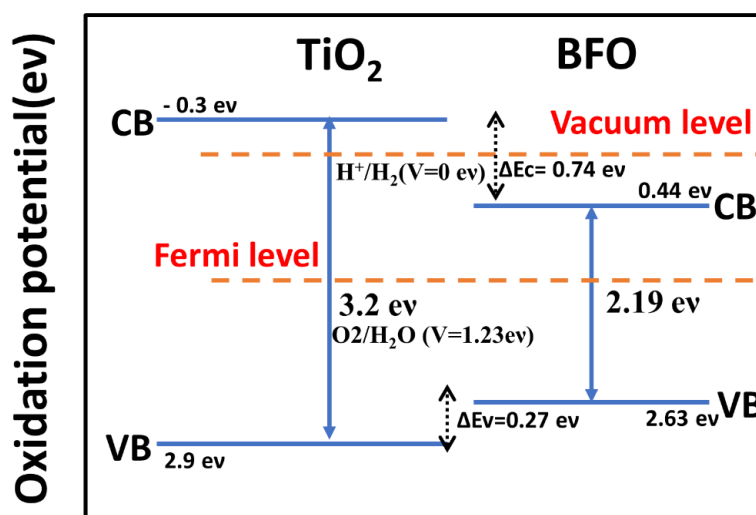
Figure 2.1: Schematic illustration for the calculated energy band level of TiO_2 and BFO

Li et al. (2009a) synthesized BFO by hydrothermal approach combined with a hydrolysis precipitation process of tetrabutyl titanate (Ti($C_4H_9O)_4$) to form BFO@TiO_2 core-shell nanoparticles. They varied the mass ratio of BFO to TiO_2 and found that the

nanoparticles with the mass ratio of 1:1 exhibited a band gap energy of 2.2 eV and showed maximum photocatalytic activity. They studied the photocatalytic degradation of CR dye under 500 W Xenon lamp with 2 g/L catalyst loading and observed 70% degradation in 120 min with 1:1 mass ratio. However, with 2:1 and 1:2 mass ratio, they were able to achieve only 50% and 48% degradation respectively. The core-shell structured BFO@TiO_2 systems reported by Li et al. (2009a) consisted of two semiconductors in contact with each other and an electronic interaction occurs at their point of contact (heterojunction). They calculated the position of a valence band and a conduction band of the BFO and the TiO_2 against the normal hydrogen electrode. As shown in Figure 2.1, when BFO and the TiO_2 are in contact, a heterojunction is created that improves the photogenerated charge carrier's lifetime by enhancing the charge separation, thus improving the efficiency of the photocatalytic activity. The separation of photogenerated electrons and holes induce redox reactions according to the relative potentials of the conduction and the valence bands of the two semiconductors and the redox potentials of the redox couples present at the interface.

Hengky (2013) has synthesized BFO by auto combustion method with glycine as a fuel and coated BFO with TiO_2 by hydrolysis of Titanium Tetra (IV) Iso Propoxide (TTIP) with various molar ratios of $BiFeO_3$ to Ti precursor of 1:1, 1:2 and 2:1. They observed a thin film of TiO_2 of around 1-3 nm thickness around the BFO particle. Maximum photocatalytic activity was exhibited by TiO_2 coated BFO synthesized with 1:2 molar ratio, which resulted in >90% degradation of 10 ppm Rh-B in 150 min with 3 g/L catalyst loading under solar simulator. They proposed that in TiO_2 coated BFO, the heterojunctions are created at the contact point of $BiFeO_3$ and the TiO_2, which improves the life time of the photogenerated charge carriers by enhancing the charge separation. It enhances photo redox reactions and improves photocatalytic activity.

Zhu et al (2014) developed the BFO/TiO_2 Nanotube (NT) arrays composite electrode system. TiO_2-NTs were prepared by anodic oxidation of a titanium sheet, BFO synthesized by solution precipitation method, followed by deposition of $BiFeO_3$ nanoparticles on TiO_2-NTs via an ultrasonic-immersion strategy to form the composite electrode system with a band gap energy of 2.12 eV. They found that the surface modifications of $BiFeO_3$ nanoparticles can extraordinarily improve the surface

photovoltage. The photochemical responses of BFO/TiO$_2$-NTs composite electrode exhibited much greater photoelectrocatalytic activity for Rh-B degradation under visible-light irradiation compared to TiO$_2$-NTs. Though 20 mg/L Rh-B was completely degraded in 150 min by photo electrocatalytic process, only 16% degradation was achieved by photocatalytic process with visible light irradiation under 500 W Xenon lamp. They found that, the BFO component plays a key role in promoting the generation of photo-induced charges under visible light and an appropriate positive bias voltage to the composite electrode could greatly enhance BFO/TiO$_2$-NT photochemical performance. They attributed it to the ferroelectric properties of polarized BFO nanoparticles in the composite. The photocatalytic activity of this BFO/TiO$_2$-NT arrays composite electrode system was found to be very low.

Liu et al. (2017b) synthesized BiFeO$_3$ by a citrate self-combustion method and coated with TiO$_2$ by hydrolysis of titanium butoxide to form BFO@TiO$_2$ core shell structured photocatalyts. They studied the photocatalytic activity by photocatalytic oxidation of MV, MO and CR dyes under visible-light irradiation with 400 W lamp and obtained 95%, 56% and 76%, degradation respectively in 150 min with 1g/L catalyst. BiFeO$_3$@TiO$_2$ synthesized with a mass ratio of 1:1 and TiO$_2$ shell thickness of 50-100 nm showed a band gap energy of 1.77 eV and the highest catalytic activity. The high visible light activity was reported to be due to its strong photo-absorption ability and charge recombination rate. The low electron–hole recombination rate of BFO@TiO$_2$ is credited to the presence of electronic-accumulation centres formed by the electronic interaction between the BiFeO$_3$ core and TiO$_2$ shell. These centres effectively separate the electrons and holes, leading to high quantum efficiency. Theoretically, an internal electric field from TiO$_2$ to BFO will be generated when BFO and TiO$_2$ come in contact and form a heterojunction interface. Driven by this internal electric field, the holes and electrons will flow in opposite directions, thus leading to the efficient separation of photogenerated electrons and holes and enhanced photocatalytic activity.

Liu and Wu (2019) conducted studies on the BiFeO$_3$/TiO$_2$ core-shell nanocomposites (NCs) and reported different degradation mechanism involving the piezo catalytic, photocatalytic, and piezophototronic activity. They synthesized micrometre-sized BiFeO$_3$ particles by a hydrothermal process and ball milled it to reduce to nano-size. The BiFeO$_3$ nanoparticles were then coated with TiO$_2$

nanoparticles by sol gel method, and an external bias was applied through a high voltage power supply for polling the composite. They found that $BiFeO_3/TiO_2$ shows a much high piezophototronic catalytic activity than piezo catalytic or photocatalytic process. They have reported that, in photocatalytic process, the charge carriers migrate to either side from TiO_2 to $BiFeO_3$ and $BiFeO_3$ to TiO_2. In piezophototronic catalytic process, the p-n junction has a band alignment which is steeper than that in photocatalytic process. When, the polarization is from the $BiFeO_3$ to TiO_2 side, the electrons migrate from the TiO_2 to $BiFeO_3$ direction while the holes move in the opposite direction. They have reported that TiO_2 plays vital role as photo-induced charge carriers, while the BFO acts to narrow down the band bending for charge transfer, which significantly enhances the separation of the electron and hole pairs at the heterostructure interface. Therefore, both the individual components are very important to enhance the activity and heterostructure formation. Without the presence of each of the components, the persuaded charge carriers in the catalysts may be blocked. These $BiFeO_3/TiO_2$ with polling when used for photocatalytic degradation of 10 ppm MV dye under irradiation by 150 W xenon lamp and they obtained only 50% degradation in 120 min, showing that the synthesis approach adopted by Liu and Wu (2019) is not favourable to develop an efficient photocatalyst.

The literature review suggests that there are very limited reports on BFO@TiO_2 nanocomposites which are core-shell structured or as composite electrode system. They have studied the degradation of a single dye and obtained very low degradation even with high power lamps or when appreciable degradation was achieved high catalyst loading was used. It appears that there is a necessity to modify the synthesis method, calcination conditions and/or or optimize the composition so as to improve the photocatalytic activity.

2.5 PANI based nanocomposite as visible light driven photocatalyst

Recently, conducting polymers with extending π conjugated electron systems have been widely studied for their electronic and optoelectronic properties. Due to their excellent high absorption coefficients in the visible spectrum, high electron-hole mobility, and environmental stability, conducting polymers have attracted considerable

attention of researchers. Due to their essential electron-hole mobility properties, conducting polymers have been demonstrated to perform as constant photo-sensitizers for semiconductors, such as ZnO, WO_3, TiO_2, ZnS, BFO etc. (Aksu 2005; Autin et al. 2013; Chen et al. 2012; Golsheikh et al. 2015; Nasreen et al. 2013; Sadek et al. 2008; Shahabuddin et al. 2016). In integrative scientific research areas, conducting polymers, such as, polyphenylene, polyaniline, polypyrrole, polyacetylene and polythiophene, have been studied vastly, including for sensors (Sadek et al. 2007), batteries (Sengodu and Deshmukh 2015), electronics and thermoelectric, electromagnetic, electro-luminescence and electromechanical applications (Bhadra et al. 2009; Hu et al. 2015b; Sengodu and Deshmukh 2015).

Owing to its notable physical and chemical properties, such as thermal stability, high conductivity, easy preparation procedure, better processability, excellent optical and magnetic properties and low cost (Karim et al. 2009; Lu et al. 2011; Riaz et al. 2014) PANI is the widely examined conducting polymer amid all of the conducting polymers. Moreover, PANI is an efficient electron donor and an excellent hole transporter upon visible light excitation. It has been studied broadly because of its unique conjugation mechanism, engaging benzenoid and quinoid rings accompanying to three different oxidation states (Ahuja et al. 2018; Reddy et al. 2016). PANI has been proved as a potential candidate in commercial applications owing to its significant absorption coefficient in a visible region, easy protonation reversibility, excellent redox properties, and good environmental stability (Ahuja et al. 2018; Ayad and El-Nasr 2010; Xiong et al. 2012; Karim et al. 2009; Lu et al. 2011; Tran et al. 2009; Wang et al. 2010b). Because of these useful properties, the photoactivity can be enhanced by using PANI as a photosensitizer to modify the photocatalysts by extending its spectral response to visible region (Shang et al. 2009). And forming a composite of PANI with a semiconductor, the spatial separation of charge carrier increases, which leads to reduction in the probability of recombination which is due to interfacial charge transfer (Sarmah and Kumar 2011). On absorption of visible light π- π* transition is induced in PANI. The electrons in the excited state of PANI are transported into the d-orbital of TiO_2. The energy level of the d-orbital of TiO_2 (CB) and the π*-orbital of PANI match well. The electrons then lead to redox reaction (Sandhya et al. 2013).

PANI as a semiconductor polymer and semi-flexible rode polymer has been used to improve the photocatalytic performance of several semiconductors (Cui et al. 2018; Liu et al. 2017a; Shirmardi et al. 2018). In the combined state with wide bandgap semiconductors, PANI can handover the electrons produced upon visible light irradiation to the conduction band of semiconductor, such as TiO_2, since the lowest unoccupied molecular orbital (LUMO) level of PANI is energetically higher than the conduction band (CB) edge of TiO_2 (Kalikeri et al. 2018; Wang et al. 2010). As per a significance, a considerable quantity of interfacial charge transfer occurs, and recombination of the electron-hole pair is considerably reduced, which could provide a significant photo response in the visible/solar light range of the spectrum. This expansion will benefit the application of the photocatalysis under visible/sunlight. Composite materials comprising conjugated polymers and wide bandgap inorganic semiconductors have been widely investigated for exploring optical, photocatalytic and photoelectric conversion applications (Glimcher and Sparks 1992; Jang et al. 2000; Luzzati et al. 2002; Pron and Rannou 2002).

2.5.1 PANI based nanocomposites for photocatalytic degradation of dyes

Various modified photocatalysts based on PANI such as PANI/TiO_2 (Li et al. 2008), PANI/ $BiVO_4$ (Li et al. 2008), PANI /SnO_2 (Geng et al. 2007), and PANI/MoO_3 (Wei et al. 2010) have been reported for photocatalytic applications. Wang et al. (2016) have designed and synthesized monodisperse PANI @CdS core-shell nanospheres to probe the mechanisms of photo-corrosion inhibition and for photocatalytic H_2 production. Zhang et al. (2012) revealed that the exciting enhanced visible light photocatalytic activity and excellent anti-photo corrosion performance of CdS photocatalysts are obtained after hybridizing by monolayer PANI. Table 2.2 presents PANI based nanocomposites used for photocatalytic degradation of dyes. These studies suggest that PANI with various semiconductors acts as a visible light active photocatalysts, with good performance in degradation of dyes.

Table 2.2: **PANI based nanocomposite as photocatalyst in dye degradation.**

Catalyst /Dye	Dye	Dye concentration (mg/L)	Amount of catalyst (mg/L)	Percentage Degradation/ Time (min)	Source of light	Reference
Fe_3O_4@Polyaniline@Au	Rh-B	25	25	85% / 10 min	Visible light	Xuan et al. (2009)
PANI@TiO_2 Ratio 1:9; 2:8; 3:7	Malachite Green (MG)	10	10	94.4% / 360 min 99.4% / 360 min 92.2% / 360 min	UV-Light	Sarmah and Kumar (2011)
Polyaniline/graphene (PANI–Gr)	Rose Bengal (ROB)	10	-	56% / 180 min	Visible light	Ameen et al. (2012)
PANI-ZnO	Reactive Brilliant Blue KN-R (RBB)	20	20	72% / 180 min	Visible-light	Ma et al. (2011)
PANI/TiO_2	MO	20	80	100% / 360 min	Visible light	Lin et al. (2012)
PANI/TiO_2	MO	10	10	50% / 120 min	Visible light	Olad et al. (2012)

PANI/ZnO	MB	10	30	82% / 60 min	Visible light	Olad and Nosrati (2012)
Polyaniline/graphene (PANI–Gr)	Rh-B	-	-	56% / 180 min	Visible light	Ameen et al. (2012)
PANI/CdO	MB	4.8	0.4	97% / 240 min	Sunlight	Gülce et al. (2013)
PANI/Ag/Ag$_3$PO$_4$	Rh-B	10	30	95% / 10 min	Visible light	Bu and Chen (2014)
Chitosan Grafted-Polyaniline/CO$_3$O$_4$	MB	10	15	-	Visible light	Shahabuddin et al. (2015)
PANI-Fe$_3$O$_4$@ZnO	MB	10	20	90% / 40 min	Visible-light	Zhang et al. (2016b)
GR-PANI	Rh-B	4	10	55% / 10 min	Visible-light	Neelgund et al. (2016)
RGO/PANI/Cu$_2$O	CR	10	25	81% / 30 min	Visible-light	Miao et al. (2016)

Photocatalyst	Dye	Concentration	Dosage	Degradation / Time	Light source	Reference
PANI–Fe$_3$O$_4$	Acid violet 19 (AV-19)	20	60	90% / 80 min	Visible light	Patil et al. (2016)
PANI/ZnO (different molar ratio (1 M, 1.5 M and 2 M polyaniline)	MO and MB	100	100	69.8% / 180 min 74.6% / 180 min 98.3% / 180 min 99.2% / 180 min 24.7% / 180 min 39.9% /180 min	Visible light	Saravanan et al. (2016)
Polyaniline/ZnO/chitosan	Reactive orange (RO) and MB	50	30	96% / 120 min 88.5% / 120 min	Sunlight	Pandiselvi and Thambidurai (2016)
SrTiO$_3$ /Polyaniline	MB	30	10	84% / 90 min 97% / 90 min	Visible light Sunlight	Shahabuddin et al. (2016)
Polyaniline/Fe$_3$O$_4$	Acid violet 19	20	600	95.2% / 80 min	Visible light	Patil et al. (2016)
PANI@TiO$_2$	MB	30	40	71% /-	Visible light	Yang et al. (2017)

Polyaniline/BiYTi$_2$O$_7$	Azocarmine G (AG)	20	20	78% / 60 min	Visible light	Luan et al. (2017)
Ag/AgCl–Polyaniline	MB	10	70	50% / 90 min	Sunlight	Ghaly et al. (2017)
PANI/TiO$_2$	Reactive Red 45(RR-45)	30	100	77% / 90 min 95% / 90 min	Visible light Sunlight	Gilja et al. (2017)
CdS, Hybrid Nanocomposites, (CdS/PTh), (CdS/PPy), (CdS/PANI),	MB	10	25	71% / 300 min 77% / 300 min 67% / 300 min	Sunlight	Hiragond et al. (2018)
ZnSe/PANI	MB	-	-	50% / 30 min	Visible light	Shirmardi et al. (2018)
PANI/TiO$_2$	RB	50	1000	100% / 120 min 100% / 120 min 98.4% / 120 min	Sunlight Visible light UV-light	Kalikeri et al. (2018)
Polyaniline/ZnO	MO	100	100	87.5% / 60 min	Visible Light	Nerkar et al. (2018)

PANI-ZnO 1:1; 1:2; 1:3	MB	50	-	52% / 120 min 90% / 120 min 58.9% / 120 min	Visible-light	Qin et al. (2018)
CdS/PANI	MB	10	25	60% / 360 min	Solar light	Hiragond et al. (2018)
Activated Charcoal (AC)/PANI Zinc oxide activated charcoal polyaniline (ZACP)		50	50	62% / 120 min 95% / 120 min	Visible light	Steplin Paul Selvin et al. (2018)
PANI/ZnO	AB	30	10	80% /60 min	Solar	Gilja et al. (2018)
PANI/RGO	MG Rh-B CR	10	17	99.68% / 15 min 99.38% / 30 min 98.73% / 40 min	Visible-light	Mitra et al. (2019)
Hydrolysed pectin (HPEc)-g-PANi CdS@HPEc-g-PANi mCdS@HPEc-g-PANi	RB	10	250	76% / 150 min 84% / 150 min 86% / 150 min	UV-light	Alipour and Mansour Lakouarj (2019)

PANI@TiO$_2$	MB MG Eosin Yellow (EY) Rose Bengal (RoB)	10	23	12.2% / 60 min 32.5% / 60 min 44.2% / 60 min 14.2% / 60 min	UV-light	Raveendran et al. (2018a)
MoS$_2$-PANI	MB	33	50	75% / 150 min	UV-light	Saha et al. (2019)
g-C3N4/ TiO$_2$@polyaniline		20	30	100% / 150 min	Solar light	Alenizi et al. (2019)
Fe$_3$O$_4$/ZnO/PANI	MO	100	100			Habibi-Yangjeh and Shekofteh-Gohari (2019)
PANI/TiO$_2$	AY	10	10	89%	Visible light	Nair and Shetty Kodialbail (2020)

2.5.2 BFO@PANI nanocomposites

Luo and Maggard (2006) and Sandhya et al.(2013) have shown the ability of PANI to photosensitize TiO_2 under visible light by having PANI as the shell. Sandhya et al (2013) have reported that PANI coating may also serve to prevent photocorrosion and chemical corrosion. Chaturvedi et al. (2015) have reported that the agglomeration of BFO could be prevented by having a PANI shell around BFO. Additionally, on irradiation by light, PANI not only acts as an electron donor (Shirota and Kageyama (2007), but also as an outstanding hole acceptor. These distinct characteristics of PANI makes it a perfect material to achieve enhanced charge separation efficiency in the photocatalysis. On considering the excellent properties of PANI in acting as a photosensitizer for other semiconductors to utilize the spectral region in visible range, and also based on its charge carrier efficiencies to prevent the electron-hole recombination rate, it can be considered as a suitable candidate to form a shell/coating over BFO to prevent photocorrosion and aggregation.

The synthesis of BFO@PANI core-shell statured nanocomposites (NCPs) is challenging as it requires generating the polymer coating uniformly and completely on the surface of the metal oxide core by a polymerization reaction in a solution phase (Prabhakaran and Hemalatha 2008). The difficulty is at slowing down the rate of polymerization and controlling the polymerization on the surface of the core rather than in the solution. In the process of coating of BFO with PANI, the requirement of high acidic environment for polymerization of PANI leads to etching of the BFO core of the material. To overcome this problem, Chaturvedi et al. (2014, 2015) and Prabhakaran and Hemalatha (Prabhakaran and Hemalatha 2008, 2012) have adapted synthetic route which effectively controls the polymerization of PANI onto the surface of BFO. Multiferroic polymer core-shell combination for tuning the band gap and coercivity has been reported by Chaturvedi et al. (2015). They achieved a variation in the band gap of BFO from 2.24 eV to 1.98 eV and changes in the coercivity from 118 to 100 Oe by increasing the polyaniline shell thickness from 0 nm to 15 nm. BFO@PANI nanocomposites showed the ability to prevent the agglomeration of the particles to crate the heterojunction between individual particles and structural changes in terms of lattice parameters and bond angles which is due to shifts in the vibrational frequencies. PANI

exhibited significant reduction in coercivity and change in exchange bias fields compared to that of BFO nanoparticles. They concluded that the magnetic properties observed in BFO@PANI core-shell nanoparticles are a result of de-agglomeration as well as PANI induced structural changes. Zhu et al. (2017a) used the BFO particles of size 200 nm synthesized by normal citric acid sol-gel method in synthesizing BFO/ PANI composites with the different weight ratio by in situ emulsion polymerization. They studied the microwave absorption properties of BFO/PANI composite and found it to be promising lightweight and multiband microwave absorber.

However, to the best of our knowledge there is no reports on the photocatalytic activity of BFO@PANI nanocomposites. Hence, detailed studies on the photocatalytic degradation of single and mixed dye system are required.

With a view that BFO is a visible light active photocatalyst it was hypothesized that the BFO nanoparticles with TiO_2 or PANI as the shell, forming a core shell nanoparticle can not only enhance the visible light activity either by photosensitization or band gap tuning but also can prevent photocorrosion and aggregation of BFO. Therefore, the present study reports the synthesis of BFO@TiO_2 and BFO@PANI core shell nanoparticles and their application in photocatalytic degradation of dyes under visible light irradiation.

2.6 Photocatalytic degradation of dyes in water containing mixture of dyes

As the dye-containing industrial effluents may include a mixture of many dyes, hence it is essential to study the degradation of the dyes in the mixed dye system. The presence of other dyes may influence the degradation rate of a target dye. The photocatalytic degradation process starts with the adsorption of the dyes on the catalyst surface. It is well known that when several components are present, there is interference and competition between the different components for the adsorption sites. The adsorption isotherms for a single component system are thus inapplicable for the thematic-component system. The interference or competition by other dye molecules thus affects the rate of degradation of the dyes. Thus, detailed studies on the photocatalytic degradation of dyes in a mixed dye system are required.

2.6.1. Photocatalytic degradation of dyes in mixed dyes aqueous systems and the photocatalysts

Photocatalytic degradation of dyes in mixed dye aqueous solutions using various photocatalysts have been reported. Various photocatalysts employed in degradation of dyes from mixed dye aqueous solutions is presented in Table 2.3. When many organic compounds like dyes are present in wastewater, selective treatment is possible in defined conditions. It is possible to prioritise the degradation of one or the other pollutants when they coexist in wastewater (Robert and Malato 2002). Conditions like pH and catalyst loading have been found to influence the selectivity of compounds towards degradation. Robert and Malato (2002) have studied selective photocatalytic degradation of organic compounds under solar irradiation for the mixture of 4-hydroxybenzoic acid (4-HBz) and benzamide (Bz) using TiO_2 as a catalyst. They observed that at pH 4, the selectivity for degradation was towards 4- HBz than Bz, whereas at pH 8 the selectivity for degradation was towards Bz than 4- HBz. At pH 6, the degradation rates for both the organic compounds were similar. They have also found that at higher TiO_2 concentrations, the catalyst loading differently influenced the degradation of different organic compounds, thus showing that catalyst loading influences the selectivity.

The presence of another dye in the solution influences the degradation of the target dye. The presence of other dye may promote or inhibit the degradation of a target dye. Sahel et al. (2010) have investigated the photocatalytic degradation of a mixture of two anionic dyes, Remazol Black (RB5) and Red Procion (MX-5B) using TiO_2 (Degussa P-25) as a catalyst under irradiation with light of wavelength higher than 290 nm. They observed that adsorption of MX-5B was not affected by RB5. However, extent of RB5 adsorption from the mixed dye solution was different as compared to that when it was present individually as a single dye. They observed that, above 15 μmol/L dye concentration, both anionic dyes competed for the same adsorption site. But at lower concentration of dyes, the rate of disappearance of the dyes in single dye solution or in mixed dye solutions were found to be similar, even though adsorption of RB5 was modified. At high concentration their disappearance rates in the mixture decreased owing to decrease in the number of available sites. This difference of behaviour was

explained by considering the modification of pH on increasing the initial concentration of MX-5B in the mixture. Their studies on analysis of Total Organic Carbon (TOC) and inorganic ions suggested that the degradation mechanism for a dye in the mixed dye solution is different than that when it is present as a single dye.

Veldurthi et al. (2015) assessed the photocatalytic activity of $LiMg_{0.5}Mn_{0.5}O_2$ based on the degradation of dyes from mixed aqueous solutions containing MB and MO under visible light. MO was found to be preferentially decomposed when compared to MB in the mixed dye solution. Photocatalytic degradation of both the dyes when they were present as single dyes was lower than that when they were in mixed dye solution. The presence of MB promoted the degradation of MO in the mixed dye solution. Romão and Mul (2016) studied photocatalytic decomposition of MO and Atrazine in mixed dye aqueous solution in a top illumination reactor with irradiation using UV tubular lamps with TiO_2- P25. At catalyst concentration of 0.25 g L^{-1}, the catalyst showed substrate selective activity favouring the degradation of MO over Atrazine. At higher catalyst loading, decomposition of both the compounds was achieved simultaneously. However, the presence of MO did not affect the decomposition rate of Atrazine when initial concentration of MO was 10 times lower than that of Atrazine. Their results proved that the adsorption of dyes on the catalyst is one of the determinant steps in simultaneous degradation of dyes by photocatalysis. They attributed the lower rate of Atrazine decomposition in the presence of MO as associated with strong adsorption of MO on the catalyst surface under acidic and neutral conditions of pH.

Hassan Zaki and Mohamed Ali. El Rouby (2019) studied the photodegradation of the three mixed organic dyes: Tartrazine (Tz), Rh-B and MB using Au-functionalized sodium titanate nanotubes (Au-NaTNT) as catalyst under simulated sunlight. 65% of MB was decomposed after 240 min, while Tz and Rh-B remained in solution showing no trace of reaction after that time. The authors reported that Au-NaTNT composite showed selectively to MB degradation. They attributed the selectivity towards MB to the net charge of the dyes under consideration. Xie et al. (2018) have reported the degradation of RhB and MB in a simulated dye effluent of binary dye mixture using carboxymethylcellulose (CMC-Na) modified $SrTiO_3$ as a photocatalyst under UV light.

They found that, group hindrance significantly enhanced the preferential adsorption and photodegradation to MB in Rh-B-MB binary solution at 10 mg/L.

Saha and Chaudhuri (2003) studied the solar light mediated photocatalytic degradation of three metal complex azo dyes Acidol yellow, Acidol grey and Acidol scarlet from the dye mixture and treatment of woolen textile dye house waste using ZnO as a catalyst. They found that when the dyes were simultaneously degraded, 67-93% decrease in degradation was obtained as compared to that obtained with single dye degradation. The studies by Chomkitichai et al. (2019) showed that MB degradation is faster as compared to Rh-B in mixed dye solution of MB and Rh-B solution under UV light irradiation with multi–phase $BiVO_4$ as the catalyst. A preferential degradation of MB over MO was also observed by Alzahrani (2017) in their studies on degradation of binary azo dyes, MO and methylene blue in aqueous solution under UV light irradiation using core-shell $Fe_3O_4/SiO_2/TiO_2$ nanospheres with magnetic cores.

Taghdiri (2017) in their studies on photocatalytic degradation of dyes from the mixtures of MB, MO, Rh-B, in various combinations using magnetic activated carbon (MAC) nanoparticles coated with an organic hybrid of silicotungstic acid under sunlight, visible, and UV irradiation have found that, while the MO and Rh-B were not degraded when present as single dye under sunlight, these dyes were degraded in mixed dye solution containing MO, Rh-B and MB. Their results also showed that the composite can selectively adsorb MB molecules from binary mixtures of MB/MO or MB/Rh-B.

Wongkalasin (2011) studied on photocatalytic degradation of binary mixture of azo dyes AY and Acid Black (AB) using TiO_2. They noticed that at any given initial concentrations of AY and AB mixtures, AY degradation was always greater than AB, which indicated that AY was easily degraded, as it is a mono azo dye with less complexity in molecular stature than AB, which is a diazo dye. The resultant oxygen species actively react with the AY dye.

The review of literature suggests that, the adsorption and photocatalytic degradation rates of dyes are altered by the presence of other dyes. Preferential degradation of one dye over the other in mixed dye aqueous solutions depends on

solution pH, catalyst concentration and concentration of the dyes which are present in the solution. In a mixed dye solution, each of the dye gets degraded to a different extent based on the nature of the dyes and the complexity of the molecular structure of the dyes. The photocatalytic degradation behaviour of dyes in mixed dye solutions also depend on the type of catalyst used. Most of the catalysts used for mixed dye degradation are semiconductor oxides.

Table 2.3: Photocatalytic decolorization of mixture of dyes

Dyes	Catalyst used	Irradiation source	Percentage degradation and Time (min)	Reference
Yellow Procion H-4R; Bright Blue Remazol (blue reagent-19), Red Procion H-7B	TiO_2 (Degussa P-25)	Solar and UV-light	A mixture of blue and red dyes took 6 h for complete removal under UV-light in presence of 30% H_2O_2, whereas complete removal at 3 h under solar light; A mixture of red and yellow dyes around 93% in 6 h under UV- light with presence of 30% H_2O_2 and 5 h under solar light.	Costa et al. (2004)
Methyl Red (MR) and Crystal Violet (CV)	Ag+ doped TiO_2	UV-light	>86% mineralization of dyes in 90 min	Gupta et al. (2006)
a) Binary dye mixture 25 ppm Reactive Orange 84 (RO 84) and 25 ppm Reactive Black 5 (RB 5) b) Binary dye mixture 25 ppm Reactive Orange 16 (RO 16) and 25 ppm RB 5	TiO_2	Visible-light	a) 14% RO84 and 63% RB5 in 360 min b) 39% RO16 and 43% RB5 in 360 min	Chatterjee et al. (2008b)

Basic Red 46 (BR46) and Basic Yellow 28 (BY28)	TiO$_2$	UV-light	68, 76 and 75% mineralization were obtained for 100 mg/L BY28, 100 mg/L BR46 and 50 + 50 mg/L mixed solutions in 180 min	Gözmen et al (2009)
Acid Orange 7 (AO-7) and Reactive Red 2 (RR-2)	TiO$_2$	UV-light	100% of RR-2 and 80% of AO-7 in 120 min	Juang (2010)
Mixture of two anionic dyes, RB5 and MX-5B	TiO$_2$ (P-25)	light of >290 nm	20-25 ppm TOC removal in 480 min	Sahel et al. (2010)
Mixtures of two azo dyes AY and AB	Mesoporous-assembled TiO$_2$ nanocrystal	UV-light	98% of AY and 97% of AB degradation in 90 min	Wongkalasin et al. (2011)
Mixture of six commercial azo dyes namely, Solophenyl yellow, Solophenyl orange, Solo phenyl black, Solophenyl scarlet, and Solophenyl blue	TiO$_2$ P-25 with H$_2$O$_2$	UV-light	Complete decolourisation in 240 min for all the dyes	Palácio et al. (2012)

Bright Blue Remazol (BR-19), Red Procion H-7B (RP H-7B)	TiO$_2$ (P-25)	Solar and UV-light	Hydrogen peroxide used as bleaching reagent in degradation system; Complete degradation of dye mixture under solar light in 300 min; 70% of RP H-7B and 93% of BR-19 degraded under UV-Light in 360 min	Costa and Alves (2013)
Binary mixture of Rh-B and 4-(P-Nitrophenyl) Resorcinol (Magneson I)	TiO$_2$ catalysed microsphere	Solar	Complete degradation of Rh-B and 66.7% degradation of 4-(P-Nitrophenyl) Resorcinol (Magneson I) in 120 min under solar	Li et al. (2014)
Mixture of MO and Acid Orange (AO)	P25, Hombikat, Pt promoted P25 (Pt/P25); TiO$_2$ P25 showed better activity	UV tubular lamps	Complete degradation of the both the dye in 60 min	Romão and Mul (2016)
Mixed dye solution of MO, Rh-B, MB	Ni-oxide @ TiO$_2$ core-shell materials	UV and Visible lights	100% of MO, 90% Rh-B and 80% MB degradation at 360 min under UV-light; 100% of MO, 95% Rh-B and 83% MB degradation in 360 min under Visible-light	Lee et al. (2016b)

Binary dye mixture containing Acid Blue 113 (AB113) and Acid Red 114 (AR114))	TiO_2	UV light (UV-C)	Around 93% mineralization of the dyes as evidenced through TOC removal at 180 min	Garg et al. (2017)
MB + MO	Core-Shell $Fe_3O_4/SiO_2/$ TiO_2 Nanospheres	UV light irradiation (365 nm)	90.2% of MB and 100% MO degradation in 5 h	Alzahrani (2017)
MB + Indigo Carmine (IC)	Cellulose acetate CNT/TiO_2–NH	UV -light	Complete degradation of IC and MB in 180 and 300 min respectively.	Salama et al. (2018)
Rh-B, MB binary dye mixture	CMC-Na modified $SrTiO_3$ solution at 10 mg/L	UV light.	97% of MB, 60.7% of Rh-B in 180 min	Xie et al. (2018)
MB+ Brilliant Green (BG)+ MO	gC_3N_4-TiO_2 Nanocomposites	Solar and Visible light	100% degradation of the dyes mixed solution in 270 min	Sutar et al.(2020)

Three metal complex azo dyes Acidol yellow (ACY), Acidol grey (ACG) and Acidol scarlet (ACS) from the dye mixture and treatment of woolen textile dye house waste	ZnO	Solar light	93-67% decrease in degradation in mixed dye solution compared to singe dye solutions; 63% COD reduction in dye house waste; 86% of ACY; 85% of ACG; 85% of ACS in 15 min	Saha and Chaudhuri (2003)
Binary mixture of Safranin O and MG	ZnO nanorod-loaded activated carbon	Ultrasonic-assisted adsorption	99% of MG and 95% of SO short time	Nasiri Azad et al. (2015)
MO and Methyl green (MYG) mixture	ZNO micro/Nanoflowers	UV-light	93.83% of 2.5 mg/L MO and 100% of 5 mg/L MYG were degraded at solution pH of 6.5 at 240 min and COD removal around 94.14% at 240 min	Kee (2017)
Binary dye mixture system of (Rh-B) and Malachite Green Oxalate (MGO)	SnO_2	UV (254 and 365 nm),	86% of Rh-B and 94% of MGO in 120 min	Venkatesh et al. (2019)

MB and MO	BiVO$_4$@CeO$_2$	Visible light	40% of MB and 60% of MO degradation in 90 min	Wetchakun et al. (2012a)
Mixed dye solution of MB and Rh-B	Ag-loaded BiVO$_4$	Visible-light	99% MB and 98% Rh-B in 180 min	Regmi et al. (2018)
Mixed dye solution of MB and Rh-B.	Multi–phase BiVO$_4$	UV-light	74% MB and 24% Rh-B in 60 min	Chomkitichai et al.(2019)
Mixed dye solution of two acidic azo dyes orange II and ponceau 4R	AgI–Ag$_3$PO$_4$/ MWCNTs 95.4	Visible-light	95.4% of dyes degraded	Cai et al.(2015)
Mixed dyes MB, CR	Mesoporous Co–Fe/Al$_2$O$_3$–MCM-41 nanocomposite	Visible-light	100% degradation in 60 min	Pradhan et al (2016)
Mixture of MB, MO, Rh-B with MB/MO, MB/Rh-B binary dye solutions	MAC nanoparticles coated with an organic hybrid of silicotungstic acid	Sunlight, visible, and UV irradiation	MB/MO; 91% and 5O% degradation at 75 min MB/Rh-B; 90% and 63.8% at 120 min	Taghdiri (2017)

Three mixed organic dyes: Tz, Rh-B, and MB	Au-functionalized sodium titanate nanotubes	Simulated Sunlight	65% of MB was decomposed after 240 min, while Tz and RhB remained in solution showing no trace of reaction after that time	Hassan Zaki and Mohamed Ali. El Rouby (2019)
Mixture of three dyes as CV; Rh-B; MB from the mixture	Graphene nanosheets isolated from the BC soot	Sunlight.	Complete degradation took 180 min for MB, and 225 min for CV and Rh-B	Gunture et al.(2019)
Mixed CI (BR46), MG and CI Basic Blue 3 (BB3) dyes	CNT/graphite in the presence of H_2O_2.	UV-light	90.52% of BR46; 100% of MG and 97.88% of BB3 degraded at 30 min	Khataee et al. (2012)
MO+ Bromocresol Green (BG)	CuS	Solar light	60% MO and 80% BG degraded at 500 min	Nezamzadeh-Ejhieh and Moazzeni (2013)
Rh-B + MB	CuO/nano-zeolite X	Solar light	15% Rh-B and 35% MB degraded in 160 min	Nezamzadeh-Ejhieh and Karimi-Shamsabadi (2013)

				Nezamzadeh-Ejhieh and Zabihi-Mobarakeh (2014)
MB+ Bromophenol Blue (BMP)	CuO clinoptilolite	UV-light	45% MB and 23% BMP degraded at 250 min	
Rh-B + Janus green (JG)	Fe_2O_3/Cu_2O	Visible light	75% and 70% of Rh-B and JG degraded in 120 min	Abhilash et al. (2019)
Remazol-red (RR) and MB in mixture (10 ppm each)	$CoFe_2O_4$-humic acid (HA) nanocomposite fabricated via co-precipitation	-	Dye removal reached to 99.6% RR and 98.1% of MB respectively.	Badawy et al. (2020)
A mixture of RB and MB dyes under irradiation.	$CeO_2/CuO/Ag_2CrO_4$ ternary nanocomposite fabricated by electrospinning	LED light	90% and 87% of RB and MB at 80 min, respectively.	Sabzehmeidani et al. (2020)

As presented in Table 2.3, there are very few reports on photocatalytic degradation of dyes from mixed dye solutions using nanocomposites. Only one report on photocatalytic degradation of dyes from mixed dye solutions using Bismuth based nanocomposites, viz. $BiVO_4/CeO_2$ (Wetchakun et al. 2012a) has been reported . The degradation efficiencies of the mixed solution of MO and MB over the composite evidently showed that both MB and MO dyes were favourably degraded, which is due to the strong interaction between CeO_2 and $BiVO_4$.

To the best of our knowledge, there is no report on the application of bismuth ferrite-based nanocomposites in the degradation of dyes from mixed dye aqueous solutions. In the present study, the visible light and solar light-mediated photocatalytic degradation of dyes from mixed dye contaminated water containing three dyes namely Rh-B, AY and MB using two BFO based nanocomposites, BFO@TiO_2 and BFO@PANI heterostructured nanocomposites is reported.

2.6.2. Quantification of dye degradation in mixed dye solutions

Photocatalysis encompasses mainly three important steps/process. i) Removal of chromophore group in the dye molecule or change in the position in organic ring in terms of decolourization by photocatalysis ii) Complex dye molecule breakdown into simpler molecule or make the solution complete colourless. iii) In a dye molecule, creation of stable inorganic ions mainly to complete mineralization. Decolourization of dye can be determined using UV-visible spectrophotometer by measurement of decrease in dye concentration. Mineralization of the dye can be confirmed by decrease in COD and upsurge in CO_2 of dye solution.

Photocatalytic degradation studies on, the wastewater containing mixture of dyes, requires the analysis of dye concentration in mixed dye aqueous system. The spectrophotometric measurement of absorbance in a mixture of dye compounds has been complex due to passible interaction between individual components (Peralta-Zamora et al. 1999). There are number of analytical methods for quantitative analysis of colourant mixture in aqueous solution. Among all the methods, UV-visible absorption spectroscopic method is simpler and the best to determine the concentration of each dye in the mixture of dyes in aqueous solution. Many methods have been

reported, such as H-point standard addition method to avoid the superimposition of absorbance resultant from the interaction between the individual component of the binary mixtures, including derivative methods. First order derivative method is identified as a simple method to prevent spectral interferences caused by the interaction of the dyes in the mixture (Ekrami et al. 201; O'Haver et al. 1982). In the First order spectrophotometric method, the zero-order spectrum is transformed into its corresponding first order derivative. The zero crossing points can then be used for the determination of the wavelength of dye analysis without the spectral inference of the other compounds in the mixture (Ekrami et al. 2010).

Derivative spectrophotometry (DS) method is based on the principle that the rate of absorption changes according to the wavelength. It obeys all the law of classical spectroscopy e.g., dependence of derivative value on analyte concentration and additivity law and derivatives. DS is one of the advanced spectrophotometric method in past few decades, based on derivative spectra which are generated from parent zero-order ones (Karpińska 2004; Talsky 1994). The removal of background signal caused by occurrence of other compounds in a sample which is due to derivatisation of zero order spectrum, can lead to separation of overlay signals. The stated properties can permit quantification of one or other analyte without early separation or purification. Currently, this method becomes very beneficial and used versatile, especially in clinical, biochemical, pharmaceutical, environmental, as well as in inorganic or organic analysis. However, it helps in solving the issues involved in analytical problems associated with determination of concentration in complex systems. DS is accurate in multicomponent analysis. It can determine one or other analyst in complex matrix/mixture, which lead to increased selectivity, sensitivity and/or accuracy of assays.

The features stated above allow the determination of a number of components (x) in a mixture by measuring the amplitude of derivative spectrum of mixture at several (minimum x) wavelengths. If the measurements of the height of derivative peak of analyte is performed at those wavelengths at which the spectra of other components undergo zeroing, the measured amplitude is proportional only to concentration of assessed compounds. This approach of quantitative determination is called 'zero-

crossing method'. It allows concurrent resolve of a few analytes in a sample. The extra property of DS, as compared with the classical method, is the dependence of derivatisation result on the shape of zero-order spectra. The signals of analyte which are in basic spectrum narrow, undergo amplification, whereas broad even intense zero-order signals undergo flattening and, in the end, derivatisation leads to their zeroing. This property allows to eliminate the influence of the background and increases selectivity of determination.

The above discussed properties of derivative spectrophotometry technique are valuable from analytical point of view. The derivative technique has found wide application in resolving these analytical problems where analyte is accompanied by constant matrix, mainly in analysis of pharmaceuticals, cosmetics or food additivities.

Turabik (2008) in their studies on adsorption of basic dyes from binary mixture of R46 and BY28 on bentonite, reported the dye analysis by zero order and first order derivative spectrophotometric method. As shown in the Figure 2.2 (a) the individual BR46 and BY28 dyes (initial concentration of each dye is 10 mg/L) were recorded between 300 and 700 nm by zero order absorption spectra. It showed the wavelength of maximum absorbance (λ_{max}) of BR46 at 529 nm and BY28 at 437 nm, respectively. The BR46 and BY28 dyes were overlying due to interference in the zero order spectra, thus concentrations of each dye in mixed condition could not be determined by direct absorbance measurement. Thus, derivative spectrophotometric method and simultaneous analysis was used by them to determine the concentration of each dye in binary mixture. They further plotted the first order derivative spectra of BR46 and BY28 dyes in single and binary mixture aqueous solution as shown in Figure 2.2 (b). They chose 560 nm as the wavelength for the analysis of BR46 in the presence of BY28, where the first order derivative of absorbance for BY28 dye is zero. Similarly, 380 nm was chosen for the analysis of BY28 in the presence of BR46, where the first order derivative for absorbance of BR46 was zero. The calibration for BR46 and BY28 dyes were then obtained at 560 nm and 380 nm to analyses their concentration in binary dye solution respectively.
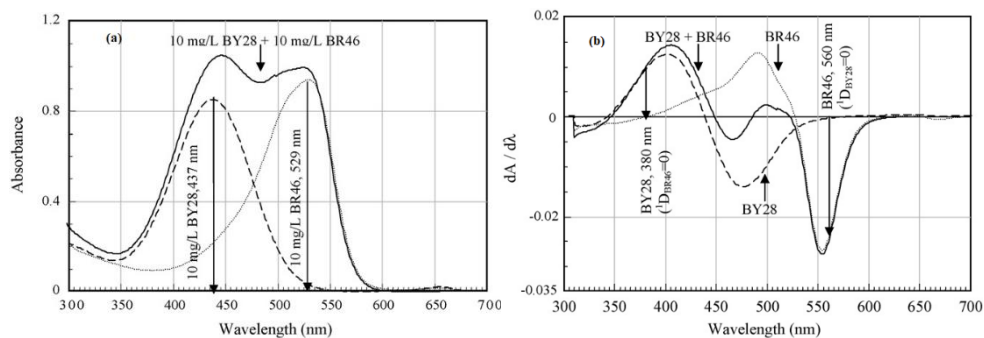
Figure 2.2: (a) Zero order absorption spectra of BY28 and BR46 in single and binary solutions. (b) First order derivative spectra of BY28 and BR46 in single and binary solutions (initial dye concentration of 10 mg/L) (Turabik 2008).

Juang et al. (2010) in their studies on degradation of single and mixed dyes namely Acid Orange 7 (AO7) and Reactive Red 2 (RR2) using TiO_2 nanoparticles under UV-light, determined the wavelengths at 482 nm for AO7 and 538 nm for RR2 by zero-order absorption spectra for individual dyes. Due to overlap and interference between the zero-order spectra of both the dyes, their concentrations could not be concurrently determined by direct absorbance measurements at these wavelengths. They found 425 nm for AO7 in presence of RR2 and 571 nm for RR2 in the presence of AO7 by first order derivative spectral method.

Wongkalasin et al. (2011) studied on the photocatalytic activity for single and mixed azo (AY and Acid Black-AB) degradation use TiO_2 catalyst. They noticed that in the binary dye mixture, the dyes don't interfere with each other, and individual dye absorption spectra showed the maximum absorption of AY at 425 nm and AB at 619 nm, respectively. The photodegradation of each dye in mixed condition confirmed in terms of decreases in maximum absorbance at their wavelength. Similarly, in the binary mixture of CV and MR, each of the dyes could be examined alone by using their corresponding maximum absorption values of 590 and 430 nm, respectively (Gupta et al. 2006).

Gadigayya Mavinkattimath et al. (2017) in their studies on the adsorption of Remazol brilliant blue (RBB) and Disperse orange 25 (DO_{25}) dyes from mixed aqueous solution, found that the wavelengths which showed maximum absorbance for single dyes by zero order spectral analysis viz. 608 nm and 475 nm for RRB and DO_{25}

respectively, showed interference effect in the case of mixed dyes. So, they used first order derivative method and determined the wavelengths for analysis of RBB at 550 nm in the presence of DO_25 and 480 nm for DO_25 in the presence of RBB.

Garg et al. (2017) used two different methods, namely multivariate calibration and first order derivative spectrophotometric method to quantify each dye separately in binary dye solutions of Acid Blue 113 (AB-113) and Acid Red 114 (AR-114) in their studies on photocatalytic treatment in a slurry pond reactor using TiO_2 as a photocatalyst with UV light irradiation .

Zero-order method of analysis may not be suitable for mixed dye solutions; Hence, DS is a systematic method and advantage for dye mixtures with overlying spectra. The issue of overlapping of the spectra and interference between the dyes can be overcome by the plot of wavelength against the rate of change of absorbance; viz., the first-order derivative spectrophotometry (Gözmen et al. 2009; Kapoor et al. 2006; Turabik 2008). The zero-order spectrum derivatization can separate overlapped signals, narrow down the effect of spectral background interferences caused by the presence of other dye molecule (Bosch Ojeda and Sanchez Rojas 2004; Kapoor et al. 2006; Karpińska 2004; Konstantinou and Albanis 2004). Therefore, the concurrent analysis of the dye mixtures are to be carried out using the first-order derivative spectrophotometric method (Ben Douissa et al. 2014; Turabik 2008).

Garg et al. (2017) used two different methods, namely multivariate calibration and first order derivative spectrophotometric method to quantify each dye separately in binary dye solutions of AB-113 and AR-114 in their studies on photocatalytic treatment in a slurry pond reactor using TiO_2 as a photocatalyst with UV light irradiation (UV-C). They used TOC measurements to obtain total mineralization of the dyes.

The dye may be degraded to form specific intermediates during the oxidation and few of them might be more toxic than the parental/original compounds. Thus, it is important to understand the mineralization of the dye (Kalikeri et al. 2018; Medien and Khalil 2010). Mineralization accounts for the oxidation of the dye into CO_2, water and other simpler compounds. The decrease in oxygen demand during the enhancement of reaction checks the degradation of the dye during the photocatalytic process

(Nezamzadeh-Ejhieh and Karimi-Shamsabadi 2013). COD determines the natural stability of wastewater and can be assessed with reference to the total oxygen required for the oxidation of organic matter to CO_2 and H_2O .COD test determines the oxygen required for the chemical oxidation of organic matter with the help of strong chemical oxidant (APHA 2012). COD is the most often used parameter in measuring the pollution level in wastewater and it is used as a parameter to show the amount of dye mineralization.

Pare and Singh (2009) measured colour intensity and decrease in COD level with increase in the time for better understanding of decolorization and degradation processes in their studies on degradation of Lissamine Fast Yellow under visible light using ZnO nano catalyst.

Ps et al. (2013) have also monitored the decrease in COD level to study the degradation and mineralization of mixed dyes under UV-light using TiO_2 nanoparticles fabricated by precipitation method covered with biopolymer calcium (Ca)-alginate. They observed that even when the dye solution looked very clear due to decolourization, toxic trace molecules remained indicating incomplete mineralization as observed from COD test. Thus, COD test is very important in waste water treatment.

Nezamzadeh-Ejhieh and Karimi-Shamsabadi (2013) reported the decolorization of a binary dye mixture (MB and Rh-B) and the mineralization as determined by COD, in their studies on photocatalytic treatment using CuO/nano-zeolite X (CuO/NX) catalyst under solar irradiation. A decrease in COD level approved that the dyes are degraded in photocatalytic process. MB produce 'N' and Rh-B dyes may produce either of NO_3-NH_3 or N_2, CO_2 and H_2O due to mineralization (Gupta et al. 2006; Li et al. 2008). Kee (Kee and Wei 2017) used COD analysis by HACH Reactor Digestion Method 8000 to measure the level of mineralization Mahalingam and Ahn (2018) measured COD values using APHA (American Public Health Association) method (APHA 2012), in their studies on degradation of Methyl green (MYR) and CV under visible light using graphene oxide Fe_3O_4-NiO hybrid nanocomposite. Kalikeri et al. (2018) adopted dye concentration measurement by spectral method and mineralization in terms of COD levels in their studies on degradation of Reactive Blue (RB-19) using PANI-TiO_2 nanocomposite under visible light. Zuorro et al. (2019)

indicated dye degradation in terms of COD removal efficacy in the studies on photocatalytic degradation of Reactive Violet 5 (RV5) using Fe-doped TiO_2 nanoparticles under visible light. Kiwaan et al. (2020) reported COD removal in the degradation of Rh-B and Acid Red 57 (AR57) under UV-light with TiO_2 catalyst. Thus, the analysis of dye concentrations can show the extent of decolourization and COD analysis gives the extent of mineralization.

2.7 Factors affecting photocatalytic activity of nanocomposites and the rate of photocatalysis

The photocatalytic activity of the nanocomposites is influenced by intrinsic factors such as morphology, size, structure and composition of the catalyst which are governed by synthesis method, synthesis conditions and calcination conditions. The factors that affect the rate of photocatalysis leading to degradation of dyes are: pH of the solution, catalyst loading, initial dye concentration and light intensity.

2.7.1. Factors affecting photocatalytic activity of nanocomposites

Photocatalytic activity of nanocomposites depends on morphology, size, structure and the composition. These characteristics are dependent on synthesis method, synthesis conditions and calcination conditions.

Nanocomposites have been developed as appropriate substitutes to get rid of some of the limitations of nanoparticles containing a single component like, metal, metal oxide or semiconductor oxides. They possess unique properties. However, a lot of challenges in terms of their preparation to get a desired composition such as, stoichiometric ratios of components in the nanocluster, phase control and elemental composition are involved (Camargo et al. 2009; Gawande et al. 2015). Usually, NCs are made up of two components depending on the compositions and preparation of these materials, NCs can be divided into different classes, including inorganic/inorganic, inorganic/organic, organic/inorganic and organic/organic type NCs (Amouri et al. 2012; Lauhon et al. 2002; Park et al. 2013). Attention is towards developing specific nanomaterials with multifunctional abilities with improved properties. NCs have conducive and multipurpose compositions and structures (Douvalis et al. 2012; Jiang et al. 2011a; Maity et al. 2012; Pang et al. 2011). Furthermore, NCs may have properties

that are synergistic between the cores and shells NCs and/or offer new properties depending on interactions between the two metals, core and shell or other heterostructures (Adijanto et al. 2013; Cha et al. 2013; Kitchin et al. 2004; Wang et al. 2011a).

When TiO_2, ZnO or WO_3 are used as a photocatalyst, fast recombination of photogenerated electron-hole pairs takes place resulting in the low quantum efficiency of TiO_2 and reduced photocatalytic activity. In order to minimize the above drawbacks and improve the photocatalytic activity, composites made from TiO_2 and other metal, metal oxides or semiconductor oxides are often used (Li and Zhao 2013).

Secondary semiconductors can act as either electron or hole acceptors and improve charge separation. Thus, junction architecture plays an important role in photocatalysis (Moniz et al. 2015). Metal, metal oxides or semiconductor oxides trap the photogenerated electrons of TiO_2 and reduces the electron-hole recombination time of TiO_2 (Bahadur et al. 2019).

The electron characteristics of semiconductors like TiO_2 and ZnO are often amended to harvest visible light with interfacial charge carrier transfer (Habibi-Yangjeh et al. 2020). The coupling of two semiconductors (i) allow these catalysts to absorb visible light (ii) modify the energy levels of the conduction and valence bands for charge transfer to external entities (iii) favour charge separation and (iv) make them more photostable (Ganguli et al. 2020). It has been proved that the heterojunctions constructed among semiconductors with proper alignment of their band edges and the synergistic effect between them promotes the harvesting of visible light absorption, prevent the recombination of electro and hole pairs and enhance the transfer of charge carriers (Akhundi et al. 2019; He and Zhang 2019; Koutavarapu et al. 2019; Kumar and Rao 2017; Pirhashemi et al. 2018; Shekofteh-Gohari et al. 2018). Heterojunction is formed at the interface of two dissimilar semiconductors. The heterostructures are formed on the basis of band gap, electron affinity and band position which leads to formation of new energy levels (Wang et al. 2013c). The type of heterostructures depend on the band alignment and the movement of charge carriers in a reaction is controlled by the formation of heterojunctions (Agrawal et al. 2014; Kroemer 2001; Wang et al. 2013c).

The advanced nanocomposite structures like core-shell structured nanocomposites (CSNs) have been designed such that the shell material improves the reactivity, thermal or oxidative stability of the core material (Ghosh Chaudhuri and Paria 2012; Srdic et al. 2013). The composition of the core and the shell material, its geometry and design, impart unique properties to CSNs. Core-shell architectures provide more uniform and larger area of contact between the components, promoting better transfer of the charges and excitation lifetime. Reactivity can be altered and thermal or oxidative stability of the core material may be enhanced by the shell materials (Ganguli et al. 2020). Chen et al. (2019) synthesized $mBiVO_4/BiOI$ core-shell heterostructured photocatalyst and they ascribed the excellent photocatalytic activity and superior adsorption capability to formation of the p–n heterojunction, close core-shell heterostructure and high specific surface area. These factors were reported to favour the electron-hole separation and transfer. Liu and Wu (2019) synthesized $BiFeO_3/TiO_2$ core-shell nanocomposites by a sol-gel-assisted hydrothermal process forming a p-n heterojunction at the interfacial area which creates an internal electric field by the band alignment. Li et al. (2009a) have synthesized BFO by hydrothermal method and coated it with TiO_2 by controlled hydrolysis of TiO_2 precursor in the presence of BFO to form BFO/TiO_2 core-shell nanocomposites and they reported that the good visible-light absorption property of the nanocomposite is induced by Fe or Bi/Ti interdiffusion in the interfaces.

CSNs are generally synthesised using solution methods involving two steps of synthesis of the core structure followed by coating the core structure with the shell (Ishii et al. 2013; Nomoev et al. 2015; Sahu et al. 2012). In this heterostructure (core-shell), the shell formed on the core increases the specific surface area and possess high porosity, and also decrease the band-gap thus it shows high catalytic activity in photocatalytic field. Superior efficacy/selectivity in catalytic applications may be achieved by synergetic effect between the core and shell.

2.7.1.1. Synthesis methods and conditions

Numerous synthetic strategies have been attempted to fabricate nanocomposites in different ways such as chemical and physical methods. including sol-gel, wet chemical, seeding method, electroless plating, layer-by-layer self-assembly, *in-situ* reduction, stabilizer- or core-assisted reduction, and spraying, microwave ultrasound irradiation, and electrodeposition, etc (Choi et al. 2013; Gawande et al. 2015; Ghadami and Rouh Aghdam 2020; Liao et al. 2019; Manivannan and Ramaraj 2009)

Particle size plays a crucial role in determining the properties of nanoparticles. Shape, size, and surface morphology controls the physiochemical, biological, electronic and optical and catalytic properties of nanomaterials. High surface area nanoparticles are highly reactive, and most of them undergo aggregation due to unprotected surfaces (Freeman et al. 1995; Gomathi et al. 2019; Qiu et al. 2010). Photocatalytic activity has been found to vary with the change in particle size and surface areas (Adhikari and Lachgar 2016). The improved photocatalytic activity with decrease in particle size has been observed by several researchers (Amano et al. 2013; Retamoso et al. 2019). However, Dodd et al. (2006) have found that there exists an optimum particle size at which the photocatalytic activity was maximized. The existence of an optimum size was attributed to counteracting effect of increase in the charge carrier recombination rate with increased activity due to higher specific surface area when particle size is very small. Similar observations were made by Li et al. (2013b).

Shape of the nanoparticles are dependent on their energy which stimulates the changes in shapes (José Yacamán et al. 2001). The shape and nature of the nanoparticles significantly affect their chemical properties (Baer et al. 2013). By controlling the size and tailoring the shape of the nanoparticles, photocatalytic activity may be improved (Liao and Liao 2007; Wu et al. 2010a).

Nucleation is a process to form a crystal which has a crucial role in the growth of particles and crystallites. Nucleation process involves the growth species generation, diffusion, adsorption and growth on the surface to produce crystallite. At lower synthesis temperatures, the nucleation rate predominates over the growth rate of the species, leading to narrow size distribution. At high synthesis temperatures, the growth

rate is high, the nucleation and growth species are simultaneous. Earlier formed nuclei grow to larger particles than the newly formed ones, resulting in a broad grain-size distribution (Cao 2004; Gao et al. 2003; Yu 2006). Thus, nucleation and growth rates are governed by synthesis method and conditions, which govern the size distribution.

The type and quality of nanoparticles fabricated are significantly influenced by the time of reaction for synthesis in the reaction medium (Darroudi 2011; Patra and Baek 2014). Similarly, characteristics of the synthesized nanoparticles changed with the synthesis process and the time, contact with light, and storage conditions (Kuchibhatla et al. 2012; Mudunkotuwa et al. 2012). The aggregation and shrink of the particles is influenced by the synthesis process, variation in synthesis time, shelf-life and storage (Patra and Baek 2014).

Darroudi (2011) in their studies on the synthesis of silver nanoparticles (Ag-NPs) synthesised by green chemistry route reported that the reaction time influences the composition and size of the synthesized nanoparticles. Ahmad et al. (2016) and Sundarrajan et al. (2018) reported that the synthesis time affects the rate of reduction, size and stability of the nanoparticles through their studies on the synthesis of gold and silver nanoparticles respectively by green synthesis methods.

pH of reaction plays a key role in the creation of nanoparticles. pH controls the creation of nucleation centres, framing the size as well as morphology of the NPs. The pH of the solution medium impacts on the surface of the fabricated nanoparticles (Armendariz et al. 2004; Gamez et al. 2003). The size and shape of the particles are altered by varying the pH as nucleation and aggregation is influenced by pH (Armendariz et al. 2004; Handayani et al. 2020; Rajesh et al. 2016; Soni and Prakash 2015). Okitsu et al. (2009) reported that pH affects the size and the aspect ratio of gold nanorods. The structure, morphology and interaction strength of the nanoaprticles depend on the pH of the syntheis media (Zhang et al. 2010; Handayani et al. (2020).

Li and co-workers (2015) reported the sol-gel technique for the synthesis of sAg@SiO$_2$ core-shell nanostructure, which effectively avoided the Ag core agglomeration. Chen et al. (2017a) prepared Ni-Cu-Zn ferrite@SiO$_2$@TiO$_2$Ag nanocomposites Via sol-gel route, to reduce the particle size and shape of the magnetic

nanocomposites and they obtained desired NCs with an average particle size of 20 nm. Islam et al. (2019) reported that a visible light active $Bi_{0.9}HO_{0.1}FeO_3$ nanoparticles/TiO_2 nanocomposite thin films with different molar ratio can be prepared through sol-gel method and they found that nanocomposite film can be a possible candidate for a better photocatalyst. Ratova et al. (2016) found that Bismuth Tungstate onto Titania Nanoparticulate materials obtained via deposition method are good for visible light active photocatalysis. Hirakawa and Kamat (2005) are synthesized Ag@TiO_2 by one pot synthesis method with simultaneous reduction of Ag ions and hydrolysis of TiO_2 precursor, which prevented corrosion/leakage of Ag. Electrons excited from TiO_2 shell are stored in Ag core and prevented recombination.

According to literature survey, researchers have observed that size of the catalyst and band gap depend on the synthesis method or condition involved (Dong et al. 2009). In spite of the nanoscale providing high surface area and surface defects, the charge recombination become dominant at nanoscale, which thus reduces the benefits of nanosized semiconductors (Serpone et al. 1995; Zhang et al. 1998). The highest activity may not always be achieved with the smallest size. So optimum size of the nanoparticles is a key factor for achieving highest photocatalytic efficiency (Bao et al. 2007; Ishihara et al. 2004). Crystallinity of nanoparticles plays a more important role than the high surface area (Kudo and Miseki 2009). In the heterojunctions, the defects of O (oxygen) vacancies offer a greater contribution to the photocatalytic process than the defects at deep levels and the direct transfer of charge between the conduction and valence bands (Coleto et al. 2019).

Currently, researchers are gaining interest on discovering different methods of synthesis of NCs, their nucleation, subsequent arrangement as well as on the influence of the surface (Armelao et al. 2006). The diverse physical/chemical structures of different nanocomposites can be obtained by using different methods and conditions. The changes in synthesis process or conditions involved in the process are very important factors in nanocomposites, and these factors influence the photocatalytic activity. However, by changing the synthesis methods or by using different substitutes for chemicals or by changing the calcination temperature and time, dopant (adding other metal for making capping agents) or by using surfactant as electrostatic stabilization

agent, or by varying the pH of precursor solution the formation a catalyst with desired characteristics and activity can be achieved. Hence synthesis method and conditions involved in the methods play vital role in the photocatalytic activity.

Commonly catalyst with a narrow band gap is good for photocatalysis to produce more electron-hole pairs (Wu et al. 2010b). Moreover, small band gap incites the impurity energy level, and oxygen-deficient sites in the catalyst to enhance the photocatalytic activity (Asahi 2001; Cao et al. 2013; Fuerte et al. 2002; Rodríguez-González et al. 2008; Zaleska 2008). The activity of any photocatalyst depends on how the recombination of photoinduced electron-hole pairs is prevented (Liu et al. 2010; Sobana and Swaminathan 2007). It may be changing the morphology, particle size (Ma et al. 2010), crystal structure (Rajabi et al. 2013), and surface area of nano catalyst which are important factors that resolve the photocatalytic activity of prepared photocatalyst. Proper composition of the material plays a vital role in the interactions of the material and strengthen filler matrix in the composite. Bharadwaj (2001) reported that composition ratio of the composite materials is one of the important factors that governs the microstructure and morphology of nanocomposites, and also determines the charge transport mechanism. The uniformity and orientation of the nanocomposite which leading to a more bending path and improved barrier properties, depends on the composition (Bharadwaj 2001). Camargo et al. (2009) reported that the characteristics of nanomaterials such as, crystalline structure, large surface area and reactivity and its interaction with the environment are related to their composition. Mirzadeh and Kokabi (2007) reported that the composition of the composite plays a key role in solubility and orientation of the material. Variations in the composition alters the solubility factor and it supress the barrier effect of orientation and also diffusion coefficient might be affected.

In the TiO_2/ZnO nanocomposites, the band gap energy, morphology and photocatalytic activity have been reported to be dependent on the levels of Zn precursor used for the synthesis, and molar ratio of ZnO to TiO_2 in the composite (Prasannalakshmi and Shanmugam 2017; Wang et al. 2013a). It has been reported by Li et al. (2019a), that the band gap energy and photocatalytic activity of BFO/TiO_2 nanocomposite is influenced by BFO to TiO_2 mass ratio (Li et al. 2009a; Liu et al.

2017b). The charge carrier efficiency, charge separation tendency, band gap energy and photocatalytic activity have been found to be influenced by mass percentage of N-TiO$_2$ in BiFO$_2$@nitrogen doped mesoporous TiO$_2$ in BFO/n-TiO$_2$ composite (Mohamed et al. 2020). The variation in mass ratio of SnO$_2$ to g-C$_3$N$_4$ in SnO$_2$/g-C$_3$N$_4$ photocatalyst influenced the photocatalytic activity (Singh et al. 2019). The photocatalytic activities depended on the mass ratio of CdS : Graphene or CdS : CNT in CdS-Graphene and CdS-CNT nanocomposites (Ye et al. 2012). In Zn$_3$(VO$_4$)$_2$/BiVO$_4$, as the ratio of BiVO$_4$ increased, particle size increased, which was attributed to aggregation/agglomeration of the particle. The photocatalytic activity was also found to be influenced by mole ratio of Zn$_3$(VO$_4$)$_2$ to BiVO$_4$ (Sajid et al. 2018).

Zalfani et al. (2015) reported that in BiVO$_4$/TiO$_2$ nanocomposites, the crystallite size of TiO$_2$ was lower than that of pure TiO$_2$ and concluded that BiVO$_4$ nanoparticles prevent grain aggregation. They further found that increasing the BiVO$_4$ content in BiVO$_4$/TiO$_2$ lifted the nanocrystals of BiVO$_4$ to an agglomerated state to coagulate in the development of the crystal. Mai et al (2019) studied on influences of silicon dioxide nanoparticles (SiO$_2$) on structure and phase transition of a conventional ferroelectric of triglycine sulphate (TGS). Sajid et al. (2018) noticed numerous irregularities in the composite and it caused wide range band stretch in the composite with an increase in BiVO$_4$ content in the composite.

From the review of literature, it was concluded that the composition of the nanocomposite greatly influences the photocatalytic activity and composition may be varied by varying the ratio of precursors for the components. Thus, the optimization of the ratio of precursors for the components to maximize the photocatalytic activity was required.

2.7.1.2. Calcination conditions

The structural properties of a photocatalyst such as crystalline phase, crystallite size, surface area and pore distribution, are important for its photocatalytic activity and these factors are influenced by calcination temperature and time (Cai et al. 2016; Yu et al. 2006). Crystallinity and particle size are the critical parameters that influences the photocatalytic performance of photocatalyst (Leghari et al. 2011; Zhang et al. 2011a).

Several researchers have reported that the crystallinity of the particles increases with increase in calcination temperature, in turn resulting in enhanced photocatalytic activity (Kusuma and Chandrappa 2019; Menon et al. 2018). An increase in calcination temperature results in nanocomposites with well-defined morphology (Menon et al. 2018). Though in certain cases, the particle size increased with increase in calcination temperature (Kusuma and Chandrappa 2019; Menon et al. 2018; Pranwadee Kaewmuang et al. 2018), in other cases it decreased (de Luna et al. 2018). Calcination influences morphology of the nanoparticles (Satapathy et al. 2014).

Common synthesis methods for nanoparticles involve high-temperature calcination to convert amorphous form into crystalline structure, for fine particle growth and to decrease the surface area in order to enhance the photocatalytic efficiency (Gnanaprakasam et al. 2015; Jing et al. 2013; Shi et al. 2009; Venkatachalam et al. 2007). Shi et al. (2009) reported that, with an increase in calcination temperature for TiO_2 nanoparticles, the light absorption turns from lower wavelength to longer wavelength. The concentration of anatase phase in TiO_2 increased with increase in calcination temperature. Anatase to rutile transformation was found between calcination temperature of 500 and 600°C, and then completely transformed to rutile phase at 600°C (Wetchakun et al. 2012b). Higher calcination temperature favour particles growth and agglomeration occurred which decreased specific surface area (Wetchakun et al. 2012b; Zhang et al. 2006a). Higher calcination temperatures led to formation of anatase phase at the surface of TiO_2 than that at bulk during phase transformation (Zhang et al. 2006a). Shi et al. (2009) and Zhang et al.(2001) have also reported that increase in calcination temperature leads to higher stability and photocatalytic activity. Calcination temperature influences the band gap energy and native defects distribution (Sifontes et al. 2013; Sugihartono et al. 2019). Hence calcination temperature influences the crystallinity, size, shape, morphology and optical property of the particle, and thus governs the photocatalytic activity (Liang et al. 2006; Rai et al. 2006; Sifontes et al. 2013).

Gharagozlou (2011) studied the effect of calcination temperature in the range of 400 to 1000°C on the structural properties of $CoFe_2O_4/SiO_2$ nanocomposite synthesized by sol-gel process. They obtained higher crystallinity without impurity

phases on calcination. Crystallite and particle sizes were found to slightly increase with increase in calcination temperature. Satapathy et al. (2014) in their studies on Nd doped Y_2O_3 nanoparticles reported that, both crystallite and particle size increases with increase in calcination temperature and morphology of the particles also changes with changing calcination temperature. Kayani et al. (2015) have found that the crystallinity, band gap, crystallite and particle size of ZnO nanoparticles synthesised via sol-gel method increased with an increase in calcination temperatures. Similar results of the effect of calcination temperature on crystallinity, band-gap and particle size distribution were observed by Ali et al. (2018) in ZnO/SnO_2 (ZS) nanocomposites, fabricated via co-precipitation route. However, they obtained lesser photocatalytic activity in the nanocomposites calcined at higher temperatures due to the creation of new transitional phase in the composite and bigger bandgap with larger particle size.

Amadine et al. (2017) in their studies on $CuO@CeO_2$ composite synthesised via surfactant-template process have found that calcination temperature plays a vital role in the formation of the composite with good co-occurrence and stability of the nanoparticles, due to oxygen vacancies on the surface of the particles. They also attributed calcination temperature as the reason for lattice expansion. The increase in crystallite size of the composite with increase in calcination temperature has been observed in Ni–NiO nanocomposites fabricated by coprecipitation and Sol–Gel (SG) method (da Silva et al. 2019).

Desiati et al. (2019) in their studies on TiO_2/Ag nanocomposites synthesised via sol-gel route, have found that the particles size and its distribution are dependent on calcination temperature. Calcination temperature plays a crucial rule in adhesion of particles in the composite, Zhang et al. (2020) studied on morphology of silica microspheres surface-coated nano-TiO_2 composite material (MS-SiO_2/TiO_2) at different calcination temperatures and found that increase in the temperature leads to a stronger bond between TiO_2 and MS-SiO_2. Wang et al. (2012) reported on that in ordered titanate nanoribbon (TNR)/SnO_2 films synthesized via electrophoretic deposition (EPD) method, increase in the calcination temperature and time led to increase in crystallinity. Dudhe and Nagdeote (2014) reported that increase in calcination time, improved the structure and size of $CaNb_2O_6$ nanomaterials fabricated

through co-precipitation process. BR and XR (2016) reported that for nickel oxide (NiO) nanoparticles fabricated by coprecipitation method, increase in calcination time particles, results in increase in the crystallite size. Mohammed et al. (2020) studied on $Ca_3Co_4O_9$ nanoparticle synthesised by sol–gel method (using starch as a fuel) with different calcination temperatures (773, 873, 973, and 1073 K) and time (4, 6, 8,10, 12, and 14 h). They found out particles size increases as calcination time increased from 4 to 12 h which is due to the grain growth. But after 12 h, the size remained same due to saturation. They also reported that crystallite size and percentage of crystallinity in the crystal structure depends on calcination time.

The review suggests that photocatalytic activity of any catalyst depends on the calcination conditions like temperature and time. Thus, it is important to study the effect of calcination temperature and time to improve the photocatalytic activity of the catalyst in terms of the degradation of dyes.

2.7.2 Factors affecting the rate of photocatalysis/photocatalytic degradation efficiency

2.7.2.1 Effect of pH of the solution

The pH plays a vital role in photocatalytic degradation (Reza et al. 2017), though the effect may vary with the type photocatalyst and the reaction media compositions, as the process takes place on the catalyst surface (Akpan and Hameed 2009; Neppolian 2002). The effect is related to the ionization state of the surface, as well as that of the reactant dyes and products such as acids and amines (Akpan and Hameed 2009; Kiwaan et al. 2020). It also affects the charge on the catalyst surface, aggregation of the particle in terms of size and the positions of conduction and valence bands (Giwa 2012; Neppolian 2002; Shah et al. 2019). The pH can influence the adsorption of dye molecules onto the catalyst surfaces, an important step for the photocatalytic oxidation to take place (Shah et al. 2019). The holes (positive) are considered as the major oxidation species at low pH, whereas hydroxyl radicals are considered as the key species at neutral or high pH levels. Under acidic condition, the excitation of H_2O and *OH radicals will be suppressed due to an excessive concentration of H^+ and a low concentration of OH^-. Furthermore, the formation of

HO_2^- from H+ and O_2^- radical proceeds inversely and, thus, is inhibited when the pH exceeds the acid dissociation constant (pKa). As a result, there will be less ^-OH radicals, which are lower in redox potential and leading to lesser oxidizing capacity in the reaction system (Paul et al. 2019). Furthermore, the lack of HO_2 radicals will also inhibit oxidation, as they produce oxidizing substances lower in oxidize ability (Xue et al. 2015). Thus, pH is a very important factor which governs the photocatalytic rate.

Costa et al.(2004) reported, the effect of pH on mixed dye (Red Procion and Bright Blue Remazol) solutions during photooxidation with changing pH from 8 to 12. During photodegradation in the mixture of dye solution, a slight change in the photooxidation time was observed, which meant there is no variation on the acid dissociation constant (pKa) or base dissociation constant (pKb).

Gözmen et al. (2009) studied the photocatalytic degradation and mineralization of BR46 and BY28 dyes in single and mixed solutions in the presence of periodate ion (IO_4^-), at different pH conditions. They reported that degradation is pH dependent and a diverse behaviour with the chemical nature of the dye was observed. The degradation of BY28 insignificantly influenced by varying the pH, but the degradation of BR46 was significant at pH 3.2 compared to other pH. According to percentage degradation, the optimum pH value was achieved at pH 3.2 for the degradation of both the dyes, which is due to the point of zero charge (pHzpc) for anatase TiO_2, Sakthivel et al. (2003) and Vohra and Tanaka (2001) have reported that the catalyst surface charge is positive at acidic medium and negative at basic medium. As BR46 and BY28 are cationic dyes, the repulsive forces between the catalyst surface and dyes do not facilitate their adsorption on the catalyst surface in acidic medium. But hydroxyl radicals formed react with dye molecules in acidic medium. Therefore, high degradation was achieved at acidic solution. At higher pH value such as 5.2, 6.1 and 7.0, TiO_2 particle surface is neutral, causing agglomeration of the catalyst and leading to lower degradation. The greater degradation efficiency of BY28 in alkaline pH (8.0) could be attributed to weak adsorption or molecular interaction of the BY28 on catalyst surface than BR46. Hence, the dye molecules are directly oxidized by the TiO_2 holes.

Juang et al. (2010) in their studies on photodegradation and mineralization of individual and mixed dye solutions of AO7 and RR2 dyes under UV irradiation by TiO_2 photocatalyst found that degradation increased with increase in solution pH from 1.5 to 6.3.The pHpzc of TiO_2 is 6.2 - 6.6 (Doong et al. 2001; Hoffmann et al. 1995). The TiO_2 particle surface charge may be negative, positive, or neutral depending on whether the pH of the solution is greater than, smaller than or equal to pHpzc. The degradation and mineralization do not only depend on the adsorption–desorption properties of catalyst surface, it also depends on the pollutants and their surface charge. However, both the dyes being negatively charged, the reactions of hydroxylase of both the dyes form a complex in the entire pH range.

Romão and Mul (2016) studied the degradation of MO and Atrazine dyes in mixed dye aqueous solutions with TiO_2. According to their report, the degradation of mixed dyes was better in acidic condition and lower degradation was observed in neutral condition. MO degradation rate was much slower in basic medium compared to acidic condition, in both individual or mixed dye system. However, it was found that the degradation of atrazine was not affected by the presence of MO. The catalyst surface charge affected by pH, was reported to play a vital role in the degradation of the dyes.

Alzahrani (2017) studied the effect of pH on mixed MO(anionic)+MB (cationic) dye degradation using core-shell $Fe_3O_4/SiO_2/TiO_2$ nanospheres synthesized via precipitation method. They reported that dye degradation does not depend on the formation of hydroxyl radicals at the edge of nanospheres. The dye degradation was totally dependent on the photocatalyst surface charge and the dye stuff charges; their physical and chemical properties. In a mixed dye condition, competition between the two dyes for adsorption at catalyst surface may occur (Nezamzadeh-Ejhieh and Karimi-Shamsabadi 2013; Wang et al. 2011c). In addition, for catalysts suspended in aqueous solution, the surface of the catalyst is enclosed by hydroxyl groups, and the surface charge of TiO_2 is the main function of the solution pH. When pHpzc of the catalyst is higher than the pH of the solution, catalyst surface charge is positive and favour the MO (anionic) degradation, If the pHpzc of the catalyst is lower than the pH of the solution, catalyst surface charge is negative and it favours MB (cationic) degradation (Alzahrani 2017; Sahel et al. 2010).

Taghdiri (2017) studied the degradation of mixed dyes (MO and Rh-B/MB) on MAC nanoparticles coated with silicotungstic acid (MAC-HMT-STA-MB) nanocomposites under sunlight with different pH. The photocatalytic degradation of Rh-B, the adsorption process was studied in aqueous solution (pH =7.4). Rh-B in the mixed dye solution was not adsorbed on the catalyst under neutral pH. However, both of the dyes were degraded at other pH conditions, but degradation of MB was greater than Rh-B. The composite surface charge is being negative and MB dye being charged positive; MB degradation was superior than Rh-B. The degradation of Rh-B was superior at lower pH which was due to anionic form of Rh-B is at pH 2.5 in mixed dye solution.

Salama et al. (2018) in their studies on photocatalytic degradation of MB and Indigo carmine (IC) using combination of cellulose acetate (CA), multiwall carbon nanotubes (MCNT) and TiO_2 nanocomposite under UV light, reported that dye degradation is dependent on pH of the solution. They reported that in lower pH, TiO_2 produces extreme oxidizing capacity. Both the dyes degraded under strong acidic conditions (pH2), which was attributed to the electrostatic interactions between the positive and negative surface charge of catalyst and dye molecule respectively, leading to strong adsorption of dye molecule. In addition, the enhanced efficacy of the process was attributed to the creation of hydroxyl radicals by interaction of hydroxide ions with the positive holes which are considered as the main oxidation species at low pH.

Chomkitichai et al. (2019) studied the photocatalytic degradation of a mixture of MB and Rh-B solution under UV light irradiation by multi–phase bismuth vanadate ($BiVO_4$) nanoparticles. They studied the effect of pH on degradation of mixed dye (MB/Rh-B) solution and found that the degradation of MB/Rh-B increased with increases the pH, which was attributed to the repulsive force between the hydroxyl ions of the solution and the negatively charged catalyst.

Venkatesh et al (2019) studied the effect of pH on degradation of mixed dyes, Rh-B and MGO, in aqueous medium using SnO_2 nanoparticles synthesized via co-precipitation method. They showed that adsorption between dyes and the catalyst surface and redox processes of photocatalysts playing a role in degradation (Gupta et

al. 2017). In mixed dye solution the degradation of Rh-B was faster at pH 7 and degradation of MGO was faster at pH 9. The degradation rate of dyes was lower in strong acidic (pH4) and strong alkaline (pH9) conditions, which is due to surface charge and suspension of nanoparticles in acidic medium. In acid medium, the catalyst surface charge is negative so it enhances reaction rate and stronger electrostatic repulsion with dye molecules. So, this catalyst prevents adsorption of hydroxide ions, collapse oxidative species in the reaction (Yang et al. 2016). In alkaline medium, the generated reactive species and dye molecules interacted to enhance the dissolved oxygen level, so photocatalytic activity also increased.

These literature review suggest that, pH of the solution affects the degradation of dyes differently and the optimum pH depends on the catalyst and dye characteristics. So, it is important to study the effect of pH for any catalyst-dye system to facilitate maximization of degradation.

2.7.2.2. Effect of catalyst loading

The rate of the photocatalytic reaction depends on catalyst loading. Many researchers reported that the photocatalysis rate increases with increase in catalyst loading, but after certain loading, the rate decreases and becomes independent of catalyst loading. The increase in the catalyst loading increases the number of available active sites and thus increases the dye molecules being adsorbed. But., further increase in catalyst loading beyond a certain limit leads to interception of the light by the suspension which decrease the rate of photocatalysis (Saquib and Muneer 2002). The density of particles in the area of illumination increases when catalyst loading is increased (Adesina 2004; Paul et al. 2019). Higher amount of the catalyst may not be useful in view of possible aggregation as well as reduced irradiation field due to increase in light scattering. The catalyst amount has both positive and negative impact on the photodecomposition rate.

Juang et al. (2010) in their studies on the effect of TiO_2 concentration range from 0.1–6.0 g/L on photodegradation and mineralization of sole and mixed dyes AO7 and RR2 under UV irradiation, observed that the photodegradation of individual dyes

and mixed dyes, increases with increasing catalyst concentration. Many researchers have reported that photodegradation is dependent on the catalysts and their active sits on the surface (Lathasree et al. 2004). With appropriate increase in the concentration of the catalyst, the creation of electron/hole pairs increases and thus the formation of OH radicals for higher photodegradation.

Wongkalasin et al. (2011) studied the effect of catalyst concentration on the photocatalytic degradation of mixed dyes AY and AB in aqueous solution using mesoporous-assembled TiO_2 nanoparticles. They observed an increase in the rate of photocatalysis with an increase in the catalyst concentration upto 10 g/l. However, with further increase catalyst concentration, they observed that the degradation rate decreased. Hence, they found catalyst concentration of 10 g/l as the optimum. A superior TOC removal for the individual dye aqueous solution was 92.5%, which was greater than that of mixed dye aqueous solution (91.3%), which was attributed to the availability of active site on TiO_2 surface, the light absorption capability of the catalyst, and light penetration depth in the dye solution (Konstantinou and Albanis 2004). They inferred that in the catalyst concentration range of less than 10 g/l, the active sites of TiO_2 surface and the light absorption ability increase due to a greater number of TiO_2 particles available in the system. Contrarily, further increase in the catalyst concentration beyond the optimum, light penetration and active sites on the surface of the catalyst restricted. More concentration of the catalyst hinders the light penetration and also leads to agglomeration of the catalyst which is due to interaction of the particles. Hence, photocatalytic activity is less reduced as compared to optimum catalyst concentration.

Romão and Mul (2016) in their studies on the effect of TiO_2 (P25) concentration on the photocatalytic decomposition rates for MO and Atrazine, have reported that catalyst loading is an important parameter to optimize the photocatalytic efficacy. They observed that the rate constant of MO and Atrazine increased with increase in catalyst concentration. MO showed a similar rate constant value when decomposed in the presence of Atrazine, while for Atrazine in the presence of MO, the increase in rate constant by increasing the catalyst concentration was insignificant.

Venkatesh et al. (2019) studied the photocatalytic degradation of Rh-B and Rh-B + MGO degradation on SnO_2 nanoparticles synthesized via co-precipitation method, and the effect of catalyst dosage on photocatalytic activity. Increase in degradation with increase in catalyst dosage was observed by them. They attributed it to the formation of active sites and generation of oxidative species ($\bullet OH$ and $\bullet O_2^-$) which improves the adsorption and catalytic activity as proposed by Wang et al. (2018). The optimum concentrations of SiO_2 for Rh-B were reported to be 50 mg in 100 mL and Rh-B + MGO as 75 mg in 100 Ml. They reported that at these catalyst concentrations, a greater number of active cites would be available and more photons pass through the dye solution. So, the catalyst effectively endorses the electron/hole generation to degrade the dye molecules (Poulios et al. 2000).

Chomkitichai et al. (2019) studied on multi–phase bismuth vanadate ($BiVO_4$) nanoparticle synthesised via solvothermal method for photocatalytic degradation of MB and Rh-B in mixed dye solution under UV light irradiation. MB being a cationic dye, gets adsorbed more on $BiVO_4$ surface (negative charge) than Rh-B (anionic). The degradation efficiency increased with an increase in the concentration of the catalyst till the optimum level was reached, but further increase in catalyst concentration above the optimum resulted in a reduction in degradation efficiency. The main mechanism behind the photocatalytic efficiency for mixed dye aqueous solution is dependent on the number of active sites and photo–absorption ability of the catalyst. The catalyst concentration increases the creation of electron-hole pairs and thus the producing OH radicals for increase in the degradation. Further increase in the concentration of the catalyst, hinders the light penetration through defensive effect of the suspended catalyst and so decreases the photocatalytic efficacy (Chiou et al. 2008; Guillard et al. 2003; Sayılkan et al. 2006).

The review of literature on the effect of catalyst concentrations (loading), there exist an optimum catalyst concentration which depends on the catalyst-dye combination. The optimum depends on the active sites available on the catalyst and the light scattering effect or hindrance caused for light absorption due to high concentrations of the catalyst. Thus, a study of the effect of catalyst loading for any

dye-catalyst combination is important to obtain an optimum for maximum degradation of any dye.

2.7.2.3 Effect of initial dye concentration

The degradation of dyes by photocatalysis prominently depends on the concentrations of the dyes. The industrial effluents containing the dyes, may be diverse in nature with varying concentrations of the dyes. So, the photocatalytic reactor may be subjected to varied dye concentrations. Even though dye concentration increases, the number of active sites remains constant, with fixed catalyst loading (Mohan and Pittman Jr. 2006). Once the catalyst is saturated there will be no more active sites for the degradation of dyes (Kalikeri et al. 2018). The increase in dye concentration also hinders the light penetration (Mortazavian et al. 2019). As the initial dye concentration increases, the residual dye concentration in the reactor also increases.

Gözmen and co-workers (2009) have reported a decrease in the dye degradation with increase in the dye concentration in their studies on the activity of TiO_2 for the degradation of BR46 and BY28 dyes in separate and mixed condition under UV irradiation with different concentrations range of 20 to 100 mg/L, in the presence of 3 mM periodate ion concentration (IO_4). Juang et al. (2010) have also reported a decrease in the photocatalytic degradation of dyes with increases the dye concentration in their studies on the degradation and mineralization of single and mixed dyes (AO7 and RR2) using TiO_2 nanoparticles under UV-light. They attributed the decrease to the prevention of light penetration on to the catalyst, as well as high turbidity due increase the dye concentration. Kiriakidou et al. (1999) reported a decrease in azo dye degradation with increase in the initial dye concentration at pH 6 for initial dye concentration range from 25 to 100 mg/L. However, several researchers have stated that photodegradation is dependent on initial dye concentration up to a certain level, after which it reaches a saturation (Glaze et al. 1993; Ku and Hsieh 1992).

Wongkalasin et al. (2011) studied on photocatalytic degradation of binary mixture of azo dyes AY and AB using TiO_2. In order to understand the optimum degradation rate using different mixture conditions, they investigated on six different

concentration mixtures. They used initial concentrations AY such as 2.5, 5 and 10 mg/l and AB initial concentrations in the range of 0-10 mg/l and vice versa. With the initial concentration of both the dyes increasing, there was no change in degradation observed upto 2.5 mg/L, whereas further increase in the concentration of these dyes resulted in a gradual decrease in degradation rate. Wongkalasin et al. (2011) have attributed it to the presence of a greater number of the dye molecules making the solution turbid and preventing light penetration on to the catalyst to react with the dye molecule. They noticed that, with a constant concentration of AB and varying initial AY concentration, the degradation rate was higher than constant concentration of AY and varying concentrations of AB.

Romão and Mul (2016) reported that decomposition of MO and Atrazine in aqueous solutions using TiO_2. They reported how one dye is affected other dye decomposition in mixed condition. Their studies revealed that when the MO initial concentration was 10 times lower than Atrazine, the rate of degradation of Atrazine was not affected significantly by the presence of MO. However, in their studies on the degradation of AO and MO in mixed condition by TiO_2, MO degradation was fund to be significantly delayed by the presence of AO.

Kee (2017) in his studies on application of ZnO micro/nanoflowers synthesised through a PVP assisted co-precipitation technique for photodegradation of mixed dyes (MO and MYG) in aqueous solution, reported the effect of initial concentration of dyes on the degradation efficiency. He reported a decrease in the photocatalytic degradation of dyes with increase in the dye concentration. He opined that, since the catalyst concentration and light intensity is constant, dyes do not get degraded instantly due to higher adsorption of dye molecules on the catalyst surface. According to Gupta et al. (2013) the light penetration in the aqueous solution reduces to reach the catalyst surface, as the dye concentration increases, causing limited creation of free super hydroxy radicals on the catalyst surface to react with the dye molecules, so photocatalytic degradation decreases (Gupta et al. 2013).

Venkatesh et al. (2019) studied the effect of initial concentration of the dyes on the degradation of Rh-B and MGO dye in individual and binary dye aqueous solution using

SnO$_2$ nanoparticles under UV light. They reported that the degradation of dyes was effective at low concentrations and as the concentration increased the dye degradation decreased.

Many other researchers Abu Tariq et al.(2008; Daneshvar et al. 2007; Sobana and Swaminathan 2007) also reported a decrease in dye degradation efficiency with increase in the dye concentration in the solution. Overall, the mentioned reports explained high dye concentration with fixed catalyst concentration, hinder the light absorption capacity, hence low degradation is achieved. Salama et al. (2018) in their work on photocatalytic degradation of MB and indigo carmine (IC) using cellulose acetate, MCNT and TiO$_2$ composite nanofibers under UV-Light, have reported that degradation rate depended on the concentration, the nature of the compound and presence of other existing compounds in the solution.

Mohamed et al. (2018) in their studied the photodegradation of pharmaceuticals, viz Ibuprofen (IBP), Naproxen (NPX), and Cetirizine (CIZ) using MWCNT/TiO$_2$-NH$_2$ composite under UV-Light have reported that the high concentration of pharmaceuticals inhibits the reaction with hydroxyl radicals, due to indirect contact. They also reported that the UV-light is absorbed by drug due to increase in the drug concentration and the photons are unable to reach the photocatalyst surface to generate hydroxyl radicals (Li et al. 2018).

As the industrial effluent may contain dyes of varying composition, studies on the effect of dye concentration is important from the view point of extent of degradation achievable or to study the kinetics of degradation which helps in the design of reactors for photocatalysis. When different dyes co-exist in wastewater, the presence of one dye may inhibit the degradation rate of the other and it may depend on the concentration of each of the dyes. Higher dye concentrations may also inhibit the redox reactions during the photocatalysis and thus reduce the degradation efficiency. As the allowable concentration of the dye in the treated effluent is limited by regulatory standards, it is important to investigate, what is the residual concentration achievable with the given dye concentrations in the reactor influent and to suitably vary the parameters or design the reactor to achieve the desired residual concentration. Thus, it is important to study

the effect of initial dye concentrations on the photocatalytic degradation of dyes for any dye-catalyst system.

2.7.2.4 Effect of irradiation source and light intensity

The wavelength and intensity of the light play a crucial rule in the photocatalytic activity. The type of irradiation source which can be used depends on the nature of the catalyst. The artificial UV-light is more duplicatable than sunlight and enhance the dye degradation rate. However, solar energy is cost effective and abundant and non-hazardous nature, so expected to develop as an alternate light source (Muruganandham 2004; Neppolian 2002). Generally, solar light is directly used for photocatalytic degradation reactions or by using parabolic collectors (Goncalves et al. 2005; Malato et al. 2002).

Rao et al. (2004) found that the AO7 degradation rate with TIO_2 is around 1.5 times higher under sunlight than artificial UV light. Even though in AO7, sunlight influence in direct photocatalysis was found to be low. The wavelength of the light was found to play a vital rule in degradation rate. Shorter wavelength irradiation can promote to create an electron-hole generation and catalyst efficiency in terms of degradation with TiO_2 catalyst (Nguyen et al. 2014). However, suitably modification of the catalyst to reduce the band gap energy may impart visible light activity and thus solar energy can be utilized for photocatalysis.

Ollis et al. (1991) stated that: Light intensity governs the reactor deigns and distribution in the reactor, and also determine the conversion of pollutant and degradation (Pareek et al., 2008). Light intensity is playing a vital rule in degradation as well as the reaction rates (Carneiro et al. 2011). Creation of the electron-hole pair, which is the initiation step in the photochemical reaction is dependent on the light intensity. The light intensity governs the rate of photocatalysis.

- The rate of reaction increases linearly with increase in light intensity at low intensity lights (0–20 mW/cm^2) (first order).
- Beyond certain value, at middle light intensities (approximately 25 mW/cm2) rate of reaction is dependent on the square root of the light intensity (half order).

- The rate of the reaction is not dependent on light intensity, at high light intensities. At high light intensities, due to more photons per unit area and unit time; the probability of activation of catalyst surface by photons is higher, so catalyst activity increases. Even though, light intensity increases the number of active sites remain same on the catalyst, thus reaction rate reaches a saturation level even though light intensity continuously increases.

Neppolian (2002) studied the photocatalytic degradation of Reactive Yellow 17, Reactive Red 2, Reactive Blue 4 dyes using TiO_2 under solar/UV irradiation. They noticed that solar irradiation is less effective compared to UV-light. Band gap of the catalyst is smaller than the wavelength of UV-light. So, UV-light excites the electrons leading to electron-hole formation. However, as sunlight contains less than 5% of light in UV range, only this part of the of the total optimum energy can be utilized with TiO_2 (Fatin et al. 2012). Hence, degradation rate is less under solar light. Neppolian (2002) have noticed that the percentage degradation of the dyes increased with increase the solar light intensity, which they attributed to creation of electron–hole pair and prevention of recombination. However, at lower light intensity, electron–hole recombination rate is high, which decreases the creation of free radicals, hence the degradation rate reduces (Bahnemann 1999). Chanathaworn et al. (2012) used the light intensity of black light lamp in the range of 0–114 W/m^2 and observed the effects of light intensity on Rh-B decolorization. They obtained enhanced dye degradation with increase in the light intensity. Liu et al. (2006) studied on photodegradation of AY affected by three different light intensities (1.24 mW/cm^2, 2.04 mW/cm^2, 3.15 mW/cm^2) and they observed that decolorization increases with increasing light intensity. Several researchers reported an increase in decolorization rate with increasing light intensity (Sakthivel et al. 2003; So et al. 2002).

Bharathkumar et al.(2015) in their studies on MB dye degradation using BFO mesh under sunlight, have reported that when the light intensity increases photocatalytic activity increases. They attributed this effect to increase in the reaction rate between the dye and the catalyst, and more importantly to bend-bending. Band bending provides an extra penetration path for transport of photo-generated charge carriers to dye and

photocatalyst interface region, which prevent the recombination rate of charge carriers, resulting in an enhanced photocatalytic performance.

Romão and Mul (2016) studied the effect of light on decomposition of MO and Atrazine in aqueous solutions using TiO_2. They noticed that the degradation rate of MO is slower at lower light intensity. The degradation of Atrazine proceeded at a significantly slower rate in the presence of MO at low light intensity, as compared to high light intensity. The rate constant for MO degradation followed a non-linear (0.5-order) dependency with light intensity. However, the influence of light intensity on the rate of degradation of Atrazine was significant, as rate constant increased exponentially.

Anku et al. (2016) reported the photocatalytic degradation of MO and CR under Simulated Visible Light using Fe^{3+}/C/S-doped-TiO_2 nanoparticles with varied visible light intensities such as 0.5 sun, 0.7 sun, 1.0 sun and 1.3 sun intensities. The dye degradation was found to increase with the light intensity upto 1 sun. With an increase in light intensity upto 1 sun, the number of photons that reach the surface of the catalyst increases. However, at the light intensity to 1.3 sun, the degradation efficiency was found to be moderate, which is due to optimum number of photons required for a degradation of the dye. So, at 1.3 photon numbers more than that required to fact reaction and doesn't change the reaction rate. Hence, there was no change in degradation efficiency.

Salama et al. (2018) reported on photocatalytic degradation of MB and IC using CA/CNT/TiO_2 composite nanofibers under UV-Light. They reported that photodegradation rate dependent by the light intensity, and photodegradation rate increased with increase in the light intensity. Sun et al. (2018) a non-linear dependency of degradation of benzene on light intensity in their studies using nitrogen-doped TiO_2 (N-TiO_2) under visible light irradiation, wherein benzene degradation improved with increasing light intensity. Chiu et al. (2019) in their studies on the effect of light intensity on photocatalytic degradation of dyes, noticed that photodegradation rate increases linearly with light intensity at low intensities, whereas at higher light intensities, the photodegradation rate was independent of light intensity. At low light intensity, the photoexcited electron and holes are contest with for their recombination,

consequently hindering the generation of reactive radicals. The electron-hole pair generation increases as the light intensity increases, resulting in a greater photodegradation efficiency. However, as the active sites on the catalyst for degradation remains constant, the reaction rate demonstrates a maximum rate, although the light intensity endures to increase (Ollis et al. 1991).

Alkaykh et al. (2020) studied the MB degradation using $MnTiO_3$ nanoparticle synthesized via sol-gel technique under sunlight with varying source of irradiation. The light intensity and the wavelength play a crucial rule in photo-degradation of pollutants (Ahmed et al. 2010; Kaneco et al. 2004; Li Puma and Yue 2002). They were changed the light source and intensity and noticed that the degradation of MB under solar light was more effective compared to artificial UV light. However, they observed that the percentage degradation under artificial UV-C radiation was higher than UV-A radiation. However, they did not notice any change in degradation rate with increase in light intensity, which was due to optimum number of photons essential for photocatalytic degradation being reached with the lowest intensity light used in their study. So, the higher intensity light was incapable to affect for degradation rate (Anku et al. 2016; Reza et al. 2017).

The review suggests that the studies on various irradiation sources are important to suitably apply the photocatalytic process in an economic and energy efficient manner. The knowledge on the effect of light intensity on degradation would help in better understanding of the kinetics of degradation under the irradiation conditions used. This information is important in the design of photocatalytic reactors.

2.8 Scope and Objectives of the Research Work

Based on the literature review and the research gaps identified thereof, the scope and objectives of the present study were specified.

2.8.1 Scope of the study

The main focus of this research work is to synthesize two BFO based nanocomposites (BFO@TiO$_2$ and BFO@PANI) for their application in the degradation of dyes from mixed dye contaminated water containing, MB, AY and Rh-B dyes under visible light irradiation. The degradation of the dyes in water is represented in terms of decrease in dye concentrations as analyzed by spectrophotometric analysis and COD removal. The base constituent in the synthesis of BFO@TiO$_2$ and BFO@PANI is BFO. According to literature, the method used for synthesis of individual constituents of the nanocomposite greatly affects the properties of the nanocomposite. Thus, a best method for the synthesis of BFO which is the base constituent for both the nanocomposites (BFO@TiO$_2$ and BFO@PANI) is to be chosen, based on the maximum photocatalytic activity in terms of degradation of MB, AY and Rh-B, dyes and COD removal from mixed dye contaminated water under visible light irradiation.

The optimization of the ratio of BFO to the precursor of other semiconductor to be used in the synthesis mixture is essential. The properties that determine the photocatalytic activity of any nanocomposite vary with the synthesis conditions and the ratios of the individual constituents or precursors used in the synthesis. The ooptimization of catalyst composition plays a very important role in determining the structure and morphology of the catalyst. The structure of the composite helps in the charge transfer at the heterojunction interface (Liu et al. 2017). It is well known that calcination temperature and time are the significant factors that influence the crystallinity, phase transition, morphology, and surface area of nanoparticles, which can clearly affect the photocatalytic activity (Li et al. 2005; Sathish et al. 2007). Thus, the optimization of the ratio of BFO to the precursor of other semiconductor, calcination conditions like calcination temperature and time is to be carried out in order to maximize the degradation of dyes and COD removal.

The characterization of nanocomposite particles is essential in order to compare and understand the variations in their activities and functionalities. It is required to characterize the synthesized nanocomposite particles by X-Ray Diffraction (XRD), Scanning Electron Microscopy (SEM), Transmission Electron Microscopy (TEM), Fourier Transform Infrared spectroscopy (FTIR), UV–Vis absorption spectroscopy, X-Ray Photoelectron Spectroscopy (XPS) analysis in order to determine the crystallinity, crystalline composition, morphology, shape, size, presence of surface chemical groups and light absorption properties of the synthesized nanocomposites.

The dye degradation and COD removal efficiency can be enhanced by adequate optimization of the photocatalytic process parameters such as pH, catalyst loading and light intensity. The studies on optimization of these parameters by a simple *One factor at a time optimization strategy* is essential in order to maximize the degradation of the dyes. Further, the degradation of a target dye in mixed dye contaminated water depends not only on its own concentration, but also on the presence and concentration of the other dyes. The degradation of dyes and COD removal efficiency may vary due to interaction between the dye molecules and competition for the catalyst sites. The studies on the effect of presence of the other dyes and dye concentrations on the degradation of each of the dyes in the mixed dye contaminated water would be beneficial to understand how the simultaneous degradation of dyes is affected.

The ultimate focus of development of visible light active catalysts is to harness solar energy for photocatalytic water treatment. The assessment of the photocatalytic activity of the synthesized nanocomposites in terms of degradation of the dyes from mixed-dye contaminated water under solar irradiation is an important aspect of any study on photocatalysis. The design and scale up of any largescale photocatalytic reactors to be used for effluent treatment makes to evaluate the kinetics of photocatalytic degradation. The studies on reusability potential of the nanocomposite particles are required to assess if, these nanocomposites can be reused in multiple batches of photocatalysis. A study on the leachability of the metals from the nanocomposite to the reaction mixture during photocatalysis is essential to assess if the nanocomposites contribute to any secondary metal pollution of treated water.

2.8.2 Objectives of the Research Work

The main objective of the research work is to study the efficacy of BFO@TiO$_2$ and BFO@PANI heterostructured nanocomposites as photocatalysts for the degradation of dyes from mixed dye contaminated water containing three textile dyes: Methylene Blue (MB), Acid Yellow-17 (AY) and Rhodamine B (Rh-B), under visible light irradiation.

The specific objectives are:

- To choose a suitable method for the synthesis of BFO to be used in the synthesis of heterostructured nanocomposites, based on maximum photocatalytic activity in terms of degradation of the dyes and COD removal from mixed dye contaminated water.

- To synthesize BFO @TiO$_2$ nanocomposite by varying the molar ratio of BFO to Ti in the synthesis mixture, calcination temperature, calcination time and to optimize these parameters for maximum photocatalytic activity in terms of degradation of dyes and COD removal from mixed dye contaminated water.

- To optimize the ratio of BFO to aniline in the synthesis of BFO@PANI nanocomposite for maximum photocatalytic activity in terms of degradation of dyes and COD removal from mixed dye contaminated water.

- To characterize the nanocomposites

- To optimize the initial pH of the reaction mixture and catalyst loading for the degradation of dyes from mixed dye contaminated water using BFO@TiO$_2$ and BFO@PANI nanocomposites.

- To study the effect of the initial concentration of individual dyes in the mixed dye contaminated water on photocatalytic dye degradation and COD removal to assess the mutual interacting effect of the dyes in photocatalysis.

- To determine the effect of light intensity on the degradation of dyes from mixed dye contaminated water using BFO@TiO$_2$ and BFO@PANI nanocomposites.

- To assess the solar photocatalytic activity of BFO@TiO$_2$ and BFO@PANI nanocomposites for degradation of dyes from mixed dye contaminated water.

- To study the kinetics of degradation of dyes from mixed dye contaminated water under visible and solar light irradiation**.**

- To assess the reusability potential of the BFO@TiO$_2$ and BFO@PANI nanocomposites for subsequent batch photocatalysis.

CHAPTER 3

3 MATERIALS AND METHODS

This chapter describes the experimental details and various methodologies adopted to achieve the stated objectives in the current study. The detailed procedure for the synthesis of BFO, BFO@TiO$_2$ and BFO@PANI heterostructured nanocomposites is presented. The experimental set up and the method for photocatalytic degradation of three textile dyes, viz. MB, AY and Rh-B present in mixed dye contaminated water is also presented. The procedure for the analysis of dye concentration and COD are presented. All the experiments for the study were conducted in triplicates and the average values are reported.

3.1. Materials

Acid Yellow-17 (60% pure), Rhodamine-B (90% pure), Titanium Tetra (IV) isopropoxide (TTIP), Bismuth (III) nitrate pentahydrate (BiN$_3$O$_9$-5H$_2$O) (99.99%, trace metals basis), Iron (III) nitrate nonahydrate (FeN$_3$O$_9$-9H$_2$O) (99.99%), trace metals basis), polyvinylpyrrolidone (PVP: MW 40 000), Sodium dodecyl sulphate (SDS) (NH$_4$)$_2$S$_2$O$_8$ (APS- di ammonium per sulphate) and citric acid were purchased from Sigma-Aldrich Chemicals Pvt. Ltd., Bangalore, India. Methylene Blue (100% pure) and acetylacetone were purchased from Merck specialities Pvt. Ltd, Mumbai, India. Nitric acid and potassium hydroxide (KOH) were purchased from NICE Chemical Pvt. Ltd, Cochin, India. Degussa P-25 (TiO$_2$) which was used for the comparison studies was purchased from Intelligent Material Pvt. Ltd, Haryana, India.

3.2. Synthesis of Bismuth ferrite particles (BFO)

BFO nanoparticles were synthesized by three different Methods: Co-precipitation method (Method I); Auto-combustion Method (Method 2) and Combustion synthesis method (Method 3).

Method 1: Co-precipitation method using KOH as the precipitant:

Co-precipitation method for the synthesis of BFO particles was adopted from Egorysheva et al.(2010) and Li et al. (Li et al. 2009a). For the synthesis of BFO by co-precipitation method, bismuth nitrate (BiN$_3$O$_9$-5H$_2$O) and iron nitrate (FeN$_3$O$_9$-9H$_2$O)

in 1:1 molar ratio was used. One hundred millilitres of 0.3 M bismuth nitrate and iron nitrate solutions were prepared in distilled water separately. Bismuth nitrate solution was sonicated for 15 min and then mixed with iron nitrate solution. Ten millilitres of 0.1 M nitric acid were added to the above solution. The mixture was then precipitated slowly by adding 10 mL of 12 M KOH solution. After stirring for an hour, the mixture was centrifuged at 1200 rpm for 10 min to separate the nanoparticles and washed with distilled water and ethanol. The nanoparticles were further separated by centrifugation and dried. The particles were calcined at 400 °C for a duration of 2 h in a muffle furnace. Synthesis procedure of Method 1 is shown in the Figure 3.1.
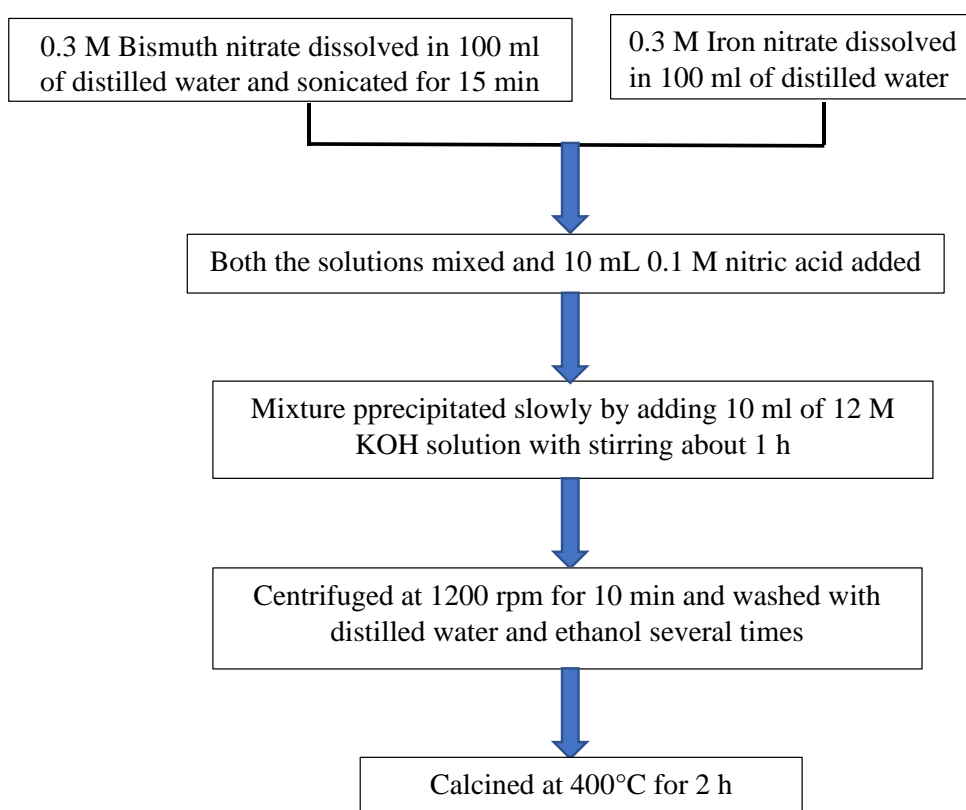
Figure 3.1: Synthesis procedure of Method 1.

Method 2: Auto-combustion method

Three different modifications of the auto-combustion method with citric acid as the chelating agent have been used in the present work.

Method 2A

The auto-combustion method reported by Bo et al. (2010) was adopted for the synthesis of BFO nanoparticles in Method 2A. 4.85 g of bismuth nitrate and 4.04 g of iron nitrate were dissolved in 50 mL solution of 3% glacial acetic acid to obtain bismuth ferrite to iron nitrate with molar ratio of 1:1. 0.21 g of citric acid was added to the above solution, and the solution was stirred for an hour followed by evaporation of solvent at 80°C for two hours. The granular product was collected, washed and filtered with deionized water for several times. Finally, the product was calcined at 600°C for 4 h in a muffle furnace. Synthesis procedure of Method 2A is shown in the Figure 3.2.

| 4.85 g of bismuth nitrate and 4.04 g of iron nitrate were dissolved in 50 mL solution of 3 % glacial acetic acid |
| 0.21 g of citric acid added to the solution and stirred for 1 h and solvent evaporated at 80°C for 2 h |
| Granular product was washed and filtered with water several times and calcined at 600°C for 4 h |
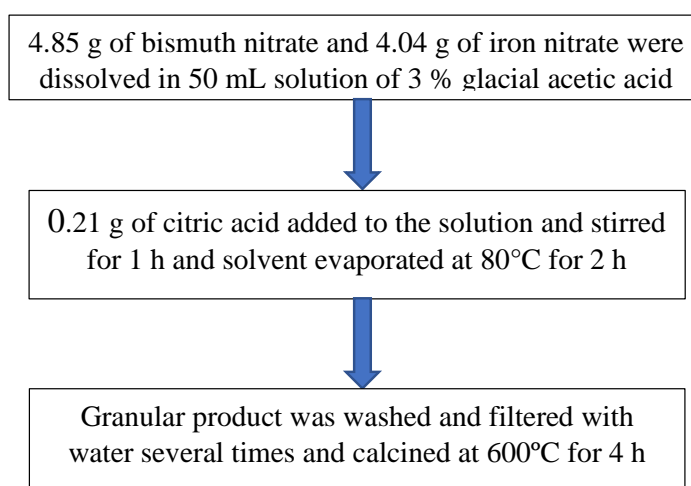
Figure 3.2: Synthesis procedure of Method 2A.

Method 2B

BFO nanoparticles were also synthesized by the auto-combustion method as reported by Lu et al. (2015). Bismuth nitrate (4.85 g) and iron nitrate (4.04 g) in 1:1 molar ratio was dissolved in 20 mL of acetic acid, and a yellow solution was obtained. Then, 10 g citric acid was added slowly into the solution under stirring conditions. The mixture was heated at 50°C under vigorous stirring conditions for one hour to form the sol, which was then dried at 150°C for 2-3 hours to obtain a dry gel. Finally, the dry gel was calcined at 550°C for 3 h in a muffle furnace. Synthesis procedure of Method 2B is shown in the Figure 3.3.

| 4.85 g of Bismuth nitrate and 4.04 g of Iron nitrate were dissolved in 20 mL acetic acid |
| 10 g citric acid added slowly into the solution at 50ºC under stirring for 1 h to form the sol |
| Dried at 150ºC for 2-3 h |
| Dry gel was ccalcined at 550°C for 3 h |
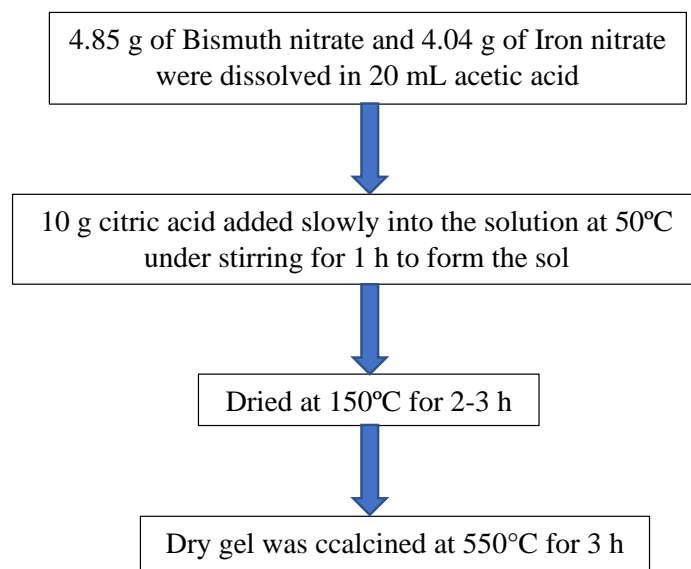
Figure 3.3: Synthesis procedure of Method 2B.

Method 2C

BFO nanoparticles were prepared by following the auto combustion method reported by Ganapathi (2015). Bismuth nitrate and iron nitrate in 1:1 molar ratio was used. 4.85 g of bismuth nitrate was dissolved in dilute nitric acid. 4.04 g of iron nitrate was dissolved in a minimum amount of double distilled water. Then both the solutions were mixed. The stoichiometric amount of citric acid (3.9 g) required for the molar ratio of 1:1 (total moles of metal nitrates to citric acid in the synthesis mixture) was dissolved in an equal amount of double distilled water separately. Then, the aqueous solution of citric acid was added drop by drop into the metal nitrate solution. This mixed solution was stirred continuously on a hot plate at 45°C for the chelating of Bi^{2+} and Fe^{3+} ions in the solution. The clear brownish solution thus obtained had a pH=2. The aqueous ammonia (25% w/v) solution was then added drop by drop under constant stirring in order to adjust the pH value to about 7. Then the neutralized solution was kept on a hot plate at 80°C to get combusted powder of bismuth ferrite. The combusted powder was then annealed at 500°C for 3 h in a muffle furnace. Synthesis procedure of Method 2C is shown in the Figure 3.4.

4.85 g Bismuth nitrate dissolved in nitric acid (minimum amount) and 4.04 g Iron nitrate dissolved in distilled water (minimum amount)

↓

The metal nitrate solutions were mixed

↓

3.9 g Citric acid dissolved in same amount of water and then added drop by drop to the metal nitrate solution at 45°C under stirring

↓

Aqueous aammonia solution (25% w/v) was added drop by drop to the solution, until solution pH reaches 7. The solution was heated at 80°C to get combusted powder

↓

Calcined at 500°C for 3 h

Figure 3.4: Synthesis procedure of Method 2C.

Method 3: Surfactant-assisted combustion synthesis method with glycine as the fuel.

BFO nanoparticles were prepared by adopting the combustion synthesis process reported by Kisku (2009) with modifications. 4.85 g of bismuth nitrate (BiN_3O_9-$5H_2O$) and 4.04 g of iron nitrate (FeN_3O_9-$9H_2O$) were dissolved in dilute nitric acid to get 1:1 molar ratio of the nitrates. 0.1 mole (7.5 g) of glycine and 0.05 mole (0.66 g) of the surfactant, Triton X were then added to the solution of nitrates. This solution was then heated on a hot plate under the continuous stirring condition to its boiling temperature until all the liquid evaporated. There was an immense evolution of brown fumes, towards the end of the reaction and a fluffy brown mass was obtained at the base of the beaker. The fluffy mass was powdered and the powder was calcined at 500°C for 3 h. Synthesis procedure of Method 3 is shown in the Figure 3.5.

```
┌─────────────────────────────────────────┐
│  4.85 g Bismuth nitrate and 4.04 g Iron  │
│    nitrate dissolved in nitric acid      │
│          (minimum amount)                │
└─────────────────────────────────────────┘
                    │
                    ▼
┌─────────────────────────────────────────┐
│   7.5 g of glycine (0.1 mole) and 0.66 g │
│       (0.05 mole) Triton X added         │
└─────────────────────────────────────────┘
                    │
                    ▼
┌─────────────────────────────────────────┐
│       Heated with constant stirring      │
│         until the liquid evaporated      │
└─────────────────────────────────────────┘
                    │
                    ▼
┌─────────────────────────────────────────┐
│       Fluffy brown mass obtained was     │
│      powdered, calcined at 500°C for 3 h │
└─────────────────────────────────────────┘
```
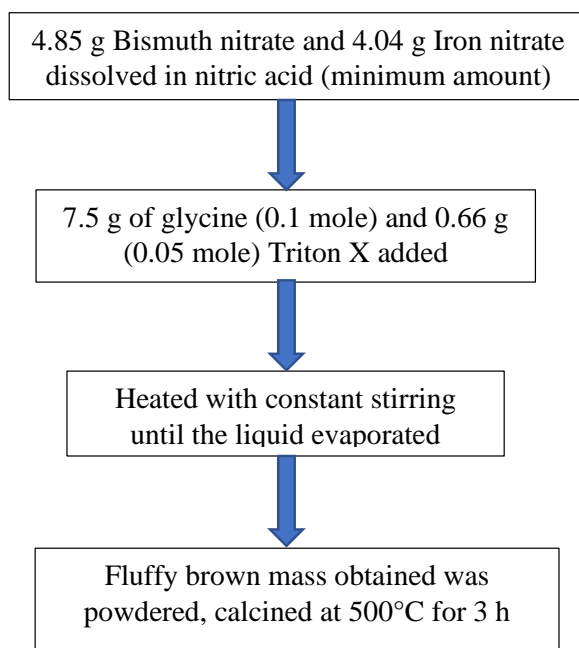
Figure 3.5: Synthesis procedure of Method 3.

3.2.1. Choice of method for the synthesis of BFO nanoparticles

The BFO nanoparticles synthesized by Method 1, Method 2A, 2B and 2C and Method 3 were used as photocatalyst for the degradation of dyes from mixed dye contaminated water containing 10 mg/L each of MB, AY and Rh-B dyes with 0.1 g/L of catalyst loading and initial unadjusted pH of 7.26, under visible light irradiation with two numbers of 18 W lamps (263 μ W/cm^2). The photocatalysis was carried out as described in Section 3.7. The method that yielded maximum percentage degradation of the dyes and COD removal was chosen for the preparation of BFO to be used in the synthesis of BFO@TiO$_2$ and BFO@ PANI heterostructured nanocomposites.

3.3. Synthesis of BFO@TiO$_2$ heterostructured nanocomposite particles

In the preparation of BFO@TiO$_2$ heterostructured nanocomposite particles, the method followed by Hengky (2013) was adopted, by varying the molar ratio of BFO to Ti in the synthesis mixture. They have used the BFO nanoparticles synthesized by combustion route using a fuel (Glycine) for the synthesis of BFO@TiO$_2$. The present study reports the use of BFO, synthesized by auto combustion method (Method 2C) for the synthesis of BFO@TiO$_2$. The mole ratio of BFO powder to Ti (Titanium tetra (IV) isopropoxide (TTIP), the precursor salt for TiO$_2$) in the synthesis mixture was varied

as 1:0.5, 1:1, 1:2, 1:3 and. 1:4. 1 g (0.0032 moles) of the BFO powder was suspended in 100 mL ethanol in beaker A. The required volume of TTIP (to get the desired ratio of BFO to Ti with 1 g BFO) was mixed in beaker B with an equal volume of acetylacetone and 100 mL of ethanol, well stirred and dispersed with sonication at 20 kHz for 1h. The volume of TTIP used for varying ratios of BFO to Ti in the synthesis mixture is presented in Table 3.1. TTIP solution from beaker B was then added to the dispersed BFO suspension in beaker A. The pH of the dispersed BFO-TTIP solution was adjusted to approximately pH 5 with dilute nitric acid and constant stirring was continued. After one hour, the sol was centrifuged at 12000 rpm for 10 minutes to separate the powder. The powder was then washed with ethanol and then water, followed by centrifugation. The powder was then dried in an oven at 100°C until it is scorched. The synthesized BFO@TiO$_2$ particles were then calcined at 500°C in a muffle furnace for 3 h. Synthesis procedure of BFO@TiO$_2$ heterostructured nanocomposite particles is shown in the Figure 3.6.

Further, for optimization of calcination temperature, the calcination temperature was varied from 300°C to 700°C, in increments of 100°C for calcination time of 3 h. For optimization of calcination time, the calcination was carried out at 400 °C, but the calcination time was varied from 1 h to 5 h at increments 1 h. BFO@TiO$_2$ nanocomposites synthesized with varying mole ratio of BFO to Ti in the synthesis mixture, calcination temperature and calcination time were used as photocatalyst for the degradation of dyes from mixed dye contaminated water containing 10 mg/L each of MB, AY and Rh-B dyes with 0.1 g/L of catalyst loading and initial unadjusted pH of 7.26, under visible light irradiation with two numbers of 18 W lamps (263 μW/cm^2). The photocatalysis was carried out as described in Section 3.7. The molar ratio, calcination temperature and time were optimized based on the maximum photocatalytic activity in terms of degradation of the dyes and COD removal from the mixed dye contaminated water.

Solution A

A required volume of TTIP (to get a desired molar ratio of BFO to Ti) mixed with equal volume of acetyl acetone and 100 mL ethanol

Solution B

1 g of BFO (0.0032M) powder suspended in ethanol and dispersed by sonication for 1 h

Solution A and B were mixed

Dilute nitric acid was added until solution pH reaches pH 5. Stirred for 1 h

Centrifuged at 12000 rpm for 10 minutes. Washed with ethanol and water

BFO@TiO$_2$ separated by centrifugation, dried in oven at 100°C

Calcined at required temperature and time

Figure 3.6: Synthesis procedure of BFO@TiO$_2$ heterostructured nanocomposite particles.

Table 3.1: Volume of TTIP used for varying ratios of BFO to Ti in the synthesis mixture.

Molar ratio of BFO to Ti in the synthesis mixture	Volume of TTIP (mL) used for 1 g BFO
1:0.5	0.47
1:1	0.94
1:2	1.88
1:3	2.84
1:4	3.76

3.4. Synthesis of BFO@PANI heterostructured nanocomposite particles

In the preparation of BFO@PANI heterostructured nanocomposite particles, the method followed by Chaturvedi et al. (2015) was adopted as a base method, with modification in terms of amount of aniline used. The molar ratio of BFO to aniline for the synthesis was varied by changing the volume of aniline used for polymerization. Chaturvedi et al. (2015) have used the BFO nanoparticles synthesized through a chemical route and coating of polyaniline was achieved by a double surfactant layer technique along with post-synthesis annealing for the synthesis of BFO@PANI. In the present study, the BFO nanoparticles synthesized by auto combustion method (Method 2C) as explained in Section 3.1 have been used for the synthesis of BFO@PANI.

To advance the reliability of the BFO core, 1 g (0.032 moles) of the BFO powder and 1 g polyvinylpyrrolidone (PVP: MW 40 000) were suspended in 120 mL Milli-Q water. The mixture was ultrasonicated for 12 h to confirm that the adsorption of PVP was complete. To remove the un adsorbed PVP molecules, the dispersion was centrifuged and washed with ethanol several times. Subsequently, PVP stabilized BFO was re-dispersed in 50 mL distilled water containing 0.08 g sodium dodecyl sulphate (SDS), and 0.01 g $(NH_4)_2S_2O_8$ (APS). This solution was held for 12 h at room temperature. Then adequate volume of aniline (to obtain desired BFO to aniline mole ratio) and 104 μL l HCl were added to the above solution, and the reaction was carried out at 4°C for 12 h with stirring (Ice packs were used to maintain the temperature during

the reaction). The resulting product was then filtered, washed with distilled water and then ethanol to remove the impurities. The product was then dried in a hot air oven. Synthesis procedure of BFO@PANI heterostructured nanocomposite particles is shown in the Figure 3.7.

The volume of aniline used for the synthesis was varied as 8μL, 10μL, 12μL, 14μL, and 16μL by keeping the amount of BFO constant at 1 g, and prepared samples were named as BFP1, BFP2, BFP3, BFP4 and BFP5 respectively. The molar ratio of BFO to aniline used in the synthesis of these BFO@PANI samples were 1:0.0027; 1:0.0034; 1:0.0041; 1:0.0048 and 1:0.0055. BFO@PANI nanocomposites thus synthesized with varying mole ratio of BFO to aniline, were used as photocatalyst for the degradation of dyes from mixed dye contaminated water containing 10 mg/L each of MB, AY and Rh-B, dyes with 0.1 g/L of catalyst loading and initial unadjusted pH of 7.26, under visible light irradiation with two numbers of 18 W lamps (263 μ W/cm^2). The photocatalysis was carried out as described in Section 3.7. The molar ratio of BFO to aniline, that yielded maximum photocatalytic activity of the synthesized photocatalyst in terms of degradation of the dyes and COD removal from the mixed dye contaminated water was chosen as the optimum ratio.

1 g of BFO particles and 1 g polyvinylpyrrolidone (PVP: MW 40 000) were dispersed in 120 ml Milli-Q water, ultrasonicated for 12 h

The dispersion was centrifuged and washed with ethanol several times

PVP stabilized BFO was redispersed in 50 ml of distilled water containing, 0.08 g sodium dodecyl sulphate (SDS), and 0.01 g $(NH_4)_2S_2O_8$ (APS)

Solution was held for 12 h at room temperature

Desired volume of aniline (8-16 μl) and 104 μl of HCl was added to the solution

The reaction at 4°C for 12 h with stirring

The resulting solid product separated by centrifugation and washed several times with water and ethanol

The product was then dried in a hot air oven

Figure 3.7: Synthesis procedure of BFO@PANI heterostructured nanocomposite particles.

3.5. Characterization of synthesized nanoparticles

X-Ray diffraction, normally called as XRD, is a non-destructive test tool used to analyse crystal structure, and to identify the crystalline phases present in the material and their chemical composition information (Bunaciu et al. 2015). XRD analysis of the calcined BFO nanoparticles and BFO@TiO$_2$, and BFO@PANI nanocomposite particles was carried out by using Rigaku diffractometer (Miniflex 600) under Cu-Kα radiation (1.5406 Å). And the crystallite size was determined by using the Debye Scherrer's formula (Equation 3.1).

$$D = \frac{K\lambda}{\beta cas(\theta)}$$ ………………………………………………………………………..(3.1)

where D = crystallite size

K = 0.90 the Scherrer's constant

λ = X-ray wavelength

β = the peak width at half maximum (FWHM)

θ = the Bragg diffraction angle

The Scanning Electron Microscope (SEM) is a type of electron microscope which produces images of a sample by scanning the surface with a focused beam of electrons (Akhtar et al. 2018). The electrons interact with atoms in the sample, producing various signals that contain information about the surface morphology of the sample. SEM image of the nanoparticle samples was recorded by using Jeol (JSM-6380A) microscope operated at 20kV, after sputtering. To make surface of the sample conductive, 10 minutes gold sputtering was done with a sputtering unit. Most commonly used sputter coating has been gold, due to its high conductivity and its relatively small grain size that enables high resolution image.

Transmission Electron Microscopy (TEM) is a microscopy technique in which a beam of electrons is transmitted through a sample to form an image (Wang 2003). An image is formed from the interaction of the electrons with the sample as the beam is transmitted through the specimen. The nanoparticle samples were suspended in double distilled water (10 mg in 10 ml), sonicated for 30 minutes, poured on copper grid evenly and dried overnight. TEM of the prepared sample was performed using a Tecnai G2T20 model with filament LaB6, and point resolution was 0.24 nm. Energy Dispersive

Spectroscopic (EDS) analysis was carried out using TEM, to determine the elemental composition of the samples.

Fourier transform infrared spectroscopic (FTIR) technique used to obtain an infrared spectrum of absorption or emission of a solid, liquid or gas (Dendisová et al. 2018). An FTIR spectrometer simultaneously collects high-spectral-resolution data over a wide spectral range. FTIR analysis of the particles was performed using Bruker Alpha FTIR spectrometer by using KBr pellets.

Zeta potential of the particles were analysed using Horiba scientific zetasizer, SZ-100 to determine the stability of the nanoparticles (Bhattacharjee 2016).

To determine the band gap energy of the synthesized BFO@TiO$_2$ and BFO@PANI articles, the UV-Vis spectra of the photocatalyst suspended in distilled water (1 mg/mL) was obtained using Hitachi U-2000 spectrophotometer in a wavelength range of 200 to 800 nm and the absorbance values were recorded. The optical band gap energy of the synthesized nanoparticles was calculated by using Tauc's plot drawn from the data of the absorption spectra. Tauc's plot of $(Ah\nu)^2$ vs $(h\nu)$ was plotted, where A is the absorption coefficient, h is the Plank's constant, and $\nu = c/\lambda$ (c = speed of light and λ is the wavelength). The extrapolation of the linear region of the Tauc's plot intersecting the x-axis gives the value of the optical band gap. (Feng et al. 2015; Kalikeri et al. 2018)

X-ray photoelectron spectroscopy (XPS), also called as electron spectroscopy for chemical analysis (ESCA) is used to analyse the surface chemistry of a material, and measure the elemental composition, empirical formula, chemical state and electronic state of the elements within a material (Pamidimukkala 2006). X-Ray penetrates a depth of a few nanometres (approximately 5 nm). The XPS analysis was performed using PHI Versa Probe II with AES X-ray photoelectron spectroscopy.

XPS analysis involves exciting a sample surface with monochromatic X-ray. When a sample surface is bombarded with X-rays in a vacuum, the energy of the photoelectrons (50–2000 eV) are emitted. From intensity of a photoelectron peak and the binding energy, the chemical state, elemental identity, and quantity of a detected element can be determined.

3.6. Preparation of mixed dye contaminated water (aqueous solution of mixture of MB, AY and Rh-B)

100 mg/L stock solution of MB, AY and Rh-B were prepared separately. The desired volume of the stock solution of each of the dyes were taken in 100 mL standard flask and diluted with distilled water up to the mark to get desired concentration of each of the dyes in the mixed dye aqueous solution. e.g., mixed dye contaminated water with 10 mg/L of each of the dyes was prepared by taking 10 mL each of 100 mg/L stock solution of each of the dyes in 100 mL volumetric flask, followed by dilution with distilled water up to the mark.

3.7. Photocatalysis for degradation of dyes from mixed dye aqueous solution

Photocatalysis was carried out in a reactor which is a 500 mL borosilicate glass beaker placed at the center of an aluminium chamber of dimensions 40 cm X 70 cm X 70 cm, equipped with two irradiating visible lamps (unless otherwise specified) of 18 W (Polite gold tube light, Mysore Lamps, India) each adjacent to the side walls of the chamber. The reactor was placed at the centre equidistant from both the lamps. The distance between the lamps was 20 cm and the distance between the lamp and beaker walls was 7 cm. As shown in Figure 3.8 (a), the batch experiments for the photocatalytic degradation of dyes from mixed dye contaminated water containing Rh-B, AY and MB, dyes were carried out using the fabricated BFO, BFO@TiO$_2$ and BFO@PANI nanocomposite particles as the photocatalysts under visible light irradiation with 150 mL of aqueous dye solution containing 10 mg/L (unless otherwise specified) of each of the dyes. The airflow of 2 LPM was provided into the reactor to ensure the supply of oxygen as the oxidant. The experiments were conducted with the catalyst loading of 0.1 g/L unless otherwise specified. The unadjusted initial pH of the mixed dye contaminated water was pH 7.26. The reactor contents were magnetically stirred. During photocatalysis, the samples were withdrawn from the reaction mixture at regular intervals of time and then centrifuged at 12,000 RPM for 10 min to separate the catalyst particles from the liquid samples before the analysis of dye concentration. The photocatalysis was carried out for a total duration of 210 min. The light intensity at the reactor walls was measured using lux meter (KM-LUX-100K) and the average intensity was found to be 263 μ W/cm^2, with two lamps.

Studies on mixed dye solution face challenges in the measurement of dye concentration due to problems encountered with interferences. Thus, the simultaneous analysis of AY, MB, and Rh-B dyes was carried out using the first order derivative spectrophotometric method. The wavelength for the analysis was chosen by first-order derivative spectrophotometric method to avoid the interference of the dyes in the analysis. These wavelengths were found to be 531 nm for Rh-B, 415 nm for AY, and 694 nm for MB analysis. The first order derivative method for the choice of wavelength for analysis of MB, AY and Rh-B in mixed dye solution is explained in Section 3.10. The absorbance of the reactor samples containing the mixture of these dyes was measured at all the three wavelengths using a UV–Visible spectrophotometer (model: U-2000, Hitachi) and the concentrations of, MB, AY and Rh-B were determined using the calibration plots at the corresponding wavelengths. The COD of the dye solution was analysed by APHA (2012) standard method explained in Appendix II.

For optimization of pH for photocatalytic degradation of dyes from mixed dye solution, the photocatalysis was carried out at different initial pH conditions of pH 3, pH 5, pH 7, pH 9 and pH 11. The pH of mixed dye contaminated water was adjusted using 0.1 N NaOH and 0.1N HCl. For optimization of catalyst loading for photocatalytic degradation of dyes from mixed dye solution, the photocatalysis was carried out at optimum initial pH 5 by varying the catalyst loading from 0.1 g/L to 0.5 g/L at increments of 0.1 g/L. For the optimization of light intensity, the experiments on photocatalysis were carried out at optimum initial pH 5, and optimum catalyst loading of 0.3 g/L for BFO@TiO$_2$ and 0.2 g/L for BFO@PANI nanocomposite. To study the effect of light intensity, the number of lamps were varied from 1 to 4. The positioning of the lamps for these cases are shown in Figure 3.8 (b). The lamp was placed horizontally above the beaker adjacent to the top roof wall of the chamber for one lamp. For two and four lamps the lamps were placed vertically adjacent to the side walls of the chamber, For the experiments with three lamps, one of the lamps was placed horizontally above the beaker adjacent to the top roof wall of the chamber and other two were placed vertically adjacent to the side walls of the chamber.

The experiments under solar light were performed in the month of March between 10.00 AM to 1.00 PM, in the same reactor set-up without any enclosure in the

open terrace. The light intensity at the beaker walls was measured at regular intervals of time during photocatalysis using lux meter (KM-LUX-100K) and the average intensity was determined as 739 μW/cm^2.

A wireless lux meter was used to determine the light intensity. One lux equals one lumen per square metre. Light intensity was measured by converting lux into watt per square centimetre (μW/cm^2) at 555 nm, and was estimated using the formula, 1 lux [lx] = 1.464 X 10^{-01} μW / cm^2 (555 nm). The maximum intensity of the emitted solar energy occurs at a wavelength of about 555 nm and the fluorescent lamp maximum also occurs generally in the range of 480 nm to 630 nm, the average being at 555 nm. So, the conversion of lux to μW/cm^2 was made with 555 nm as the reference.

To study the effect of dye concentrations, the photocatalytic degradation experiments were conducted by varying the concentration of each of the dyes in the range of 10 mg/L to 30 mg/L at increments of 10 mg/L. Totally 27 (3^3) experiments were conducted with mixed dye aqueous solutions containing three dyes, by varying the individual dye concentrations with BFO@TiO$_2$ and BFO@PANI (synthesized under optimum conditions) as photocatalyst. These experiments were conducted at initial pH 5, catalyst loading of 0.3 g/L for BFO@TiO$_2$ and 0.2 g/L for BFO@PANI nanocomposites under irradiation by two lamps. The dye concentration conditions are specified in Table 5.1 and 5.2 respectively. Experiments were also conducted with aqueous solutions containing two dyes and single dye, to compare with those containing all the three dyes in order to study the effect of presence of one dye on the degradation of other dyes. The percentage degradation of each dye and the COD removal were analysed under each set of conditions of concentrations.
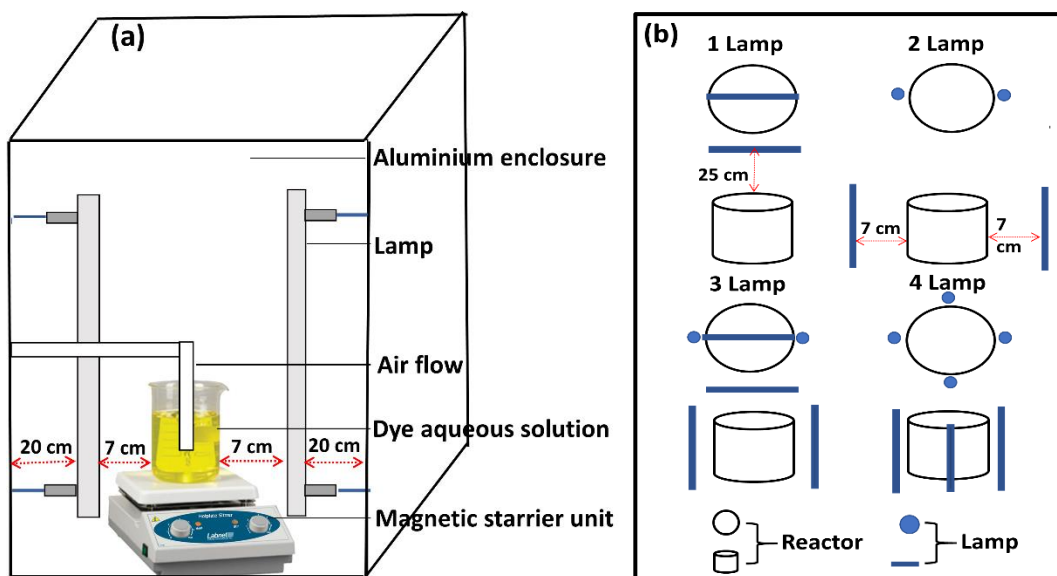
Figure 3.8: (a) Experimental set up of dye degradation under artificial visible light and (b) positioning of lamps in experimental set up chamber.

The percentage of degradation of each of the dye was estimated using Equation 3.2

$$\% \ Degradation = \frac{Ci-C}{Ci} * 100 \text{-}\ldots\ldots,\ldots\ldots\ldots\ldots\ldots\ldots\ldots\ldots\ldots\ldots\ldots\ldots\ldots\ldots\text{(3.2)}$$

Where C_i and C are the initial concentration and the concentration of dye at a particular time in the reactor, respectively. Percentage COD removal was determined using Eq. (3.2), but by using the COD values in mg/L in place of dye concentrations. All the experiments on photocatalysis were carried out in triplicates, and the average values with error bars are presented.

3.8. Method to assess the reusability potential of BFO@TiO₂ and BFO@PANI nanocomposites synthesized under optimum conditions

The reusability potential of BFO@TiO₂ and BFO@PANI nanocomposites synthesized with optimum conditions were assessed. The BFO@TiO₂ nanocomposites synthesized with the optimum molar ratio of BFO to Ti and calcined at optimum temperature and time are herein after referred as BFO@TiO₂opt. The BFO@PANI nanocomposites synthesized with the optimum molar ratio of BFO to aniline; calcined at optimum temperature and time are herein after referred as BFO@PANIopt. The photocatalytic experiments were carried out with similar reaction conditions under visible light irradiation with the fresh and recycled BFO@TiO₂opt and BFO@PANIopt

as photocatalyst. For these experiments, photocatalytic degradation of dyes was carried out at optimum initial pH 5, and optimum catalyst loading of 0.3 g/L for BFO@TiO$_{2opt}$ and 0.2 g/L for BFO@PANI$_{opt}$ nanocomposite with irradiation by two lamps. After completion of the photocatalysis experiment with a fresh catalyst (cycle I), the reaction mixture was centrifuged at 10000 rpm for 10 minutes and the nanocomposite particles were separated. These particles were washed with water and then with ethanol for 3 to 4 times, further centrifuged, the recovered catalyst was dried in hot air oven and reused for the next batch of photocatalysis. BFO@TiO$_{2opt}$ and BFO@PAN$_{opt}$ ware reused thrice, and four experiments were done, out of which the first cycle was with the fresh catalyst, and the remaining three cycles were with the recycled catalyst. Before the next cycle (reuse) of experiment, the catalyst recovery was carried out as explained earlier. Then the next cycle of batch experiments was conducted, and the same experimental conditions were used for all the four cycles. The percentage degradation of dyes and COD removal using fresh particles (Cycle 1), particles of single previous use (Cycle 2), particles of two previous uses (Cycle 3), and particles of three previous uses (Cycle 4) after 210 minutes of irradiation were noted.

3.9. Method to assess the leachability of metals from the nanocomposites

The batch photocatalysis was carried out for degradation of dyes from mixed dye contaminated water containing 10 mg/L of and Rh-B, AY and MB at initial pH 5, a catalyst loading of 0.3 g/L and 0.2 g/L under irradiation with visible light (2 lamps) with BFO@TiO$_{2opt}$ and BFO@PANI$_{opt}$ nanocomposite particles respectively. The liquid sample was collected after 210 min, centrifuged at 10000 rpm for 10 min to remove the catalyst. The supernatant was subjected to analysis of metals such as Bi, Fe and Ti by Inductively Coupled Plasma Optical Emission Spectroscopy (ICP-OES) made by Agilent Technologies (Modal 5100 ICP-OES) to determine if these metals have leached out from the nanocomposites during the photocatalysis process under the conditions of the study.

3.10. Analysis of dye concentration in mixed dye contaminated water

Figure 3.9 (a) shows the wavelength scan for the aqueous solutions of Rh-B, AY and MB as single dyes and as mixture of dyes with 10 mg/L concentration of each of the dyes. As shown in the Figure 3.9 (a), Rh-B, AY and MB have maximum

intensities at 535 nm, 418 nm, and 690 nm respectively when used as single dye aqueous solutions. So, when these dyes are present singly, the dye analysis can be done by using the UV-Vis spectrophotometer calibration at the corresponding wavelengths. However, the wavelength scan of the mixed dye aqueous solution shown in Figure 3.9 (a) indicates that, the peak at 418 nm corresponding to AY and the peak at 690 nm for MB has higher intensity in the mixed dye solution, compared to that in aqueous solution of corresponding single dyes. The intensity at 535 nm corresponding to Rh-B in the mixed dye solution is lower than that in aqueous solution of Rh-B. Thus, it is clear that when these dyes are present together in solution, the presence of other dyes interferes with the analysis of any given dye in the solution. Thus, the concentration of MB, AY and Rh-B, in the mixed dye aqueous solution, if determined using the calibration plots drawn using the absorbance readings at 690 nm, 418 nm and 535 nm respectively, would lead to erroneous results.

3.10.1. First order derivative spectrophotometric method to choose the wavelengths for analysis of dyes present in mixed dye aqueous solution

The derivative spectrophotometric method has been used to determine the wavelengths at which these dyes show minimum interference. First order derivative method is identified as a simple resolution enhancement technique for attrition of spectral interferences caused by the interaction of the components (i.e.) dyes in the mixture (O'Haver et al. 1982). In the first order spectrophotometric method, the zero-order spectrum is transformed into its corresponding first order derivative (dA/dλ) (O'Haver et al. 1982). The zero crossing points can then be used for the determination of the wavelength of dye analysis without the spectral inference of the other compounds in the mixture.

The first order derivative spectra for single dye aqueous solutions of Rh-B, AY and MB at 10 mg/L concentrations were recorded and are shown in Figure.3.9 (b). The wavelength of 531 nm was chosen for the analysis of Rh-B in the mixed dye solution, as the ordinate of derivative spectra for AY and MB is zero at that wavelength. The wavelength of 415 nm was chosen for the analysis of AY in the mixed dye solution, as the ordinate of derivative spectra for Rh-B and MB is zero at that wavelength. The

wavelength of 694 nm was chosen for the analysis of MB in the mixed dye solution, as the ordinate of the derivative spectra for Rh-B and MB are zero at that wavelength.

3.10.2 Calibration of spectrophotometer and analysis of dye concentrations in mixed dye solution

The UV-Visible spectrophotometer (Hitachi) was calibrated with the single dye solutions at wavelengths of 694 nm for MB, 415 nm for AY and 531 nm for Rh-B. Figure 310 (a), (b) and (c) present the calibration plots for MB at 694 nm, AY at 415 nm and Rh-B at 531 nm, in 1-10 mg/L concentration range respectively.

The mixed dye aqueous samples collected from the reactor at regular intervals of time during photocatalysis were centrifuged at 10000 rpm for 10 min and the absorbance of the supernatant was measured using the spectrophotometer at 531 nm, 415 nm and 694 nm. The concentration of MB, AY and Rh-B, were determined using the calibration plots drawn at 694 nm, 415 nm and 531 nm respectively. If the concentration of dyes in the reactor samples are at higher range than that used in calibration, then the liquid sample was diluted using distilled water before determining the absorbance values. The concentration obtained from the calibration plot was multiplied by the dilution factor to obtain the concentration in the reactor samples.
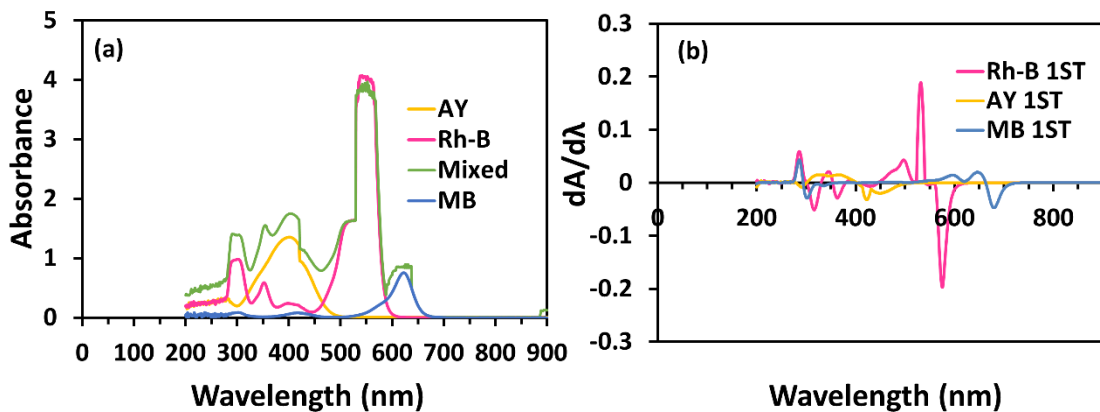
Figure 3.9: (a) UV-Visible spectrum of single and mixed dye containing MB, AY and Rh-B aqueous solution. (b) First order derivative spectroscopy of mixed dye containing Rh-B, AY and MB aqueous solution.
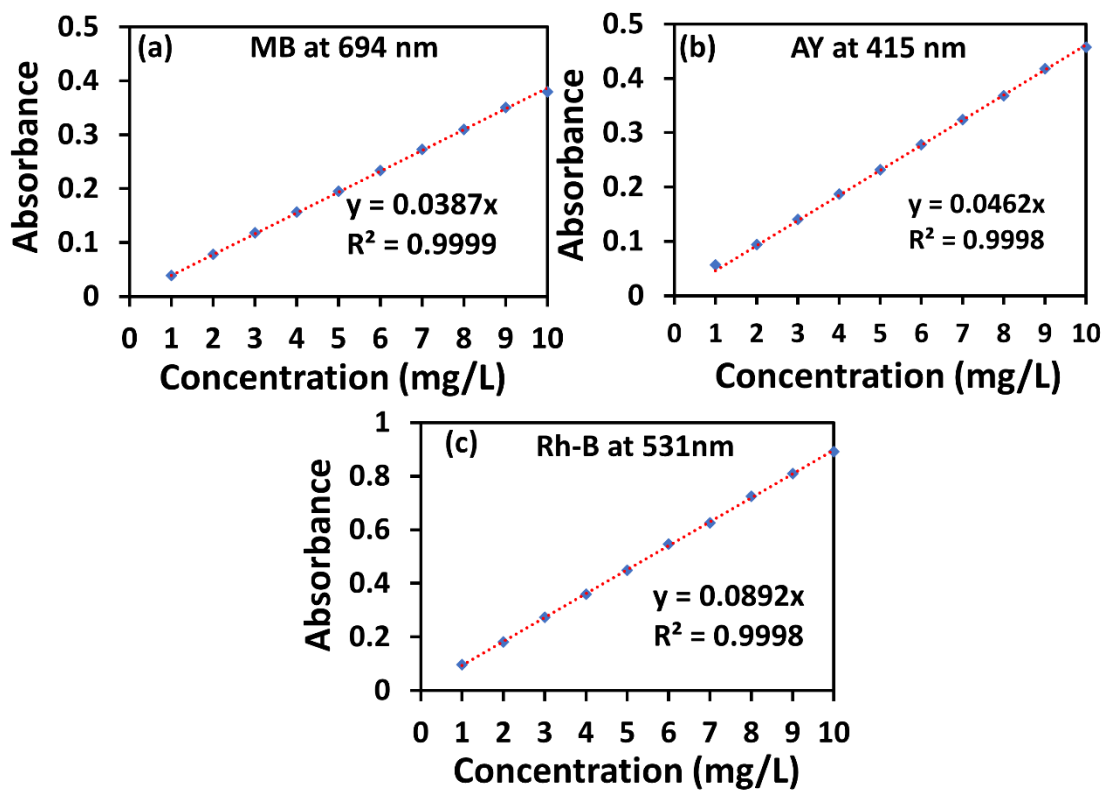
Figure 3.10: Calibration plots for (a) MB at 694 nm (b) AY at 415 nm and (c) Rh-B at 531 nm.

CHAPTER 4

RESULTS AND DISCUSSION

OPTIMIZATION OF NANOCOMPOSITE SYNTHESIS CONDITIONS

This chapter presents the results of the experiments conducted to meet the stated objectives of the research work along with the discussions thereof. BFO@TiO$_2$ and BFO@PANI nanocomposites were synthesized and were used for the degradation of dyes from mixed dyes contaminated water containing three dyes, *viz,* MB, AY and Rh-B, under visible light irradiation. Their efficacy in solar photocatalytic degradation of dyes were also evaluated. Initially, a best method for the synthesis of BFO nanoparticles were chosen among the available methods, based on maximum photocatalytic activity of the synthesized BFO nanoparticles in terms of degradation of the dyes from mixed dye aqueous solution. The method thus chosen, was further used for the synthesis of BFO nanoparticles to be used in the synthesis of BFO@TiO$_2$ and BFO@PANI nanocomposites. Further, various synthesis and calcination parameters in the synthesis of BFO@TiO$_2$ and BFO@PANI nanocomposites were optimized in order to maximize the degradation of the dyes from mixed dye aqueous solution. The synthesized nanocomposites were characterized and further used in photocatalytic degradation of dyes from mixed dye aqueous solution under visible light irradiation. The parameters affecting the photocatalytic reaction were further optimized to maximize the degradation efficiency.

4.1. Choice of synthesis method for BFO nanoparticles and characterization

4.1.1 Choice of synthesis method for BFO nanoparticles

BFO nanoparticles were synthesized using different methods (I) Co-precipitation method (Method 1) (II) Auto-combustion method with three different modifications (Method 2A,2B, and 2C) and (III) Combustion synthesis method (Method 3). Batch experiments for the photocatalytic degradation of dyes from mixed dye aqueous solution containing MB, AY, Rh-B dyes were carried out using the BFO nanoparticles fabricated by the above methods, as photocatalysts under visible light irradiation with an initial concentration of each of the dye at 10 mg/L and catalyst loading of 0.1 g/L. The synthesis method which yielded a maximum degradation of dyes from mixed dye

aqueous solution was chosen for the synthesis of BFO nanoparticles to be used further for the synthesis of BFO@TiO$_2$ and BFO@PANI nanocomposites.

As observed in Figure 4.1(a), maximum degradation of each of the dyes could be achieved with the BFO nanoparticles synthesized by auto-combustion method (Method 2C) with the removal of 93% MB; 71% AY and 67% of Rh-B in 210 minutes of irradiation. The percentage removal of each of the dyes in the presence of BFO nanoparticles synthesized by different methods under dark conditions did not exceed 10%. However, the dye removal in the presence of BFO nanoparticles on irradiation with visible light was appreciably higher. It shows that the removal of dyes cannot be attributed solely to adsorption process and the contribution of adsorption on dye removal is minimal. The dye removal under light irradiation in the absence of catalyst has also been found to be very less, confirming that photolytic degradation of the dyes is a very slow process.

The reaction intermediates can form during the oxidation of the dyes and some of them could be long-lasting and extra toxic than the parent compounds. Consequently, it is essential to realize the mineralization of these dyes concurrently (Medien and Khalil 2010). COD is the most commonly used parameter for pollution levels in water and it is used as the indicative parameter for dye mineralization (Vineetha et al. 2013). The COD of mixed dye aqueous solution was measured at regular intervals during photocatalysis to ensure the degradation of dyes into simpler compounds. The percentage of COD removal (mg/L) by photocatalysis is presented in Figure 4.1 (b). As observed in Figure 4.1 (b), the COD removal occurs by photocatalysis in the presence of BFO nanoparticles. Maximum removal of COD (~76.6%) has occurred in the presence of BFO nanoparticles synthesized by Method 2C, confirming that maximum extent of mineralization of dyes can be achieved with these BFO nanoparticles. The reduction in oxygen demand during the progress of reaction confirms the degradation of the dyes during the photocatalytic process (Nezamzadeh-Ejhieh and Karimi-Shamsabadi 2013).

Figure 4.1 (c) is a representative plot showing the effect of light and the catalyst on the dye removal process. It shows that in the presence of BFO nanoparticles synthesized by Method 2C and under visible light irradiation for 210 minutes, all the three dyes have been degraded to an appreciable extent. The dyes are photocatalytically

degraded successfully in the mixed dye aqueous solution in the presence of BFO nanoparticles. These results show that BFO particles are visible light active photocatalysts and the BFO nanoparticles synthesized by Method 2C exhibit a superior visible light mediated photocatalytic activity as compared to the BFO nanoparticles synthesized by other methods.
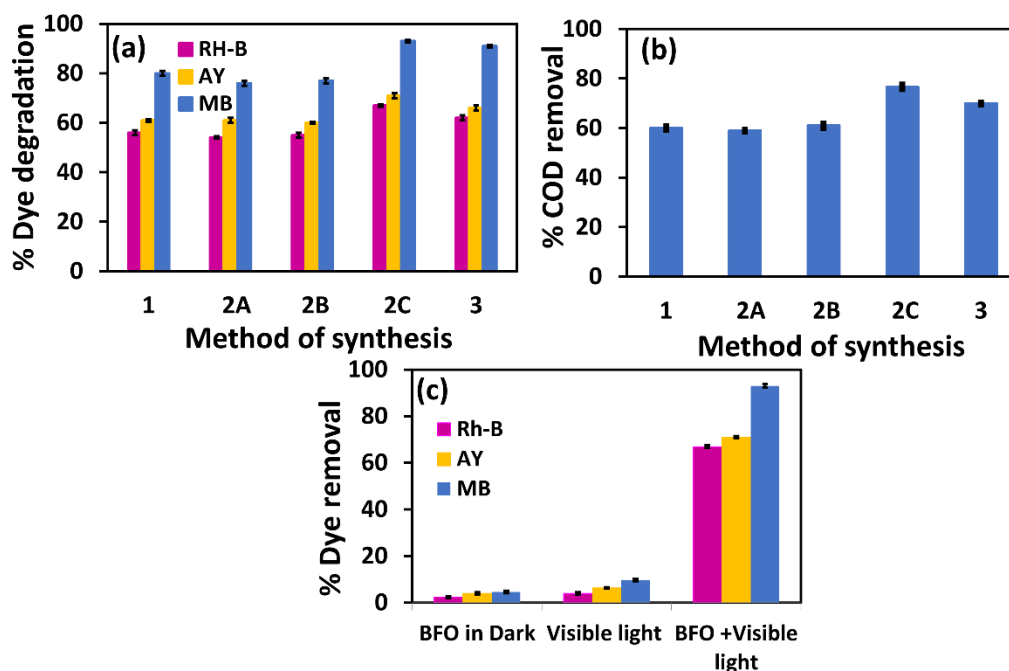
Figure 4.1: (a) Percentage dye degradation;(b) Percentage COD removal by BFO nanoparticles synthesized by different methods; (c) Percentage dye removal by BFO particles (Method 2C) of mixed dye aqueous solution. Conditions: catalyst loading-0.1g/L; concentration of each dye-10 mg/L; irradiation time-210 min.

Owing to the highest photocatalytic activity and better mineralization ability of the BFO nanoparticles synthesized by Auto-combustion method (Method 2C), it serves as the best photocatalyst for the degradation of dyes from mixed dye aqueous solution as compared to those synthesized by other methods under visible light irradiation in the present study.

4.1.1.1 Characterization of BFO nanoparticles

In order to understand the reason for the maximum activity of the BFO nanoparticles synthesized by Method 2C, the BFO nanoparticles synthesized by different methods were characterized using XRD, SEM and UV-VIS spectroscopy and the results are compared.

Figure 4.2 shows the XRD of BFO particles synthesized by co-precipitation method (Method 1) with KOH as a precipitant. Prominent peaks are exhibited at 2θ = 22.4°, 31.8°, 32.07°, 46°, 51.5°, 51.8°, 56.46° and 57.16° corresponding to $BiFeO_3$ of different crystalline plane (100), (110), (1-10) (200), (210), (2-12), (211) and (1-2 1) respectively, which confirmed the formation of perovskite $BiFeO_3$ (JCPDS NO-01-072-2035) with rhombohedral crystal system. The peaks at 2θ = 12.4°, 24.7°, 27.6°, 32.8°, 35.2°, 37.5°, 39.5°, 42°, 43.5°, 48.9°, 54.09°,56.5°, 61.74°, and 64.7°, corresponding to $Bi_{25}FeO_{40}$ of different crystalline planes (110), (220), (310), (321), (400), (330), (024), (332), (442), (521), (600), (631), (631) and (710) indicate the formation of $Bi_{25}FeO_{40}$ (JCPDS reference NO-01-078-1543) with cubic crystal system. The peaks at 2θ = 26.8°, and 47° correspond to the impurity phase $Bi_2Fe_4O_9$ with planes (201) and (141) indicating the formation of $Bi_2Fe_4O_9$ (JCPDS reference NO-00-025-0090) with orthorhombic crystal system. XRD revealed the formation of mixed phase BFO nanoparticles of crystallite size 70 nm (Table 4.1) as calculated using Scherrer equation, containing the impurity phases $Bi_{25}FeO_{40}$ and $Bi_2Fe_4O_9$ along with $BiFeO_3$.

Figure 4.2 presents the XRD pattern of BFO nanoparticles synthesized by auto combustion method viz. Method 2A, 2B and 2C. The XRD pattern for the particles synthesized by Methods 2A and 2B, exhibit common prominent peaks at 2θ =22.3°, 31.7°, 32°, 39.4°, 51.6°, and 56.3°, corresponding to $BiFeO_3$ of different crystalline planes (012), (112) (202) (122) and (018). It confirmed the formation of perovskite $BiFeO_3$ (JCPDS NO-01-071-2494) with rhombohedral crystal system by both the modifications of the auto-combustion methods of synthesis. However, for the particles synthesized by Method 2A, the peaks were also observed at 2θ = 12.4°, 24.7°, 27.6°, 45.3°, and 54° corresponding to $Bi_{25}FeO_{40}$ of different crystalline planes (110), (220), (310), (134), and (600) indicating the formation of $Bi_{25}FeO_{40}$ (JCPDS reference NO-01-078-1543) with cubic crystal system and another peak at 2θ = 26.8° corresponding

to the impurity phase $Bi_2Fe_4O_9$ with planes (201) with orthorhombic crystal system (JCPDS reference NO-00-025-0090). Thus, the XRD of the particles synthesized by Method 2A revealed the formation of mixed phase BFO nanoparticles of crystallite size 42 nm (Table 4.1), containing $BiFeO_3$ and the impurity phases $Bi_{25}FeO_{40}$ and $Bi_2Fe_4O_9$. However, the XRD of the particles synthesized by Method 2B has one impurity peak exhibited at $2\theta = 12.4°$, corresponding to $Bi_{25}FeO_{40}$ of the crystalline plane (110) with cubic crystal system. The XRD shows that the particles synthesized by Method 2 B are the mixed phase BFO nanoparticles of crystallite size 45 nm (Table 4.1), consisting of $BiFeO_3$ with the impurity phase $Bi_{25}FeO_{40}$.

The XRD pattern of BFO particles synthesized by auto combustion method at neutral pH (Method 2C), shown in Figure 4.2, exhibits the presence of prominent peaks at $2\theta = 22.3°$, $31.7°$, $32.0°$, $37.5°$, $39.9°$, $51.7°$, corresponding to perovskite $BiFeO_3$ of different crystalline planes (012) (104) (110) (202) (024) (125) (JCPDS NO-01-086-1518) with Rhombohedral crystal system. A peak at $2\theta = 27.6°$, corresponds to $Bi_{25}FeO_{40}$ (JCPDS NO-01-078-1543) of the crystalline plane (310) with cubic crystal system. The XRD showed the formation of BFO particles majorly consisting of $BiFeO_3$ with one impurity phase $Bi_{25}FeO_{40}$. The average crystallite size was found to be 33 nm (Table 4.1). The particles synthesized by Method 2A and 2B have higher crystallite size of 42 nm and 45 nm (Table 4.1) compared to those synthesized by Method 2C. The broader peaks in XRD of particles synthesized by Method 2 A and 2B suggests poor crystallinity of these particles.

The XRD pattern of BFO synthesized by Surfactant-assisted combustion synthesis method (Method 3) shown in Figure 4.2 exhibit peaks at $2\theta =22.3°$, $31.7°$, $32.0°$, $37.5°$, $38.9°$, $39.9°$, $50°$, corresponding to $BiFeO_3$ of the different crystalline planes (012) (104) (110) (003) (006) (021) as referenced in JCPDS NO-01-071-2494, with Rhombohedral crystal system. The peaks at $2\theta = 27.6°$, $32.8°$, $45.3°$, $54°$ and $57.1°$ corresponding to $Bi_{25}FeO_{40}$ of the different crystalline plane (310), (321), (134) (600) and (620) indicate the formation of impurity phase $Bi_{25}FeO_{40}$ (JCPDS NO-01-078-1543) with cubic crystal system. XRD showed the formation of mixed phase BFO nanoparticles containing $BiFeO_3/Bi_{25}FeO_{40}$ phases with the crystallite size of 35 nm (Table 4.1).

XRD analysis shows the formation of binary phase BFO containing $BiFeO_3/Bi_{25}FeO_{40}$ by Method 2B, 2C and Method 3; whereas the mixed phase BFO containing $BiFeO_3/Bi_{25}FeO_{40}/Bi_2Fe_4O_9$ was formed by Method 1. The formation of $Bi_{25}FeO_{40}$, the oxygen-deficient impurity phase and $Bi_2Fe_4O_9$, which is the Bi deficient or Fe rich impurity phase might be ascribed to the decomposition of $BiFeO_3$ during the slow heating process. The involved chemical reactions can be expressed as following (Wang et al. 2011b):

$$4BiFeO_3 \rightarrow Bi_2Fe_4O_9 + Bi_2O_3 \dots\dots\dots\dots\dots\dots\dots\dots\dots\dots\dots\dots\dots\dots\dots..(4.1)$$

$$BiFeO_3 + 12Bi_2O_3 + 0.5O_2 \rightarrow Bi_{25}FeO_{40} \dots\dots\dots\dots\dots\dots\dots\dots\dots\dots\dots(4.2)$$
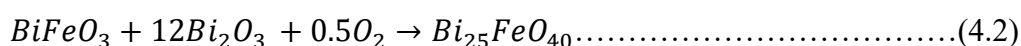
XRD analysis showed that the BFO particles synthesized by Method 1 and Method 2A contain $BiFeO_3$ along with two impurity phases, $Bi_{25}FeO_{40}$ and $Bi_2Fe_4O_9$. However, Method 2A has only one peak of Bi_2FeO_9 and Method1 has two peaks of $Bi_2Fe_4O_9$. The peaks for $Bi_2Fe_4O_9$ are absent in XRD of the particles synthesized by Method 2B, 2C and Method 3. The BFO particles synthesized by Method 2B, 2C and Method 3 contain only two phases of BFO, *viz*. $Bi_{25}FeO_{40}$ and $BiFeO_3$. The particles synthesized by Method1, 2B and 2C showed maximum intensity of the peak corresponding to $BiFeO_3$ (110), which show that these particles contain maximum fraction of $BiFeO_3$ (110). The particles synthesized by Method 2A and Method 3 showed maximum intensities for peaks corresponding to $Bi_{25}FeO_{40}$, but with different crystalline planes corresponding to 2θ of 12.49° and 28° respectively. Thus, these particles contained maximum fraction of $Bi_{25}FeO_{40}$. Particles synthesized by Method 2C showed only one peak of $Bi_{25}FeO_{40}$ (310), which is with similar intensity as that of $BiFeO_3$ (110). The BFO particles synthesized by Method 2C and Method 3 showed much better photocatalytic activity compared to those synthesized by Methods 1, 2A and 2B as shown in Figure 4.1 (a and b). The lower activity of particles synthesized by Methods 1 and 2A may be attributed to the presence of the impurity phase $Bi_2Fe_4O_9$. The particles synthesized by Method 2C and Method 3 contained considerable fractions of both $BiFeO_3$ and $Bi_{25}FeO_{40}$, which appear to be the reason for their better photocatalytic activity. The lower photocatalytic activity of particles synthesized by Method 2B as compared to Method 2C and Method 3, may be attributed to the presence of a very small fraction of $Bi_{25}FeO_{40}$. The particles synthesized by Method 2C contained almost similar fractions of $BiFeO_3$ (110) and $Bi_{25}FeO_{40}$ (310) corresponding

to 2θ of 12.48° and 28.08°. The results of XRD and the photocatalytic activity show that whenever, the impurity phase $Bi_2Fe_4O_9$ is present in BFO, it renders lower photocatalytic activity. However, the BFO nanoparticles synthesized by Method 3 showed several peaks of the oxygen-deficient impurity phase indicating that the percentage of impurity is higher in BFO synthesized by Method 3 as compared to that synthesized by Method 2C. BFO synthesized by Method 2C, which showed only one peak of oxygen deficient impurity phase exhibits better visible light mediated photocatalytic activity. The presence of $Bi_{25}FeO_{40}$ (310) in considerable fraction as $BiFeO_3$ (110) and absence of other peaks for $Bi_{25}FeO_{40}$, may have rendered better photocatalytic activity.

Gao et al. (2014) have reported the visible light activity of pure $BiFeO_3$ synthesized by sol-gel method with ethylene glycol as the solvent, in the degradation of MO dye. Xian et al. (2011a) have synthesized pure $BiFeO_3$ by thermal decomposition process of xerogel and have reported its UV and visible light photocatalytic activity for the degradation of MO dye. Zhang et al. (2016a) have shown that the oxygen-deficient phase of bismuth ferrite, $Bi_{25}FeO_{40}$ also shows excellent visible light mediated photocatalytic activity. Zhang et al. (2015b) have successfully synthesized $Bi_{25}FeO_{40}$ tetrahedrons through a facile, mild and rapid hydrothermal route, and have reported visible light photocatalytic activity for the degradation of Rh-B. The BFO particles synthesized by Method 2C and Method 3 are mixed phase BFO majorly containing $Bi_{25}FeO_{40}$ and $BiFeO_3$, both of which have been reported to have an excellent visible light photocatalytic activity. Thus, the mixed phase BFO nanoparticles synthesized by Method 2C and Method 3 in the present work, exhibit good visible light activity. Many oxides have different polymorphic crystal structures, which can be used for heterojunction performance because their different crystal structures at two sides of the interface may be helpful for carrier separation across the interface (Fan et al. 2012; Ju et al. 2014; Ohno et al. 2002). For example, rutile-anatase mixed-phase TiO_2 has been shown to have much higher activity than single-phase systems for water splitting (Li and Gray 2007; Ohno et al. 2002; Pan et al. 2011). Thus, the maximum photocatalytic activity of BFO synthesized by Method 2C is attributed to the absence of $Bi_2Fe_4O_9$ and presence of almost similar fractions of $BiFeO_3$ (110) and $Bi_{25}FeO_{40}$ (310), with a smaller number of peaks for the $Bi_{25}FeO_{40}$. Thus, it can be concluded that BFO particles

containing appropriate amount of oxygen deficient impurity phase can serve as a better photocatalyst. Thus, the presence of appropriate amounts of $Bi_{25}FeO_{40}$ provides heterojunction with $BiFeO_3$ and enhances the photocatalytic activity by reducing the rate of electron-hole recombination.

The SEM images of the BFO nanoparticles synthesized by different methods are presented in Figure 4.3 (a-e). As observed in Figure 4.3 (a), the BFO particles synthesized by Method 1 are large sized, aggregated and polymorphic containing quasi-spherical and oval shaped particles. As observed in Figure 4.3 (b and c), the BFO particles synthesized by Method 2A and 2B are highly aggregated. As observed in Figure 4.3 (e), the particles synthesized by Method 3 are also large sized. However, as observed in Figure 4.3 (d), BFO nanoparticles synthesized by Method 2C shows the presence of smaller, uniform sized, seemingly cubic structured, distinct particles. The BFO particles synthesized using Method 2A and 2B are highly aggregated leading to reduced specific surface area resulting in lower photocatalytic rate of degradation of dyes. One of the factors attributing to lower photocatalytic activity of BFO particles synthesized using Method 1, 2A, 2B and 3 as compared to those synthesized by Method 2C may be the higher size and aggregated nature of the particles.

The TEM image of the BFO nanoparticles synthesized by Method 2C is presented in Figure 4.4 (a) which confirms that the particles formed are distinct, uniform sized and approximately hexagonal structured. The particles are with average size of 42.7 nm.

Zeta Potential is an important tool for understanding the surface state of the nanoparticles and predicting its long-term stability. Dispersions with a low zeta potential value will eventually aggregate due to Van-Der Waal inter-particle attractions. The stability of colloidal suspensions of nanoparticles depends on the charged species present at the particle surface, which influence the aggregation and the consequent collapse. The more positive or negative is the zeta potential, larger is the colloidal stability. Generally, zeta potentials outside the range of -30 mV to +30 mV are considered stable (Agrawal and Patel 2011; Bhattacharjee 2016). Zeta potential of +/- 30 to 40 mV are sufficient to ensure good colloidal stability (Chatterjee et al. 2008a). The zeta potential values of the nanoparticles synthesized by various methods are presented in Table 4.1 and the values indicate good stability of these nanoparticles.

To determine the band gap energy, the absorption spectrum of the BFO nanoparticles was obtained using UV–Vis spectrophotometer. The optical energy band gap of the synthesized BFO nanoparticles was calculated by using Tauc's plot drawn from the data of the absorption spectra. Tauc's plot of $(Ah\nu)^2$ vs $(h\nu)$ was plotted, where A is the absorption coefficient, h is the Plank's constant, and $\nu = c/\lambda$ (c = speed of light and λ is the wavelength). The extrapolation of the linear region of the Tauc's plot intersecting the x-axis gives the value of the optical band gap, E_g. The values are presented in Table 4.1. The band gap energy values range from 1.9 eV- 2.3 eV indicating their high visible light activity. The band gap value is the lowest for BFO nanoparticles synthesized by Method 2C, which is another reason for maximum visible light activity as compared to those synthesized by other methods. The Tauc's plot for BFO particles synthesized by Method 2C is shown in Figure 4.4 (b). As observed in Table 4.1 the BFO particles synthesized by Method 2C has the smallest band gap energy as compared to those synthesized by other methods used in the present study. The cut off wavelength for the particles synthesized by Method 2C was found to be 652 nm showing that these nanoparticles can absorb light in almost the entire visible range. The calculated value of band gap energy of 1.9 eV is lower than the bandgap values reported by Xie et al. (2014) and Li et al. (Li et al. 2009a) for BFO synthesized by co-precipitation and hydrothermal method. Lower band gap values of the synthesized BFO nanoparticles show them to be the promising and highly active visible-light photocatalysts.

In Figure 4.4 (c) the FTIR spectra of BFO nanoparticles synthesized by Method 2C is shown. Three intense peaks at 500 cm^{-1} are due to stretching and bending vibrations of the Fe-O bond and are fundamental absorptions of FeO$_6$ octahedral in perovskite. The formation of perovskite structure of BFO in the present work can be confirmed by the presence of metal oxide band at 400-600 cm^{-1} (Ke et al. 2011). The peak around 1300 cm^{-1} is due to the strong vibration of NO$_3^-$ (Zalesskii et al. 2003) attributed to nitro compounds formed by the residual nitric acid which was used during the synthesis. The strong and broad peak at 3500 cm^{-1} indicates O-H stretching vibration due to intermolecular H bonds. The peaks around 1700 cm^{-1} are the characteristics of C=O stretching (Gabbasova et al. 1991; Simões et al. 2008), which may be due to the

presence of residual citric acid used during the synthesis or thermal decomposition products of citric acid.
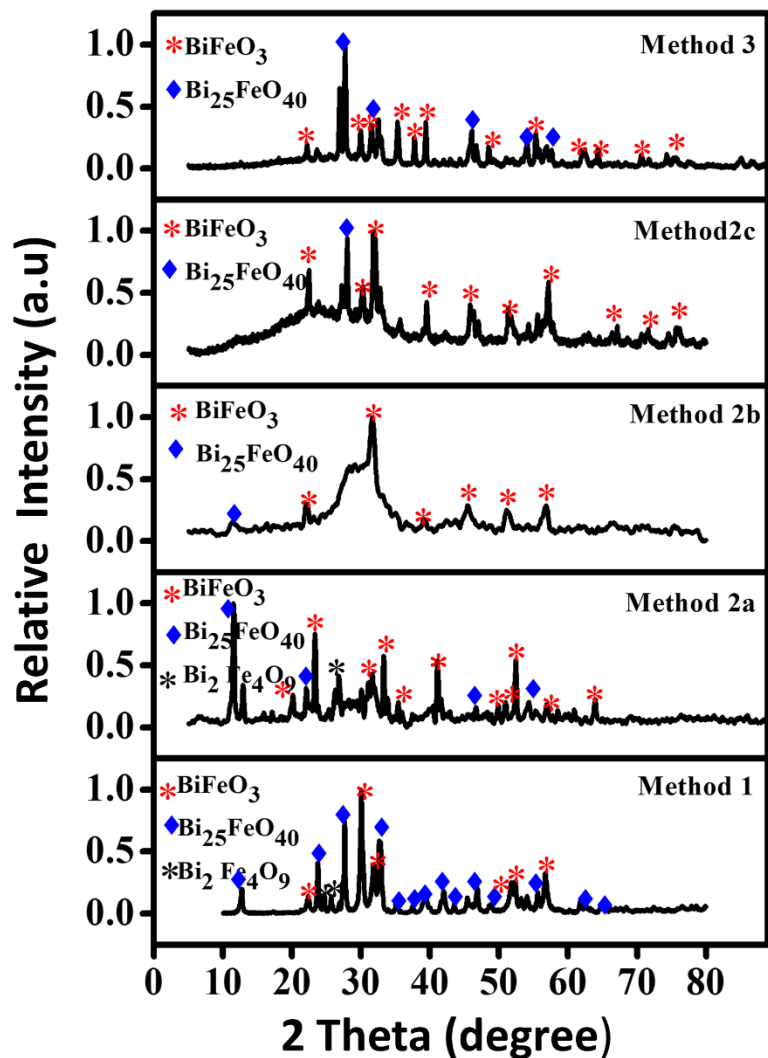
Figure 4.2: XRD pattern of BFO nanoparticles synthesized by Co-precipitation method (Method 1), Auto-combustion method (2A, 2B and 2C) and combustion method (Method 3).
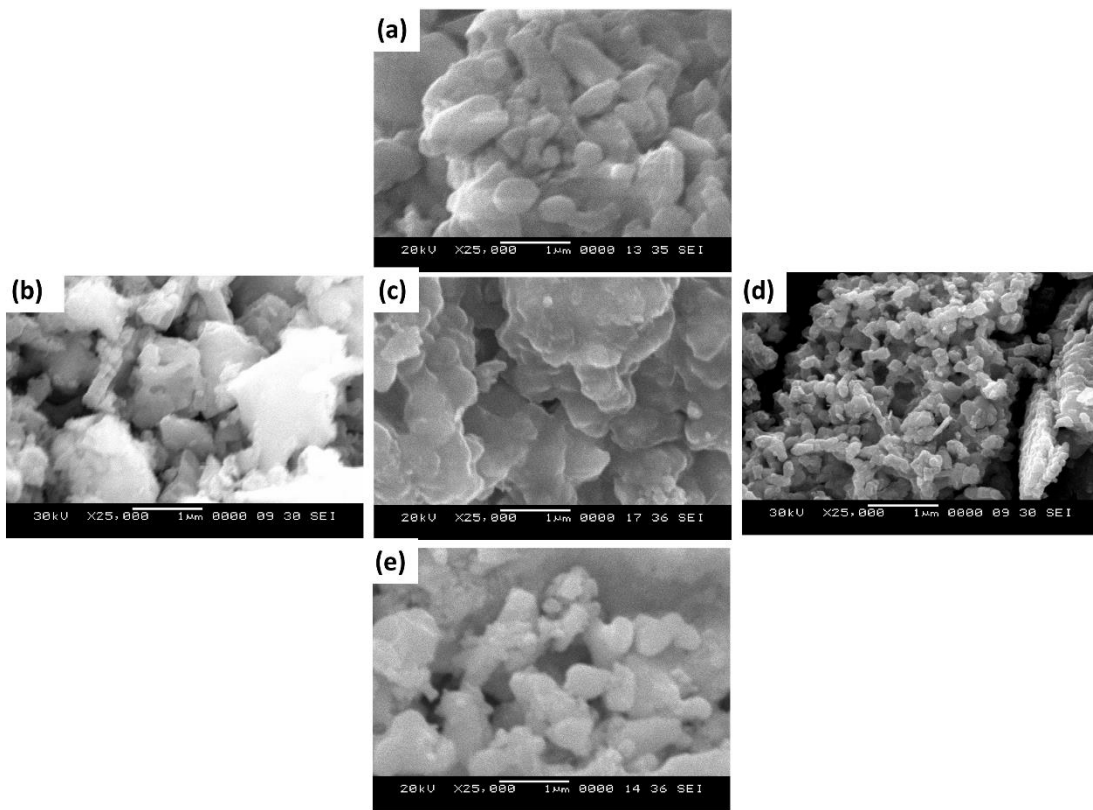
Figure 4.3: SEM images of BFO nanoparticles synthesized by Co-precipitation method (Method 1-(a)), Auto-combustion method (2A(b), 2B(c) and 2C (d)) and combustion method (Method 3(e))
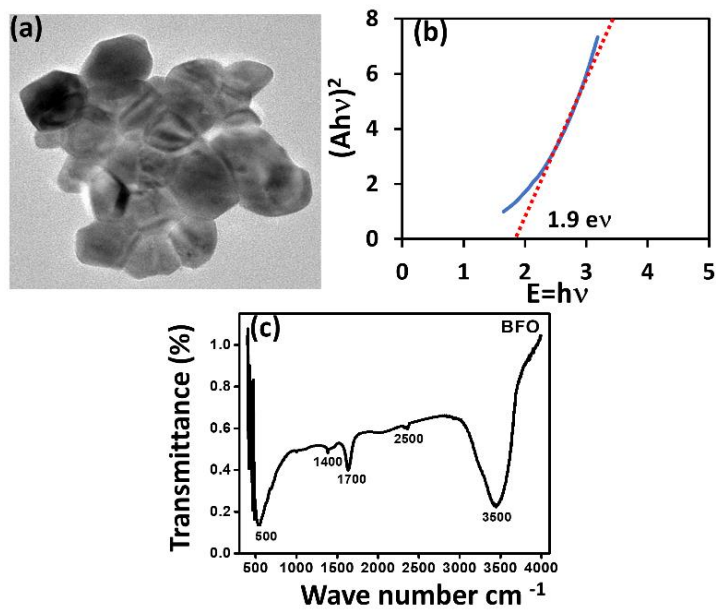
Figure 4.4: (a) TEM image (b) Tauc's plot for band gap (c) FTIR spectra of BFO nanoparticles (Method 2C)

Table 4.1: Crystallite size, Absorbance edge, Bandgap (eV), Zeta potential (mV) and Particle size (TEM) of BFO particles by different synthesis method.

Method	Crystallite size(nm) by Debye-Scherrer equation	Absorbance edge(nm)	Band gap (eV)	Zeta potential (mV)	Particle size TEM (nm)
Method 1	70	563	2.2	-38.0	-
Method 2A	42	620	2	- 46.0	-
Method 2B	45	539	2.3	80.4	-
Method 2C	33	652	1.9	-79.1	42.7
Method 3	35	620	2	-55.6	-

The mixed-phase BFO nanoparticles containing $BiFeO_3$ along with a considerable fraction of $Bi_{25}FeO_{40}$ (310) were formed by Method 2C and these particles were found to have the lowest crystallite size, smallest band gap energy and a small average particle size of 42.7 nm, which attributed to the highest visible light activity of these nanoparticles. Owing to the maximum dye degradation efficiency of these nanoparticles from the mixed dye aqueous solution under visible light irradiation, further for the synthesis of $BFO@TiO_2$ and BFO@PANI nanocomposite particles, the BFO nanoparticles synthesized by Method 2C were used.

4.2. Synthesis of engineered $BFO@TiO_2$ nanocomposite particles by optimization of synthesis mixture composition and calcination conditions, in terms of visible light photocatalytic activity for dye degradation from mixed dye contaminated water.

Further to enhance the photocatalytic activity, $BFO@TiO_2$ nanocomposite particles were synthesized as described in Section 3.2.1 using the BFO nanoparticles prepared by Method 2C (Auto combustion Method at neutral pH), by varying the molar ratio of BFO to Ti in the synthesis mixture and calcination conditions such as calcination temperature and time. The $BFO@TiO_2$ nanocomposite particles were

engineered by optimization of these parameters in order to maximize the degradation of dyes and COD removal from mixed dye contaminated water.

4.2.1 Optimization of BFO to Ti molar ratio in in the synthesis mixture

Optimization of catalyst composition plays a very important role in the structure and morphology of the catalyst. The contact area between BFO and TiO_2 is increased by the composite structure of BFO@TiO_2, which also helps charge transfer at the BFO and TiO_2 heterojunction interface. It can be inferred that TiO_2 shells of different thickness can be achieved by changing the loading amount of Ti in the synthesis process. It is known that only when a suitable amount of TiO_2 is composited with BFO, both BFO and TiO_2 efficiently form a heterojunction interface to speed up the photocatalytic process (Li et al, 2009a). Hence, mass or molar ratio BFO to Ti in the synthesis mixture is a crucial parameter that controls the morphology of the BFO@TiO_2 heterostructured nanocomposite particles. Thus, the molar ratio of BFO to Ti was optimized by varying the amount of TTIP and BFO in the synthesis mixture for the formation of BFO@ TiO_2 heterostructured nanocomposite.

Figure 4.5 (a and b) show the effect of BFO: Ti molar ratio on percentage degradation (after 210 min of irradiation) and COD removal of the mixed dye aqueous solution by the nanocomposite particles calcined at 500°C for 3 h. Batch experiments for the photocatalytic degradation of dyes from mixed dye aqueous solution containing MB, AY, Rh-B dyes were carried out using BFO@TiO_2 nanoparticles synthesized with different molar ratios of BFO to Ti in the synthesis mixture, as photocatalysts under visible light irradiation with initial concentration of each of the dye at 10 mg/L and catalyst loading of 0.1 g/L.

In Figure 4.5 (a), it can be observed that as the BFO to Ti molar ratio in the synthesis mixture was varied from 1:0.5, 1:1 to 1:2, the percentage degradation increased, but further variation in the ratio to 1:3 or 1:4 has led to decrease in the degradation. The maximum degradation of the dyes occurred with nanoparticles synthesized with BFO to Ti molar ratio of 1:2. Around 97.4% of MB, 81.5% of AY and 78.7% of Rh-B dye were degraded with BFO@TiO_2 nanocomposite particles synthesized with BFO to Ti molar ratio of 1:2 in 210 min of irradiation time under visible light.

The COD of mixed dye aqueous solution was measured at intervals during photocatalysis to confirm the degradation of the dyes into simpler compounds. The percentage of COD removal (mg/L) during photocatalysis is presented in Figure 4.5 (b). The COD removal gradually increased as the molar ratios of BFO to Ti used in the synthesis of BFO@TiO$_2$ nanocomposite particles was varied from 1:0.5, 1:1 to 1:2. However, further variation in molar ratios to 1:3 or 1:4 resulted in gradual decrease in COD removal. The BFO@TiO$_2$ nanocomposite particles synthesized with molar ratio of 1:2 shows highest COD removal of 80% compared to those synthesized with other molar ratios.

The results show that the dyes are photocatalytically degraded successfully in the mixed dye aqueous solution in the presence of BFO@TiO$_2$ nanocomposite particles. The study revealed that BFO@TiO$_2$ nanocomposite particles synthesized with 1:2 molar ratios of BFO to Ti show better photocatalytic activity and mineralization ability compared to those synthesized with other molar ratios of BFO and Ti. Thus, BFO to Ti molar ratio of 1:2 in the synthesis mixture may be considered as the optimum for the synthesis of BFO@TiO$_2$ nanoparticles for maximum photocatalytic activity and dye mineralization ability.

The BFO@TiO$_2$ particles show a high photocatalytic activity under visible light, which is due to its strong photo absorption ability and charge recombination rate. The low electron-hole recombination rate of BFO@TiO$_2$ is credited to the formation of BFO and TiO$_2$ heterojunction and the presence of electronic- accumulation centres formed by the electronic interaction between the BFO and TiO$_2$. These centres effectively separate the electrons and holes, leading to high quantum efficiency. Wang and Zhang (2011) and Humayun et al. (Humayun et al. 2016) have explained that theoretically an internal electric field from TiO$_2$ to BFO will be generated when BFO and TiO$_2$ come in contact and form a heterojunction interface. Driven by this internal electric field, the holes and electrons will flow in opposite directions, thus leading to the efficient separation of photogenerated electrons and holes and enhanced photocatalytic activity.

Li et al. (2009a) and Liu et al. (2017b) have synthesised BFO by hydrothermal method and by citrate self-combustion method respectively, and further coated with TiO$_2$ by hydrolysis of titanium butoxide to form BFO@TiO$_2$ nanocomposites with different mass ratios of BFO to TiO$_2$. They have also found that the ratio influences the

thickness of the shell and the photocatalytic activity of BFO@TiO$_2$ nanoparticles. Li et al. (2009a) and Liu et al.(2017b) have reported that, too much or too little Ti in the synthesis mixture is not favourable to form a BFO@TiO$_2$ heterostructured nanocomposite particles with highly efficient charge transfer.
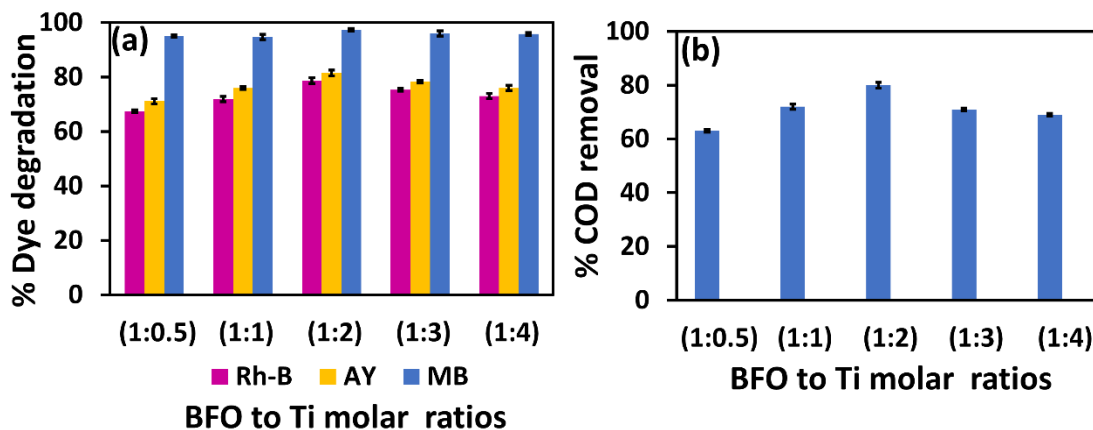
Figure 4.5: (a) Percentage dye degradation (b) Percentage COD removal from mixed dye aqueous solution by BFO@TiO$_2$ particles synthesized with different molar ratio of BFO to Ti, Conditions: catalyst loading-0.1g/L; concentration of each dye-10 mg/L; irradiation time-210 min.

4.2.1.1 Characterization of BFO@TiO$_2$ nanocomposite particles synthesized with different molar ratios of BFO to Ti

Figure 4.6 shows the XRD pattern of BFO@TiO$_2$ nanocomposite particles synthesized with different molar ratios of BFO to Ti as 1:0.5, 1:1, 1:2, 1:3 and 1:4 calcined at 500°C for 3 h. The prominent peaks are exhibited at $2\theta = 22.4°$, $32.01°$, $45.7°$, $50.7°$ and $57.1°$. The peaks correspond to perovskite BiFeO$_3$ of the different crystalline plane (100), (1-10), (200), (2-10), and (1-20) with Rhombohedral crystal system, respectively (JCPDS NO-01-073-0548). The peaks at $2\theta = 27.43°$, and $39.18°$, corresponding to TiO$_2$ of crystalline planes (110), and (200) indicate the formation of Rutile phase of TiO$_2$ (JCPDS NO-00-034-0180) with tetragonal crystal system. The same peaks were observed in BFO@TiO$_2$ nanoparticles synthesized with all the five-mole ratios. The presence of TiO$_2$ in XRD indicates the formation of the layer of TiO$_2$ on the BFO particle surface. However, the impurity phase of BFO, Bi$_{25}$FeO$_{40}$ that was present in the BFO particles (synthesized by Method 2C) used for the synthesis of BFO@TiO$_2$ nanocomposite particles, had disappeared when BFO@TiO$_2$ was formed.

The process of synthesis of BFO@TiO$_2$ has resulted in impurity free BFO, which confirms that there is no impurity phase formation in the interface between TiO$_2$ and BFO (Li et al. 2009). The process of formation of BFO@TiO$_2$ nanocomposite particles may lead to filling of oxygen vacancies in the Bi$_{25}$FeO$_{40}$ lattice which results in removal of impurity phase. This suggests the occurrence of lattice strain change in BFO during the formation of TiO$_2$ over BFO.

The XRD patterns of the BFO@TiO$_2$ nanocomposite particles show that, with an increase in Ti content in the synthesis mixture the intensity of TiO$_2$ peaks at $2\theta =$ 27.3° have decreased till the ratio was varied from 1:0.5 to 1:2. However, the TiO$_2$ peaks at $2\theta = 39.79$° have remained the same. It appears that, even though the amount of Ti added during the synthesis (with reference to the amount of BFO used) was increased, the TiO$_2$ fraction in the composite has reduced till BFO:Ti ratio of 1:2. The decrease in intensity with increase in Ti precursor used in the synthesis may be due to the dominating nucleation rate as compared to growth rate. But with further increase in Ti with ratio of 1:3 and 1:4, the TiO$_2$ peak intensity has been found to increase. The increase in the amount of Ti used for the synthesis, further above that in 1:2 ratio, may have resulted in growth rate dominating over the nucleation rate, causing maximum. amount of TiO$_2$ formed over BFO with BFO: Ti ratio of 1:4.

The average crystallite sizes for BFO and TiO$_2$ in BFO@TiO$_2$ nanocomposite particles were calculated and are presented in Table 4.2. The crystallite size was also found to decrease as the BFO:Ti ratio was changed from 1:0.5 to 1:2. Further increase in the Ti content of the ratio, resulted in increase in the crystallite size of both BFO and TiO$_2$ in BFO@TiO$_2$ nanocomposite. The particles synthesized with BFO to Ti molar ratio of 1:2 contained BFO and TiO$_2$ with the smallest crystallite size of 6.4 nm and 5.3 nm respectively. These results show that the particles are nanocrystalline. It has been observed that the crystallite size of BFO in the composite is much lesser than that of BFO presented in Table 4.1.

The morphology of the nanoparticles was further characterized using SEM and are presented in Figure 4.7 (a-e). As observed in Figure 4.7 (c) the BFO@TiO$_2$ nanocomposite particles synthesized with BFO to Ti molar ratio of 1:2 appear to be smaller and distinct, less agglomerated as compared to the particles synthesized with other molar ratios.

The TEM image of the BFO@TiO$_2$ nanocomposite particles synthesized with BFO to Ti molar ratio of 1:2 presented in Figure 4.8 (a), shows that the nanocomposite consists of BFO nanoparticle, apparently quasi-spherical in shape and surrounded by nanocrystalline TiO$_2$ shell, confirming the formation of BFO core-embedded in TiO$_2$ shell. BFO core size is found to be 37 nm and the TiO$_2$ shell is of the average thickness of around 8 nm. The TEM confirms that the BFO@TiO$_2$ nanocomposite particles are core-shell structured.

A comparison of the size of BFO in the BFO@TiO$_2$ nanocomposite particles (Table 4.2) with that of BFO particles synthesized by Method 2C (Table 4.1) indicate that the crystallite size and the particle size of BFO has reduced during the process of formation of BFO@TiO$_2$ nanocomposite. The process of formation of BFO@TiO$_2$ nanocomposite particles may have caused lattice strain changes and reorientation of crystal structure causing phase transformation to remove the impurity phase, Bi$_{25}$FeO$_{40}$. Densification and shrinkage may also result due to the bonding of TiO$_2$ with BFO, leading to reduction in the size of BFO on forming the nanocomposite. Similar results were observed by Lu et al. (2007), when they synthesized magnetic silica aerogels and they attributed the shrinkage to formation of Fe-O-Si bond. The calcination of BFO@TiO$_2$ nanocomposite particles may also lead to shrinkage of the particles, thus reducing the size (Lu et al. 2007).

The optical band gap energy of the BFO@TiO$_2$ nanocomposite particles synthesized with different molar ratios of BFO to Ti, were calculated and are presented in Table 4.2. The Tauc's plot for the particles synthesized with BFO: Ti ratio of 1:2 is shown in Figure 4.8 (b). The absorption edges for the BFO@TiO$_2$ nanocomposite are presented in Table 4.2. In comparison to pure BFO (absorption edge of 652) or pure TiO$_2$ (absorption edge 387.5), a shift in the absorption edges of BFO@TiO$_2$ nanocomposite to longer wavelength regions of the visible and Near Infrared Region (NIR) range is observed. This could be attributed to the interaction of BFO and TiO$_2$ in the composite. These results prove that BFO@TiO$_2$ nanocomposite is intrinsically different from a physical mixture of BFO and TiO$_2$. Umrao et al. (2014) in their studies on TiO$_2$-Graphene Hybrid System, have reported that addition of graphene to TiO$_2$ forming TiO$_2$-Graphene Hybrid System, caused the synergistic interaction of graphene matrix with TiO$_2$ which modifies the electronic band gap structure of TiO$_2$ and an

energy level is introduced between the conduction and valence band, leading to reduction in band gap energy of TiO_2. When two types of semiconductor materials combine together a heterostructure is formed, following which a new, narrower hybridized energy band is formed in the heterostructure (Zhang et al. 2015a). The quality of heterojunction and disorders present at the interphase govern the scattering mechanisms at the heterojunction and limit the mobility of charge carriers (Haldar et al. 2017).

As observed in Table 4.2, the band gap energy values decreased with increase in Ti content as the ratio was changed from 1:0.5 to 1:2. But further increase in Ti content with the change in ratio from 1:2 to 1:4 has resulted in increase in the band gap energy. These observations confirm results presented by Tae Kwon et al.(2000). Tae Kwon et al.(2000) have reported that the variation in band gap energy in semiconductor heterojunctions can be achieved by changing the percentage of its constituents. The formation of defective energy levels can also decrease the total energy band gap of coupled photocatalysts (Yang et al. 2014).

The band gap energy values for BFO@TiO_2 nanocomposite particles synthesized in the present work varied in the range of 1.4 eV to 1.9 eV and found to be mostly lower than that obtained with only BFO. The lowering of band gap energy may be attributed to the synergistic interaction of BFO with TiO_2 that causes modification in the electronic band gap structure of TiO_2 and an energy level is introduced between the conduction and valence band, leading to reduction in band gap energy.

The band gap energy is the lowest for BFO@TiO_2 nanocomposite particles synthesized with BFO to Ti molar ratio of 1:2 and the value is 1.4 eV. The red shift of the photo absorption spectrum of BFO@TiO_2 compared with BFO or TiO_2, is induced by Fe or Bi/Ti interdiffusion at the BFO/TiO_2 interface. The maximum photocatalytic activity of BFO@TiO_2 nanocomposite particles synthesized with BFO to Ti molar ratio of 1:2 may thus be attributed to its lowest band gap energy. The band gap energy is lower than the band gap value of 2.19 eV reported by Li et al. (2009a) or BFO@TiO_2 nanocomposite particles synthesized by two-step synthesis, wherein BFO was synthesized via hydrothermal approach combined with a hydrolysis precipitation of titanium precursor. The value is also lower than that reported by Liu et al. (2017b) for BFO@TiO_2 nanocomposite particles synthesized by two-step synthesis, wherein BFO

was synthesized by citrate-nitrate combustion method followed by hydrolysis of titanium precursor. They have reported a band gap energy value of 1.77eV.

The zeta potential values for BFO@TiO$_2$ nanocomposite particles synthesized with different BFO to Ti molar ratios are presented in Table 4.2. The values of the zeta potential being far beyond the instability range of $\pm$ 30 mV, the nanoparticles are highly stable.
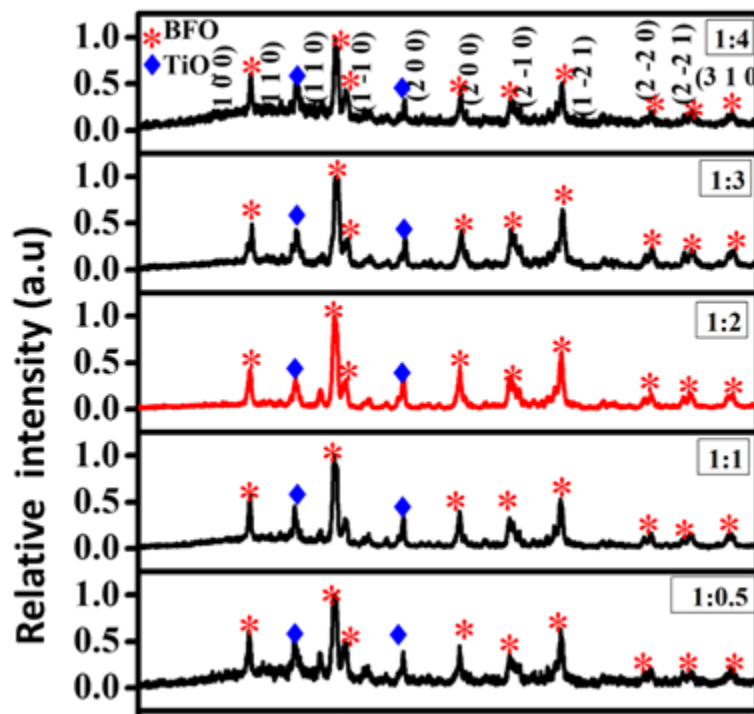
Figure 4.6: XRD patterns of BFO@TiO$_2$ particles prepared at different molar ratio of BFO and Ti: 1:0.5; 1:1; 1:2; 1:3 and 1:4.
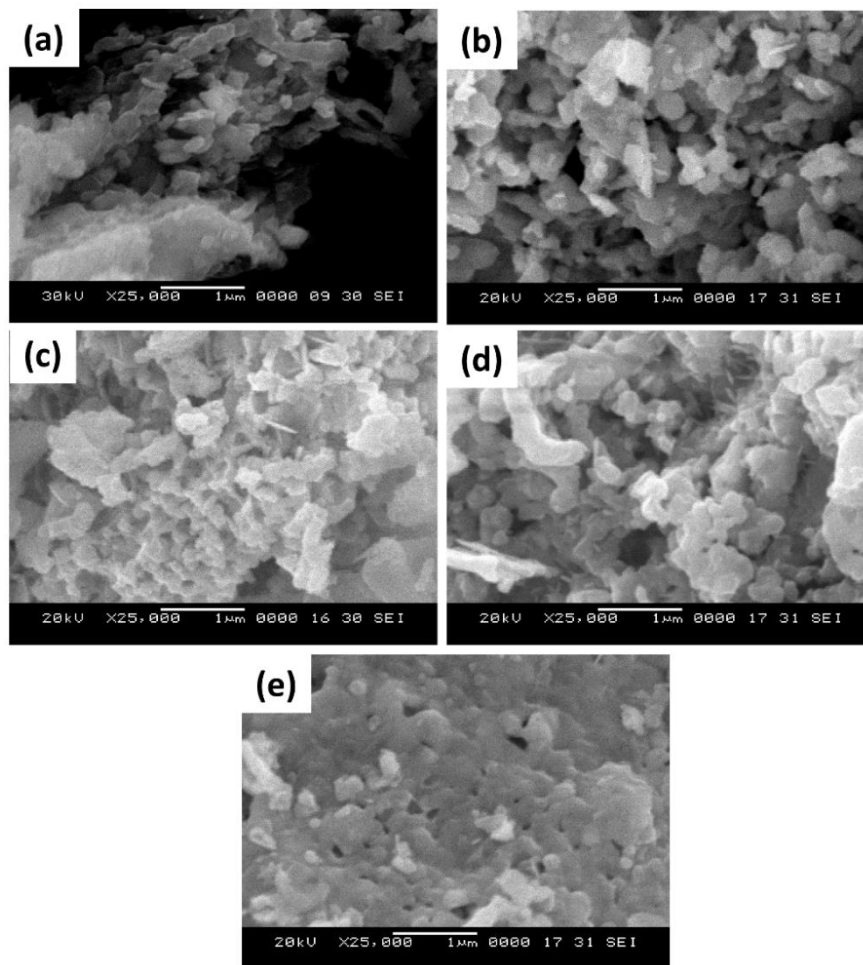
Figure 4.7: SEM images of BFO@TiO₂ particles prepared at different ratio of BFO: Ti; (a)1:0.5 (b) 1:1 (c)1:2 (d) 1:3 (e) 1:4.
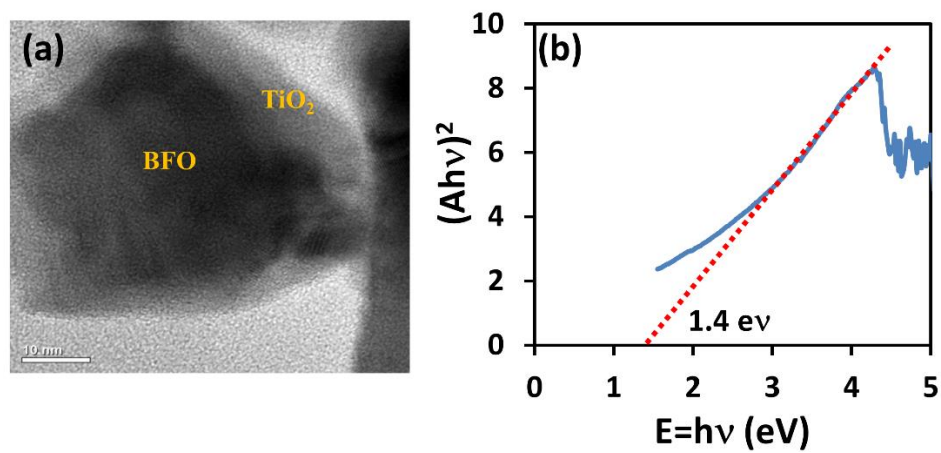
Figure 4.8: (a) TEM image and (b) Tauc plot of BFO@TiO₂ particles synthesized at optimized ratio (1:2)

Table 4.2: Size, adsorption edge, band gap and zeta potential of different ratios of BFO:Ti nanocomposite particles (calcined at 500°C for 3 h)

Different ratio	Crystallite size (nm) BFO & TiO$_2$	Absorption Edges (nm)	Bandgap (eV)	Zeta potential (mV)	Particle size (nm) by TEM
1:0.5	6.8 & 5.6	688	1.8	-92.6	
1:1	6.6 & 5.5	688	1.8	-77.9	
1:2	**6.4 & 5.3**	**885**	**1.4**	**-90.6**	**Core: 37 nm; Shell: 8 nm**
1:3	6.5 & 5.4	775	1.6	-75.5	
1:4	6.7 & 5.6	688	1.9	-80.0	

The BFO@TiO$_2$ nanocomposite particles synthesized with different BFO to Ti molar ratio, are also visible light active like BFO and those synthesized with 1:2 and 1:3 ratio can also absorb light in NIR. The BFO@TiO$_2$ nanocomposite particles synthesized with BFO to Ti molar ratio of 1:2 have the minimum band gap energy value of 1.4 eV and being highly crystalline have exhibited highest photocatalytic activity under visible light. These particles, which enable the light absorption extended to even NIR region of the spectra. Higher photocatalytic activity also implies that the material synthesized may provide heterojunctions which facilitate high charge transfer rate, thus reducing electron hole recombination rates and increasing the rate of photocatalysis.

4.2.2. Optimization of calcination temperature

It is well known that calcination temperature is a significant feature that influences the crystallinity, morphology and surface area of nanoparticles, which can clearly affect the photocatalytic activity (Li et al. 2005; Sathish et al. 2007). To study the effect of calcination temperature on the catalyst properties, the BFO@TiO$_2$ nanoparticles were synthesized with BFO to Ti molar ratio of 1:2 and were then subjected to calcination at different temperature ranging from 300 to 700° C for 3 h. The photocatalytic degradation of dyes in mixed dye contaminated water was studied

using these BFO@TiO$_2$ nanoparticles as photocatalysts with 0.1 g/L loading and with 10 mg/L of each dye in the mixed dye aqueous solution. Figure 4.9 (a and b) show the effect of calcination temperature of BFO@TiO$_2$ nanoparticles on percentage degradation of dyes and COD removal by photocatalysis. It is observed that, as the calcination temperature increased from 300°C to 400°C, the percentage degradation of dyes, especially AY and Rh-B have increased. Further increase calcination temperature to 500°C to 700°C has led to decrease in the degradation of these dyes. The degradation of MB is almost complete with the particles calcined at all the calcination temperatures. COD removal has appreciably increased with increase in calcination temperature from 300°C to 400°C. But further increase in calcination temperature has resulted in decrease in the COD removal. The maximum degradation of dyes and COD removal occurred with BFO@TiO$_2$ nanoparticles calcined at temperature of 400°C as compared to those calcined at other calcination temperature. Around 84% AY, 92% Rh-B and 99.7% MB have been degraded and around 94% COD removal could be achieved with BFO@TiO$_2$ nanoparticles calcined at temperature of 400°C. Thus, calcination temperature of 400°C is considered as the optimum.

Figure 4.9: (a) Percentage degradation and (b) COD removal of dyes from mixed dye aqueous solution by BFO@TiO$_2$ particles calcined at different temperature. Conditions: catalyst loading -0.1g/L; concentration of each dye-10 mg/L; calcination time-3 h; and irradiation time-210 min.

4.2.2.1. Characterization of BFO@TiO$_2$ nanocomposite particles calcined at different temperatures

Figure 4.10 shows the XRD patterns of BFO@TiO$_2$ nanoparticles calcined at different temperatures such as 300°C, 400°C, 500°C, 600°C and 700°C and the prominent peaks are exhibited at 2θ =22.4°, 32.01°, 45.7°, 50.7° and 57.1°. The peaks correspond to perovskite BiFeO$_3$ of different crystalline plane (100), (1-10), (200), (2-10), and (1-20) with rhombohedral crystal system, respectively (JCPDS NO-01-073-0548). The peaks at 2θ = 27.43°, and 39.18°, corresponding to TiO$_2$ of different crystalline planes (110) and (200) indicate the presence of rutile phase of TiO$_2$ (JCPDS NO-00-034-0180) with tetragonal crystal system. XRD analysis shows that the BFO@TiO$_2$ nanoparticles calcined at different temperatures contain BFO and TiO$_2$ phases without any impurity. No change in the crystalline phases have been observed with increase in calcination temperature.

As shown in the XRD patterns of the BFO@TiO$_2$ nanoparticles calcined at different temperatures ranging from 300 to 700°C for 3 h, the change in calcination temperature does not result in change the crystalline phases of BFO and TiO$_2$. The variation in peak intensities is not considerable with increase in calcination temperature from 300°C to 600°C. With further increase in the temperature to 700°C, the peak intensities have considerably increased. Variation in peak intensity values with changing calcination temperature may be attributed to changes in composition of crystalline phases in the catalyst with varying calcination temperature. Further crystallite size of BFO and TiO$_2$ in BFO@TiO$_2$ nanocomposite were calculated using Debye Scherrer's equation and are presented in Table 4.3. The crystallite size of BFO and TiO$_2$ in BFO@TiO$_2$ nanocomposite particles calcined at 400°C were found to be 6.2 nm and 5.1 nm respectively and were the least among the particles calcined at various temperatures. An increase in calcination temperature till 400°C, causes removal of volatile impurities from the crystal lattice and reorientation of atoms in the crystal lattice to form a regular structure. This results in decrease in the crystal size. However, on further increasing the calcination temperature to 500°C and above, rising temperatures increase the diffusional movement of atoms. The increase in diffusion of atoms leads to the growth of crystals causing increase in crystallite size (Ratnawulan et

al. 2017). Thermally promoted crystallite growth takes place at high temperatures (Praserthdam et al. 2003).

The morphology of the nanoparticles was further characterized using SEM and Figure 4.11 (a-e) show the SEM images of the BFO@TiO$_2$ nanoparticles calcined at different temperatures. In Figure 4.11 (a, c and e), the SEM images of the particles calcined at 300°C, 500°C and 700°C show the presence of some aggregated particles. Though, the particles calcined at 600°C (Figure 4.11 (d)), do not show aggregation, the particles are not distinct. The BFO@TiO$_2$ nanoparticles calcined at 400°C (Figure 4.11 (c)), seem to be uniformly shaped, seemingly quasi-spherical structure and distinct with apparently smaller size showing no aggregation as compared to those calcined at other temperatures.

The TEM images shown in Figure 4.12 (a and b), reveal that BFO nanoparticles are oval structured and surrounded by nanocrystalline TiO$_2$ shell, confirming the formation of core-shell structured nanoparticles. The core is with shorter dimension (SD) of 11 nm and longer dimension (LD) of 15 nm. The average thickness of TiO$_2$ shell is around 9 nm. The measured zeta potential values for the nanoparticles calcined at different temperatures are presented in Table 4.3 and the particles have been found to be highly stable.

The optical band gap energy of the synthesized BFO@TiO$_2$ nanoparticles calcined at different temperatures were calculated by using Tauc's plot. The absorption edges and the band gap energy values are presented in Table 4.3. The particles calcined at different temperatures have shown absorption edge extended up to near infrared range. The band gap energy value has decreased as the calcination temperature increased from 300°C to 400°C. But further increase in calcination temperature has increased the band gap energy. The band gap energy for the particles calcined at 400°C is the lowest and the value is 1.3 eV. Figure 4.12 (c) shows the optical band gap energy of the synthesized BFO@TiO$_2$ nanoparticles calcined at 400°C as calculated by using Tauc's plot. The particles calcined at 400°C have shown the maximum photocatalytic activity due to lowest band gap energy. The interface disorders, lattice defects and irregularities may have been lesser at the heterojunctions when calcined at 400°C. The quality of interface created under this condition would facilitate effective charge transfer across the heterojunction interface, thus leading to high photocatalytic activity

compared to heterojunction formed under other calcination temperatures. The absorption edge values in Table 4.3 shows that BFO@TiO$_2$ nanoparticles can act as photocatalyst in the visible as well as NIR range. The calcination temperature of 400°C was found to be the optimum for BFO@TiO$_2$ nanocomposite particles synthesized with BFO: Ti of 1:2 with calcination time of 3 h. Several researchers have shown that the calcination temperature during preparation procedure influences the energy band gap and band gap energy can be tuned by varying the calcination temperature (Chireh and Naseri 2019; Mioduska et al. 2016; Mornani et al. 2016). Sun et al.(2019) have also shown that calcination temperature influences the structure and photocatalytic activity of hybrid photocatalysts.
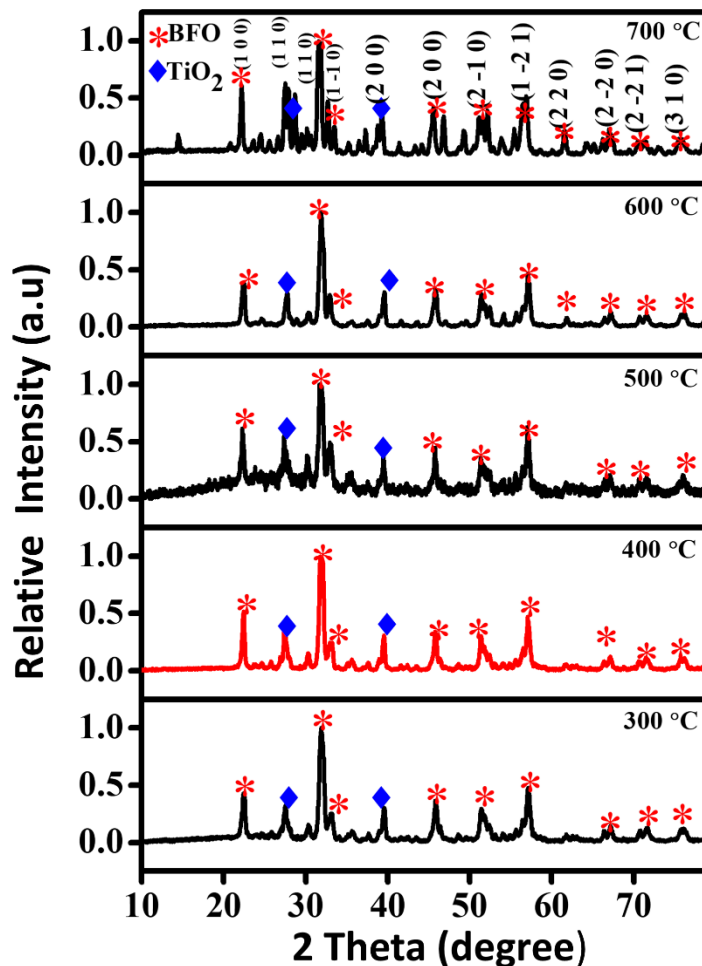
Figure 4.10: XRD patterns of BFO@TiO$_2$ particles calcined at different temperature such as 300°C, 400°C, 500°C, 600°C and 700°C.
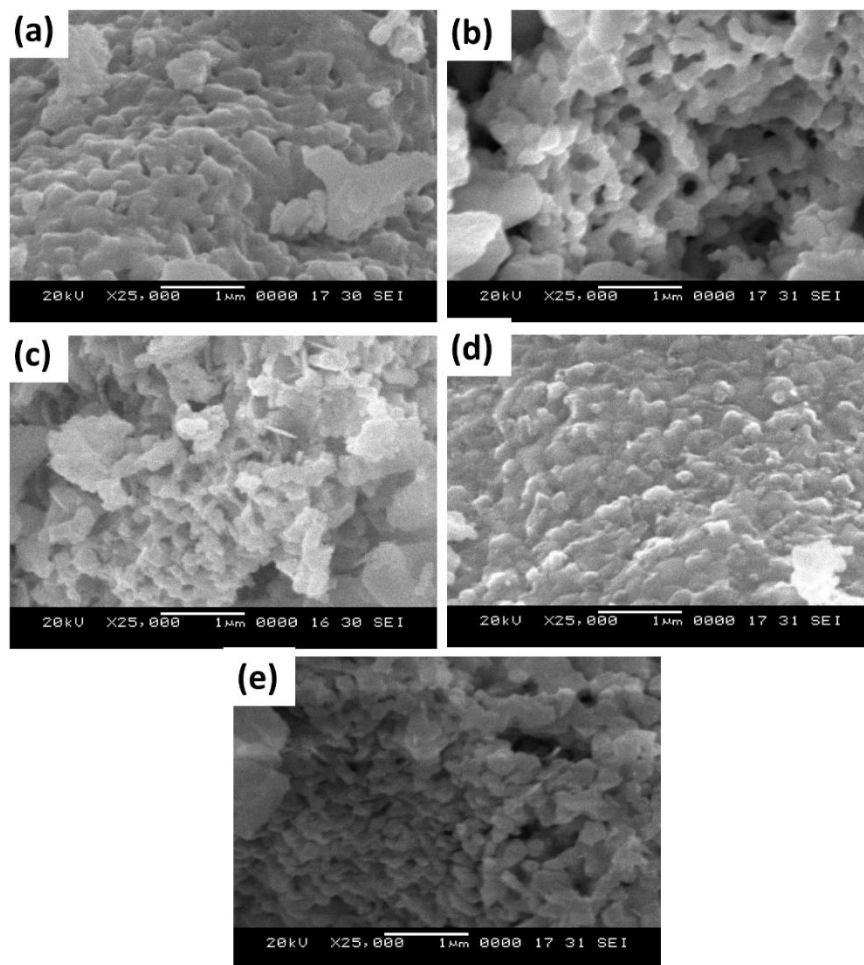
Figure 4.11: SEM images of BFO@TiO₂ particles prepared at different temperature: (a) 300°C (b) 400°C (c) 500°C (d) 600°C (e) 700°C
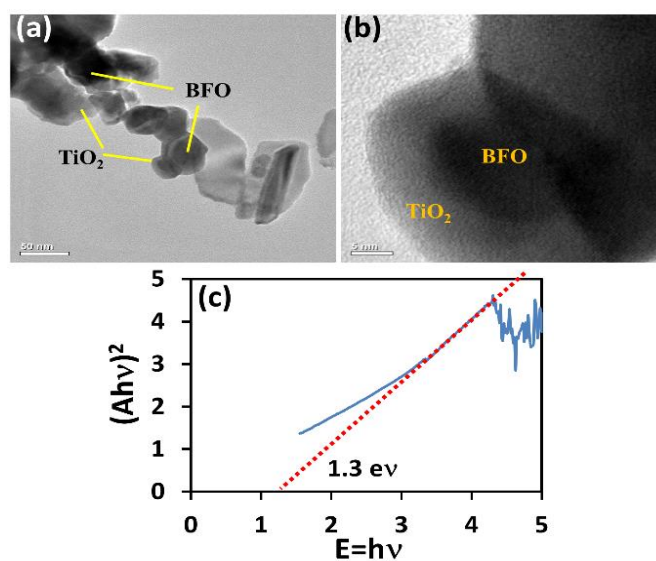
Figure 4.12: (a and b) The TEM images with different magnification (c) Tauc's plot of BFO@TiO₂ particles (optimized temperature:400°C)

Table 4.3: Size, absorption edge, band gap and zeta potential of BFO@TiO₂ nanocomposite particles (BFO: Ti of 1:2) calcined at different calcination temperature for 3 h

Calcination Temperature (time: 3 h)	Crystallite size (nm) BFO & TiO₂	Absorption Edge wavelength (nm)	Band gap (eV)	Zeta potential (mV)	Particle size (TEM)
300°C	6.7 & 5.4	882	1.4	-82.4	-
400°C	**6.2 & 5.1**	**953**	**1.3**	**-79.0**	**Core of SD 11 nm and LD 15 nm with shell thickness of 9 nm ***
500°C	6.4 & 5.3	882	1.4	-90.6	-
600°C	6.6 & 5.4	772	1.6	-86.0	-
700°C	6.8 & 5.5	726	1.7	-79.4	-
*SD-smaller dimension; LD-longer dimension					

4.4.2 Effect of calcination time

Calcination time also affects the photocatalytic activity by determining the existence of crystalline phases. The change in crystalline structures may happen at temperatures higher than certain temperatures. To avoid it, lower temperatures should be used but it may require higher treatment times. Therefore, temperature and, time of calcination are generally a compromise. Calcination time has a direct effect on the crystalline growth; more time may lead to large crystallite size and increase in calcination time can aid in impurity removal from the photocatalyst (Reli et al. 2012). The photocatalytic activity has also been reported to increase with increase in calcination time, reach a maximum and decrease with further increase in calcination time (Reli et al. 2012; Zhang et al. 2011c).Calcination time influences the porosity of the catalyst (Zhang et al. 2013, 2011c). So, the effect of calcination time was studied by keeping the calcination temperature as 400°C for BFO@TiO₂ nanocomposite

particles synthesized with BFO to Ti molar ratio of 1:2. The photocatalytic activity of these nanocomposite particles were studied by conducting the visible light mediated photocatalysis for the degradation of dyes in mixed dye contaminated water containing 10 mg/l of each of the dyes (MB. AY and Rh-B) and 0.1 g/L catalyst loading.

Figure 4.13 (a) shows the effect of calcination time on the percentage degradation of dyes in mixed dye aqueous solution by photocatalysis carried out with BFO@TiO$_2$ nanoparticles prepared with BFO to Ti molar ratio of 1:2 and calcined at 400°C. The degradation of dyes from mixed dye solution increased when the calcination time was increased from 1 h to 2 h. On increasing the calcination time further to 3 h and beyond, has resulted in reduction in degradation of dyes. Maximum degradation was achieved with BFO@TiO$_2$ nanoparticles calcined at 400°C for 2 h. A complete degradation of MB, 96% of AY and 88% of Rh-B, degradation was achieved with BFO@TiO$_2$ nanoparticles calcined at 400°C for 2 h. As shown in Figure 4.13 (b) maximum COD removal of 95% could be achieved with the BFO@TiO$_2$ nanoparticles calcined at 400°C for 2 h. Based on maximum photocatalytic activity and COD removal, 2 h calcination time has been chosen as the optimum for BFO@TiO$_2$ nanoparticles with calcination temperature of 400°C.
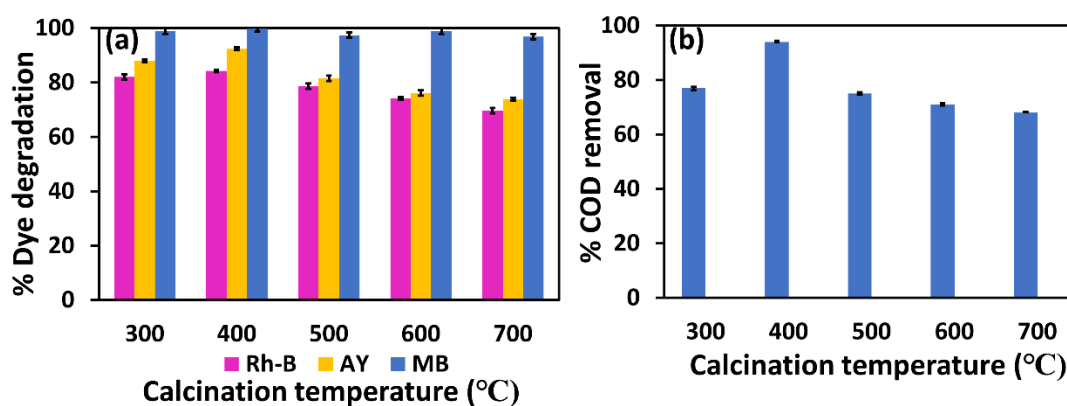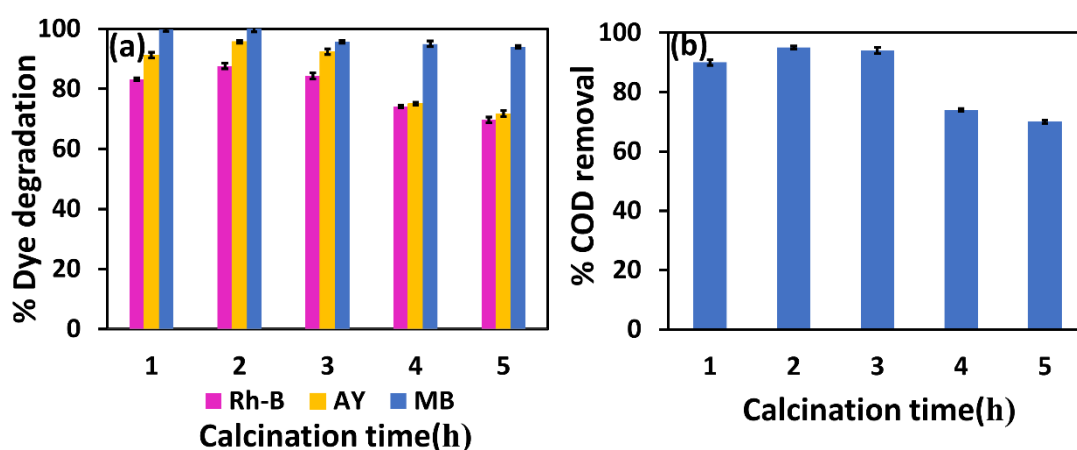

Figure 4.13: (a) Percentage degradation (b) Percentage COD removal from mixed dye aqueous solution by BFO@TiO$_2$ particles calcined at different time.
Conditions: catalyst loading -0.1 g/L; concentration of each dye-10 mg/L;
calcination temperature - 400°C; irradiation time -210 min.

4.4.2.1 Characterization of BFO@TiO$_2$ nanoparticles calcined for different calcination time

Figure 4.14 shows the XRD patterns of BFO@TiO$_2$ nanoparticles prepared at different calcination time such as 1, 2 ,3, 4 and 5 h and the prominent peaks are exhibited at 2θ = 22.4°, 32.01°, 45.7°, 50.7° and 57.1°. The peaks correspond to perovskite BiFeO$_3$ of different crystalline plane (100), (1-10), (200), (2-10), and (1-20), respectively, which showed the presence of (JCPDS NO-01-073-0548) with rhombohedral crystal system. The peaks at 2θ=27.43°, and 39.18°, corresponding to TiO$_2$ of different crystalline planes (110), and (200) indicate the formation of Rutile phase of TiO$_2$ (JCPDS NO-00-034-0180) with tetragonal crystal system. XRD analysis shows that the same crystalline phases of BFO and TiO$_2$ have been retained even with variation in calcination time and the change in calcination time has not resulted in any phase change. However, increase in calcination time has shown variation in the intensity of peaks indicating a change in composition when calcination time was varied. Table 4.4 shows that the crystallite size of BFO and TiO$_2$ have reduced with increase in calcination temperature from 1 h to 2 h, but further increase in calcination time led to increase in the crystallite size. When the calcination time is increased from 1 h to 2 h, some volatile impurities in the crystal lattice may have been removed and further relocation of the atoms in crystal lattice may occur leading to reduction in crystallite size. However, calcination for prolonged time of 3 h or higher would provide longer exposure to the calcination temperature and would provide enhanced diffusion of atoms and may lead to thermally promoted nucleation and crystal growth. An increase in calcination time has been reported to cause an increase in crystallinity (Wang et al. 2012b), improved structure and size of the particles (Dudhe and Nagdeote 2014). Mohammed et al.(2020) have also found that particles size increases as calcination time increased and then reaches a saturation. According to them, the increase in size is due to the grain growth. They also reported that crystallite size and percentage of crystallinity in the crystal structure depends on calcination time.

The morphology of the nanoparticles was further characterized using SEM and Figure 4.15 (a-e) shows the SEM image of the BFO@TiO$_2$ nanoparticles calcined at 400°C for different calcination time. The particles calcined for 1 h and 3 h (Figure 4.15 (a and c)) seem to be agglomerated and not uniform. The particles calcined for 4h

or 5 h (Figure 4.15 (d or e)) seem to be non- uniform shaped with heterogenous morphology and larger size. The particles calcined for 2 h (Figure 4.15 (b)) seem to be regular structured, uniform and better sphericity, compared to the particles calcined for 1, 3, 4 and 5 h. These particles are distinct and not agglomerated. The size appears to be smaller than those calcined for 1, 3, 4 and 5 h. The measured zeta potential values for the nanoparticles calcined at 400°C for different times are presented in Table 4.4 and the particles have been found to be highly stable.

The TEM image presented in Figure 4.16 (a and b) reveals that the BFO nanoparticles which are nearly spherical shaped, are surrounded by nanocrystalline TiO_2 shell confirming the formation of core-shell structured nanoparticles. The analysis reveals that, the BFO core is with shorter dimension (SD) of 12 nm and longer dimension (LD) of 14 nm. The average thickness of TiO_2 shell is around 11 nm. On comparison of the shape and size of the particles calcined at 400°C and 3 h (Figure 4.12 a and b) with that calcined for 2 h, it is evident that the shape of the particles has been modified and conformed from oval to spherical form with reduction in calcination time. Similarly, the size of the core has reduced with slight increase in the shell size.

The FTIR spectrum of the BFO@TiO_2 nanocomposite particles synthesized with BFO to Ti molar ratio of 1:2, calcined at 400°C for 2 h is shown in Figure 4.16 (c). The main intense peak at 500 cm^{-1} is due to stretching and bending vibrations of the Fe-O bond, and fundamental absorptions of FeO_6 octahedral in perovskite. The formation of perovskite structure of BFO in the present work can be confirmed by the presence of metal oxide band at 500 cm^{-1} (Ke et al. 2011). The small narrow peaks at wave number below 1200 cm^{-1} are due to stretching and bending vibrations of Ti-O-Ti bond, to which the formation of TiO_2 is attributed (Chellappa et al. 2015; Hamadanian et al. 2010; Mohan et al. 2012). The strong and broad peak at 3500 cm^{-1} and that at 1600 cm^{-1}, indicates O-H stretching vibration due to hydroxyl groups on the surface of nanoparticles (Gao et al. 2015a) and intermolecular H bonds (Vinet and Zhedanov 2011). The band at 1400 cm^{-1} is due to stretching and bending vibrations of C-H group (Wang et al. 2011c).

The optical band gap energy of the synthesized BFO@TiO_2 nanoparticles calcined at 400°C for different calcination time are presented in Table 4.4. The band gap energy has been found to decrease with increase in calcination time from 1 h to 2h.

A further increasing the calcination time, has resulted in increase in the band gap energy. The band gap energy value was found to be the minimum for particles calcined for 2 h and the value is 1.2 eV. The absorption edges are shown in Table 4.4. The particles calcined for 4 h and 5 h have exhibited two absorption edges while those calcined for 1 h to 3 h showed only one absorption edge. Tauc's plot drawn from the data of the absorption spectra for particles calcined for 2 h which is the optimum calcination time is shown in Figure 4.17 (a). The Tauc's plot shows one absorption edge, indicating the absence of disorder at the heterojunction of the semiconductors. A Tauc's plot for the particles calcined for 5 h is shown in Figure 4.17 (b), as a representative of the particles showing two absorption edges. The particles calcined for 4 h and 5 h have shown two absorption edges. Each material (core and shell) has a distinct absorption onset. Figure 4.17 (b) clearly has two regimes and similar is the case for the particles calcined for 4h. The values of absorption onsets are shown in Table 4.4. Appearance of two absorption edges in nanocomposite materials, have been reported by (Cao and Wang (2015) in the $YBiO_3/Bi_2O_3$ heterostructure composite synthesized by them. Umrao et al. (2014) in their studies on TiO_2-Graphene Hybrid System, have also reported an-appearance of additional band edge. These researchers have attributed each band edge to the individual components of the composite. They have reported red shift in absorption edges of individual components in the composite as compared to the absorption edge of single components, which they attributed to synergetic interaction between the individual components. Thus, in the present study the two absorption edges observed in the particles calcined for 4 h and 5 h, is attributed each to TiO_2 and BFO which may be due to discontinuities present at the heterojunction, and have shown red shifts from that of the individual nanoparticles.

The BFO@TiO_2 particles calcined for 2 h possessed a band gap energy of 1.2 eV, which is lower than the band gap values of the particles calcined for other calcination times, thus providing an evidence for the highest photocatalytic activity. The zeta potential values for the particles calcined for different times is shown in Table 4.4. The BFO@TiO_2 nanoparticles calcined at different temperatures are highly stable. The atomic concentration values of the elements present in the BFO@TiO_2 nanocomposite particles (optimum) is shown in Table 4.5.

To determine the surface composition and chemical states of the elements in BFO@TiO$_2$ nanocomposite particles synthesized with BFO to Ti molar ratio of 1:2, calcined at 400°C for 2 h, XPS measurements were conducted and the spectrum is shown in Figure 4.18 (a). It can be seen from Figure 4.18 (b-e) that the BFO@TiO$_2$ core-shell structured nanocomposite particles composed of Bi, O, Fe, and Ti elements. As shown in Figure 4.18 (b), the spectrum exhibits two strong peaks of Bi 4f at binding energies of 153 eV and 163 eV corresponding to the core lines of Bi 4f$_{7/2}$ and 4f$_{5/2}$ respectively. It clearly represents the '+3' oxidation state of Bi in BFO without any trace of metallic Bi in the matrix (Das et al. 2013; Sarkar et al. 2015). The spectrum shown in Figure 4.18 (c), also exhibits two peaks for Fe 2p at 710 eV and 722 eV corresponding to core lines of Fe 2p$_{3/2}$ and Fe 2p$_{1/2}$ respectively arising from the spin-orbit interaction and corresponding to Fe^{3+} oxidation state in BFO (Mukherjee et al. 2018; Quickel et al. 2015) Furthermore, a satellite peak of Fe 2p$_{3/2}$ is situated approximately 2 eV higher than the main Fe 2p$_{3/2}$ peak (Yamashita and Hayes 2009). The position of the satellite peak at 710 eV in the Fe 2p spectra is in good agreement with the Fe^{3+} oxidation state in BFO as reported by Mukherjee et al. (2018) and Quickel et al. (2015). In addition, this indicates the possibility of bonding between Fe and oxygen of the TiO$_2$ (Fe–O–Ti bonds) (Bajpai et al. 2018; Hu et al. 2015a). Moreover, no significant peaks were observed for the Fe^{2+} ionic state, suggesting that iron predominantly exists in the Fe^{3+} state.

Figure 4.18 (d) shows peaks of Ti 2P. The peaks are symmetric, sharp and intense representative of the presence of Ti^{4+} surface states (Gautam et al. 2016). The peak obtained near 455 eV and 464 eV correspond to the Ti 2p$_{3/2}$ state and Ti 2p$_{1/2}$ state (Wang et al. 2012a) The peak positions and line separation between Ti 2p$_{1/2}$ and Ti2p$_{3/2}$ are 7.5 eV, which is consistent with the standard binding energy reported for TiO$_2$ nanoparticles (Hu et al. 2013; Sanjinés et al. 1994).

The XPS spectra in Figure 4.18 (e), shows one peak at 527 eV. This peak is attributed to the lattice oxygen in the O$_2^-$ state (Gautam et al. 2016; Mali et al. 2012; Zhu et al. 2017b). However, the deconvolution of the O 1s spectra give two peaks at 527 eV corresponding to the Bi–O bond. Thus, the XPS result shows that the Bi and Fe elements exist in the '+3' valence state in BFO@TiO$_2$. Table 4.5 presents atomic concentration of the elements present in BFO@TiO$_2$ nanocomposite particles

synthesized with BFO to Ti molar ratio of 1:2, calcined at 400°C for 2 h as determined from XPS. These results show the presence of Ti, Bi, Fe and O which are the main constituents of BFO@TiO$_2$. However, the presence of carbon may be attributed to the residuals of solvents or titanium precursors used in the synthesis.
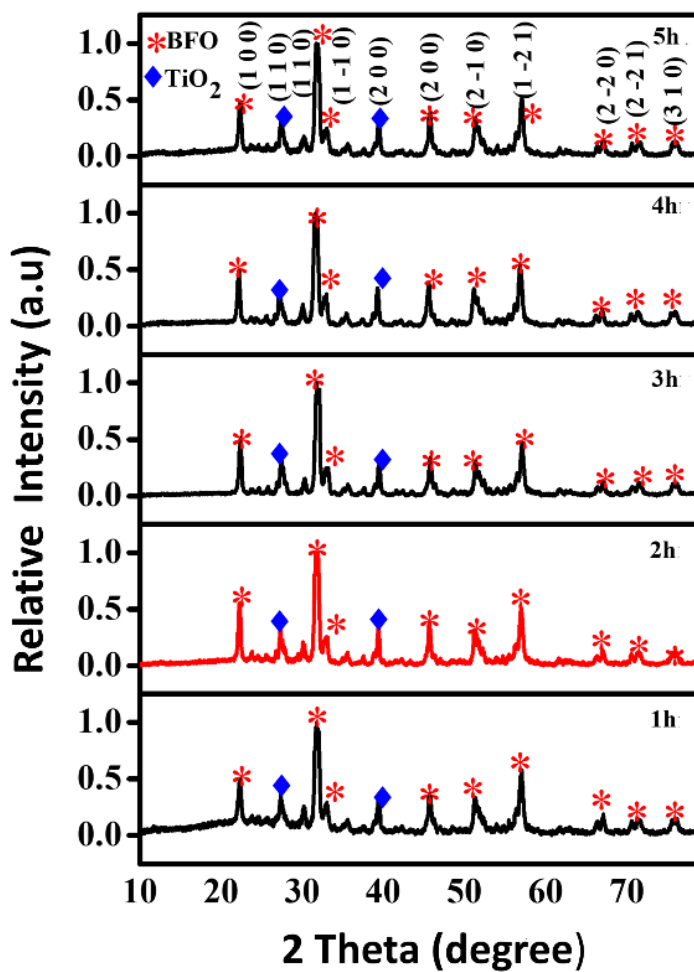
Figure 4.14: XRD patterns of BFO@TiO₂ particles prepared at different calcinations time: 1 h; 2 h; 3 h; 4 h and 5 h.
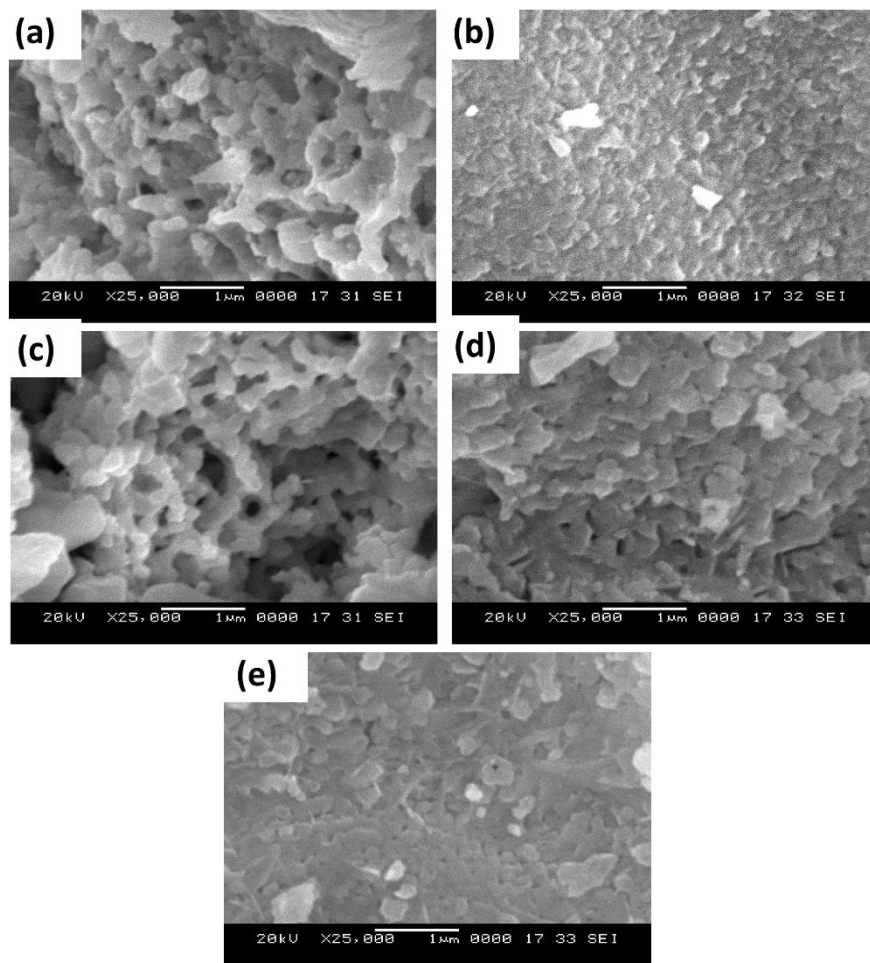
Figure 4.15: SEM images of BFO@TiO$_2$ particles prepared at different calcinations time: (a) 1 h (b) 2 h (c) 3 h (d) 4h (e) 5 h
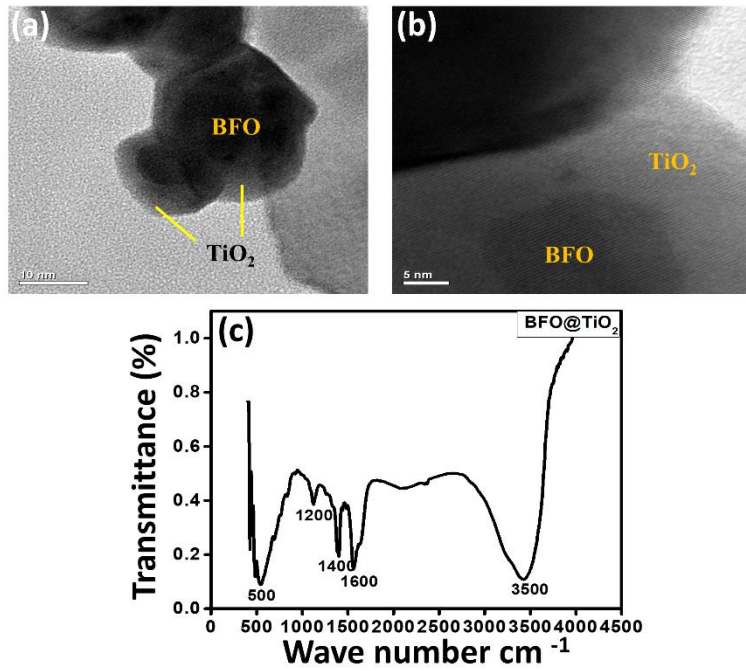
Figure 4.16: (a and b) TEM image of BFO@TiO₂ particles with different magnification and (c) FTIR analysis of BFO@TiO₂ particles (calcined for 2 h).
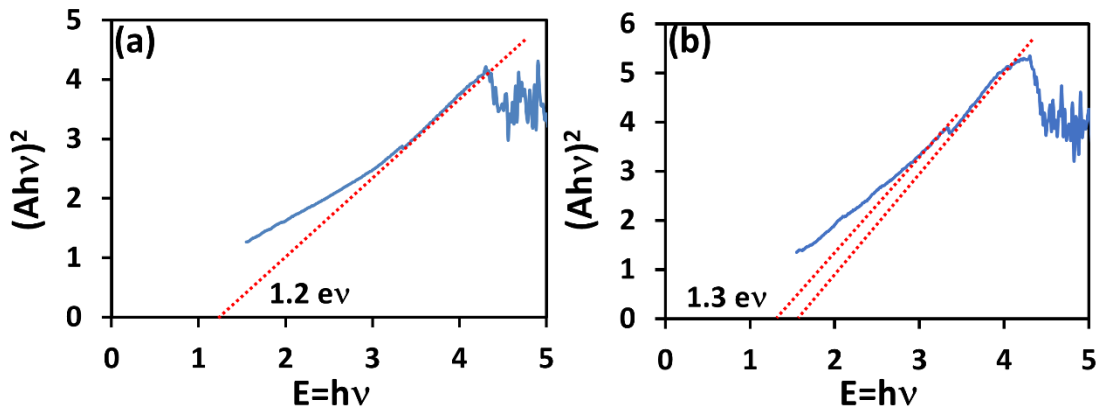
Figure 4.17: Tauc plots for the BFO@TiO₂ particles calcined for (a) 2 h and (b) 5 h (indicating double absorption edge)
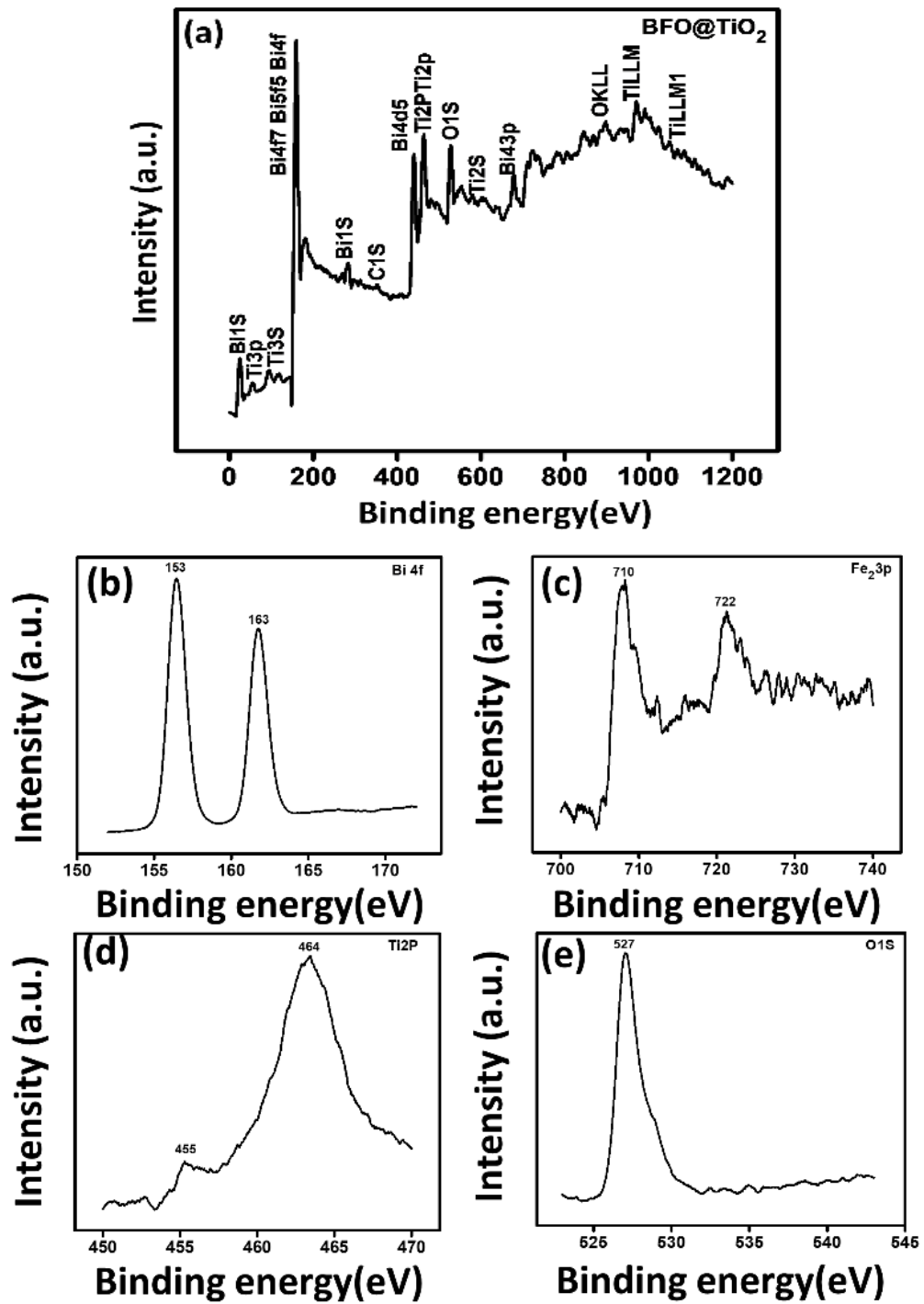
Figure 4.18: (a) XPS analysis for binding energy of BFO@TiO₂ nanoparticles and XPS spectra of (b) Bi 4f (c) Fe 2p (d) Ti2p (e) Os1.

Table 4.4: Size, absorption edge, band gap, zeta potential of BFO@TiO₂ nanocomposite synthesized with BFO: Ti molar ratio of 1:2 calcined at 400°C for different calcination time

Calcination time	Crystallite size BFO & TiO₂	Absorption Edge (nm)	Bandgap (Ev)	Zeta potential (mV)	Particle size TEM
1 h	6.6 & 5.2	885	1.4	-65.1	
2 h	**6.1 & 5**	**1033**	**1.2**	**-64.6**	***Core of SD 12 nm and LD 14 nm & shell thickness of 11 nm**
3 h	6.2 & 5.1	953	1.3	-79.0	
4 h	6.3 & 5.3	1033 & 885	1.2	-66.4	
5 h	6.7 & 5.4	953 &774	1.3	-48.9	
*SD: shorter dimension; LD: longer dimension					

Table 4.5: Atomic concentration of the elements presents in BFO@TiO₂ nanocomposite particles

BFO@TiO₂	CIs	O1s	Ti2p	Fe2p3	Bi4f
Atomic percentage	25.00	33.62	14.71	13.40	13.28

The optimization of synthesis, calcination conditions and the characterization studies have revealed that BFO@TiO₂ nanocomposite particles synthesized with BFO to Ti molar ratio of 1: 2 and calcined at 400°C for 2 h show maximum photocatalytic activity in terms of degradation of MB, AY and Rh-B dyes present in mixed dye contaminated water and COD removal. This nanocomposite is hereinafter referred as BFO@TiO$_{2opt}$.

4.3 Synthesis of engineered BFO@PANI nanocomposite particles by optimization synthesis mixture composition in terms of visible light photocatalytic activity for dye degradation from mixed dye contaminated water.

Optimization of catalyst composition plays a crucial role in the structure and morphology of the nanocomposites when used as a catalyst. It has different properties by the tenability of the composition, surface morphology and structural order of nanoparticles (Zhang et al. 2014). Synthesis mixture composition governs the composition of the catalyst. Chaturvedi et al (2015) and Prabhakaran and Hemalatha (2012) synthesized BFO nanoparticles via a chemical route and coating of polyaniline was attained by a double surfactant layer technique. They found that the volume of aniline used in the synthesise mixture influences the thickness of the shell in BFO@PANI nanocomposite particles. Hence, the molar ratio of BFO to aniline is an essential parameter in controlling the morphology and properties of the resulting BFO@PANI nanocomposite particles. So, optimization of BFO to aniline molar ratio was carried out in the present study by varying the volume of aniline used in the synthesis mixture for the formation of BFO@PANI nanocomposite particles. BFO@PANI nanocomposite particles were synthesized by varying the molar ratio of BFO to aniline used during the synthesis. The BFO@PANI nanocomposite particles were engineered by optimization of composition in order to maximize the degradation of dyes and COD removal from mixed dye contaminated water.

Figure 4.19 (a and b) show the effect of BFO@PANI nanocomposite particles with varying BFO: aniline molar ratio on percentage degradation (after 210 min of irradiation) of dyes and percentage COD removal in the mixed dye aqueous solution by the BFO@PANI nanocomposite particles. Batch experiments for the photocatalytic degradation of dyes from mixed dye aqueous solution containing MB, AY, Rh-B dyes were carried out using BFP1, BFP2, BFP3, BFP4 and BFP5 (BFO to aniline molar ratio of 1:0.0027, 1: 0.0034, 1:0.0041, 1:0.0048 and 1:0.0055 respectively) as photocatalysts under visible light irradiation with initial concentration of each of the dye at 10 mg/L and catalyst loading of 0.1 g/L.

It can be observed that, as the moles of aniline used in the synthesis mixture was increased from 0.0027 moles to 0.0041 moles (BFP1 to BFP3), the percentage of degradation of each of the dyes and the COD removal percentages have increased. But,

137

further increase in the moles of aniline to 0.0048 (BFP3) and 0.0055 (BFP4) moles, a decrease in the degradation of dyes and COD removal was observed. The maximum degradation of the dyes occurred with BFO@PANI nanocomposite particles synthesized with BFO to aniline molar ratio of 1: 0.0041 (BFP3), showing around 100% of MB, 98% of AY and 90% of Rh-B dye degradation and around 96% COD removal in 210 minutes of irradiation time under visible light.

The results show that the dyes present in the mixed dye contaminated water are photo-catalytically degraded effectively in the presence of BFO@PANI nanocomposite particles. The study reveals that BFO@PANI nanocomposite particles synthesized with 1: 0.0041 (BFP3) molar ratio of BFO to aniline show better photocatalytic activity and mineralization ability compared to those synthesized with other molar ratios of BFO and aniline. Thus, BFO to aniline molar ratio of 1: 0.0041 (BFP3) in the synthesis mixture may be considered as the optimum for the synthesis of BFO@PANI nanocomposite particles for maximum photocatalytic activity and dye mineralization ability. These BFO@PANI nanocomposite particles show good photocatalytic activity under visible light, which is due to its strong photo absorption ability and charge recombination rate (Shahabuddin et al. 2016; Wang et al. 2010).

The removal of dyes from mixed dye contaminated water containing MB, AY, Rh-B dyes using the highly active fabricated BFO@PANI nanocomposite (BFP3) during batch photocatalysis under visible light irradiation, was also compared with that obtained under dark conditions in the presence of catalyst and under visible light in the absence of catalyst. Figure 4.19 (c) shows that the percentage removal of each of the dyes under dark conditions in the presence of catalyst is very minimal (less than 10%) as compared to that in the presence of catalyst on irradiation with visible light. Thus, the dye removal by adsorption on the catalyst is minimal. The effect of the light irradiation in the absence of catalyst is also very less, confirming a small effect of photolytic removal of the dyes by visible light irradiation.

As observed in Figure 4.19(c) around 100% of MB: 98% of AY and 90% of Rh-B degradation from the mixed dye aqueous solution could be achieved respectively, in 210 minutes of irradiation time under visible light. It shows that the dyes in the mixed dye contaminated water are photo-catalytically degraded successfully in the presence of BFO@PANI nanocomposite particles. The study reveals that the BFO@PANI

nanocomposite particles serve as efficient photocatalysts for the degradation of dyes from mixed dye aqueous solutions under visible light irradiation.
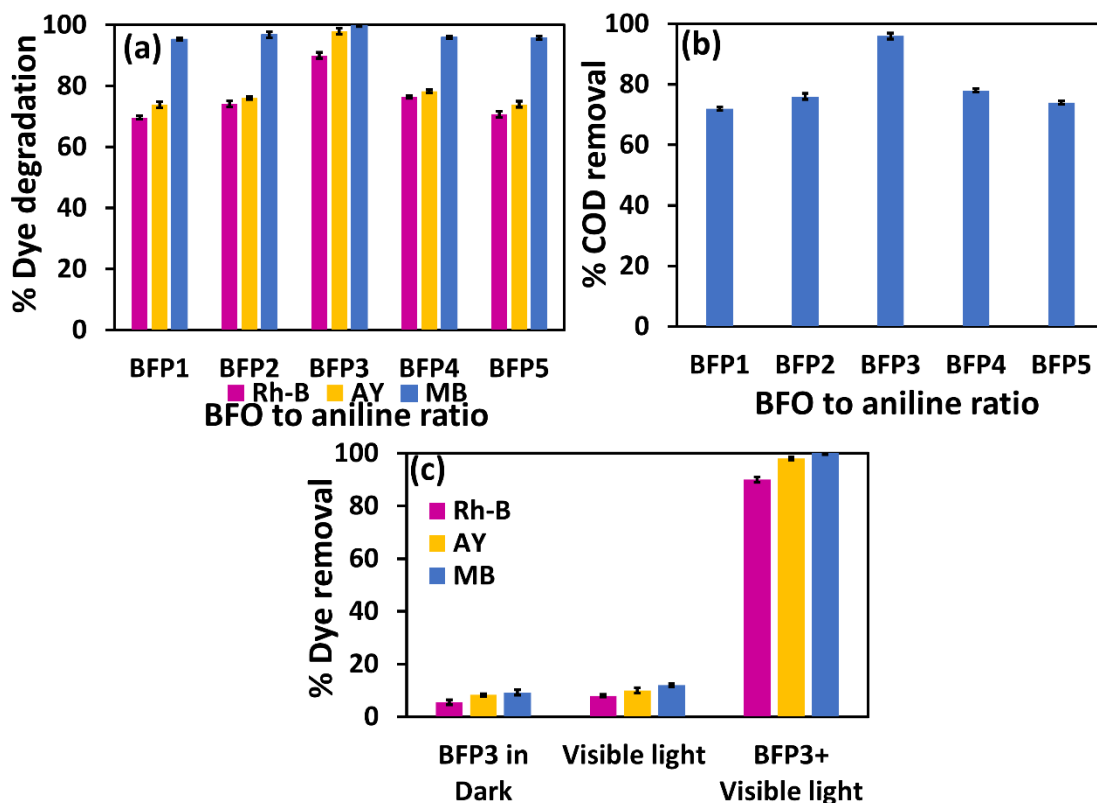
Figure 4.19: (a) Percentage degradation and (b) percentage COD removal from mixed dye aqueous solution under visible light by BFO@PANI particles synthesized with different molar ratio of BFO to aniline. (c) Percentage dye removal under different conditions. Conditions: catalyst concentration-0.1g/L; concentration of each dye-10 mg/L; irradiation time-210 min

4.3.1 Characterization of BFO@PANI nanocomposite particles synthesized with different molar ratios of BFO to aniline

The BFO@PANI nanocomposite particles synthesized with different BFO to aniline molar ratios were further characterized. Figure 4.20 shows the XRD pattern of BFO@PANI nanoparticles synthesized with different molar ratios of BFO to aniline (BFP 1 to BFP 5) along with that of BFO (Method C) and PANI. The prominent peaks are exhibited at $2\theta = 22.3°, 31.7°, 32°, 39.4°, 45.6°, 50°, 51.6°, 56°, 67°, 69.9°, 71.5°, 75.5°$ and $79.4°$ and they are similar to those found in XRD of BFO nanoparticles. These peaks

correspond to perovskite $BiFeO_3$ (JCPDS NO-01-071-2494) with Rhombohedral crystal system of different crystalline plane (012), (104), (110), (202), (024), (211), (122), (300), (220), (220), (119), (312), (128) and (315), respectively. The peak for impurity phase $Bi_{25}FeO_{40}$ at $2\theta = 28°$ present in BFO is also being observed in BFP1 to BFP5 with a small shift in 2θ to around 27.84 to 27.92. XRD reveals that impurity phase is being retained in BFO@PANI nanocomposite particles synthesized with all the different molar ratios. However, the impurity peak intensity is small in BFO@PANI as compared to that in BFO. The impurity peak intensity reduced as the ratio is changed from BFP1 to BFP 5. In the XRD of PANI, a sharp peak corresponding to crystalline PANI (JCPDS No.4-0477) is observed at $2\theta =25.44°$. The PANI peak at around 25.4° has also been shown in XRDs reported by many researchers (Kalikeri et al. 2018; Pant et al. 2006; Pawar et al. 2010; Razalli et al. 2017; Sydulu Singu et al. 2011). This peak is not visible in the XRD of BFP1 and BFP2, indicating that the volume of aniline used in the synthesis of BFP1 and BFP2 nanocomposite particles is very small and thus the layer of PANI that would have formed around BFO is negligibly small. The quantity being very small, it is not being detected by XRD. However, the peak for PANI appeared in BFP3 to BFP5. The peak shifted to the right to $2\theta =25.56°$, 25.6° and 25.67° as the aniline content was increased to 0.0048 and further to and 0.0055 moles respectively. The shift in peak of PANI in BFO@PANI nanocomposite particles is due to the interfacial binding of BFO with PANI. Identical peaks were observed in BFO@PANI nanocomposite particles synthesized with all the five different molar ratios, except for the presence of PANI. The presence of PANI in XRD of BFP3 to BFP5, designates the formation of layer of the PANI on the BFO particle surface. However, the impurity phase $Bi_{25}FeO_{40}$, that existed in BFO is present in BFO@PANI nanocomposite too, though very small. The process of synthesis of BFO@PANI has not removed the impurity phase of BFO. All the peaks of BFO in BFO@PANI nanocomposite are similar to that of BFO, indicating that the crystal structure of BFO is maintained even after the coating process. Chaturvedi et al. (2015) synthesized BFO using a soft chemical route combined with post synthesis annealing and then used the entire amount of thus synthesized BFO to prepare BFO@PANI core-shell nanoparticles by double surfactant method by adding different aniline volumes of 8μL,10μL and 12μL. The diffraction peak for PANI was not observed in the XRD of

bismuth ferrite-polyaniline core-shell nanoparticles synthesized by them. They reported that, such a result is due to a very thin layer of PANI. The present study showed the presence of PANI in XRD at higher ratios. Figure 4.20 shows that, in BFP3 to BFP5, with an increase in aniline content in the synthesis mixture the intensity of PANI peaks have increased, which shows that the PANI content in BFO@PANI nanocomposite has increased with increase in the amount of aniline used in the synthesis mixture.

In Figure 4.20, the peak doublets are exhibited at $2\theta = 31.7°, 32°$ of BFO, which shows distinctive splitting of the rhombohedral peak at around $32°$. The split (doublet) near $32°$ remains same for all the samples. However, broadening of this doublet peak is observed with increase in the amount of aniline used for the synthesis as shown in the inset of Figure 4.20 which can be attributed to decreasing values of lattice parameters because of incorporation of PANI (Chaturvedi et al. 2014, 2015). Increasing aniline in the synthesis mixture may have enhanced the coordination of PANI with lattice oxygen, which may distort the crystal lattice of BFO leading to changes in optical properties and interrupting the overall charge compensation of the BFO lattice. It may disturb overall charge compensation of BFO and produce some lattice defects, declining the lattice parameters (Chaturvedi et al. 2014). The average crystallite sizes of the BFO@PANI samples were calculated using Scherrer formula, and are presented in Table 4.6. It shows that the particles are nanocrystalline and the particles synthesized with BFO to aniline molar ratio of 1:0.0041 (BFP3) is with the smallest crystallite size for BFO (5.9 nm) and that for PANI is 4.5 nm. The atomic concentration values of the elements present in the BFP@PANI nanocomposite particles (optimum) as analysed by XPS are presented in Table 4.3

Figure 4.21 (a-e) shows the SEM images of BFP1, BFP2, BFP3, BFP4 and BFP5. The nanocomposites appear to be flaky structured with sharp edges. But the in BFP 5 nanocomposite, the particles appear aggregated.

Figure 4.22 (a-e) shows the TEM images of BFP1, BFP2, BFP3, BFP4 and BFP5, respectively. The images reveal that BFO nanoparticles are slightly ellipsoidal and surrounded by nano-dimensional PANI coating confirming that BFO nanoparticles are embedded in PANI matrix, forming a nanocomposite structure. Even though, XRD showed an absence of BFO peak in BFP1 and BFP2, TEM showed the presence of PANI layer around the BFO particles. In BFP1, the BFO particles are aggregated and

the aggregates are surrounded by a layer of PANI. The BFP2 particles are distinct and each BFO particle is surrounded by a layer of PANI forming a core-shell structure. However, BFP3 consists of distinct BFO particles embedded in thick layer of PANI matrix. The thickness of PANI matrix has increased with increase in aniline content in the synthesis mixture. Table 4.6 presents the size of BFO particles and PANI layer thickness in the BFO@PANI nanocomposite particles. Moreover, it shows that the particles synthesized with BFO to aniline molar ratio of 1:0.0041 (BFP3) are the smallest size, with BFO nanoparticles of average diameter 7.03 nm and embedded in PANI matrix approximately 4.9 nm thick.

The optical band gap energy of the synthesized BFO@PANI nanoparticles synthesized with different molar ratios of BFO to aniline were calculated by using Tauc's plot. A representative Tauc's plot is shown in Figure 4.23 (a) for BFP3. The BFP1 to BFP5 showed only one absorption onset. As observed in Table 4.6, the band gap energy value is the lowest for BFP3 and the value is 1.4 eV, and this value is also lower than that obtained with only BFO. The maximum photocatalytic activity was achieved with BFO@PANI nanocomposite particles synthesized with BFO to aniline molar ratio of 1:0.0041 (BFP3). It may thus be ascribed to its lowest band gap (1.4 eV) energy and smallest particle size. The band gap energy of the BFP1, BFP2, BFP4 and BFP5 are similar and equal to 1.6 eV. Their photocatalytic activity is lesser than that of BFP3 owing to higher band gap energy. This may be due to inappropriate formation of heterojunction between BFO and PANI owing to the structure and morphology of BFO@PANI. The contact area between BFO and PANI depends on the structure of BFO@PANI, which assists in charge transfer at the BFO and PANI heterojunction interface. It is known that only when the amount of polyaniline in BFO@PANI is appropriate, both BFO and PANI efficiently form a heterojunction interface to accelerate the photocatalytic process. An excessive or too little aniline is not favourable to form a BFO@PANI structure with extremely well-organized charge transfer (Chaturvedi et al. 2015). The band gap energy values of BFP1 to BFP5 are lower than the band gap value of 1.98 eV reported by Chaturvedi et al. (2015) for BFO@PANI nanocomposite particles synthesized by double surfactant method; wherein BFO was synthesized by soft chemical route combined with post-synthesis annealing. Chaturvedi et al (2015) have reported that the band gap values of nanoparticles are determined by

the macrostrain, oxygen defects and exchange interactions. The absorption edge wavelength values of BFP1 to BFP5 are shown in Table 4.6, fall in the NIR region. These results indicate that BFO@PANI nanocomposite particles synthesized in the present study can be excited by even longer wavelength light extending from visible to NIR region. Thus, these nanoparticles have all the potential to be good photocatalysts even under solar light, as maximum excitation can occur by utilization of light in the entire solar spectra ranging from UV to NIR.

The effective polymerization of aniline on top of the surface of BFO was complete as evidenced by Fourier Transform Infrared Spectroscopy (FTIR), as shown in Figure 4.23 (b). The characteristic peak of BFO appeared at 552 cm^{-1} in all the samples and the intensity of the peak varied with an increase in the aniline concentration but it is negligible. The characteristic peak at 645 cm^{-1} and 845 cm^{-1} are C-H band stretching and benzene ring absorption (Emran 2018; Vinet and Zhedanov 2011). The characteristic peak at 924 cm^{-1} is due to the presence of trapped nitrates (used in the synthesis) on the surface, caused by stretching vibrations of trapped NO^-_3 ions in the BFO nanostructures (Dhanalakshmi et al. 2016; Zalesskii et al. 2003). The characteristic peak at 1119 cm^{-1} is an evidence of C-N stretching (Vinet and Zhedanov 2011). The characteristic peaks at 1385-1600cm^{-1} signify the carbonate groups (Dhanalakshmi et al. 2016; Mukherjee et al. 2012). The carbonate bands were also observed due to the surface adsorbed species, which is reasonable because these nanostructures have high surface area (Ju et al. 2011). However, in terms of PANI, The characteristic peaks of PANI appeared at 1604, 1385 cm^{-1}, due to benzenoid and quinone ring stretching in PANI, and C–N; C-C and N-H stretching of a secondary aromatic amine respectively (Emran et al. 2018; Huang and Wan 2002; Mirmohseni et al. 2019). These results are similar to those reported by Huang et al.2002 (Huang and Wan 2002). The peaks at 2922–2850 cm^{-1} are due to medium C–H stretch. The characteristic peak around 3425 cm^{-1} is due to normal polymeric OH stretching (Vinet and Zhedanov 2011). FTIR measurements show the evidence that the polymerization of PANI has been successfully obtained on the surface of the BFO NPs.

To determine the surface composition and chemical states of the BFO@PANI nanocomposite particles (BFP3), XPS analysis was conducted and the spectrum is shown in Figure 4.24 (a). XPS survey spectrum of BFP3 shows the presence of

elements Bi 4f at 157 eV and 164 eV; Fe 2p at 710 eV and 724 eV; O 1S at 529 eV and 530 eV; C 1s at 284, and N1s at 400 eV.

As shown in Figure 4.24 (b) the spectrum shows two strong peaks of Bi 4f at binding energies of 157 eV and 164 eV corresponding to the core lines of Bi 4f $_{7/2}$ and 4f $_{5/2}$ respectively, and that are in good agreement with the highest oxidation state '+3' of Bi due to synergistic action between Bi to Bi '+3' (Zheng et al. 2018). It clearly represents the '+3' oxidation state of Bi in BFO without any trace of metallic Bi in the matrix (Guo et al. 2016; Pugazhvadivu et al. 2014; Rauf et al. 2015).

The spectrum shown in Figure 4.24 (c) also exhibits two peaks for Fe 2p at 710 eV and 724 eV consistent to core lines of Fe 2P $_{3/2}$ and Fe 2P $_{1/2}$ respectively arising from the spin-orbit contact and correspond to Fe^{3+} oxidation state in BFO and their separation was 14 eV (Manjunatha et al. 2019; Mukherjee et al. 2018; Quickel et al. 2015). These characteristics peaks were quite similar to those reported in the literature (Li et al. 2019). The position of the satellite peak at 715eV in the Fe 2p spectra is in good agreement with the Fe^{3+} oxidation state in BFO (Mukherjee et al. 2018; Quickel et al. 2015). Moreover, no significant peaks were observed for the Fe^{2+} ionic state, suggesting that iron predominantly exists in the Fe^{3+} state. It is evident that the binding energy for the iron lies between 700 and 735 eV (Lv et al. 2015; Manjunatha et al. 2019).

The XPS spectra in Figure 4.24 (d) shows two peaks for O 1S at 529 eV and 530 eV corresponding to the Bi–O and Fe–O bonds, respectively. These peaks were attributed to the lattice oxygen in the O_2^- state (Gautam et al. 2016; Mali et al. 2012; Zhu et al. 2017b). In addition, these two bands are possibly due to the strong interactions between the amine nitrogen and oxygen of BFO (Ansari et al. 2014b).

The XPS spectra in Figure 4.24 (e) shows one peak for C 1s at 284, This peak shows the presence of quinoid structure and benzenoid rings. This characteristic peak is similar to that reported by Patil et al. (2018).

The XPS spectra in Figure 4.24 (f) as shown in N1s spectrum exhibits only one broad peak at 400 eV which indicates the presence of more than one type of nitrogen , the quinoid phenyl structure and quaternary ammonium salt (Macdiarmid et al. 1987; Patil et al. 2018). This Peak can be attributed to benzenoid structure. Therefore, in oxidized polyaniline, quinoid and benzenoid structures exist in the carbon backbone

and electronic charges resides on nitrogen atoms (Ansari et al. 2014a). Table 4.7 presents atomic concentration of the elements presents in BFO@PANI particles.

Figure 4.20: XRD patterns of BFO@PANI nanocomposite particles prepared at different molar ratios of BFO and aniline such as 1.0.0021(BFP1), 1:0.0034 (BFP2), 1:0.0041 (BFP3), 1:0.0048 (BFP4) and 1:0.0055 (BFP5).
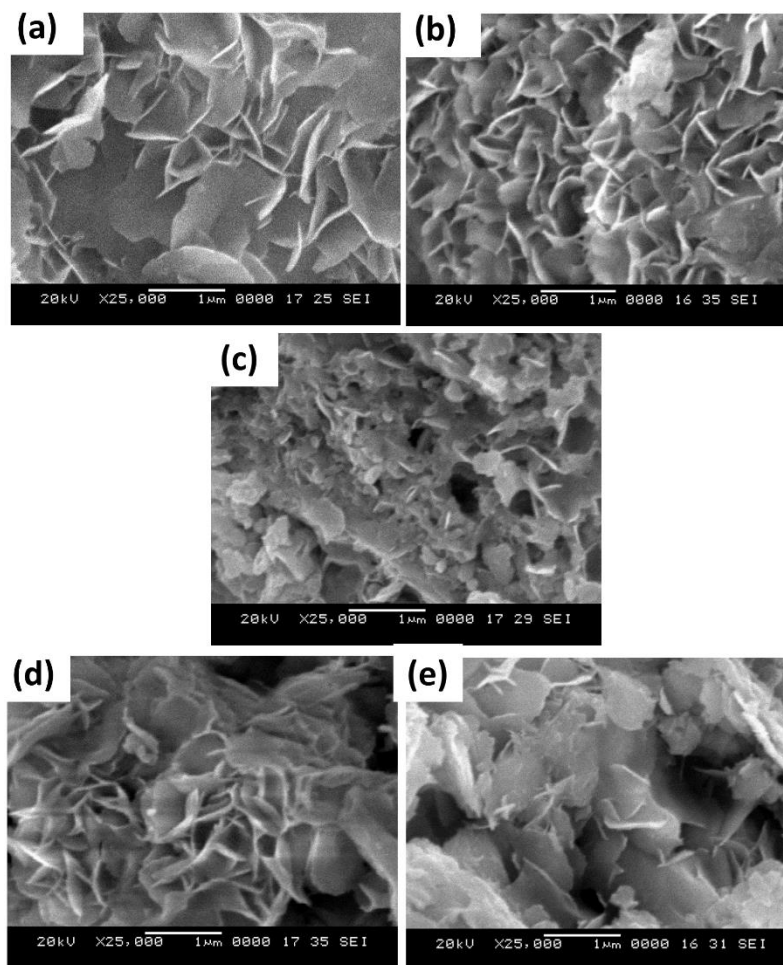
Figure 4.21: SEM images of BFO@PANI nanocomposite particles prepared at different molar ratios of BFO: aniline (a) 1:0.0027 (BFP1), (b) 1:0.0034 (BFP2) (c) 1:0.0041 (BFP3) (d) 1:0.0048 (BFP4) and (e)1:0.0055 (BFP5).
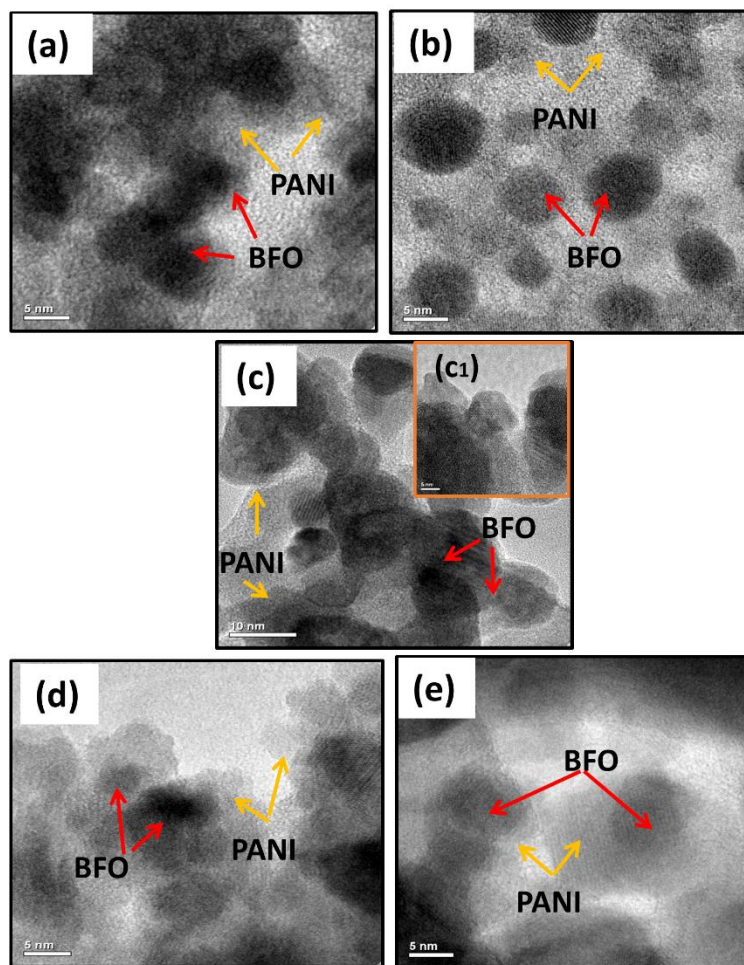
Figure 4.22: TEM images of BFO@PANI particles prepared at different molar ratios of BFO: aniline (a) 1:0.0027(BFP1), (b) 1:0.0034 (BFP2) (c) 1:0.0041 (BFP3) (d) 1:0.0048 (BFP4) and (e)1:0.0055 (BFP5).
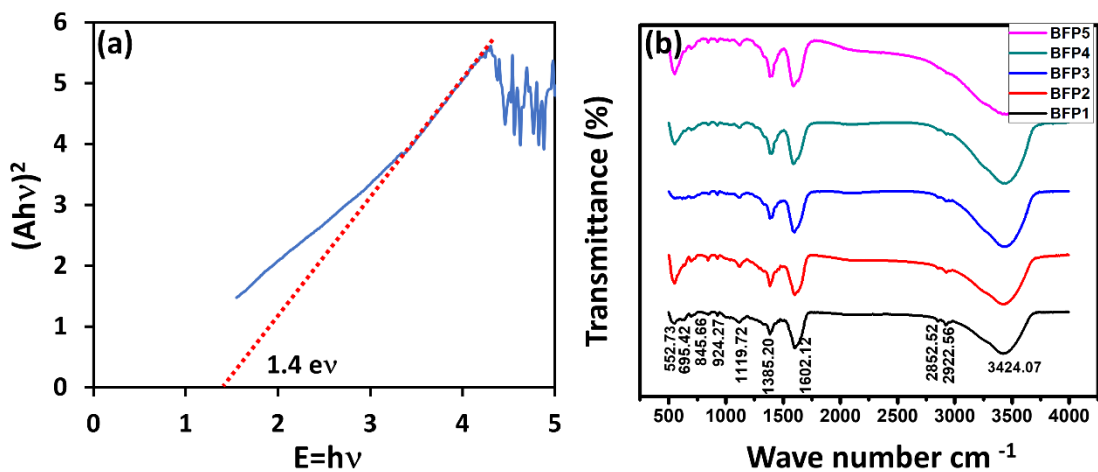
Figure 4.23: (a) Tauc plot and (b) FTIR Spectra of BFO@PANI particles (BFP3)
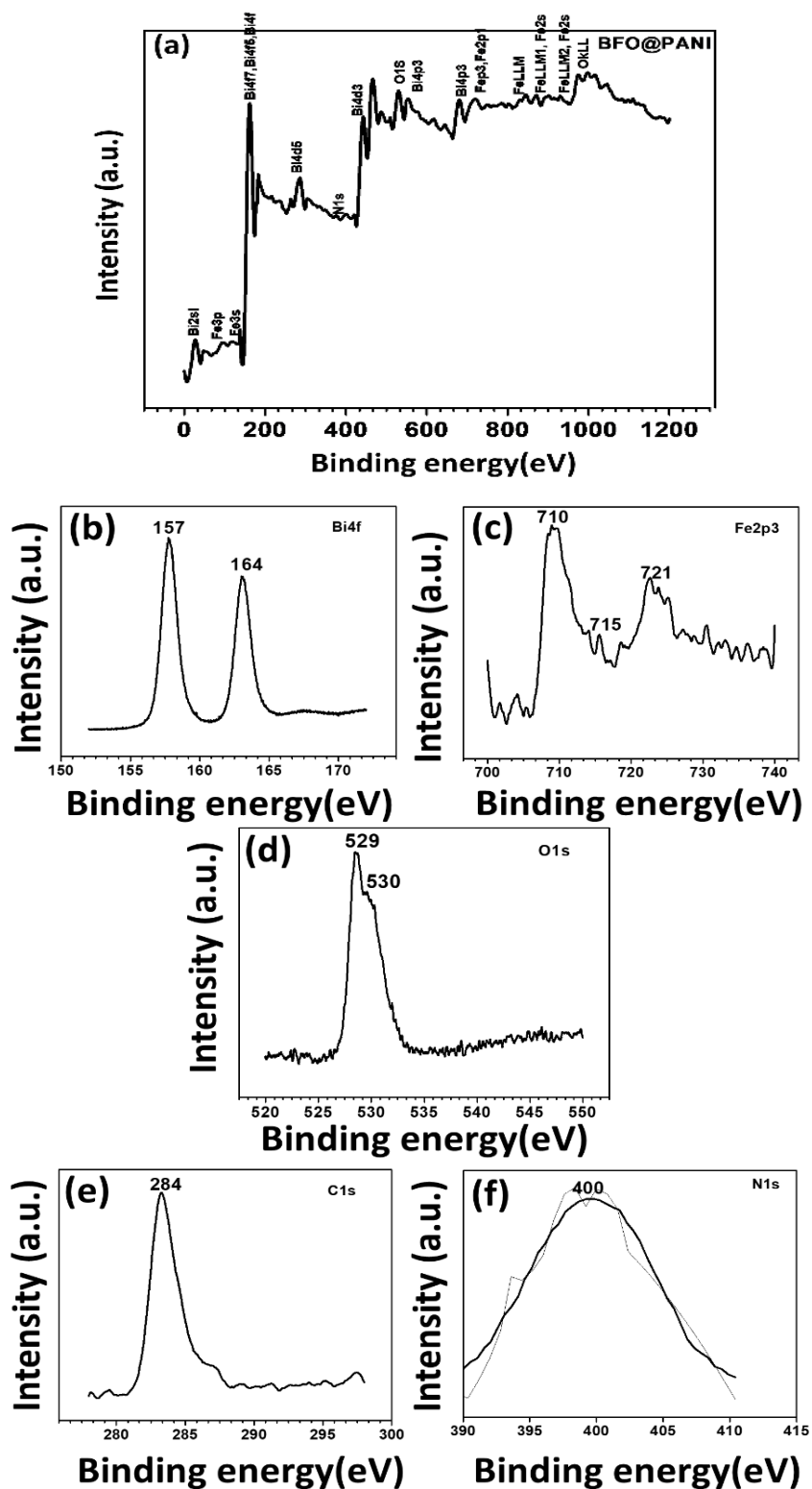
Figure 4.24: (a) XPS analysis for binding energy of BFP3 nanoparticles and XPS spectra of (b) Bi 4f (c) Fe 2p (d) Os1 (e) C1s and (f) N1s.

Table 4.6: Crystallite size, band gap, zeta potential and particle size (TEM) of Different ratio of BFO@PANI nanocomposite particles

Different ratio	Average Crystallite size in nm BFO & PANI	Absorption Edges (nm)	Bandgap (eV)	Average particle size(nm) of BFO embedded in PANI matrix (TEM)	Average thickness (nm) of PANI layer (TEM)
1:0.0027 (BFP1)	6.2 & 0.8	775	1.6	7.2	1.9
1:0.0034 (BFP2)	6.3 & 1	775	1.6	7.1	1.3
1:0.0041 (BFP3)	**5.9 & 4.5**	**885**	**1.4**	**7.03**	**4.9**
1:0.0048 (BFP4)	6.4 & 5.5	775	1.6	7.3	5.3
1:0.0055 (BFP5)	6.5 & 5.9	775	1.6	7.5	7.1

Table 4.7: Atomic concentration of the elements presents in BFO@PANI nanocomposite particles

BFO@PANI	Cls	O1s	Fe2p3	Bi4f
Atomic percentage	33.03	35.21	17.68	14.08

The optimization of molar ratio of BFO to aniline in the synthesis mixture and the characterization studies have revealed that BFO@PANI nanocomposite particles synthesized with BFO to aniline molar ratio of 1:0.0041 (BFP3) show the maximum photocatalytic activity in terms of degradation of MB, AY and Rh-B dyes present in mixed dye contaminated water and COD removal. This nanocomposite is hereinafter referred as BFO@PANI$_{opt}$.

4.4 Comparison of photocatalytic activity of BFO, TiO$_2$ and BFO@TiO$_{2opt}$ nanocomposite particles under visible light irradiation in terms of degradation of dyes

The comparison studies for the photocatalytic degradation of dyes from mixed dye contaminated water, containing MB, AY, Rh-B dyes were carried out using the BFO@TiO$_2$ nanocomposite particles synthesized with BFO to Ti molar ratio of 1:2, calcined at 400°C for 2 h (BFO@TiO$_{2opt}$), BFO nanoparticles synthesized by Method 2C and TiO$_2$ nanoparticles (Degussa P25) as photocatalysts under visible light irradiation with initial concentration of each of the dye at 10 mg/L and catalyst loading of 0.1g/L and irradiation with 2 lamps. As observed in Figure 4.25 (a and b), in the presence of BFO@TiO$_{2opt}$ nanocomposite particles around 100%, 96% and 88% of MB, AY, and Rh-B dyes were degraded respectively and 95% COD removal from mixed dyes contaminated water in 210 minutes under visible light was achieved. In the presence of BFO nanoparticles 93%, 71%, and 67% degradation of MB, AY and Rh-B dyes respectively, and 76.6% COD removal could be achieved, whereas with Degussa P25 only around 50%, 33%, and 20% degradation of MB, AY and Rh-B dyes and 20% COD removal from mixed dye contaminated water could be achieved under visible light. It was observed that the photocatalytic activity of BFO@TiO$_{2opt}$ nanocomposite particles in terms of degradation of each of the dyes from the mixed dye aqueous solution is superior to that of BFO or TiO$_2$ nanoparticles. However, TiO$_2$ nanoparticles show lower degradation of dyes compared with BFO@TiO$_{2opt}$ and BFO nanoparticles. The study reveals that BFO@TiO$_{2opt}$ nanoparticles are superior photocatalysts for the degradation of dyes from mixed dye contaminated water under visible light irradiation, which is due to its strong photo absorption ability and charge recombination rate. The low electron-hole recombination rate of BFO@TiO$_{2opt}$ is credited to the presence of electronic-accumulation centres formed by the electronic interaction between the BFO core and TiO$_2$ shell. These centres effectively separate the electrons and holes, leading to high quantum efficiency. Theoretically, an internal electric field from TiO$_2$ to BFO will be generated when BFO and TiO$_2$ come in contact and form a heterojunction interface (Wang et al. 2011c; Zhao et al. 2016). Driven by this internal electric field, the holes and electrons will flow in opposite directions, thus leading to the efficient separation of photogenerated electrons and holes and enhanced photocatalytic activity.
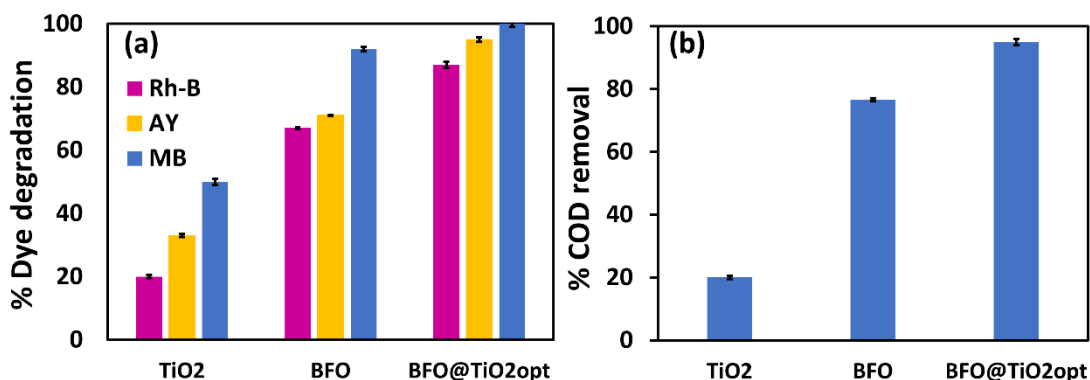
Figure 4.25: (a) Percentage degradation and (b) Percentage COD removal from mixed dye aqueous solution in presence of BFO, TiO₂ and BFO@TiO₂opt nanocomposite particles under visible light. Conditions: catalyst loading -0.1 g/L; concentration of each dye-10 mg/L; irradiation time-210 min.

Figure 4.26 shows the proposed mechanism of photocatalytic degradation of dyes from mixed dye contaminated water by BFO@TiO$_{2opt}$ nanocomposite particles under visible light irradiation. A p-n heterojunction is formed when BFO is contacted with TiO$_2$, with the Fermi level after contact being closer to the Conduction Band (CB) of TiO$_2$ and Valance Band (VB) of BFO. In the BFO@TiO$_2$ nanocomposite under visible light irradiation BFO acts as a photosensitizer. BFO absorbs the visible light and the electrons from the valence band of BFO are excited to the CB, whereas the holes get accumulated in the valence band of BFO. As the energy state of BFO conduction band is higher than that of the TiO$_2$ CB, electrons from BFO CB move to the CB of TiO$_2$. Thus, the CB of TiO$_2$ acts as an electron centre and VB of BFO acts as a hole centre. As the electrons formed by excitation of BFO are stored in the CB of TiO$_2$ and holes in the valence band of BFO, the probability of recombination of the photogenerated electrons with the holes is very low, which results in an increased lifetime of the charge carriers and an enhanced interfacial charge transfer to adsorbed organic molecules.

These electrons in CB of TiO$_2$ react with oxygen (O$_2$) molecules on the catalyst surface in the reduction process and get reduced to •O$_2$, which can oxidize the organic pollutants and degrade them to simpler molecules. The holes in the BFO VB, oxidize H$_2$O to form hydroxyl radicals which in turn lead to reduction of dye molecules. The holes can also be consumed by participating in weak oxidation of dyes directly (Li et al. 2009a). These oxidation-reduction reactions lead to degradation of the dye.

151

The visible light mediated photocatalytic activity in BFO@TiO$_2$ is attributed to the low band gap energy of the heterostructure, as well as the presence of BFO core and TiO$_2$ shell causing the charge separation, which prevents or reduces the rate of charge recombination and thus leads to higher photocatalytic rate of BFO@TiO$_2$ compared to that of BFO.
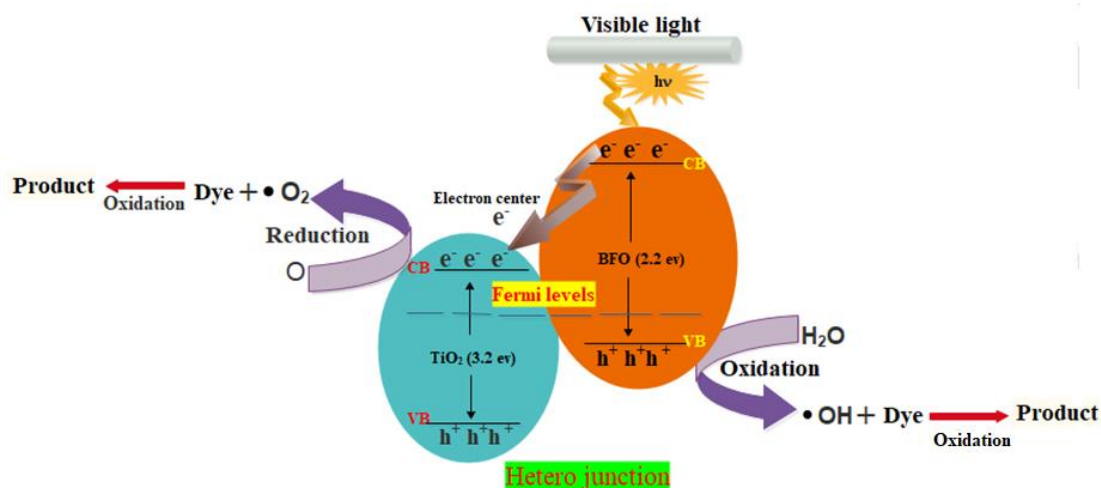
Figure 4.26: The proposed mechanism of photocatalytic degradation of dyes using fabricated BFO@TiO$_2$ particles.

4.5. Comparison of photocatalytic activity of BFO, PANI and BFO@PANI$_{opt}$ nanocomposite particles under visible light irradiation

The photocatalytic degradation of dyes from mixed dye contaminated water containing MB, AY, Rh-B dyes were carried out using the fabricated BFO@PANI$_{opt}$ nanocomposite particles synthesized with BFO to Aniline molar ratio of 1:0.0041 (BFP3), and the results were compared with that of BFO nanoparticles and polyaniline individually under visible light irradiation with an initial concentration of each of the dye at 10 mg/L and catalyst loading of 0.1 g/L and irradiation with two lamps. As observed in Figure 4.27 (a and b), in the presence of BFO@PANI$_{opt}$ nanocomposite particles around 100%, 98% and 90% degradation of MB, AY and Rh-B dyes respectively and 96% COD removal from mixed dyes contaminated water could be achieved in 210 minutes under visible light. In the presence of BFO nanoparticles 93%, 71% and 67% degradation of MB, AY and Rh-B dyes and 76.6% COD removal could be achieved respectively, whereas with PANI only around 51%, 35%, and 22 % degradation of MB, AY and Rh-B dyes respectively and 22% COD removal from

mixed dye contaminated water could be achieved under visible light. It was observed that the photocatalytic activity of BFO@PANI nanocomposite particles in terms of degradation of each of the dyes from the mixed dye aqueous solution is higher to that of BFO or PANI nanoparticles. However, PANI shows lesser degradation of dyes compared to BFO@PANI$_{opt}$ and BFO nanoparticles, which may be attributed to the unavailability of photo-generated electrons and holes for photocatalytic reaction due to their high recombination rate and due to its low surface area too (Zhang et al. 2016b). The present study reveals that BFO@PANI$_{opt}$ nanocomposite particles are better photocatalysts for the degradation of dyes from mixed dye contaminated water under visible light irradiation. Because of the interaction between BFO and PANI, the recombination rate among photo-generated electron and holes gets reduced, which enhances the photocatalytic activity of the photocatalyst (Kalikeri et al. 2018; Radoičić et al. 2013). Therefore, the presence of PANI plays an important role in the electron-hole pair separation efficiency and in improving the photocatalytic activity of the composite.
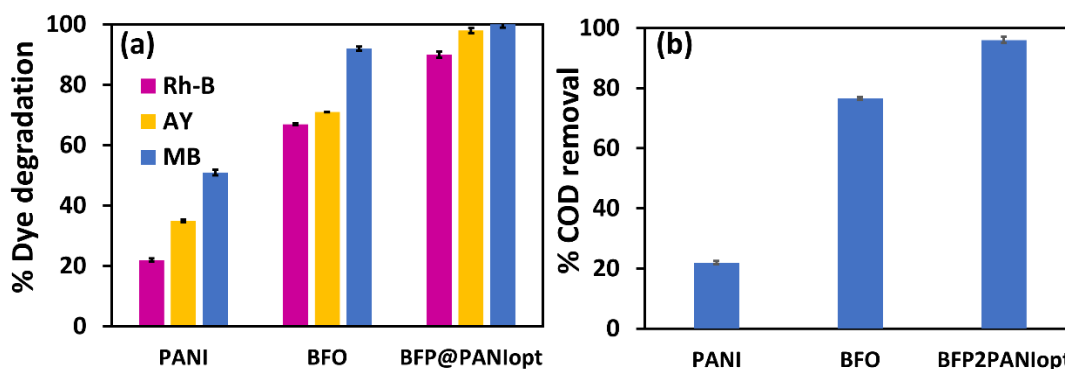
Figure 4.27: (a) Percentage degradation and (b) Percentage COD removal from mixed dye aqueous solution in the presence of BFO, PANI and BFO@PANI$_{opt}$ particles under visible light. Conditions; Catalyst concentration- 0.1 g/L; concentration of each dye-10 mg/L; irradiation time -210 min.

Figure 4.28 shows the proposed mechanism of photocatalytic degradation of dyes from mixed dye contaminated water by BFO@PANI$_{opt}$ nanocomposite particles under visible light irradiation. When irradiated by visible light, both PANI and BFO in the composite attract photons at their edge. The electrons in the VB of BFO are excited to its CB. The charge from the photon is also transferred immediately from the highest

occupied molecular orbital (HOMO) to the lowest unoccupied molecular orbital (LUMO) of PANI (Reddy et al. 2010). The excited photogenerated electrons of PANI molecules are injected from LUMO of PANI to the CB of BFO, to form electron center (Li et al. 2008; Zhang et al. 2006b) at BFO and eventually react with oxygen at the surface. This results in the configuration of highly reactive particles, such as the superoxide radical ion $O_2\bullet$ and as a result the hydroxyl radical OH•, which are responsible for the degradation of the organic compound (Elsayed and Gobara 2016; Zang 2008). At the same time, the transitions between π- polaron and polaron-π * in PANI molecules can be induced. The holes from the VB of BFO migrate to HOMO of PANI. The photogenerated holes in the π orbital of PANI along with the holes transferred from BFO, can migrate to the surface and react with water to give up hydroxyl radicals. PANI would significantly help in charge separation and to reduce the charge recombination. Therefore, the superior photocatalytic activity of BFO@PANI$_{opt}$ as compared to BFO nanoparticles is owing to quick charge separation, slow charge recombination and additional surface provided by PANI for visible light absorption. The improved visible light absorption of BFO@PANI$_{opt}$ nanocomposite owing to its low band gap, is not the only reason that induces increased photocatalytic activity but also owing to reduced electron-hole recombination rate (Radoičić et al. 2013).
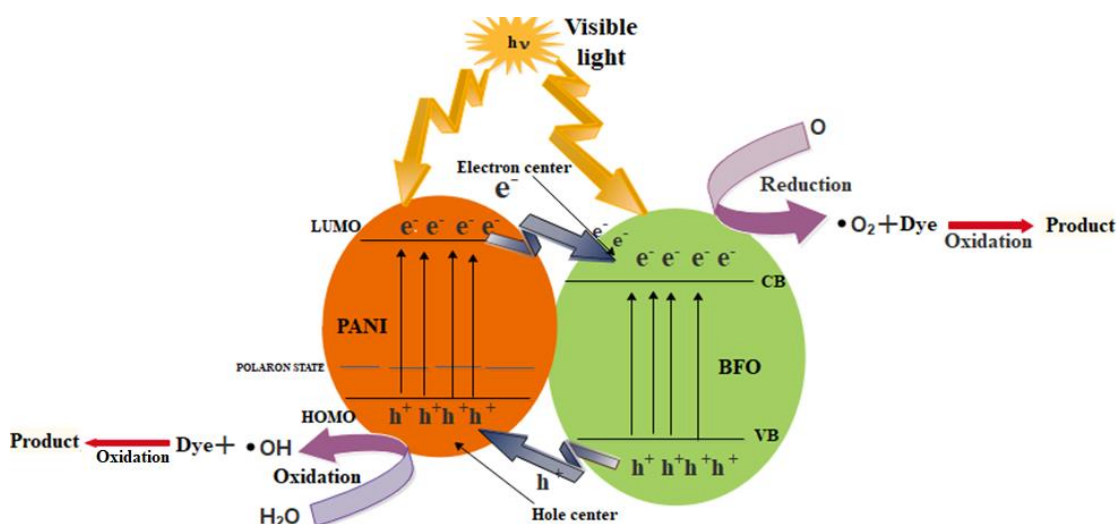
Figure 4.28: The proposed Mechanism of Photocatalytic degradation of dyes using fabricated BFO@PANI nanocomposite particles.

Based on these studies on BFO@TiO$_2$ nanocomposite particles and BFO@PANI$_{opt}$ nanocomposite particles have been found to exhibit superior photocatalytic activity in terms of degradation of dyes and COD removal from mixed dye contaminated water under visible light irradiation. Further to improve the photocatalytic reaction rates for the degradation of MB, AY and Rh-B dyes present in mixed dye contaminated water and COD removal, the photocatalytic reaction parameters such as pH, catalyst loading and light intensity are to be optimized and the effect of concentrations of the dyes on their degradation are to be studied. Such studies were carried out and the results are presented in Chapter 5.

CHAPTER 5

RESULTS AND DISCUSSION

PHOTOCATALYTIC DEGRADATION OF DYES IN MIXED DYE CONTAMINATED WATER BY BFO@TIO$_{2\text{opt}}$ AND BFO@PANI$_{\text{opt}}$ PARTICLES

5.1 Effect of photocatalysis parameters on degradation of dyes from mixed dye aqueous solution

Based on the optimization of synthesis and calcination parameters, BFO@TiO$_2$ nanocomposite particles synthesized with BFO to Ti molar ratio of 1:2, calcined at 400°C for 2 h and BFO@PANI nanocomposite particles synthesized with BFO to aniline mole ratio of 1:0.0041 (BFP3) were found to show a maximum photocatalytic activity under visible light irradiation in terms of degradation of dyes and COD removal from mixed dye contaminated water containing MB, AY and Rh-B. These nanocomposite particles are referred as BFO@TiO$_{2\text{opt}}$ and BFO@PANI$_{\text{opt}}$. Further, in order to improve the efficiency of degradation of dyes using these nanocomposite particles, the parameters affecting the photocatalysis rate are studied and optimized. Photocatalytic degradation of dyes is influenced by several parameters, such as pH, catalyst loading, light intensity and dye loading.

5.1.1 Effect of initial pH

The pH of a solution is a prominent parameter that influences the photocatalytic activity of a catalyst, as it modifies the surface charge properties of the catalyst (Akpan and Hameed 2009; Alahiane et al. 2014; Jantawasu et al. 2009). The solution pH alters catalyst–solution interface and accordingly affects the sorption-desorption characteristics and the separation of the photogenerated electron-hole pairs on the surface of the composite particles (Reza et al. 2017). pH is an essential factor that affects the activity of the composite as it may change the photocatalyst surface properties and the ionic nature of the treated compound (Bedia et al. 2018; Reza et al. 2017).

The photocatalytic degradation of dyes and COD removal in mixed dye aqueous solution containing 10 mg/L each of MB, AY, and Rh-B dyes was conducted with 0.1

g/L of catalyst loading under irradiation with two lamps. The effect of pH on the percentage degradation of dyes and COD removal by photocatalytic degradation using BFO@TiO$_{2opt}$ nanocomposite particles is shown in Figure 5.1 (a) to (c).

Figure 5.1 (a) shows the effect of pH on the degradation of dyes in a mixed dye contaminated water containing MB, AY and Rh-B using BFO@TiO$_{2opt}$. It is observed that the degradation of MB dye after 210 min of irradiation is almost complete in the entire pH range. The degradation of MB at the end of 60 min (Figure 5.1 (b)) of irradiation has increased from around 89% to 97% with an increase in pH from 3 to 5. However, a further increase in pH has resulted in a decrease in the percentage of degradation. With 210-minute irradiation, the degradation of AY has increased from 93.5% to 96.7% and degradation of Rh-B has increased from 84.2% to 87.6% when the pH was increased from 3 to 5. However, a further increase in pH has resulted in a decrease in degradation. As observed in Figure 5.1 (c), the COD removal has increased from 80% to 95% with an increase in pH from 3 to 5 and a further increase in pH has resulted in a reduction in COD removal.

The effect of pH on the percentage degradation of dyes and COD removal by photocatalytic degradation using BFO@PANI$_{opt}$ nanocomposite particles is shown in Figure 5.1 (a) to (c). Figure 5.2 (a) shows the effect of pH on the degradation of the dyes a mixed dye contaminated water containing MB, AY and Rh-B using BFO@PANI$_{opt}$ It is observed that the degradation of MB dye after 210 minutes of irradiation is almost complete in the entire pH range. The degradation of MB at the end of 60 min (Figure 5.2 (b)) of irradiation has remained constant at around 100%, with an increase in pH from 3 to 5. However, the further increase in pH has resulted in a decrease in the percentage degradation. With 210-minutes irradiation, the degradation of AY has increased from 95.6% to 97.8% and that for Rh-B had increased from 85% to 89.8% when the pH was increased from 3 to 5. However, a further increase in pH has resulted in a decrease in the degradation. As observed in Figure 5.2 (c), the COD removal has increased from 85% to 97% with an increase in pH from 3 to 5 and a further increase in pH has resulted in a reduction in COD removal.

The results show that with both the catalysts, the individual dye degradation and COD removal from mixed dye solutions increased with increase in pH from 3 to 5 and

with further increase in pH to values greater than pH 5 has resulted in decrease in degradation.

The adsorption of dye onto the catalyst surface is hugely influenced by pH at the point of zero charges (pHpzc) of the prepared catalyst (Bechambi et al. 2015; Ghaly et al. 2017). The pHpzc of PANI and BFO are in the range of 8.0 to 8.2, whereas TiO_2 is 6.8. Thus, at pH values lesser than these, the surface of the catalyst is positively charged and at pH above pHzpc, the surface is negatively charged. The dye molecules may also dissociate into positively or negatively charged ions depending on the pH. So, it appears that at acidic pH conditions the surface and the dye are opposite charged, leading to columbic attraction of the dye molecules onto the catalyst surface followed by adsorption which favours the degradation of the dyes. However, at alkaline pH the dye molecules and the catalyst surface may be similarly charged and thus repel from each other. This reduces the adsorption of the dye on the catalyst and thus the rate of degradation is lowered at alkaline pH.

The specific interactions between the dye and the catalyst surface is reliant upon the configuration of the dye as well as the surface charge of the catalyst. Considering these interactions, specific knowledge on the influence of the pH variation on the dye structure as well as on the surface charge of the catalyst is required.

MB is a cationic dye and hence it is positively charged. Adsorption of MB is generally favoured at pH values above pHpzc of the catalyst, as the surface is negatively charged under those conditions (Neethu and Choudhury 2018). Thus, the adsorption of MB should be favoured at alkaline conditions, as each of the materials involved in BFO@PANI has pHpzc of around 8 and those in BFO@TiO_2 has 8 and 6.8. Many studies have shown that adsorption of MB on TiO_2 or BFO is favoured under alkaline conditions (Azeez et al. 2018; Mohd Azmy et al. 2017; Neethu and Choudhury 2018). However, Soltani and Entezari (Soltani and Entezari 2013b) have observed that adsorption of MB is favoured under acidic conditions. In acid solution, the MB molecules are excited to a triplet state MBH_2^{3+}, MBH_3^{3+} and MBH_3^{2+}. MB^+ basic solutions present one intensive singlet attributed to $\dot{MB}$ radical by reduction of the MB^+ by OH^- ion. The reactivity of the triplet state increases at the same extent with the protonation degree of the corresponding species (Bonneau et al. 1974). Firstly, these

species are excited to their triplet states and the species disappear through two competitive processes on irradiation with visible light: spontaneous deactivation pathways and reduction by electrons provided by the system (Contineanu et al. 2009). Thus, in the presence of light and under acidic pH conditions, the reactivity of protonated states is very high, which results in higher degradation of the dye. Thus, in MB degradation, the role of protonation and increase in reactivity is higher than the role of adsorption on photocatalysis. Thus, pH 5 has been found to yield maximum rate of degradation of MB. In the studies reported by Mohamed et al. (2012), alkaline condition did not favour degradation of MB by $Fe/ZnO/SiO_2$ nanoparticles under visible light.

Since AY is an anionic dye with good solubility, the sodium ion is dissociated in water and leaves the dye molecule with negative charges (Liu et al. 2006). The catalyst surface is positively charged at pH values lesser than pH_{pzc} .Due to the charge difference between negatively charged dye molecules and highly positive charged catalyst, the coupling between dye and catalyst molecules is higher at acidic pH, which in turn increases the electrostatic interactions between the photocatalyst surface and dye anions and lead to adsorption (Sevimli and Kinaci 2002). In contrast, under alkaline and neutral conditions, little adsorption occurs on the surface of the catalyst due to coulombic repulsion between the negatively charged catalyst and negatively charged dye molecule, which decreases the formation of hydroxyl radicals and hence decreases the photocatalytic degradation (Chiou and Li 2002). At higher pH, the concentration of OH− ions would be high enough to cover the surface of the catalyst and hence causes it to be negatively charged. Moreover, the oxidation efficiency of OH- may decrease due to decomposition or deactivation of the catalyst by the formation of complexes hence the production of hydroxyl radical may decrease. The low degradation at alkaline pH may also be due to the formation of a complex in the catalyst that inhibits the reaction between H_2O_2 and catalyst (Deng and Englehardt 2006; Khan et al. 2018).

Though Rh-B is a cationic dye, it has been found from the experiments; acidic pH is favourable for degradation. The pKa value for the aromatic carboxyl group present in the Rh-B molecule is about 4.0. When the pH of the solution is < 4, the carboxylic acid groups can be ionized and the zwitterion form of Rh-B is formed (Merka et al. 2011). The zwitterion form of Rh-B in water leads to an increase in the

formation of dimers from monomers of Rh-B due to electrostatic interaction between carboxylic and xanthene's groups of monomers. The smaller monomeric Rh-B may be adsorbed on the surface of the catalyst readily than the dimeric form, thus leading to a higher rate of adsorption at acidic pH conditions. Under pH values of above pH 5, the dimers formed may block the active sites. The density of the charges is also reduced due to the mutual interactions between two monomers, and under this condition, the Rh-B removal might be inhibited (Soltani and Entezari 2013b). In the present study, pH 5 has been considered as an optimum for the photocatalytic degradation of mixed dye aqueous solution under visible light irradiation using BFO@TiO$_{2opt}$ and BFO@PANI$_{opt}$ nanocomposite particles, as pH 5 yielded maximum degradation of all the three dyes in the mixed dye solution and in terms of COD removal. The optimum pH for degradation of individual dyes from mixed dye contaminated water cannot be solely based on the individual dye-catalyst surface interaction. The surface charges of the nanocomposite catalyst surface may vary with solution pH and the protonation or deprotonation of dye molecules would also depend on the mutual interaction among the dyes. In mixed dye aqueous solution, the adsorption process may not be solely based on electrostatic interaction. Other adsorption mechanism like chemisorption may occur due to interaction between the functional groups in the molecules of different dyes. The mutual interaction between the dye molecules is also pH dependent. Li et al. (2017) through their studies on adsorption of methylene blue and MO from mixed solution on a zirconium-based adsorbent, have found that the presence of one dye influences the adsorption of the other dye and the extent of enhancement in adsorption is pH dependent. Presence of other dyes may inhibit or enhance the protonation of a dye and thus optimum pH is dependent on the mutual interaction effect of the dyes and the charges on the catalyst surface. Chomkitichai et al. (2019) have studied the degradation of MB and Rh-B from mixed dye solution using Multi-Phase BiVO$_4$ photocatalyst under UV irradiation. They found that degradation of both MB/Rh-B increased as the pH increased to neutral pH and reduced when the solution was alkaline (Chomkitichai et al. 2019). In the present study, maximum COD removal and dye degradation from mixed dye solutions are achieved at pH 5. Thus pH 5 is the optimum pH for photocatalysis of mixed dye system containing MB, AY and Rh-B using BFO@TiO$_{2opt}$ and BFO@PANI$_{opt}$ nanocomposite particles.
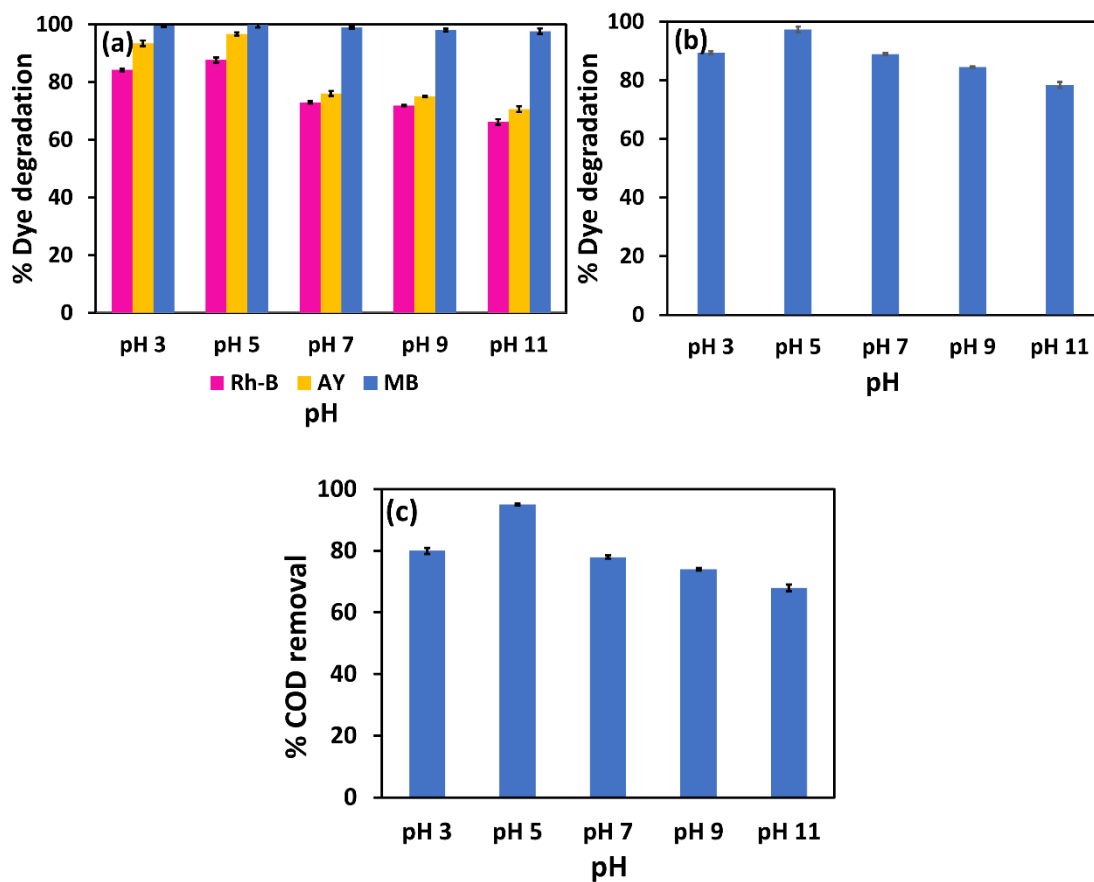
Figure 5.1: Effect of initial pH on (a) dye degradation at 210 min irradiation time (b) Percentage degradation of MB at 60 min (b) COD removal at 210 min irradiation time, from a mixed dye aqueous solution. Condition; catalyst concentration-0.1g/L (BFO@TiO$_{2opt}$); concentration of each dye -10 mg/L.
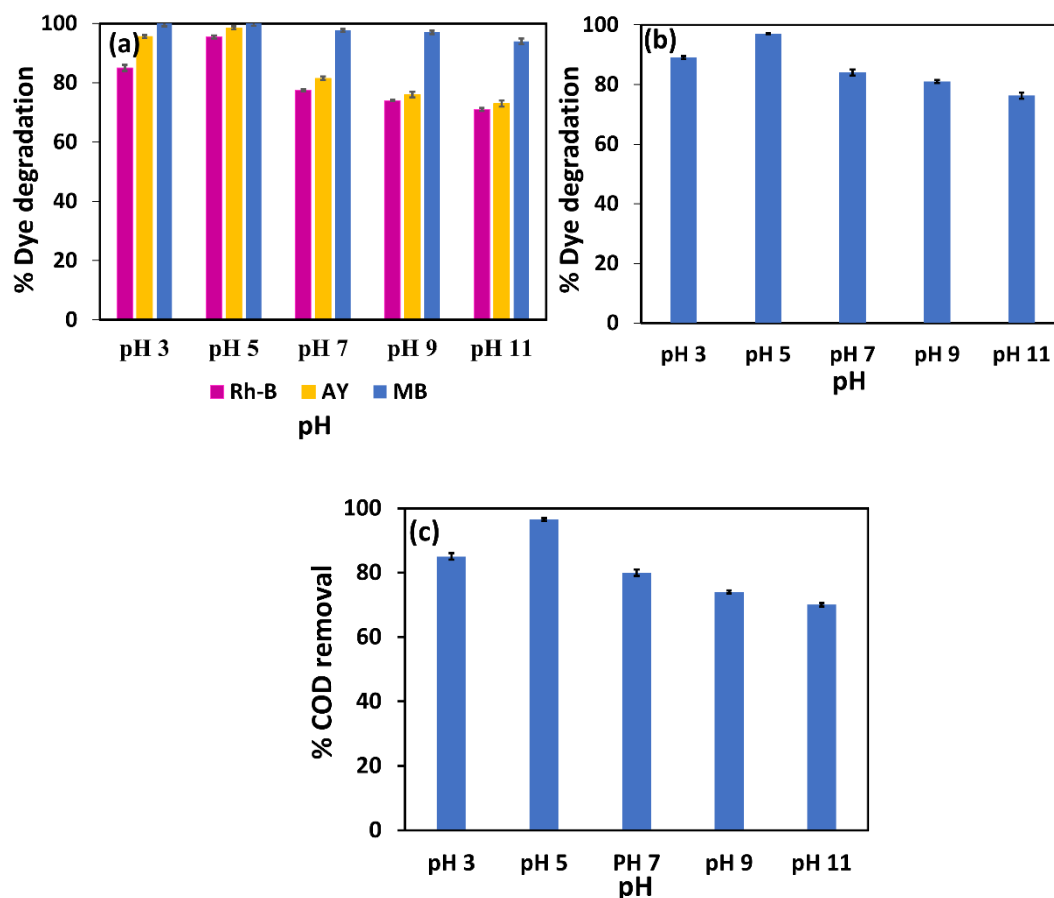
Figure 5.2: Effect of initial pH on (a) dye degradation at 210 min irradiation time (b) Percentage degradation of MB at 60 min (b) COD removal at 210 min irradiation time, from a mixed dye aqueous solution. Condition; catalyst concentration-0.1g/L (BFO@PANI_{opt}); concentration of each dye-10 mg/L

5.1.2 Effect of catalyst loading

The rate of photocatalytic degradation depends on the nature and concentration of photocatalyst and the pollutant concentration (Habibi and Vosooghian 2005). Therefore, with a given catalyst it is necessary to find the optimum catalyst loading for the photocatalytic process since the reaction rate is a function of catalyst loading in photocatalytic oxidation process (San et al. 2001; Saquib and Muneer 2002). The effect of catalyst loading with BFO@TiO_2opt and BFO@PANI_{opt} on the visible light mediated photocatalytic degradation of dyes in mixed dye contaminated water containing 10 mg/L of each dye at optimum pH 5, was studied by varying the concentration of catalyst from 0.1 to 0.5 g/L and with irradiation using two lamps. The

effect of catalyst loading on the percentage degradation of dyes and COD removal from mixed dye contaminated water containing MB, AY, and Rh-B are shown in Figure 5.3 (a and b) and Figure 5.3 (c) respectively for BFO@TiO$_{2opt}$.

The effect of catalyst loading on percentage degradation obtained at the end of 210 min of irradiation time is shown in Figure. 5.3 (a) The percentage degradation of MB after 210 min irradiation was almost complete at all the catalyst loading conditions, So, the degradation of at the end of 60 min was compared as shown in Figure 5.3 (c). The effect of catalyst loading on percentage COD removal (mg/L) after 210 minutes irradiation is presented in Figure 5.3 (c)

As shown in Figure 5.3 (a and b) and Figure 5.3 (c), the percentage dye degradation and COD levels increased as catalyst loading increased from 0.1g/L to 0.3 g/L. However, the reduction in dye degradation and COD level are observed at 0.4 and 0.5 g/L loading by BFO@TiO$_{2opt}$.

The effect of catalyst loading on the percentage degradation of dyes and COD removal from mixed dye contaminated water containing MB, AY, and Rh-B are shown in Figure 5.3 (a and b), and Figure 5.3 (c) respectively for BFO@PANI$_{opt}$. The effect of catalyst loading on percentage degradation obtained at the end of 210 min of irradiation time is shown in Figure. 5.4 (a). The percentage degradation of MB after 210 min irradiation was almost complete at all the catalyst loading conditions, So, the degradation of at the end of 60 min was compared as shown in Figure 5.3 (c). The effect of catalyst loading on percentage COD removal (mg/L) after 210 minutes irradiation is presented in Figure 5.4 (c). As shown in Figure 5.4 (a and b) and Figure 5.4 (c), the percentage dye degradation and COD levels increased as catalyst loading increased from 0.1g/L to 0.2 g/L. However, the reduction in percentage dye degradation and COD level is observed at 0.3 to 0.5 g/L loading by BFO@PANI$_{opt}$.

The increase in the catalyst loading leads to an increase in the number of active sites on the photocatalyst due to the increase in the total surface area,, which in turn increases the rate of formation of active species (Barakat et al. 2005; Ghaly et al. 2017). The increase in the degradation rate may be attributed to the fact that, as the loading of BFO@TiO$_{2opt}$ or BFO@PANI$_{opt}$ is increased, the active sites for the adsorption of dye molecules also increase, which in turn increases the release of electron and hole pairs,

thus increasing the formation of hydroxyl radicals, and hence, an improvement in the photocatalytic reaction rate occurs.

With the additional increase in catalyst loading from 0.4 to 0.5 g/L and higher for BFO@TiO$_{2opt}$, and 0.3 to 0.5 g/L and higher for BFO@PANI$_{opt}$, the percentage degradation and COD have decreased. Although the number of active sites in solution will upsurge with catalyst loading, a saturation point occurs beyond which light penetration is hindered because of the shielding effect of suspended catalyst particles. When the catalyst loading exceeds the limiting value, the dye degradation rate would decrease (Barakat et al. 2005; Ghaly et al. 2017) due to the increase in turbidity and light scattering at high photocatalyst concentrations which lead to a decrease in the light penetration in the solution (Pourahmad et al. 2010; Sakthivel et al. 2003). At higher catalyst loading, agglomeration of particles may take place due to increased collisions of the particles resulting in a reduction in surface area available for light absorption (Eskizeybek et al. 2012; Pourahmad et al. 2010; Wong and Chu 2003). Hence, a decrease in photocatalytic degradation rate was observed at high catalyst loading. At high catalyst concentrations, many a number of active sites on the photocatalyst surface may become unusable because of the decreased light penetration, the increased light scattering and the loss in surface area occasioned by agglomeration (particle-particle interactions). The relation between the two different phenomena of increased number of surface-active sites with higher loading and decrease in usable surface sites due to light penetration. light scattering and agglomeration effects results in an optimum catalyst loading for photocatalytic degradation (Adesina 2004; Ahmed et al. 2011). Therefore, the optimum amount of catalyst loading is found to be 0.3 g/L for BFO@TiO$_{2opt}$ and 0.2 g/L for BFO@PANI$_{opt}$ for the degradation of mixed dyes with initial dye concentrations of 10 mg/L each. Similar trend of increase in degradation efficiency with increase in catalyst loading upto an optimum value and further increase in catalyst loading resulting in decrease in degradation has been observed by many researchers in their studies on photocatalytic degradation (Daneshvar et al. 2004; Neppolian 2002; SohrabI and Ghavami 2008; Zhang et al. 2002). It is important to add an optimum amount of catalyst to avoid unnecessary excess catalyst and to ensure total absorption of photons for efficient photocatalytic degradation (Herrmann 1999).

However, as reported by Herrmann (1999) optimum catalyst loading is dependent on the initial concentration of the dye.

The optimum catalyst loading for BFO@PANI$_{opt}$ is lower than that for BFO@TiO$_{2opt}$. At optimum loading of 0.3 g/L with BFO@TiO$_{2opt}$, MB is completely degraded with 97% AY and 89% Rh-B degradation. COD removal efficiency of 96.7% could be achieved at this catalyst loading. At optimum loading of 0.2 g/L with BFO@ PANI$_{opt}$, MB and AY were completely degraded and 96% Rh-B degradation was achieved with COD removal efficiency of 97%. The BFO@PANI$_{opt}$ shows superior photocatalytic dye degradation and COD removal compared to BFO@TiO$_{2opt}$ nanocomposite with lower catalyst loading.
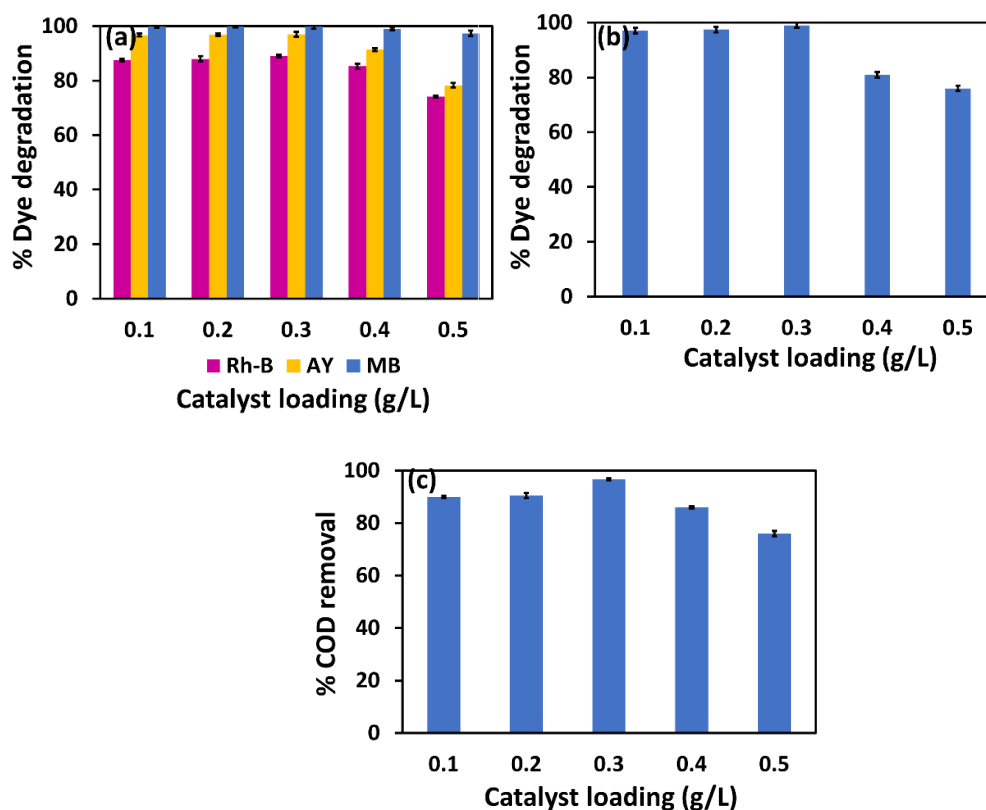
Figure 5.3: Effect of catalyst loading on (a) percentage degradation of dyes at irradiation time of 210 min (b) percentage degradation of MB at 60 min (c) COD removal at irradiation time of 210 min from mixed dye contaminated water Condition; Catalyst used: BFO@TiO$_{2opt}$; initial pH of the dye solution-pH 5; concentration of each dye -10 mg/L.
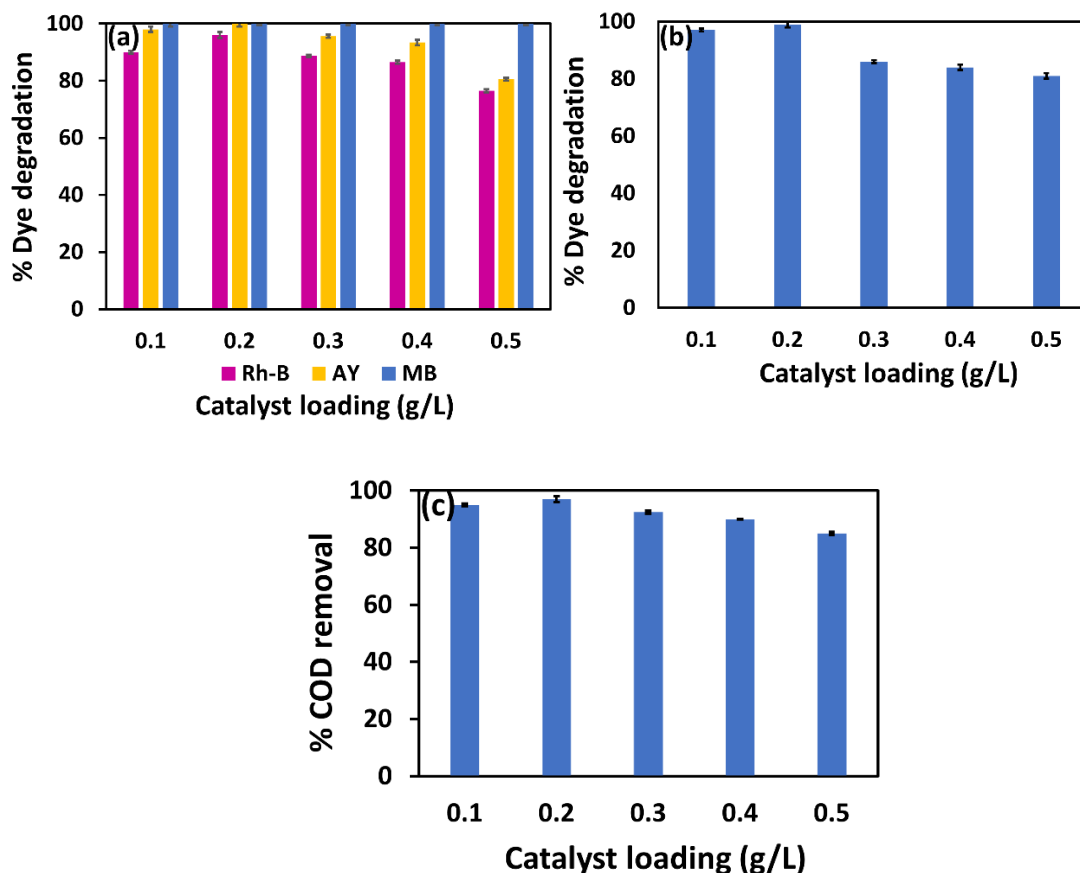
Figure 5.4: Effect of catalyst loading on (a) percentage degradation of dyes at irradiation time of 210 min (b) percentage degradation of MB at 60 min (c) COD removal at irradiation time of 210 min from mixed dye contaminated water Condition; Catalyst used: BFO@PANI_{opt}; initial pH of the dye solution-pH 5; concentration of each dye -10 mg/L.

5.1.3 Effect of light intensity

The efficiency of photocatalytic degradation of the constituents in the solution strongly depends on the intensity of the light used for irradiation (Reza et al. 2017). An increase in the intensity increases the occurrence of number of photons per unit area of the dye solution. The higher the number of photons interacting with the dye molecules, the higher the number of dye molecules that degrade per minute. Light intensity distribution in the reactor determines the pollutant degradation (Pareek et al. 2008). Formation of electron-hole is the initial step in the photochemical reaction and is dependent on the light intensity, and it governs the rate of photocatalysis.

166

The effect of light intensity on the photocatalytic degradation of dyes and COD removal from mixed dye contaminated water containing 10 mg/L each of MB, AY and Rh-B is shown Figure 5.5 (a and b) for BFO@TiO$_{2opt}$ and Figure 5.6 (a and b) for BFO@PANI$_{opt}$ respectively. These experiments were conducted in batch reactor with the optimum catalyst loading of 0.3 g/L and 0.2 g/L of BFO@TiO$_2$opt and BFO@PANI$_{opt}$ respectively, by changing the number of lamps from one to four. The positioning of the lamps around the reactor is presented in Section 3.7. One to four lamps (each of 18 W power) were used. The average illuminance (lux) at the reactor wall were measured using lux meter and the average intensity was calculated as described in Section 3.7.

The effect of light intensity in the photocatalytic degradation of dyes in mixed dye contaminated water containing MB, AY, Rh-B is shown in Figure 5.5 (a) and 5.6 (a) for BFO@TiO$_{2opt}$ and BFO@PANI$_{opt}$ respectively. The percentage of COD removal (mg/L) is presented in Figure 5.5 (b) and 5.6 (b) for BFO@TiO$_{2opt}$ and BFO@PANI$_{opt}$ respectively. These results indicate that photocatalytic degradation of the dyes have enhanced with the increase in the intensity of light from 146 μW/cm^2 (1 lamp) to 263 μW/cm^2 (2 lamps). However, with further increase in light intensity to 292 μW/cm^2 (3 lamps) and to 351 μW/cm^2 (4 lamps), there was no further change in the degradation efficiency. At lower light intensity of less than 263 μW/cm^2 (2 lamps), with increase intensity the percentage degradation has increased. An increase in the light intensity would increase the number of photons arrested per unit area per unit time of the photocatalyst surface, thus leading to enhanced rate of electron-hole pair separation and the formation of free radicals. The electron-hole formation rate is predominant and hence, electron-hole recombination rate may be negligible under these conditions, thereby increasing the rate of degradation of the dyes. However, as the light intensity increases further, the number of active sites remains the same. Thus, the reaction rate only spreads a certain level even when the light intensity continues to increase. Thus, increase in intensity does not show any further effect on the rate of photocatalysis. At low light intensity regime, the reaction is governed only by the flux of absorbed photons. The effect of factors which influence the transfer of electrons from the photocatalyst is negligible. If the light intensity is very high, the photocatalytic reaction is limited by intrinsic reaction kinetics. All of the reactive sites are completely active

as a result of high photon flux (Bloh 2019). Thus, in the present study for the reactor set up of two lamps of 18 W each with total 36 W power and imparting light intensity of 263 μ W/cm^2 can be considered as the optimum light intensity. Hung and Yuan (2000) in their studies on the effect of the irradiation intensity of black light lamps in the range of 0–114W/m^2, enhanced the Rhodamine B decolorization. Liu et al. (2006) have found that AY decolorization increased with increasing light intensity in the range 1.24 μW/m^2 -3.15 μW/m^2. The increase in light intensity resulting in enhancement of decolorization rate has been reported by Sakthivel et al. (2003) and So et al. (2002). These results show that the range of intensities in which the dye degradation enhances depends on the type of dye, type and amount of catalyst, the type of lamps used, the photocatalytic reactor type, design and the position of the lamp. Many researchers have also observed that the degradation efficiency is independent of light intensity at high light intensities (Anku et al. 2016; Chanathaworn et al. 2012; Ollis et al. 1991). At higher intensities, there are more photons per unit time and unit area; thus, the chances of photon activation on catalyst surface upsurge and so the photocatalytic power is stronger. However, as the light intensity upsurges, the number of activation sites remains the same. Thus, the reaction rate only spreads a certain level even when the light intensity continues to increase (Ollis et al. 1991).

Thus, in the present work, a maximum degradation of the dyes and COD removal could be achieved with two lamps. MB is completely degraded with 97% AY and 89% Rh-B degradation and COD removal efficiency of 96.7% could be achieved by BFO@TiO$_{2opt}$. MB and AY were completely degraded and 96% Rh-B degradation was achieved with COD removal efficiency of 97% by BFO@PANI$_{opt.}$ These results indicate that the intensity of 263 μW/cm^2 imparted by two lamps with total 36 W power is sufficient and economically advisable.
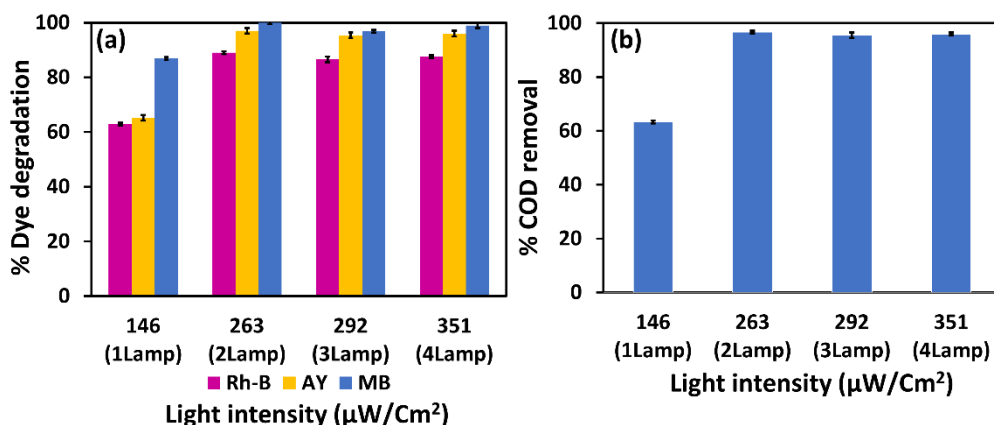
Figure 5.5: Effect of Light intensity on the (a) percentage degradation of dyes (b) percentage COD removal from the mixed dye contaminated water. Condition; pH of the dye solution-pH 5; catalyst concentration-0.3 g/L (BFO@TiO$_{2opt}$); dye concentration 10 mg/L; irradiation time-210 min
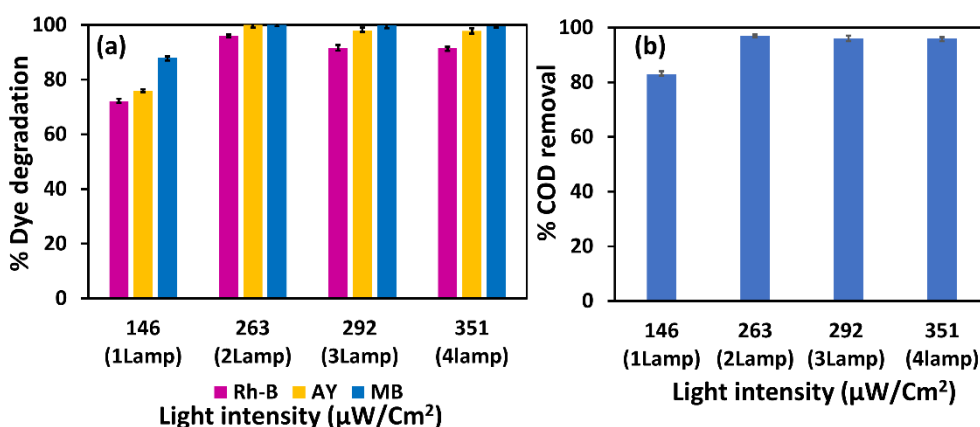
Figure 5.6: Effect of Light intensity on the (a) percentage degradation of dyes (b) Percentage COD removal from the mixed dye contaminated water. Condition; pH of the dye solution-pH 5; catalyst concentration-0.2g/L (BFO@PANI$_{opt}$); dye concentration 10 mg/L; irradiation time-210 min

5.1.4 Effect of dye loading

Coloured wastewater from industries generally contains a mixture of many dyes rather than a single dye. Presence of one dye may affect the degradation of the other dye in mixed dye contaminated water. As the industrial effluent may contain dyes of varying composition, studies on the effect of dye concentration is important to understand how much degradation is achieved and whether the dye concentrations or COD levels in the

169

effluent after the treatment attains a value lower than that prescribed by regulatory standards. Such a study would also help in understanding the kinetics of degradation and in the design of photocatalytic reactors. When different dyes co-exist in wastewater, the presence of one dye may influence the rate of degradation of the other dye and it may depend on the concentration of each of the dyes. Higher dye concentrations may also reduce the rate of redox reactions during the photocatalysis and thus reduce the degradation efficiency. It is important to investigate, what is the residual concentration achievable with the given influent dye concentrations to the reactor, so that the reactor may be suitably designed and reaction parameters may be appropriately selected. To understand the effect of concentrations of individual dyes in the solution and to study the effect of presence of one dye on the degradation of other dyes in the mixed dye contaminated water containing MB, AY and Rh-B, photocatalysis experiments were carried out with an aqueous solution of these dyes using BFO@TiO$_{2opt}$ and BFO@PANI$_{opt}$ nanocomposite particles.

5.1.4.1 Effect of dye loading on the percentage degradation of dyes from mixed dye contaminated water using BFO@TiO$_{2opt}$ and BFO@PANI$_{opt}$ nanocomposite particles.

The photocatalytic degradation experiments were conducted with mixed dye aqueous solution containing MB, AY and Rh-B by varying the concentration of dyes as indicated in Table 5.1 and 5.2, with 0.3 g/L of BFO@TiO$_{2opt}$ and 0.2 g/L of BFO@PANI$_{opt}$ as photocatalyst respectively. Totally 27 experiments were conducted with mixed dye aqueous solutions containing the three dyes, by varying the individual dye concertation's under visible light irradiation with two lamps and initial pH 5. Experiments were also conducted with aqueous solutions containing two dyes and single dye, and the results were compared with those containing all the three dyes in order to study the effect of presence of one dye on the degradation of other dyes. The percentage degradation of each dye and the COD removal obtained under each set of conditions of concentrations were determined and are presented in Table 5.1 and 5.2, for BFO@TiO$_{2opt}$ and BFO@PANI$_{opt}$ nanocomposite particles respectively.

Table 5.1: Effect of dye loading and concentration on the percentage dye degradation from mixed dye contaminated water with BFO@TiO$_{2opt}$ nanocomposite particles Condition; dye solution-pH 5; catalyst concentration 0.3 g/L; irradiation time-210 min under visible light.

SI no	Initial concentration(mg/L) AY, MB, Rh-B	Percentage degradation			Percentage COD removal
		AY	MB	Rh-B	
1	10,10,10	97	100	89	96.7
2	10,10,20	91	96	76	81
3	10,10,30	86	94	71	80
4	10,20,10	95	94	88	89.6
5	10,20,20	91	94	75	80
6	10,20,30	86	90	70	79
7	10,30,10	89	88	86	85
8	10,30,20	88	86	74	80
9	10,30,30	84	83	68	76

10	20,10,10	84	99	85	85
11	20,10,20	80	94	73	79
12	20,10,30	80	91	71	78
13	20,20,10	82	93	84	84
14	20,20,20	81	92	72	77
15	20,20,30	78	90	69	76
16	20,30,10	81	86	73	80
17	20,30,20	80	83	70	77
18	20,30,30	78	81	67	74
19	30,10,10	78	97	84	84
20	30,10,20	76	96	74	79
21	30,10,30	75	95	72	78
22	30,20,10	76	93	83	84
23	30,20,20	74	93	73	78
24	30,20,30	73	90	71	77
25	30,30,10	75	85	82	75

26	30,30,20	74	83	70	74
27	30,30,30	72	80	67	70
28	10,10,0	100	100	-	95
29	10,0,10	97	-	95	93
30	0,10,10	-	100	91	94
31	10,0,0	100	-	-	96
32	0,10,0	0	100	-	97
33	0,0,10	-	-	100	95

Table 5.2: Effect of dye loading and concentration on percentage dye degradation from mixed dye contaminated water with BFO@PANI$_{opt}$ Condition; Dye solution-pH 5; catalyst loading -0.2 g/L; irradiation time-210 min under visible light.

SI no	Initial concentration AY, MB, Rh-B	Percentage degradation			Percentage COD Removal
		AY	MB	Rh-B	
1	10,10,10	100	100	96	97
2	10,10,20	93	99.7	77.5	85
3	10,10,30	91.5	99.2	74.1	82
4	10,20,10	99	95	91	94.6
5	10,20,20	90	94	76	83
6	10,20,30	89	93	70	80
7	10,30,10	98	90	90	93
8	10,30,20	88	90	76	82
9	10,30,30	86	86	67.4	79
10	20,10,10	84.5	100	89	88.4
11	20,10,20	84	100	77	82

12	20,10,30	82	99	74	81
13	20,20,10	83.5	94	85	86
14	20,20,20	83	93	75.5	79
15	20,20,30	82	92	70	78
16	20,30,10	83	90	76	80
17	20,30,20	80	88	75	78
18	20,30,30	78	85	67	76
19	30,10,10	82.6	100	89	87
20	30,10,20	82	100	78	82
21	30,10,30	80	96	75	80
22	30,20,10	81.5	94	88	85
23	30,20,20	80	93	76	78
24	30,20,30	78	90	73	78
25	30,30,10	82	90	87	78
26	30,30,20	82	88	71	77
27	30,30,30	70	86	68	74

28	10,10,0	100	100	-	95
29	10,0,10	98	-	95	94.5
30	0,10,10	-	100	97	95
31	10,0,0	100	-	-	96
32	0,10,0	-	100	-	97.5
33	0,0,10	-	-	100	96

The Figures 5.7 (a) and 5.8 (a) show the percentage degradation of MB, AY and Rh-B when they are present as single dye, a combination of two dyes and three dyes with BFO@TiO$_{2opt}$ and BFO@PANI$_{opt}$ as catalyst. Figure.5.7 (a) and Figure.5.8 (a) also show the effect of presence of other dyes on the degradation of a target dye by photocatalysis using BFO@TiO$_{2opt}$ and BFO@PANI$_{opt}$. Figure.5.7 (a) and Figure.5.8 (a) reveal that the percentage degradation of AY has reduced by the presence of either MB or Rh-B in the aqueous solution of two dyes. The percentage degradation of Rh-B has reduced by the presence of either MB or AY in mixed dye solution containing two dyes. The percentage degradation of AY and Rh-B gets further reduced when they are present in the aqueous solution containing all the three dyes. Thus, percentage degradation of AY and Rh-B reduce, when they are present in combination of two or three dyes, in comparison to that when they are present as single dye. However, the degradation of MB is not affected by the presence of one or two other dyes. Figure 5.7 (b) and Figure 5.8 (b) show the effect of presence of other dyes on the COD removal by photocatalysis using BFO@TiO$_{2opt}$ and BFO@PANI$_{opt.}$ As observed in Figure 5.7 (b) and Figure 5.8 (b), the percentage COD removal decreases marginally by the presence of one or two dyes when the dyes coexist in the solution. These results indicate that the presence of one or two additional dyes would decrease the degradation of a target dye as well as the COD removal. The photocatalysis rate depends on the rate of adsorption. Thus, the mutual effect of enhancement or inhibition in adsorption of dyes from mixed dye solutions will have a tremendous influence on the rate of photocatalysis. The presence of one dye in a solution may affect the adsorption of the other dye on the catalyst. Allen and Koumanova (2005) have specified that the presence of two or more dyes in the solution can and will have an effect on the amount of the dyes being adsorbed. They reported that the amount of adsorption of any dye get to reduce or increase in the presence of second or third dye. The extent of this effect changes with specific dye and also with those factors which influence the adsorption of dyes from aqueous solution of mixture of dyes. The interactions between dyes may mutually enhance or inhibit the adsorption capacity. The interaction may lead to antagonism or synergism effect in adsorption. Antagonist effect or antagonism is a phenomenon wherein two or more components in combination have an overall effect that is below the sum of their individual effect. Synergism is the effect when chemical

substance interacts resulting in an overall effect that is greater than the sum of individual effect of any of them. The results obtained in the present study show that in the mixed dye solution containing MB, AY and Rh-B, the photocatalytic degradation efficiency with respect to any target dye has decreased in the presence of other dyes. The reasons for reduced degradation, may be the following: (i) presence of other dyes might have inhibited the adsorption or photocatalytic degradation of the target dye or (ii) addition of one or more of other dyes increases the total number of dye molecules in the solution. The active sites on the catalyst being limited, the degradation proceeds with a low rate (iii) addition of one or more of other dyes would lead to increase in the number of dye molecules in the solution leading to hindering of light penetration to the catalyst surface.

The effect of initial dye concentration on the photocatalytic degradation of dyes in mixed dye contaminated water containing MB, AY, Rh-B is shown in Figure 5.9 (a-i) and 5.10 (a-i) for BFO@TiO$_{2opt}$ and BFO@PANI$_{opt}$ respectively. The dye loading was varied by changing the concentration in the range of 10, 20, 30 mg/L. Hence, twenty-seven different set of experiments with varying level of concentrations were conducted. The percentage of COD removal (mg/L) is presented in Figure 5.11 (a-c). and 5.12 (a-c) for BFO@TiO$_{2opt}$ and BFO@PANI$_{opt}$ respectively. As observed in Figure 5.9 (a-i) and 5.10 (a-i), the percentage degradation of any dye decreases with the increase in its own initial concentration, while keeping the initial concentrations of the other two dyes constant. It is also observed that the percentage degradation of any dye decreases with the increase in concentration of one or both of the other two dyes, while its own initial concentration is kept constant. As observed in Figure 5.11 (a-c) and 5.12 (a-c), the COD removal also decreases with increase in the concentration of one or more dyes. The initial concentration of dye plays a significant role in the dye degradation efficiency. The chance of formation of OH$^-$ radicals on the catalyst surface and OH$^-$ radicals reacting with dye molecules determine the degradation rate. However, the dye molecules should adsorb onto the surface of the catalyst before they can be degraded by photocatalysis. The rate of adsorption of the dye molecules governs the rate of photocatalysis. Generally, the photocatalysis rate is adsorption controlled.

As the case in the present study, the reduction in degradation efficiency with the increase in dye concentration occurs due to several reasons. Large dye concentration hinders the light from reaching the catalyst surface. (Liu et al. 2006; Saggioro et al. 2011; Segne 2011). It reduces the path length of the photons (Davis et al. 1994; Saggioro et al. 2011). As the initial concentrations of the dye increases, a significant amount of light is absorbed by the dye molecules rather than the catalyst. Hence, the penetration of light to the surface of the catalyst decreases (Augugliaro et al. 2012; Daneshvar et al. 2004; Kiriakidou et al. 1999; Saquib et al. 2008). The generation of hydroxyl radicals reduces since the active sites are surrounded by the dye molecules (Grzechulska and Morawski 2002),which prevent the light energy from reaching the catalyst surface. When there are multiple dyes in solution, it may lead to multi-layered adsorption of dye molecules. These adsorbed dye molecules on the photocatalyst also inhibits the reaction of adsorbed molecules with the photo-induced positive holes or hydroxyl radicals, since there is no direct contact of the nanoparticles with them (Daneshvar et al. 2004; Grzechulska and Morawski 2002; Kiriakidou et al. 1999; Poulios et al. 2000). Again, as the initial concentration of the dye increases, the requirement of catalyst surface needed for the degradation also increases. Since illumination time and amount of catalyst are constant, the OH^- radical (primary oxidant) formed on the surface of the catalyst is also constant, while the number of dye molecules in solution is higher (Mengyue et al. 1995).This would reduce the rate of photocatalytic degradation of dyes. These results show that the photocatalysis rate with respect to a target dye depends on its concentration, the presence and nature of other dyes and their concentrations.
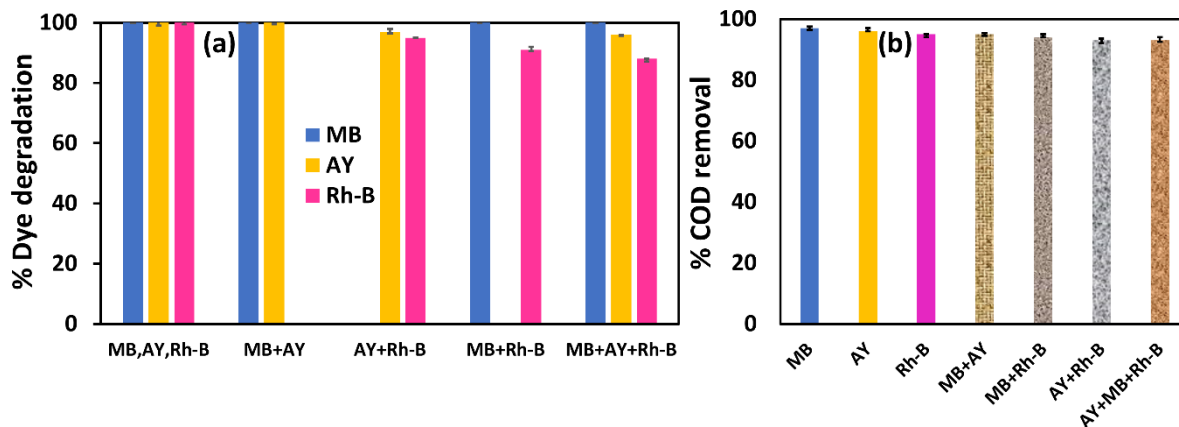
Figure 5.7: Effect of presence of other dyes on (a) the percentage degradation of a target dye and (b) percentage COD Removal by photocatalysis. Condition; dye solution-pH 5; catalyst concentration-0.3 g/L (BFO@TiO$_{2opt}$) concentration of each dye 10mg/L; irradiation time-210 min.
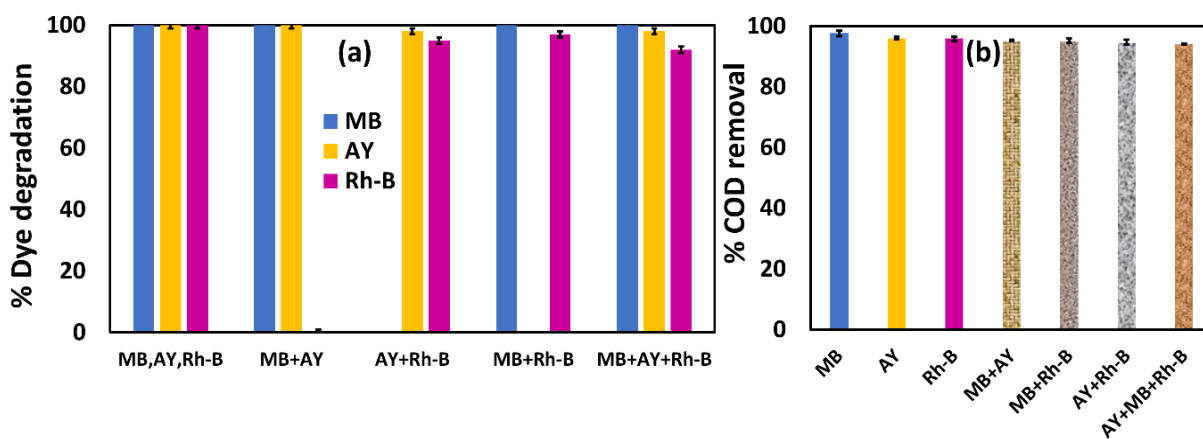
Figure 5.8: Effect of presence of other dyes on (a) the degradation of a target dye by photocatalysis on percentage dye degradation and (b) Percentage COD removal. Condition: Dye solution-pH 5; catalyst concentrtion-0.2 g/L (BFP3$_{opt}$); concentration of each dye 10 mg/L; irradiation time-210 min.
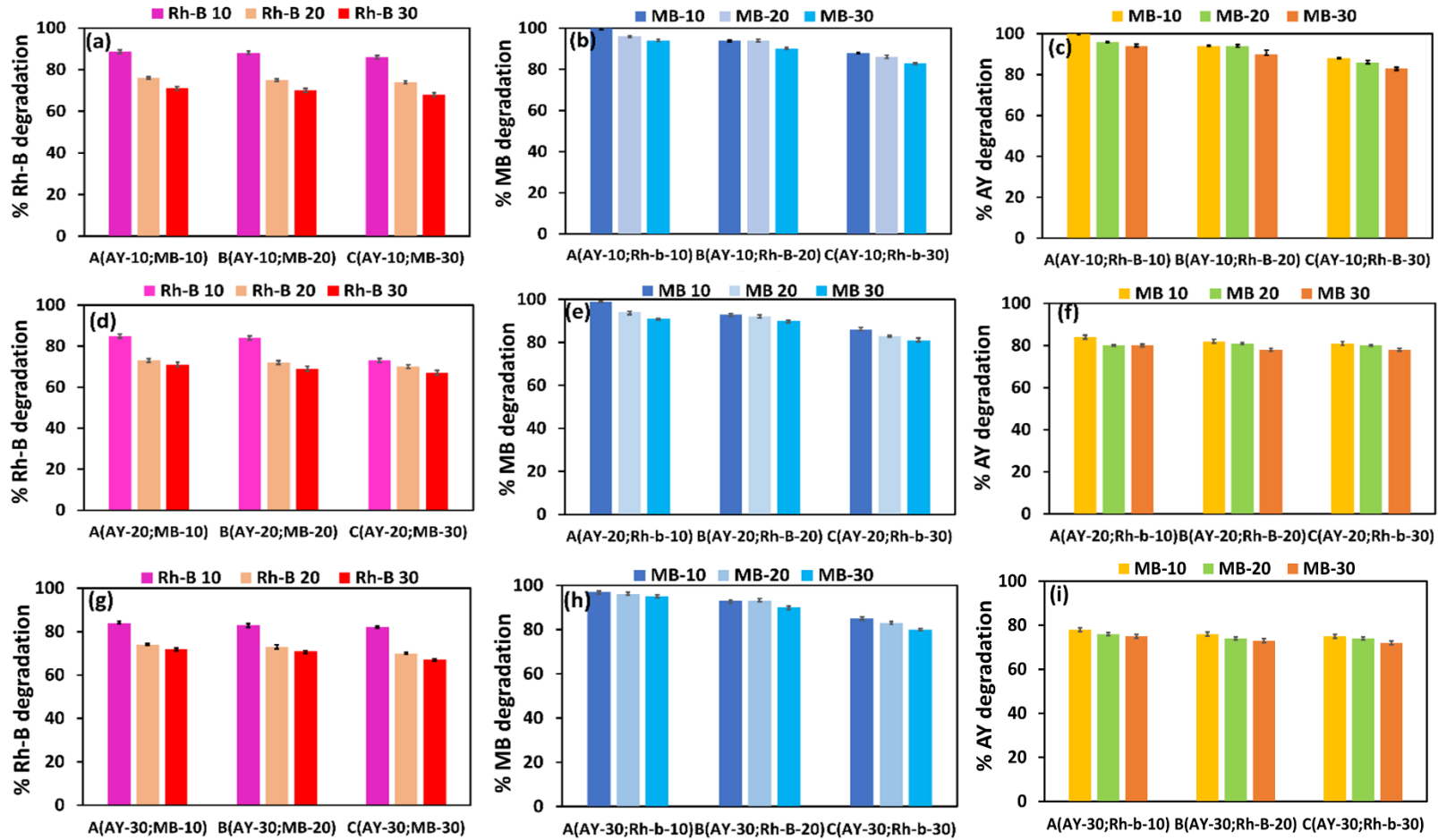
Figure 5.9: (a-i) Effect of dye concentration on percentage dye degradation from mixed dye contaminated water. Condition; dye solution-pH 5; catalyst concentration-0.3 g/L (BFO@TiO$_{2opt}$); irradiation time-210 min.
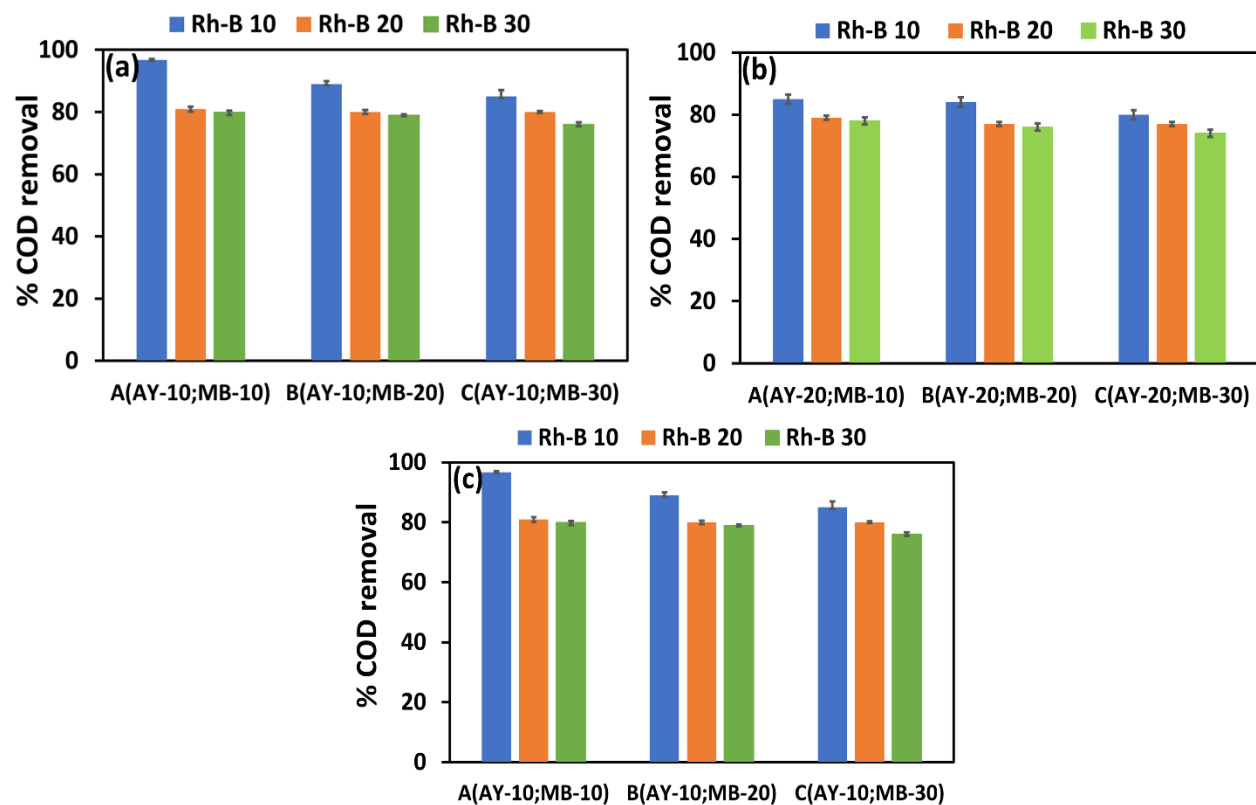
Figure 5.10: (a-c) Effect of dye concentration on percentage COD removal from mixed dye contaminated water. Condition; dye solution-pH 5; catalyst concentration-0.3 g/L (BFO@TiO$_{2opt}$); irradiation time-210 min
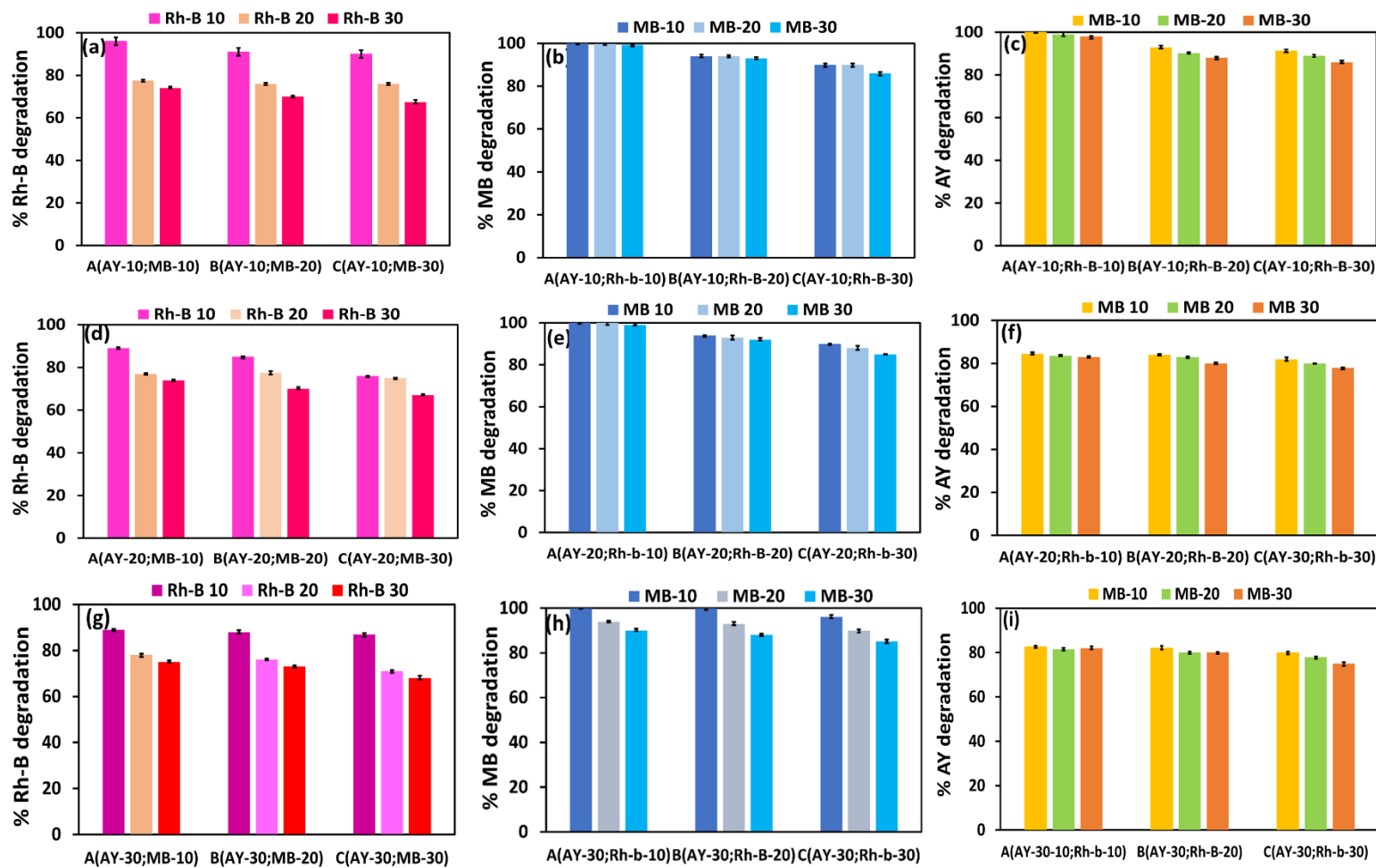
Figure 5.11: (a-i) Effect of dye concentration on percentage dye degradation from mixed dye contaminated water. Condition: dye solution-pH 5; catalyst concentrtion-0.2 g/L (BFP3$_{opt}$); irradiation time-210 min.
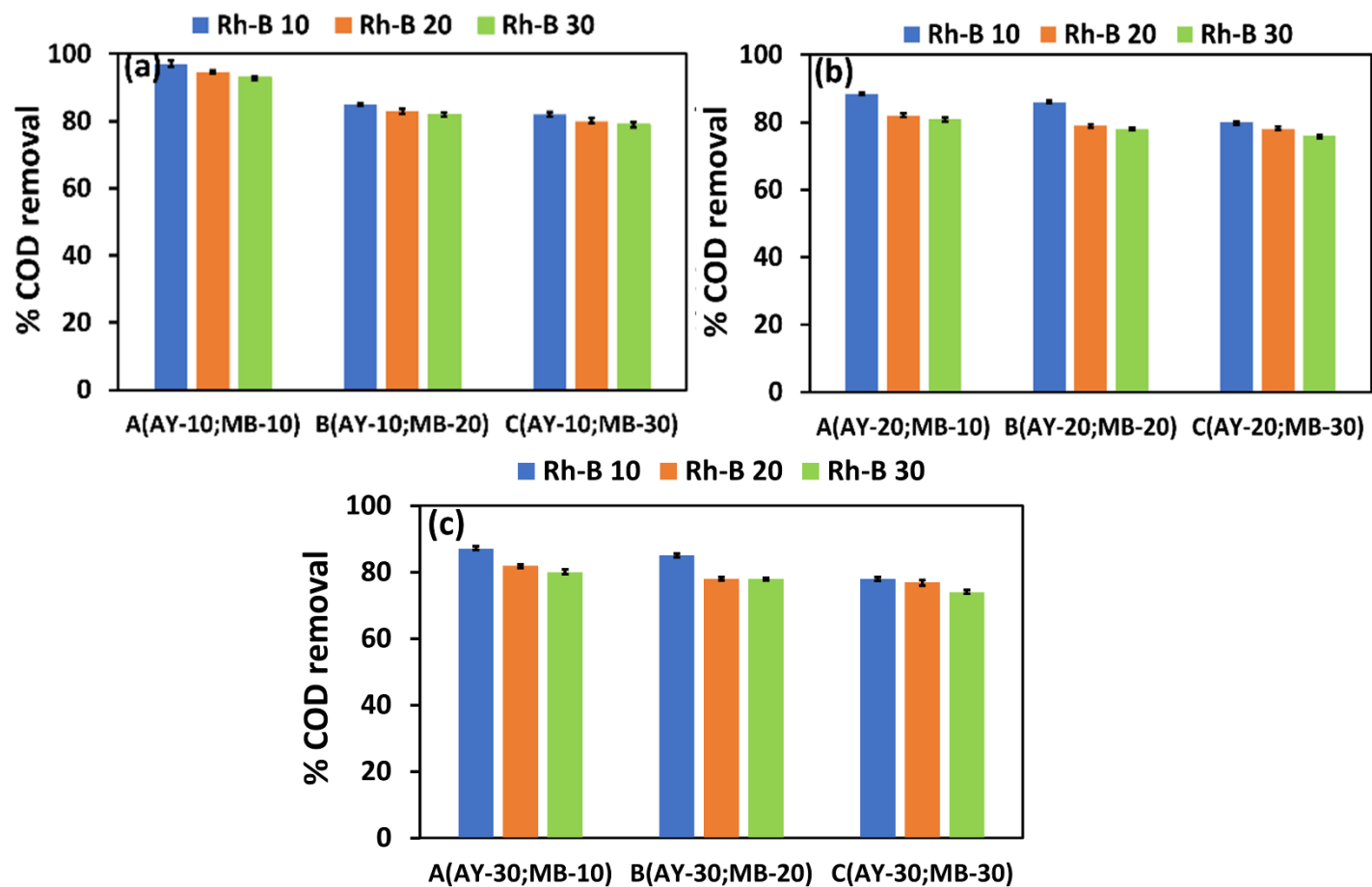
Figure 5.12: (a-c) Effect of dye concentration on percentage COD removal from mixed dye contaminated water. Condition: dye solution-pH 5; catalyst concentrtion-0.2 g/L (BFP3$_{opt}$); irradiation time-210 min.

5.2 Photocatalytic activity of BFO@TiO$_{2opt}$ and BFO@PANI$_{opt}$ nanocomposite particles under solar light irradiation

Solar spectrum consists of light in wavelength range of 100 nm to 1 micrometre. Large portion of solar light consists of low energy, longer wavelength visible light and Infrared radiations. 42.3% of solar light comprises visible range wavelength (Gajjar 1989). Too low wavelength may result in accidental side reactions. Too low wavelength means more energy, but not more photons. The photocatalyts synthesized in the present work, have been found to be effective under visible light irradiation. These photocatalysts BFO@TiO$_{2opt}$ and BFO@PANI$_{opt}$, have low band gap energy of 1.2 eV and 1.4 eV respectively, with absorption edges extending to NIR region. Thus, they may be used to harness solar energy to a maximum extent for photocatalytic degradation of dyes.

Natural sunlight is the abundantly available source of energy in topical countries, which can be harnessed for photocatalytic degradation of dyes, if visible light active photocatalysts are developed. The BFO@PANI$_{opt}$ and BFO@TiO$_{2opt}$ photocatalysts developed in the present study were tested for their solar light activity in terms of percentage degradation of dyes and percentage COD removal from the mixed dye contaminated water.

The experiments were carried out with mixed dye aqueous solution containing the three dyes (MB, AY and Rh-B) each at 10 mg/L concentrations and catalyst loading 0.3 g/L for BFO@TiO$_{2opt}$ and of 0.2 g/L for BFO@PANI$_{opt}$ and with initial pH 5 under natural sunlight during 10 am to 1 pm in the month of March. The average intensity of solar light during this period was measured using lux meter and was found to be 5047 lux (739 μW/cm^2).

Figure 5.13 (a) and (b) show the percentage of dye degradation and percentage COD removal with BFO@TiO$_{2opt}$ and BFO@PANI$_{opt}$ nanocomposite particles respectively under solar light irradiation. As observed in Figure 5.13 (a) almost complete degradation of MB, 98% AY and 91% Rh-B degradation and 97% COD removal was achieved with BFO@TiO$_{2opt}$ nanocomposite in 210 min of irradiation time under solar light. As observed in Figures 5.13 (b) almost complete degradation of MB and AY and 97% Rh-B and 98% COD removal was achieved with BFO@PANI$_{opt}$ nanocomposite. These results indicate that BFO@TiO$_{2opt}$ and BFO@PANI$_{opt}$ nanocomposites are photocatalytically active under solar light.

The dye removal was less than 8% under dark conditions in the presence of the catalyst as compared to that under light, indicating that dye removal by permanent adsorption is minimal. Thus, it is confirmed that BFO@TiO$_{2opt}$ and BFO@PANI$_{opt}$ nanocomposites act as

185

a photocatalyst in the degradation of dyes under solar light, and the rate of dye removal is high. The reactive species O_2- and $OH-$ are formed due to the illumination of the catalyst. These reactive species attack the dyes which cause the cleavage of the bonds and thereby lead to the decolourization of dye solution (Kalikeri et al. 2018) and mineralization of the dyes. The high photocatalytic efficiency is exhibited under solar light, which is due to the low band gap energy of BFO@TiO$_{2opt}$ and BFO@PANI$_{opt}$ nanocomposites particles. Both the composites have absorption edge wavelength extending to 1033 nm and 885 nm in the NIR range respectively. It has appreciable absorbance in the wavelength range from 400 to 800 nm, showing its capability to absorb in visible light range and extending to NIR. The solar light consisting of appreciable percentage of the spectra in the visible and NIR range, has been proven to facilitate the degradation of dyes with BFO@TiO$_{2opt}$ and BFO@PANI$_{opt}$ and thus these catalysts show good photocatalytic activity under solar light. These results show that BFO@TiO$_{2opt}$ and BFO@PANI$_{opt}$ nanocomposites are very active photocatalysts and can be used for wastewater treatment to degrade the dyes under artificial visible light and under solar lights in regions where solar light is abundantly available. However, artificial visible light irradiation can be adopted for photocatalytic water treatment when solar light is not available.
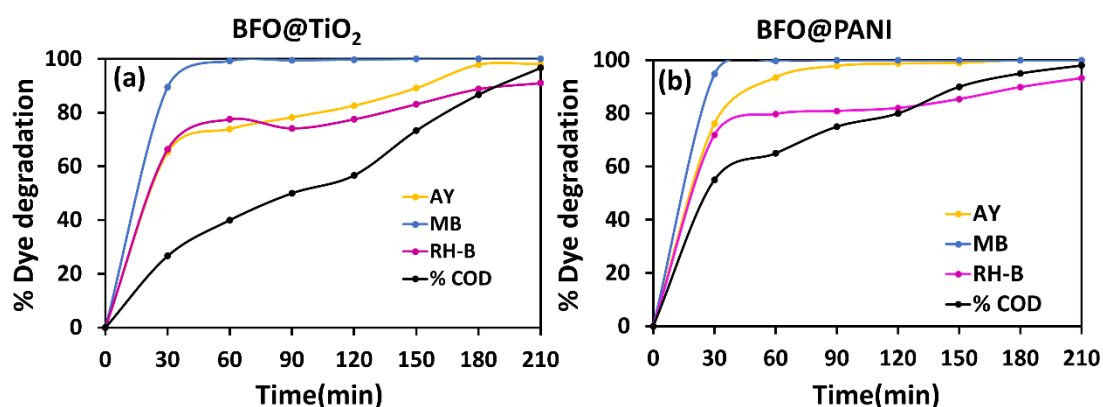
Figure. 5.13: Percentage dye degradation and COD removal from mixed dye contaminated water by (a) BFO@TiO$_{2opt}$ (b) BFO@PANI$_{opt}$ nanocomposite particles. Condition: dye solution-pH 5; concentration of each dye -10 mg/L each; Catalyst concentration- 0.3 g/L (BFO@TiO$_{2opt}$) and 0.2 g/L (BFO@PANI$_{opt}$).

5.3 Kinetics of degradation under solar light and artificial visible light irradiation using BFO@TiO$_{2opt}$ and BFO@PANI$_{opt}$ nanocomposite particles

Kinetics study aids in the design of photocatalytic reactors for treatment of contaminated water. Identification of rate equation and evaluation of parameters is a vital part of kinetics. Hence, the kinetics of degradation of dyes from mixed dye contaminated water containing MB, AY and Rh-B, at initial dye concentrations of 10 mg/L each, using BFO@TiO$_{2opt}$ and BFO@PANI$_{opt}$ as the photocatalysts under visible and solar light irradiation in terms of COD were evaluated. The catalyst loading 0.3 g/L for BFO@TiO$_{2opt}$ and 0.2 g/L for BFO@PANI$_{opt}$ with dye solution pH 5 were used. Figure 5.14 (a) and 5.15 (a) show the COD removal under visible and solar light irradiation with BFO@TiO$_{2opt}$ and BFO@PANI$_{opt}$ nanocomposites respectively. As observed in the Figure 5.14 (a), the COD level reduces from 2246 mg/L to 100 mg/L under visible and 2246 mg/L to 96 mg/L under solar light in 210 min of irradiation period with BFO@TiO$_{2opt}$ nanocomposites. As observed in the Figure 5.15 (a), the COD level reduces from 2246 mg/L to 50 mg/L under visible and 2246 mg/L to 33 mg/L under solar light in 210 min of irradiation period with BFO@PANI$_{opt}$ nanocomposite particles. The COD reduction of 97% and 96.6% were achieved under solar and visible light with BFO@TiO$_{2opt}$ nanocomposite particles, whereas the COD reduction was 98 and 97% with BFO@PANI nanocomposites respectively. These results indicate that the extent of COD removal is marginally better with BFO@PANI$_{opt}$ and thus it can be considered as a better photocatalyst both under solar and visible light as compared to BFO@TiO$_{2opt}$ nanocomposites. It may be attributed to the lower band gap energy of BFO@PANI$_{opt}$ and the photosensitizing effect of PANI.

The results obtained during batch experiments were used for evaluation of kinetics of dye degradation in terms of COD removal. The Langmuir–Hinshelwood (L–H) model presented as Eq. (5.1) (Matthews 1987) is used to describe the heterogeneous catalysis reaction involving the solid and liquid phase successfully.

$$(-\text{r}) = \frac{K_{obs}*K_r C}{1+K_r C} \dots\dots\dots\dots\dots\dots\dots\dots\dots\dots\dots\dots\dots\dots\dots\dots\dots\dots\dots \quad (5.1)$$

where r is the reaction rate, C is the concentration of the pollutant in terms of COD, K$_{obs}$ is the constant, related to adsorption, and K$_r$ is the reaction rate constant. Modified form of L–H model is given by Eq. (5.2)

$$\frac{1}{(r} = \frac{1}{(K_{obs})*(K_r C)} + \frac{1}{K_{obs}} \dots\dots\dots\dots\dots\dots\dots\dots\dots\dots\dots\dots\dots\dots\dots\dots\dots(5.2)$$

The reaction rate of COD removal at different COD levels was determined from the plots of COD vs. time data obtained by batch experiments. 1/r vs. 1/C was plotted, and values for the kinetic parameters were estimated from the plot. The applicability of L–H equation for degradation rate from mixed dye contaminated water in terms of COD was confirmed by the linear nature of the plots for visible and solar light mediated photocatalysis as shown in Figure 5.14 (b), (c) and Fig 5.15 (b), (c) for BFO@TiO$_{2opt}$ and BFO@PANI$_{opt}$ respectively. The plots are linear with a good coefficient of determination (R^2) value, indicating that the kinetics of photocatalytic degradation from mixed dye contaminated water containing MB, AY, and Rh-B dyes under visible and solar irradiation by BFO@TiO$_{2opt}$ and BFO@PANI$_{opt}$ nanocomposite particles, obey the L–H model. The R^2 values indicated in the plots show the goodness of fit. Applicability L–H model shows that the photocatalysis of dyes by BFO@TiO$_{2opt}$ and BFO@PANI$_{opt}$ nanocomposite particles are adsorption-controlled processes. Table 5.3 presents the values of K$_{obs}$ and K$_R$ of the kinetic model for the degradation from mixed dye contaminated water containing MB, AY and Rh-B dyes in terms of COD under visible and solar irradiation by BFO@TiO$_{2opt}$ and BFO@PANI$_{opt}$ nanocomposites.
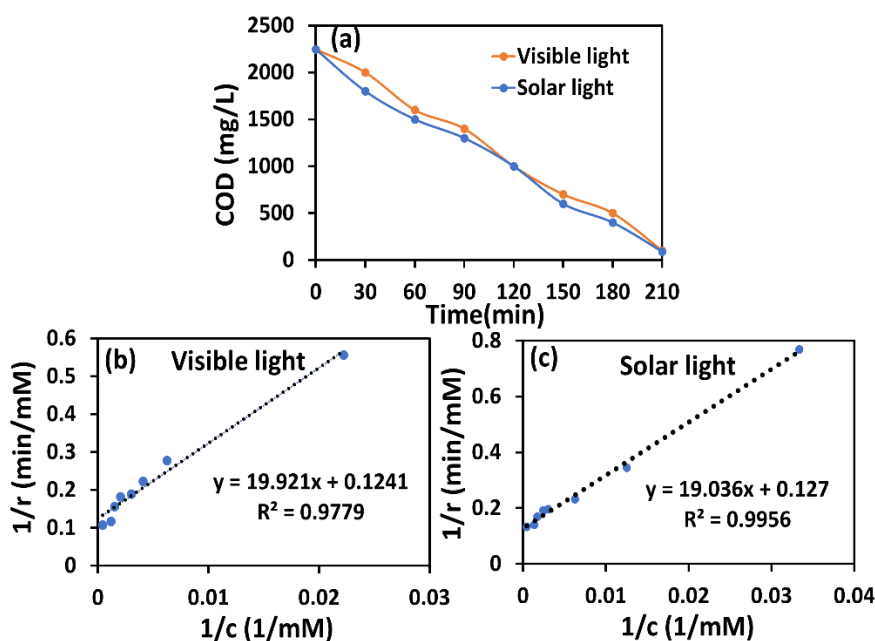
Figure. 5.14: (a) COD level under visible and solar light (b) L-H model fit for the rate kinetics of percentage COD removal under visible light irradiation (c) L-H model fit for the rate kinetics of percentage COD removal under solar light from mixed dye contaminated water. Condition: Dye solution-pH 5; concentration of each dye -10 mg/L; catalyst concentration 0.3 g/L (BFO@TiO$_{2opt}$).
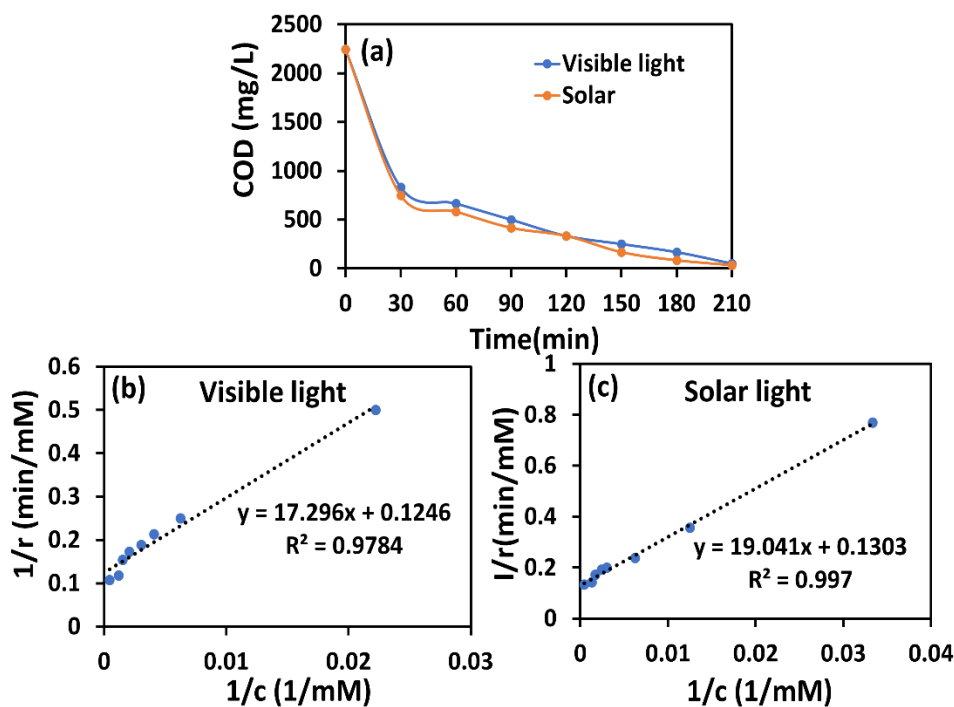
Figure. 5.15: (a) COD level under visible and solar light (b) L-H model fit for the rate kinetics of percentage COD removal under visible light irradiation (c) L-H model fit for the rate kinetics of percentage COD removal under solar light from mixed dye contaminated water. Condition: Dye solution-pH 5; concentration of each dye -10 mg/L; catalyst concentration-0.2g/L (BFO@PANI$_{opt}$).

Table 5.3: The values of COD removal kinetic parameters for Visible and Solar light using BFO@TiO$_{2opt}$ and BFO@PANI$_{opt}$ nanocomposite particles.

Nanocomposites	Source of light	K$_{Obs}$ (mg.L^{-1}.min^{-1})	K$_r$ (mg^{-1} .L)
BFO@TiO$_{2opt}$	Visible light	8.05	0.0062
	Solar light	7.87	0.0066
BFO@PANI$_{opt}$	Visible light	8.03	0.0072
	Solar light	7.66	0.0068

189

5.4. Reusability potential of BFO@TiO$_{2opt}$ and BFO@PANI$_{opt}$ nanocomposite particles

In order test the reusability potential of BFO@TiO$_{2opt}$ and BFO@PANI$_{opt}$ nanocomposite particles as photocatalysts, experiments were carried out with similar reaction conditions under visible light irradiation with the fresh and recycled catalyst. After completion of the experiment (210 min irradiation) with a fresh catalyst (cycle I), the BFO@TiO$_{2opt}$ and BFO@PANI$_{opt}$ nanocomposite particles were collected at the end of the cycle I and then utilized for the next set of recycle (reuse) experiments. BFO@TiO$_{2opt}$ and BFO@PANI$_{opt}$ ware reused thrice, and four experiments were done, out of which the first cycle was with the fresh catalyst, and the remaining three cycles were with the recycled catalyst. Before the next cycle of experiment, the catalyst particles were separated from the reaction mixture by centrifugation at 10,000 rpm for 10 min. It is then washed thrice with ethanol. In order to remove ethanol from the wet particles after centrifugation, particles were dried in an oven. Then the next cycle of batch experiments was conducted, and the same experimental conditions were used for all the four cycles. The percentage degradation of dye using fresh particles (Cycle 1), particles of single previous use (Cycle 2), particles of two previous uses (Cycle 3), and particles of three previous uses (Cycle 4) after 210 min of irradiation were noted.

As observed in the Table 5.4 almost the same degradation of MB, AY and Rh-B dyes could be achieved in 210 min of irradiation time under visible light till the second cycle. An insignificant difference in the third cycle was observed, whereas after the third cycles of reuse, decrease in photocatalytic activity from 100% to 98.5% MB, 96% to 94.2% AY and 89% to 87% Rh-B was achieved. As observed in Figure 4.16 (b) the percentage of COD removal also decreased by 96.7% to 95% under visible light with BFO@TiO$_{2opt}$ nanocomposite particles.

As observed in Table 5.4 almost the same degradation of MB, AY and Rh-B dyes occur till second cycle in 210 min of irradiation time under visible light. The insignificant difference in the third cycle, whereas after third cycles of reuse, decrease in photocatalytic activity from 100% to 99% MB, 100% to 99% AY and 96% to 90% Rh-B was achieved. As observed in Figure 4.17 (b) the percentage of COD removal also decreased by 97% to 96.2% under visible light with BFO@PANI$_{opt}$ nanocomposite particles. Table 5.4 presents the values of percentage degradation and percentage COD removal using BFO@TiO$_{2opt}$ and BFO@PANI$_{opt}$ nanocomposite particles. Only a marginal change in degradation of dyes and COD removal were observed with repeated use of the catalyst four times. Thus, these BFO@TiO$_{2opt}$ BFO@PANI$_{opt}$ nanocomposite particles exhibit a good reusability potential, without much decline in activity.

Table 5.4: The values of percentage degradation and percentage COD removal using BFO@TiO$_{2opt}$ and BFO@PANI$_{opt}$ nanocomposite particles.

Nanocomposite	Recycle	Percentage Degradation			Percentage COD removal
		AY	MB	Rh-B	
BFO@TiO$_{2opt}$	Cycle 1	96	100	89	96.7
	Cycle 2	96	100	88.9	96.7
	Cycle 3	95.5	99	88	96
	Cycle 4	95	98.5	87	95
BFO@PANI$_{opt}$	Cycle 1	100	100	96	97
	Cycle 2	100	100	96	97
	Cycle 3	99.3	99.5	93	96.8
	Cycle 4	99	99	90	96.2

5.5. Leachability of the metals from the BFO@TiO$_{2opt}$ and BFO@PANI$_{opt}$ nanocomposite particles during photocatalysis reaction

This study reports the leachability of the metals from the nanocomposite to the reaction mixture during photocatalysis to assess if the nanocomposites contribute to any secondary metal pollution of treated water, by analysis of the metals in the reaction mixture at the end of photocatalytic reaction duration of 210 min, using ICP-OES as explained in Section 3.9. There was no evidence of the presence of traceable metal ions (Bi, Fe and Ti) in the reaction mixture, indicating that no metal gets leached from the nanocomposite in 210 minutes of reaction time. Thus, the nanocomposite does not pose any risk of secondary metal pollution of treated water.

5.6. Comparison of the photocatalytic activity of BFO@TiO$_{2opt}$ and BFO@PANI$_{opt}$ nanocomposites with other photocatalysts

The photocatalytic activity of the BFO@TiO$_{2opt}$ nanocomposites synthesized in the present study is compared with other BFO/TiO$_2$ based photocatalyts used for dye degradation by other researchers. Table 5.5. presents the comparison of the photocatalytic activity of other BFO/TiO$_2$ based nanocomposite particles with that of BFO@TiO$_{2opt}$ nanocomposites.

However, there are no reports on photocatalytic activity of BFO@PANI nanocomposites in degradation of dyes or any other pollutants in water. Thus, the photocatalytic activity of other PANI-Bismuth compound-based nanocomposite particles is compared with that of BFO@PANI$_{opt}$ nanocomposites synthesized in the present study. Table 5.6. presents the comparison of the photocatalytic activity of other PANI-Bismuth compound-based nanocomposite particles with that of BFO@PANI$_{opt}$ nanocomposites. The photocatalytic activity of the BFO@TiO$_{2opt}$ nanocomposites is better than the other BFO/TiO$_2$ based nanocomposite particles as presented in Table 5.5. As observed in Table 5.5 and Table 5.6, the BFO@TiO$_{2opt}$ or BFO@PANI$_{opt}$ nanocomposite particles synthesized in the present study were used under artificial visible light irradiations with light source of lesser power than those used in literature with BFO/TiO$_2$ based nanocomposites or PANI-Bismuth compound-based nanocomposites. The amount of catalyst used in the present study is also lower than those reported in literature. The earlier literature presents the reports on the degradation of single dyes using the BFO/TiO$_2$ based nanocomposites or PANI-Bismuth compound-based nanocomposites. However, the BFO@TiO$_{2opt}$ or BFO@PANI$_{opt}$ nanocomposite particles synthesized in the present study could degrade the dyes at higher concentrations or similar concentrations from mixed dye aqueous solutions to a considerable extent in a lower time with lower catalyst loading and with irradiation by low power lamps than those reported in literature. These BFO@TiO$_{2opt}$ or BFO@PANI$_{opt}$ nanocomposite particles have shown considerably good photocatalytic activity under solar irradiation as well as under artificial visible light. Thus, on comparison with other BFO/TiO$_2$ based nanocomposites or PANI-Bismuth compound-based nanocomposites, BFO@TiO$_{2opt}$ and BFO@PANI$_{opt}$ nanocomposite particles in the present study have shown better photocatalytic activity.

Table 5.5: Comparison of photocatalytic activity of BFO/TiO$_2$ based nanocomposite particles in terms of dye degradation

BFO based nanocomposite particles	Method	Dye	Light source	Percentage degradation and time (min)	Catalyst loading (g/L)	Reference
BFO@TiO$_2$ (2.2 eV) With various ratios of Bi:Ti	BFO synthesized by hydrothermal approach combined with a hydrolysis precipitation processing.	CR	Visible light (500W)	70% (1:1) 50% (2:1) 48% (1:2) respectively in 120 min	2	Li et al.(2009b)
BFO@TiO$_2$ (2.12 eV) Nanotubes	BFO synthesized by Precipitation method and these particles were deposited into TiO$_2$-NTs via an ultrasonic-immersion strategy.	20 mg/L Rh-B	Visible light (500 W)	16% in 150 min	-	Zhu et al. (2014)
BFO@TiO$_2$ (~2.2 eV)	BFO by an auto-combustion method and coated with TiO$_2$ by hydrolysis of Titanium Tetra (IV) Iso-Propoxide (TTIP.	10 mg/L Rh-B	Solar simulator (1000W/m^2)	95% in 300 min	3	Hengky (2013)
BFO@Ce-doped TiO$_2$ (2.58 eV)	BFO prepared by a simple sol–gel technique coated by Trabutyltitanate(TiOBu)$_4$),Ce (NO$_3$)$_3$6H$_2$O are in the stoichiometric ratio via a sol–gel method.	10 mg/L MO	UV (300 W) and Visible (500 W)	93.5% in 100 min and 74.8% in 300 min	-	Gong et al (2013)

BFO@TiO$_2$ (1.77 eV)	BFO synthesized by a citrate self-combustion method and coated with TiO$_2$ by hydrolysis of titanium butoxide (Ti (OBu)$_4$).	15 mg/L MV	Visible-light (400 W)	95% at 150 min		3	Liu et al. (2017b)
BFO@TiO$_2$ **(1.2 eV)**	**BFO synthesized by auto combustion method and coated with TiO$_2$ by hydrolysis of Titanium Tetra (IV) Iso-Propoxide (TTIP)**	**MB, AY and Rh-B, 10 mg/L each. (Mixed dye condition)**	**Visible (36W)**	**~100% MB 96% AY and 89% Rh-B in 210 min**	**0.3**	**Present work**
			Solar light	**~100% MB 98% AY and 91% Rh-B 210 min**		

Table 5.6: Comparison of photocatalytic activity of PANI-Bismuth compound-based nanocomposite particles in terms of dye degradation.

PANI and Bi based nanocomposite particles	Dye	Light source	Percentage degradation	Time (min)	Catalyst loading(g/L)	Reference
Polyaniline/Bi$_3$NbO$_7$	10-5 (4.79 mg/L) Rh-B single dye solution	Visible 300W Xe lamp	~100%	300 min	1	Wu et al. (2012)
PANI/Bi$_2$WO$_6$	10^{-5} M (4.79 mg/L) Rh-B single dye solution	500W Xe lamp	99%	120 min	1	Wang et al.(2014)
PANI/BiOBr hybrids materials	2*10^{-5} M (9.58 mg/L) Rh-B single dye solution	350 W xenon lamp irradiation	99.9%	75 min	1	Hao et al. (2017)
Polyaniline coupled bismuth sulfide (PANI/Bi$_2$S$_3$) nanocomposites (1.35 eV)	10^{-5} M (3.2 mg/L) MB single dye solution	150 W visible-light source	89.7%	180 min	0.4	Sharma and Khare (2018)
PANI-bismuth selenide (Band gap 1.25 eV)	10^{-5} M (3.65 mg/L) MG 10^{-5} M (4.79 mg/L) Rh-B 10^{-5} M (3.27 mg/L) MO single dye solution	Visible Tungsten lamp 200W	97.12% MG 97.7% Rh-B 96.3% MO	15 min	0.4	Chatterjee et al. (2019)

PANI/Bi$_2$MoO$_6$ nanocomposites	10 mg/L Rh-B single dye solution	LED solar simulator (5 W)	~100%	120 min	0.2	Feng et al.(2019)
PANI/BiOBr	10 mg/L MO single dye solution	5-W white LED lamp	74%	210 min	0.6	Yaghoubi-berijani and Bahramian (2020)
BFO@PANI$_{opt}$ (1.4 eV)	**MB, AY and Rh-B, 10 mg/L each. (Mixed dye condition)**	**36 W visible light**	**~100%MB ~100% AY 96% Rh-B**	**210 min**	**0.2**	**Present study**
		Solar light	**~100% MB ~ 100% AY 97% Rh-B**			

CHAPTER 6

SUMMARY AND CONCLUSION

In this research work, bismuth ferrite nanoparticles were synthesized by various methods, and their visible light activity in terms of degradation of dyes and COD removal from the mixed dye contaminated water containing MB, AY and Rh-B have been assessed. The method for the synthesis of bismuth ferrite nanoparticles, that resulted in maximum visible light activity for degradation of the dyes was chosen, followed by synthesis of BFO@TiO$_2$ and BFO@PANI heterostructured nanocomposites in the core-shell form, and optimization of synthesis/calcination parameters to achieve maximum degradation of dyes from the mixed dye contaminated water. The effect of various parameters affecting the rate of photocatalysis was studied and the kinetics of dye degradation was evaluated.

Based on the results of the research work, the following conclusions were drawn

- The auto combustion method using citric acid at synthesis pH 7 (Method 2 C) resulted in the formation of mixed-phase BFO containing BiFeO$_3$ and Bi$_{25}$FeO$_{40}$, which yielded maximum photocatalytic activity in terms of degradation of dyes and COD removal from the mixed dye contaminated water under visible light irradiation.

- BFO@TiO$_2$ heterostructured nanocomposite particles synthesized with BFO: Ti molar ratio of 1:2 and calcined at 400°C for 2 h (BFO@TiO$_{2opt}$) exhibited a maximum photocatalytic activity in terms of degradation of dyes and COD removal from mixed dye contaminated water.

- BFO@TiO$_{2opt}$ nanocomposite contained pure phase BFO nanoparticles surrounded by nanocrystalline rutile phase TiO$_2$ shell as evidenced by TEM images, confirming the formation of core- shell heterostructured nanocomposite.

- BFO@PANI heterostructured nanocomposite particles synthesized with BFO: aniline molar ratio of 1: 0.0041 (BFO@PANI$_{opt}$) exhibited a maximum photocatalytic activity in terms of degradation of dyes and COD removal from mixed dye contaminated water.

- BFO@PANI$_{opt}$ nanocomposite contained pure phase BFO particles surrounded by PANI coating, confirming the formation of core- shell heterostructured nanocomposite.

- BFO@TiO$_{2opt}$ and BFO@PANI$_{opt}$ nanocomposite particles have a band gap energy of 1.2 eV and 1.4 eV respectively, with their absorption edges extending to NIR range.

- BFO@TiO$_{2opt}$ exhibited superior visible light assisted photocatalytic activity than BFO and TiO$_2$. BFO@PANI$_{opt}$ exhibited superior visible light assisted photocatalytic activity than BFO and PANI. However, BFO@PANI$_{opt}$ exhibited better photocatalytic activity than BFO@TiO$_{2opt}$.

- Further on optimization of photocatalytic reaction parameters, pH=5 and light intensity = 263 μW/cm^2 (2 lamps) were found to be the optimum for dye degradation and COD removal from mixed dye contaminated water under visible light irradiation with both BFO@TiO$_{2opt}$ and BFO@PANI$_{opt}$. The optimum catalyst loading were 0.3 g/L and 0.2 g/L for BFO@TiO$_{2opt}$ and BFO@PANI$_{opt}$ respectively for photocatalytic degradation of dyes from a mixed dye contaminated water containing 10 mg/L of each of the dyes.

- Under visible light irradiation and optimum process conditions (i) almost complete degradation of MB, 97% AY and 89% Rh-B degradation and 96.6% COD removal were achieved with BFO@TiO$_{2opt}$ nanocomposites (ii) almost complete degradation of MB and AY with 96% Rh-B degradation and 97% COD removal were achieved with BFO@PANI$_{2opt}$ nanocomposites.

- BFO@TiO$_{2opt}$ and BFO@PANI$_{opt}$ nanocomposite particles were found to be very effective photocatalysts even under solar light.

- During photocatalytic degradation of dyes and COD removal from mixed dye contaminated water, the presence of one or two additional dyes have been found to reduce the degradation of a target dye as well as the COD removal, showing the inhibition effect of the dyes.

- The photocatalytic degradation of a target dye and COD removal would decrease with increase in its own initial concentration or with the increase in concentration of one or both of the other two dyes.

- The kinetics of COD removal by BFO@TiO$_{2opt}$ and BFO@PANI$_{opt}$ nanocomposites under artificial visible and solar light, followed Langmuir–Hinshelwood (L-H) kinetics model (Eq.5.1) both under artificial visible and solar light by BFO@TiO$_{2opt}$ and BFO@PANI$_{opt}$ nanocomposites.

- The nanocomposites exhibit reusability potential up to four cycles of use without a notable decline in photocatalytic activity.

- The nanocomposites do not pose any risk of secondary metal pollution of treated water.

Thus, BFO@TiO$_{2opt}$ and BFO@PANI$_{opt}$ heterostructured nanocomposites can be adopted for treatment of wastewater containing multiple dyes by harnessing solar energy for
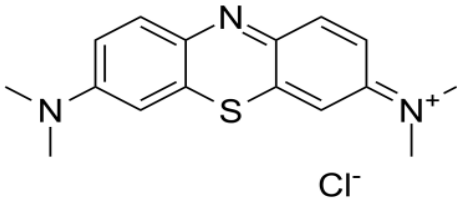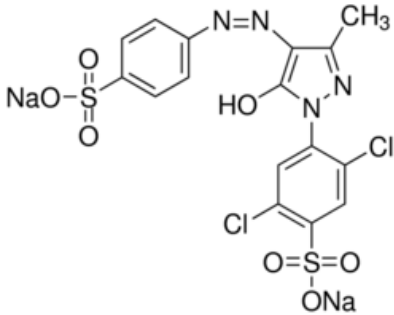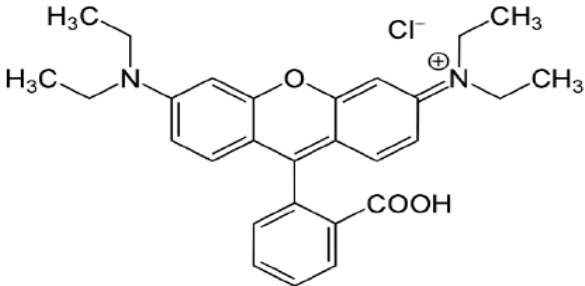
photocatalytic degradation. These photocatalysts can be employed for solar light mediated wastewater treatment for dye degradation, wherever solar energy is abundantly available. In places or seasons when solar light is not available, artificial visible light mediated photocatalysis can be adopted with these photocatalysts. The process of photocatalytic water treatment utilizing the BFO@TiO$_{2opt}$ and BFO@PANI$_{opt}$ heterostructured nanocomposites developed in the present study, may serve to be a sustainable, energy efficient and potentially economical process.

FUTURE SCOPE OF THE RESEARCH

- ✓ Studies on immobilization of BFO@TiO$_2$ and BFO@PANI nanocomposites in various matrices and to assess their activity for degradation of dyes from the mixed dye contaminated water
- ✓ Studies on the application of immobilized BFO@TiO$_2$ and BFO@PANI in continuous photocatalytic reactors
- ✓ Studies on the applicability of these nanocomposites for degradation of various organic pollutants and for other photocatalytic applications

APPENDIX I

Molecular structure of the dyes

Methylene Blue		
Formula: $C_{16}H_{18}ClN_3S$ **Molecular Weight**: 319.85 g/mol **Other names**: CI 52015, basic blue 9		

Acid Yellow 17		
Formula: $C_{16}H_{10}Cl_2N_4Na_2O_7S_2$ **Molecular Weight**: 551.29 g/mol **Other names**: Lissamine Fast Yellow; Light Fast Yellow 2G; Food Yellow 5; Acid Leather Yellow 2GL; Erio Flavine SX; Fenalan Yellow G; Erio Flavine 3G; Kayacyl Yellow GG		

Rhodamine B		
Formula: $C_{28}H_{31}ClN_2O_3$ **Molecular Weight** : 479.02 g/mol **Other names**; Rhodamine 610, Pigment Violet 1, Basic Violet 10, C.I. 45170		

APPENDIX II

Chemical oxygen demand (COD)(APHA 2012)

Principle: COD test determines the oxygen required for chemical oxidation of organic matter with the help of strong chemical oxidant. The organic matter gets oxidized completely by potassium dichromate ($K_2Cr_2O_7$) in the presence of sulfuric acid (H_2SO_4) to produce CO_2+H_2O. The excess $K_2Cr_2O_7$ remaining after the reaction is titrated with standard ferrous ammonium sulphate [Fe $(NH_4)_2(SO_4)_2$]. The dichromate consumed gives the O_2 required for oxidation of the organic matter.

Procedure

0.4 g of $HgSO_4$ was taken in a 250 mL reflux flask and 2 ml of water sample or an aliquot of sample diluted 20 ml with distilled water were added to it and mixed. Pumice stone or glass beads were added, followed by the addition of 10 ml of 0.25 N $K_2Cr_2O_7$. Then 30 mL of H_2SO_4 containing $AgSO_4$(10g $AgSO_4$ in 100 mL conc, H_2SO_4) was slowly added with continuous mixing. This would prevent the escape of fatty acid. The reflux mixture was thoroughly mixed before heat is applied. The flask was connected to the condenser, contents were well mixed and heated under reflux for a minimum of 2 hours COD and then was down the condensed with distilled water. The mixture was then diluted to a minimum of 150 mL, cooled and the excess dichromate was titrated with 0.1N Fe $(NH_4)_2(SO_4)$ using ferroin indicator. A sharp colour change from blue green to wine red indicates the end point A blank was run using 50 mL of distilled water in place of the sample together with

all reagents and subsequent treatment.

COD was calculated from the fallowing equation

$$COD \ mg/L = \frac{a-b}{sample} \times N \times 800 \text{------------(1)}$$

Where;

a= mL Fe $(NH_4)_2(SO_4)$ for blank

b= mL Fe $(NH_4)_2(SO_4)$ for sample

N=Normality of Fe $(NH_4)_2(SO_4)$

REFERENCES

Abhilash, M. R., Akshatha, G., and Srikantaswamy, S. (2019). "Photocatalytic dye degradation and biological activities of the Fe_2O_3 /Cu_2O nanocomposite." *RSC Adv.*, 9(15), 8557–8568.

Abu Tariq, M., Faisal, M., Saquib, M., and Muneer, M. (2008). "Heterogeneous photocatalytic degradation of an anthraquinone and a triphenylmethane dye derivative in aqueous suspensions of semiconductor." *Dye. Pigment.*, 76(2), 358–365.

Acemioğlu, B. (2004). "Adsorption of Congo red from aqueous solution onto calcium-rich fly ash." *J. Colloid Interface Sci.*, 274(2), 371–379.

Achenbach, G. D., James, W. J., and Gerson, R. (1967). "Preparation of Single-Phase Polycrystalline $BiFeO_3$." *J. Am. Ceram. Soc.*, 50(8), 437–437.

Adams, R. M., Fleming, R. A., Chang, C.-C., McCarl, B. A., and Rosenzweig, C. (1995). "A reassessment of the economic effects of global climate change on U.S. agriculture." *Clim. Change*, 30(2), 147–167.

Adesina, A. A. (2004). "Industrial exploitation of photocatalysis: Progress, perspectives and prospects." *Catal. Surv. from Asia*, 8(4), 265–273.

Adhikari, S. P., and Lachgar, A. (2016). "Effect of particle size on the photocatalytic activity of $BiNbO_4$ under visible light irradiation." *J. Phys. Conf. Ser.*, 758, 012017.

Adijanto, L., Bennett, D. A., Chen, C., Yu, A. S., Cargnello, M., Fornasiero, P., Gorte, R. J., and Vohs, J. M. (2013). "Exceptional thermal stability of $Pd@CeO_2$ core-shell catalyst nanostructures grafted onto an oxide surface." *Nano Lett.*, 13(5), 2252–2257.

Agrawal, A., Dar, T. A., Phase, D. M., and Sen, P. (2014). "Type I and type II band alignments in ZnO/MgZnO bilayer films." *Appl. Phys. Lett.*, 105(8), 081603.

Agrawal, Y., and Patel, V. (2011). "Nanosuspension: An approach to enhance solubility of drugs." *J. Adv. Pharm. Technol. Res.*, 2(2), 81.

Ahmad, T., Irfan, M., Bustam, M. A., and Bhattacharjee, S. (2016). "Effect of Reaction Time on Green Synthesis of Gold Nanoparticles by Using Aqueous Extract of Elaise Guineensis (Oil Palm Leaves)." *Procedia Eng.*, 148, 467–472.

Ahmed, S., Rasul, M. G., Martens, W. N., Brown, R., and Hashib, M. A. (2010). "Heterogeneous photocatalytic degradation of phenols in wastewater: A review on current status and developments." *Desalination*, 261(1–2), 3–18.

Ahmed, S., Rasul, M. G., Martens, W. N., Brown, R., and Hashib, M. A. (2011). "Advances in heterogeneous photocatalytic degradation of phenols and dyes in wastewater: A review." *Water. Air. Soil Pollut.*, 215(1–4), 3–29.

Ahuja, P., Ujjain, S. K., Arora, I., and Samim, M. (2018). "Hierarchically Grown NiO-Decorated Polyaniline-Reduced Graphene Oxide Composite for Ultrafast Sunlight-Driven Photocatalysis." *ACS Omega*, 3(7), 7846–7855.

Akhavan, O. (2009). "Lasting antibacterial activities of Ag–TiO_2/Ag/a-TiO_2 nanocomposite thin film photocatalysts under solar light irradiation." *J. Colloid Interface Sci.*, 336(1), 117–124.

Akhtar, K., Khan, S. A., Khan, S. B., and Asiri, A. M. (2018). "Scanning Electron Microscopy: Principle and Applications in Nanomaterials Characterization." *Handb. Mater. Charact.*, Cham: Springer International Publishing, 113–145.

Akhundi, A., Habibi-Yangjeh, A., Abitorabi, M., and Rahim Pouran, S. (2019). "Review on photocatalytic conversion of carbon dioxide to value-added compounds and renewable fuels by graphitic carbon nitride-based photocatalysts." *Catal. Rev.*, 61(4), 595–628.

Akpan, U. G., and Hameed, B. H. (2009). "Parameters affecting the photocatalytic degradation of dyes using TiO_2-based photocatalysts: A review." *J. Hazard. Mater.*, 170(2–3), 520–529.

Aksu, Z. (2005). "Application of biosorption for the removal of organic pollutants: a review." *Process Biochem.*, 40(3–4), 997–1026.

Alahiane, S., Qourzal, S., Ouardi, M. El, Abaamrane, A., and Assabbane, A. (2014). "Factors Influencing the Photocatalytic Degradation of Reactive Yellow 145 by TiO&lt;sub&gt;2&lt;/sub&gt;-Coated Non-Woven Fibers." *Am. J. Anal. Chem.*, 05(08), 445–454.

Alenizi, M. A., Kumar, R., Aslam, M., Alseroury, F. A., and Barakat, M. A. (2019). "Construction of a ternary g-C3N4/TiO_2@polyaniline nanocomposite for the enhanced photocatalytic activity under solar light." *Sci. Rep.*, 9(1), 12091.

Ali, W., Ullah, H., Zada, A., Alamgir, M. K., Muhammad, W., Ahmad, M. J., and Nadhman, A. (2018). "Effect of calcination temperature on the photoactivities of ZnO/SnO_2 nanocomposites for the degradation of MO." *Mater. Chem. Phys.*, 213, 259–266.

Alipour, A., and Mansour Lakouarj, M. (2019). "Photocatalytic degradation of RB dye by CdS-decorated nanocomposites based on polyaniline and hydrolyzed pectin: Isotherm and kinetic."

J. Environ. Chem. Eng., 7(1), 102837.

Alkaykh, S., Mbarek, A., and Ali-Shattle, E. E. (2020). "Photocatalytic degradation of methylene blue dye in aqueous solution by $MnTiO_3$ nanoparticles under sunlight irradiation." *Heliyon*, 6(4), e03663.

Allen, S. J., and Koumanova, B. (2005). "Decolourisation of water/wastewater using adsorption (Review)." *J.Univ. Chem. Technol. Metall.*, 40(3), 175–192.

Alzahrani, E. (2017). "Photodegradation of Binary Azo Dyes Using Core-Shell $Fe_3O_4/SiO_2/TiO_2$ Nanospheres." *Am. J. Anal. Chem.*, 08(01), 95–115.

Amadine, O., Essamlali, Y., Fihri, A., Larzek, M., and Zahouily, M. (2017). "Effect of calcination temperature on the structure and catalytic performance of copper–ceria mixed oxide catalysts in phenol hydroxylation." *RSC Adv.*, 7(21), 12586–12597.

Amano, F., Ishinaga, E., and Yamakata, A. (2013). "Effect of Particle Size on the Photocatalytic Activity of WO_3 Particles for Water Oxidation." *J. Phys. Chem. C*, 117(44), 22584–22590.

Ameen, S., Seo, H.-K., Shaheer Akhtar, M., and Shin, H. S. (2012). "Novel graphene/polyaniline nanocomposites and its photocatalytic activity toward the degradation of rose Bengal dye." *Chem. Eng. J.*, 210, 220–228.

Amouri, H., Desmarets, C., and Moussa, J. (2012). "Confined Nanospaces in Metallocages: Guest Molecules, Weakly Encapsulated Anions, and Catalyst Sequestration." *Chem. Rev.*, 112(4), 2015–2041.

An, J., Zhu, L., Zhang, Y., and Tang, H. (2013). "Efficient visible light photo-Fenton-like degradation of organic pollutants using in situ surface-modified $BiFeO_3$ as a catalyst." *J. Environ. Sci.*, 25(6), 1213–1225.

Àngels Olivella, M., Fiol, N., la Torre, F. de, Poch, J., and Villaescusa, I. (2012). "A Mechanistic Approach to Methylene Blue Sorption on Two Vegetable Wastes: Cork Bark and Grape Stalks." *BioResources*, 7(3), 3340–3354.

Anku, W., Osei-Bonsu Oppong, S., Kumar Shukla, S., and Penny Govender, P. (2016). "Comparative photocatalytic degradation of monoazo and diazo dyes under simulated visible light using $Fe_3^+/C/S$ doped-TiO_2 nanoparticles." *Acta Chim. Slov.*, 380–391.

Ansari, M. O., Khan, M. M., Ansari, S. A., and Cho, M. H. (2015). "Electrically conductive

polyaniline sensitized defective-TiO$_2$ for improved visible light photocatalytic and photoelectrochemical performance: A synergistic effect." *New J. Chem.*, 39, 8381–8388.

Ansari, M. O., Khan, M. M., Ansari, S. A., Lee, J., and Cho, M. H. (2014a). "Enhanced thermoelectric behaviour and visible light activity of Ag@TiO$_2$/polyaniline nanocomposite synthesized by biogenic-chemical route." *RSC Adv.*, 4, 23713–23719.

Ansari, M. O., Khan, M. M., Ansari, S. A., Raju, K., Lee, J., and Cho, M. H. (2014b). "Enhanced Thermal Stability under DC Electrical Conductivity Retention and Visible Light Activity of Ag/TiO$_2$ @Polyaniline Nanocomposite Film." *ACS Appl. Mater. Interfaces*, 6(11), 8124–8133.

APHA. (2012). *Standard Methods for the Examination of Water and Wastewater*. Standard Methods for the Examination of Water and Wastewater, (E. W. Rice, R. B. Baird, A. D. Eaton, and L. S. Clesceri, eds.), American Public Health Association.

Armelao, L., Barreca, D., Bottaro, G., Gasparotto, A., Gross, S., Maragno, C., and Tondello, E. (2006). "Recent trends on nanocomposites based on Cu, Ag and Au clusters: A closer look." *Coord. Chem. Rev.*, 250(11–12), 1294–1314.

Armendariz, V., Herrera, I., Peralta-videa, J. R., Jose-yacaman, M., Troiani, H., Santiago, P., and Gardea-Torresdey, J. L. (2004). "Size controlled gold nanoparticle formation by Avena sativa biomass: use of plants in nanobiotechnology." *J. Nanoparticle Res.*, 6(4), 377–382.

Aruna, S. T., and Mukasyan, A. S. (2008). "Combustion synthesis and nanomaterials." *Curr. Opin. Solid State Mater. Sci.*, 12(3–4), 44–50.

Asahi, R. (2001). "Visible-Light Photocatalysis in Nitrogen-Doped Titanium Oxides." *Science (80-.).*, 293(5528), 269–271.

Aslam, S., Zeng, J., Subhan, F., Li, M., Lyu, F., Li, Y., and Yan, Z. (2017). "In situ one-step synthesis of Fe$_3$O$_4$ @MIL-100(Fe) core-shells for adsorption of methylene blue from water." *J. Colloid Interface Sci.*, 505, 186–195.

Augugliaro, V., Bellardita, M., Loddo, V., Palmisano, G., Palmisano, L., and Yurdakal, S. (2012). "Overview on oxidation mechanisms of organic compounds by TiO$_2$ in heterogeneous photocatalysis." *J. Photochem. Photobiol. C Photochem. Rev.*, 13(3), 224–245.

Autin, O., Romelot, C., Rust, L., Hart, J., Jarvis, P., MacAdam, J., Parsons, S. A., and Jefferson, B. (2013). "Evaluation of a UV-light emitting diodes unit for the removal of micropollutants in water for low energy advanced oxidation processes." *Chemosphere*, 92(6), 745–751.

Ayad, M. M., and El-Nasr, A. A. (2010). "Adsorption of Cationic Dye (Methylene Blue) from Water Using Polyaniline Nanotubes Base." *J. Phys. Chem. C*, 114(34), 14377–14383.

Azeez, F., Al-Hetlani, E., Arafa, M., Abdelmonem, Y., Nazeer, A. A., Amin, M. O., and Madkour, M. (2018). "The effect of surface charge on photocatalytic degradation of methylene blue dye using chargeable titania nanoparticles." *Sci. Rep.*, 8(1), 7104.

Badawy, A. A., Ibrahim, S. M., and Essawy, H. A. (2020). "Enhancing the Textile Dye Removal from Aqueous Solution Using Cobalt Ferrite Nanoparticles Prepared in Presence of Fulvic Acid." *J. Inorg. Organomet. Polym. Mater.*, 30(5), 1798–1813.

Baer, D. R., Engelhard, M. H., Johnson, G. E., Laskin, J., Lai, J., Mueller, K., Munusamy, P., Thevuthasan, S., Wang, H., Washton, N., Elder, A., Baisch, B. L., Karakoti, A., Kuchibhatla, S. V. N. T., and Moon, D. (2013). "Surface characterization of nanomaterials and nanoparticles: Important needs and challenging opportunities." *J. Vac. Sci. Technol. A Vacuum, Surfaces,Film.*, 31(5), 050820.

Bahadur, N. M., Chowdhury, F., Obaidullah, M., Hossain, M. S., Rashid, R., Akter, Y., Furusawa, T., Sato, M., and Suzuki, N. (2019). "Ultrasonic-Assisted Synthesis, Characterization, and Photocatalytic Application of SiO_2@TiO_2 Core-Shell Nanocomposite Particles." *J. Nanomater.*, 2019, 1–11.

Bahnemann, D. W. (1999). "Photocatalytic Detoxification of Polluted Waters." *Handb. Environ. Chem. vol. 2*, 285.

Bajpai, O. P., Mandal, S., Ananthakrishnan, R., Mandal, P., Khastgir, D., and Chattopadhyay, S. (2018). "Structural features, magnetic properties and photocatalytic activity of bismuth ferrite nanoparticles grafted on graphene nanosheets." *New J. Chem.*, 42(13), 10712–10723.

Bao, N., Shen, L., Takata, T., Domen, K., Gupta, A., Yanagisawa, K., and Grimes, C. A. (2007). "Facile Cd−Thiourea Complex Thermolysis Synthesis of Phase-Controlled CdS Nanocrystals for Photocatalytic Hydrogen Production under Visible Light." *J. Phys. Chem. C*, 111(47), 17527–17534.

Barakat, M. A., Schaeffer, H., Hayes, G., and Ismat-Shah, S. (2005). "Photocatalytic degradation of 2-chlorophenol by Co-doped TiO_2 nanoparticles." *Appl. Catal. B Environ.*, 57(1), 23–30.

Basibuyuk, M., and Forster, C. F. (1997). "An examination of the treatability of a simulated textile wastewater containing Maxilon Red BL-N." *Process Biochem.*, 32(6), 523–527.

Bechambi, O., Sayadi, S., and Najjar, W. (2015). "Photocatalytic degradation of bisphenol A in the presence of C-doped ZnO: Effect of operational parameters and photodegradation mechanism." *J. Ind. Eng. Chem.*, 32, 201–210.

Bedia, J., Peñas-Garzón, M., Gómez-Avilés, A., Rodriguez, J., and Belver, C. (2018). "A Review on the Synthesis and Characterization of Biomass-Derived Carbons for Adsorption of Emerging Contaminants from Water." *C*, 4(4), 63.

Bhadra, S., Khastgir, D., Singha, N. K., and Lee, J. H. (2009). "Progress in preparation, processing and applications of polyaniline." *Prog. Polym. Sci.*, 34(8), 783–810.

Bharadwaj, R. K. (2001). "Modeling the Barrier Properties of Polymer-Layered Silicate Nanocomposites." *Macromolecules*, 34(26), 9189–9192.

Bharathkumar, S., Sakar, M., K., R. V., and Balakumar, S. (2015). "Versatility of electrospinning in the fabrication of fibrous mat and mesh nanostructures of bismuth ferrite (BiFeO$_3$) and their magnetic and photocatalytic activities." *Phys. Chem. Chem. Phys.*, 17(27), 17745–17754.

Bhattacharjee, S. (2016). "In relation to the following article 'DLS and zeta potential — What they are and what they are not?' Journal of Controlled Release, 2016, 235, 337–351." *J. Control. Release*, 238, 311–312.

Bisen, N., Shrivastava, P., Hariprasad, N., Anju, S. G., Yesodharan, E. P., Suguna, Y., Gaya, U. I., Abdullah, A. H., Tseng, T. K., Lin, Y. S., Chen, Y. J., Chu, H., MacWan, D. P., Dave, P. N., and Chaturvedi, S. (2013). "Sunlight induced removal of Rhodamine B from water through Semiconductor Photocatalysis : Effects of Adsorption , Reaction Conditions and Additives." *Int. J. Mol. Sci.*, 11(4), 2336–2361.

Bloh, J. Z. (2019). "A Holistic Approach to Model the Kinetics of Photocatalytic Reactions." *Front. Chem.*, 7(14), 170.

Bo, H. Y., Tan, G. Q., Miao, H. Y., and Xia, A. (2010). "Co-Precipitation Synthesis of BiFeO$_3$ Powders." *Adv. Mater. Res.*, 105–106, 286–288.

Bonneau, R., Violet, P. F. de, and Joussot-Dubien, J. (1974). "Mechanism of photoreduction of thiazine dyes by edta studied by flash photolysis-ii. pH dependence of electron abstraction rate constant of the dyes in their triplet state." *Photochem. Photobiol.*, 19(2), 129–132.

Borges, M. E., Sierra, M., Cuevas, E., García, R. D., and Esparza, P. (2016). "Photocatalysis with solar energy: Sunlight-responsive photocatalyst based on TiO$_2$ loaded on a natural

material for wastewater treatment." *Sol. Energy*, 135, 527–535.

Boroski, M., Rodrigues, A. C., Garcia, J. C., Sampaio, L. C., Nozaki, J., and Hioka, N. (2009). "Combined electrocoagulation and TiO₂ photoassisted treatment applied to wastewater effluents from pharmaceutical and cosmetic industries." *J. Hazard. Mater.*, 162(1), 448–454.

Bosch Ojeda, C., and Sanchez Rojas, F. (2004). "Recent developments in derivative ultraviolet/visible absorption spectrophotometry." *Anal. Chim. Acta*, 518(1–2), 1–24.

BR, S., and XR, J. (2016). "Effect of Calcination Time on Structural, Optical and Antimicrobial Properties of Nickel Oxide Nanoparticles." *J. Theor. Comput. Sci.*, 03(02).

Brahimi, R., Bessekhouad, Y., Bouguelia, A., and Trari, M. (2007). "Visible light induced hydrogen evolution over the heterosystem Bi₂S₃/TiO₂." *Catal. Today*, 122(1–2), 62–65.

Bu, Y., and Chen, Z. (2014). "Role of Polyaniline on the Photocatalytic Degradation and Stability Performance of the Polyaniline/Silver/Silver Phosphate Composite under Visible Light." *ACS Appl. Mater. Interfaces*, 6(20), 17589–17598.

Bucci, J. D., Robertson, B. K., and James, W. J. (1972). "The precision determination of the lattice parameters and the coefficients of thermal expansion of BiFeO₃." *J. Appl. Crystallogr.*, 5(3), 187–191.

Bumajdad, A., and Madkour, M. (2014). "Understanding the superior photocatalytic activity of noble metals modified titania under UV and visible light irradiation." *Phys. Chem. Chem. Phys.*, 16(16), 7146.

Bunaciu, A. A., Udriştioiu, E. gabriela, and Aboul-Enein, H. Y. (2015). "X-Ray Diffraction: Instrumentation and Applications." *Crit. Rev. Anal. Chem.*, 45(4), 289–299.

Cai, J., Xin, W., Liu, G., Lin, D., and Zhu, D. (2016). "Effect of calcination temperature on structural properties and photocatalytic activity of Mn-C-codoped TiO₂." *Mater. Res.*, 19(2), 401–407.

Cai, L., Xu, T., Shen, J., and Xiang, W. (2015). "Highly efficient photocatalytic treatment of mixed dyes wastewater via visible-light-driven AgI–Ag₃PO₄/MWCNTs." *Mater. Sci. Semicond. Process.*, 37, 19–28.

Camargo, P. H. C., Satyanarayana, K. G., and Wypych, F. (2009). "Nanocomposites: synthesis, structure, properties and new application opportunities." *Mater. Res.*, 12(1), 1–39.

Cao, G. (2004). *Nanostructures and Nanomaterials - Synthesis, Properties and Applications*.

Imp. Coll. Press, World Scientific Series in Nanoscience and Nanotechnology, London: World scientific.

Cao, J., and Wang, M. (2015). "Novel $YBiO_3/Bi_2OB_3$ Heterostructured Composite with Its High Visible Light Photocatalytic Activity." *Mater.Focus*, 4(6), 487–492.

Cao, Y., Yu, Y., Zhang, P., Zhang, L., He, T., and Cao, Y. (2013). "An enhanced visible-light photocatalytic activity of TiO_2 by nitrogen and nickel–chlorine modification." *Sep. Purif. Technol.*, 104, 256–262.

Carneiro, J. O., Samantilleke, A. P., Parpot, P., Fernandes, F., Pastor, M., Correia, A., Luís, E. A., Chivanga Barros, A. A., and Teixeira, V. (2016). "Visible Light Induced Enhanced Photocatalytic Degradation of Industrial Effluents (Rhodamine B) in Aqueous Media Using TiO_2 Nanoparticles." *J. Nanomater.*, 2016, 1–13.

Carneiro, J. T., Savenije, T. J., Moulijn, J. A., and Mul, G. (2011). "How Phase Composition Influences Optoelectronic and Photocatalytic Properties of TiO_2." *J. Phys. Chem. C*, 115(5), 2211–2217.

Cha, W., Jeong, N. C., Song, S., Park, H. J., Thanh Pham, T. C., Harder, R., Lim, B., Xiong, G., Ahn, D., McNulty, I., Kim, J., Yoon, K. B., Robinson, I. K., and Kim, H. (2013). "Core-shell strain structure of zeolite microcrystals." *Nat. Mater.*, 12(8), 729–734.

Chanathaworn, J., Bunyakan, C., Wiyaratn, W., and Chungsiriporn, J. (2012). "Photocatalytic decolorization of basic dye by TiO_2 nanoparticle in photoreactor." *Songklanakarin J. Sci. Technol.*, 34(2), 203–210.

Chatterjee, D., Patnam, V. R., Sikdar, A., Joshi, P., Misra, R., and Rao, N. N. (2008a). "Kinetics of the decoloration of reactive dyes over visible light-irradiated TiO_2 semiconductor photocatalyst." *J.Hazard. Mater.*, 156(1–3), 435–441.

Chatterjee, D., Patnam, V. R., Sikdar, A., Joshi, P., Misra, R., and Rao, N. N. (2008b). "Kinetics of the decoloration of reactive dyes over visible light-irradiated TiO_2 semiconductor photocatalyst." *J.Hazard. Mater.*, 156(1–3), 435–441.

Chatterjee, M. J., Ahamed, S. T., Mitra, M., Kulsi, C., Mondal, A., and Banerjee, D. (2019). "Visible-light influenced photocatalytic activity of polyaniline -bismuth selenide composites for the degradation of MO, rhodamine B and malachite green dyes." *Appl. Surf. Sci.*, 470, 472–483.

Chaturvedi, S., Das, R., Poddar, P., and Kulkarni, S. (2015). "Tunable band gap and coercivity

of bismuth ferrite–polyaniline core–shell nanoparticles: the role of shell thickness." *RSC Adv.*, 5(30), 23563–23568.

Chaturvedi, S., Shirolkar, M. M., Rajendra, R., Singh, S., Ballav, N., and Kulkarni, S. (2014). "Coercivity and exchange bias of bismuth ferrite nanoparticles isolated by polymer coating." *J. Appl. Phys.*, 115(12), 123906.

Chellappa, M., Anjaneyulu, U., Manivasagam, G., and Vijayalakshmi, U. (2015). "Preparation and evaluation of the cytotoxic nature of TiO_2 nanoparticles by direct contact method." *Int. J. Nanomedicine*, 10, 31–41.

Chen, C.-C., Jaihindh, D., Hu, S.-H., and Fu, Y.-P. (2017a). "Magnetic recyclable photocatalysts of Ni-Cu-Zn ferrite@SiO_2@TiO_2@Ag and their photocatalytic activities." *J. Photochem. Photobiol. A Chem.*, 334, 74–85.

Chen, C., Cheng, J., Yu, S., Che, L., and Meng, Z. (2006). "Hydrothermal synthesis of perovskite bismuth ferrite crystallites." *J. Cryst. Growth*, 291(1), 135–139.

Chen, D., Niu, F., Qin, L., Wang, S., Zhang, N., and Huang, Y. (2017b). "Defective $BiFeO_3$ with surface oxygen vacancies: Facile synthesis and mechanism insight into photocatalytic performance." *Sol. Energy Mater. Sol. Cells*, 171, 24–32.

Chen, F., and Liu, P. (2011). "Conducting Polyaniline Nanoparticles and Their Dispersion for Waterborne Corrosion Protection Coatings." *ACS Appl. Mater. Interfaces*, 3(7), 2694–2702.

Chen, S., Wei, Z., Qi, X., Dong, L., Guo, Y.-G., Wan, L., Shao, Z., and Li, L. (2012). "Nanostructured Polyaniline-Decorated Pt/C@PANI Core–Shell Catalyst with Enhanced Durability and Activity." *J. Am. Chem. Soc.*, 134(32), 13252–13255.

Chen, X. Z., Qiu, Z. C., Zhou, J. P., Zhu, G., Bian, X. B., and Liu, P. (2011). "Large-scale growth and shape evolution of bismuth ferrite particles with a hydrothermal method." *Mater. Chem. Phys.*, 126(3), 560–567.

Chen, Y., Liu, Y., Xie, X., Li, C., Si, Y., Zhang, M., and Yan, Q. (2019). "Synthesis flower-like $BiVO_4$/BiOI core/shell heterostructure photocatalyst for tetracycline degradation under visible-light irradiation." *J. Mater. Sci. Mater. Electron.*, 30(10), 9311–9321.

Chen, Z., Jin, W., Lu, Z., and Hu, C. (2014). "Ferromagnetic and photocatalytic properties of pure $BiFeO_3$ powders synthesized by ethylene glycol assisted hydrothermal method." *J. Mater. Sci. Mater. Electron.*, 26(2), 1077–1086.

Chiou, C.-H., Wu, C.-Y., and Juang, R.-S. (2008). "Photocatalytic degradation of phenol and m-nitrophenol using irradiated TiO_2 in aqueous solutions." *Sep. Purif. Technol.*, 62(3), 559–564.

Chiou, M.-S., and Li, H.-Y. (2002). "Equilibrium and kinetic modeling of adsorption of reactive dye on cross-linked chitosan beads." *J.Hazard. Mater.*, 93(2), 233–248.

Chireh, M., and Naseri, M. (2019). "Effect of calcination temperature on the physical properties of $LiFe5O_8$ nanostructures." *Adv. Powder Technol.*, 30(5), 952–960.

Chiu, Y.-H., Chang, T.-F. M., Chen, C.-Y., Sone, M., and Hsu, Y.-J. (2019). "Mechanistic Insights into Photodegradation of Organic Dyes Using Heterostructure Photocatalysts." *Catalysts*, 9(5), 430.

Choi, R., Choi, S.-I., Choi, C. H., Nam, K. M., Woo, S. I., Park, J. T., and Han, S. W. (2013). "Designed Synthesis of Well-Defined Pd@Pt Core-Shell Nanoparticles with Controlled Shell Thickness as Efficient Oxygen Reduction Electrocatalysts." *Chem. - A Eur. J.*, 19(25), 8190–8198.

Chomkitichai, W., Pama, J., Jaiyen, P., Pano, S., Ketwaraporn, J., Pookmanee, P., Phanichphant, S., and Jansanthea, P. (2019). "Dye Mixtures Degradation by Multi-Phase $BiVO_4$ Photocatalyst." *Appl. Mech. Mater.*, 886, 138–145.

Coleto, U., Amoresi, R. A. C., Pereira, C. A. M., Simões, A. Z., Zaghete, M. A., Monteiro Filho, E. S., Longo, E., and Perazolli, L. A. (2019). "Influence of defects on photoluminescent and photocatalytic behavior of $CaO/SrTiO_3$ heterojunctions." *Ceram. Int.*, 45(12), 15244–15251.

Contineanu, M., Contineanu, M., Bercu, C., Contineanu, M., Bercu, C., Contineanu, I., Bercu, C., and Neacsu, A. (2009). "a Chemical and Photochemical Study of Radicalic Species Formed in Methylene Blue Acidic and Basic Aqueous Solutions." *Analele Univ.*, 18(2).

Costa, F. A. P., Reis, E. M. dos, Azevedo, J. C. R., and Nozaki, J. (2004). "Bleaching and photodegradation of textile dyes by H_2O_2 and solar or ultraviolet radiation." *Sol. Energy*, 77(1), 29–35.

Costa, J. C., and Alves, M. M. (2013). "Posttreatment of olive mill wastewater by immobilized TiO_2 photocatalysis." *Photochem. Photobiol.*, 89(3), 545–51.

Cui, W., He, J., Wang, H., Hu, J., Liu, L., and Liang, Y. (2018). "Polyaniline hybridization promotes photo-electro-catalytic removal of organic contaminants over 3D network structure

of rGH-PANI/TiO$_2$ hydrogel." *Appl. Catal. B Environ.*, 232, 232–245.

Daneshvar, N., Rasoulifard, M. H., Khataee, A. R., and Hosseinzadeh, F. (2007). "Removal of C.I. Acid Orange 7 from aqueous solution by UV irradiation in the presence of ZnO nanopowder." *J. Hazard. Mater.*, 143(1–2), 95–101.

Daneshvar, N., Salari, D., and Khataee, A. . (2004). "Photocatalytic degradation of azo dye acid red 14 in water on ZnO as an alternative catalyst to TiO$_2$." *J. Photochem. Photobiol. A Chem.*, 162(2–3), 317–322.

Daniel, M.-C., and Astruc, D. (2004). "Gold Nanoparticles: Assembly, Supramolecular Chemistry, Quantum-Size-Related Properties, and Applications toward Biology, Catalysis, and Nanotechnology." *Chem. Rev.*, 104(1), 293–346.

Darroudi, M. (2011). "Time-dependent effect in green synthesis of silver nanoparticles." *Int. J. Nanomedicine*, 677.

Das, R., Khan, G. G., Varma, S., Mukherjee, G. D., and Mandal, K. (2013). "Effect of Quantum Confinement on Optical and Magnetic Properties of Pr–Cr-Codoped Bismuth Ferrite Nanowires." *J. Phys. Chem. C*, 117(39), 20209–20216.

Davis, R. J., Gainer, J. L., O'Neal, G., and Wu, I.-W. (1994). "Photocatalytic decolorization of wastewater dyes." *Water Environ. Res.*, 66(1), 50–53.

Dendisová, M., Jeništová, A., Parchaňská-Kokaislová, A., Matějka, P., Prokopec, V., and Švecová, M. (2018). "The use of infrared spectroscopic techniques to characterize nanomaterials and nanostructures: A review." *Anal. Chim. Acta*, 1031, 1–14.

Deng, Y., and Englehardt, J. D. (2006). "Treatment of landfill leachate by the Fenton process." *Water Res.*, 40(20), 3683–3694.

Desiati, R. D., Taspika, M., and Sugiarti, E. (2019). "Effect of calcination temperature on the antibacterial activity of TiO$_2$ /Ag nanocomposite." *Mater. Res. Express*, 6(9), 095059.

Devadiga, A., Vidya Shetty, K., and Saidutta, M. B. (2017). "Highly stable silver nanoparticles synthesized using Terminalia catappa leaves as antibacterial agent and colorimetric mercury sensor." *Mater. Lett.*, 207(1), 66–71.

Dhanalakshmi, R., Muneeswaran, M., Vanga, P. R., Ashok, M., and Giridharan, N. V. (2016). "Enhanced photocatalytic activity of hydrothermally grown BiFeO$_3$ nanostructures and role of catalyst recyclability in photocatalysis based on magnetic framework." *Appl. Phys. A Mater.*

Sci. Process., 122(1), 1–14.

Dodd, A. C., McKinley, A. J., Saunders, M., and Tsuzuki, T. (2006). "Effect of Particle Size on the Photocatalytic Activity of Nanoparticulate Zinc Oxide." *J. Nanoparticle Res.*, 8(1), 43–51.

Dong, F., Zhao, W., Wu, Z., and Guo, S. (2009). "Band structure and visible light photocatalytic activity of multi-type nitrogen doped TiO_2 nanoparticles prepared by thermal decomposition." *J. Hazard. Mater.*, 162(2–3), 763–770.

Doong, R.-A., Chen, C.-H., Maithreepala, R. ., and Chang, S.-M. (2001). "The influence of pH and cadmium sulfide on the photocatalytic degradation of 2-chlorophenol in titanium dioxide suspensions." *Water Res.*, 35(12), 2873–2880.

Douissa, N. Ben, Dridi-Dhaouadi, S., and Mhenni, M. F. (2014). "Study of antagonistic effect in the simultaneous removal of two textile dyes onto cellulose extracted from Posidonia oceanica using derivative spectrophotometric method." *J. Water Process Eng.*, 2, 1–9.

Douvalis, A. P., Zboril, R., Bourlinos, A. B., Tucek, J., Spyridi, S., and Bakas, T. (2012). "A facile synthetic route toward air-stable magnetic nanoalloys with Fe–Ni/Fe–Co core and iron oxide shell." *J. Nanoparticle Res.*, 14(9), 1130.

Dudhe, C. M., and Nagdeote, S. B. (2014). "Effect of Reaction Rate and Calcination Time on $CaNb_2O_6$ Nanoparticles." *J. Nanosci.*, 2014, 1–5.

Dunn, S., Jones, P. M., and Gallardo, D. E. (2007). "Photochemical growth of silver nanoparticles on c(-) and c(+) domains on lead zirconate titanate thin films." *J. Am. Chem. Soc.*, 129(28), 8724–8.

Egorysheva, A. V., Volodin, V. D., Milenov, T., Rafailov, P., Skorikov, V. M., and Dudkina, T. D. (2010). "Glass formation in the $CaO-Bi_2O_3-B_2O_3$ and $SrO-Bi_2O$ $3-B_2O_3$ systems." *Russ. J. Inorg. Chem.*, 55(11).

Ekrami, E., Okazi, M., Kang, Q., Zhou, W., Li, Q., Gao, B., Fan, J., Shen, D., Turabik, M., Rojas, F. S., Ojeda, C. B., Pavon, J. M., Lettre, D. P., Patel, K. N., Patel, J. K., Rajput, G. C., Rajgor, N. B., Sahel, K., Perol, N., Dappozze, F., Bouhent, M., Derriche, Z., and Guillard, C. (2010). "Analysis of dye concentrations using derivative spectrophotometric techniques." *Talanta*, 212(4), 139–150.

Elsayed, M. A., and Gobara, M. (2016). "Enhancement removal of tartrazine dye using HCl-doped polyaniline and TiO_2 -decorated PANI particles." *Mater. Res. Express*, 3(8), 085301.

Eskizeybek, V., Sarı, F., Gülce, H., Gülce, A., and Avcı, A. (2012). "Preparation of the new polyaniline/ZnO nanocomposite and its photocatalytic activity for degradation of methylene blue and malachite green dyes under UV and natural sun lights irradiations." *Appl. Catal. B Environ.*, 119–120, 197–206.

European Food Safety Authority. (2010). "Scientific Opinion on Dietary Reference Values for fats, including saturated fatty acids, polyunsaturated fatty acids, monounsaturated fatty acids, trans fatty acids, and cholesterol." *EFSA J.*, 8(3).

Fakhri, A., and Behrouz, S. (2015). "Photocatalytic properties of tungsten trioxide (WO_3) nanoparticles for degradation of Lidocaine under visible and sunlight irradiation." *Sol. Energy*, 112, 163–168.

Fan, H., Jiang, T., Li, H., Wang, D., Wang, L., Zhai, J., He, D., Wang, P., and Xie, T. (2012). "Effect of $BiVO_4$ Crystalline Phases on the Photoinduced Carriers Behavior and Photocatalytic Activity." *J. Phys. Chem. C*, 116(3), 2425–2430.

Farhadi, S., and Zaidi, M. (2009). "Bismuth ferrite ($BiFeO_3$) nanopowder prepared by sucrose-assisted combustion method: A novel and reusable heterogeneous catalyst for acetylation of amines, alcohols and phenols under solvent-free conditions." *J. Mol. Catal. A Chem.*, 299(1–2), 18–25.

Fatima, S., Ali, S. I., Iqbal, M. Z., and Rizwan, S. (2017). "The high photocatalytic activity and reduced band gap energy of La and Mn co-doped BiFeO 3 /graphene nanoplatelet (GNP) nanohybrids." *RSC Adv.*, 7(57), 35928–35937.

Fatin, S. O., Lim, H. N., Tan, W. T., and Huang, N. M. (2012). "Comparison of photocatalytic activity and cyclic voltammetry of zinc oxide and titanium dioxide nanoparticles toward degradation of methylene blue." *Int. J. Electrochem. Sci.*, 7(10), 9070–9084.

Feng, T., Yin, H., Jiang, H., Chai, X., Li, X., Li, D., Wu, J., Liu, X., and Sun, B. (2019). "Design and fabrication of polyaniline/Bi 2 MoO 6 nanocomposites for enhanced visible-light-driven photocatalysis." *New J. Chem.*, 43(24), 9606–9613.

Feng, Y., Lin, S., Huang, S., Shrestha, S., and Conibeer, G. (2015). "Can Tauc plot extrapolation be used for direct-band-gap semiconductor nanocrystals?" *J. Appl. Phys.*, 117(12), 125701.

Ferrari, C., Chen, H., Lavezza, R., Santinelli, C., Longo, I., and Bramanti, E. (2013). "Photodegradation of Rhodamine B Using the Microwave/UV/H_2O_2: Effect of Temperature."

Int. J. Photoenergy, 2013, 1–12.

Fonzo, F. Di, Casari, C. S., Russo, V., Brunella, M. F., Li Bassi, A., and Bottani, C. E. (2009). "Hierarchically organized nanostructured TiO$_2$ for photocatalysis applications." *Nanotechnology*, 20(1), 015604.

Freeman, R. G., Grabar, K. C., Allison, K. J., Bright, R. M., Davis, J. A., Guthrie, A. P., Hommer, M. B., Jackson, M. A., Smith, P. C., Walter, D. G., and Natan, M. J. (1995). "Self-Assembled Metal Colloid Monolayers: An Approach to SERS Substrates." *Science (80-.).*, 267(5204), 1629–1632.

Freger, V. (2000). "Separation of concentrated organic/inorganic salt mixtures by nanofiltration." *J. Memb. Sci.*, 178(1–2), 185–193.

Fuerte, A., Hernández-Alonso, M. D., Maira, A. J., Martínez-Arias, A., Fernández-García, M., Conesa, J. C., Soria, J., and Munuera, G. (2002). "Nanosize Ti–W Mixed Oxides: Effect of Doping Level in the Photocatalytic Degradation of Toluene Using Sunlight-Type Excitation." *J. Catal.*, 212(1), 1–9.

Gabbasova, Z. V., Kuz'min, M. D., Zvezdin, A. K., Dubenko, I. S., Murashov, V. A., Rakov, D. N., and Krynetsky, I. B. (1991). "Bi1-xRxFeO$_3$ (R=rare earth): a family of novel magnetoelectrics." *Phys. Lett. A*, 158(9), 491–498.

Gadigayya Mavinkattimath, R., Shetty Kodialbail, V., and Govindan, S. (2017). "Simultaneous adsorption of Remazol brilliant blue and Disperse orange dyes on red mud and isotherms for the mixed dye system." *Environ. Sci. Pollut. Res.*, 24(23), 18912–18925.

Gage, S. H., Hickman, M., Heron, J., Munafò, M. R., Lewis, G., Macleod, J., and Zammit, S. (2014). "Associations of cannabis and cigarette use with psychotic experiences at age 18: findings from the Avon Longitudinal Study of Parents and Children." *Psychol. Med.*, 44(16), 3435–3444.

Gahr, F., Hermanutz, F., and Oppermann, W. (1994). "Ozonation - An important technique to comply with new German laws for textile wastewater treatment." *Water Sci. Technol.*, 30(3)225.

Gajjar, R. B. (1989). "Solar radiation, photosynthetically active radiation and thermal time relationship with crop growth in summer groundnut (Arachis hypogaea l.)." Anand Agricultural University.

Galceran, M., Pujol, M. C., Aguiló, M., and Díaz, F. (2007). "Sol-gel modified Pechini method

for obtaining nanocrystalline KRE(WO$_4$)$_2$ (RE = Gd and Yb)." *J. Sol-Gel Sci. Technol.*, 42(1), 79–88.

Gamez, G., Gardea-Torresdey, J. ., Tiemann, K. ., Parsons, J., Dokken, K., and Jose Yacaman, M. (2003). "Recovery of gold(III) from multi-elemental solutions by alfalfa biomass." *Adv. Environ. Res.*, 7(2), 563–571.

Ganapathi, P. (2015). "Study of structural and magnetic properties of some hexaferrite material." 2014.

Ganguli, A. K., Das, A., and Natarajan, K. (2020). "Core-Shell Type Semiconducting Heterostructures for Visible Light Photocatalysis." *Chem. Rec.*, 20(5), 371–388.

Gao, F., Chen, X. Y., Yin, K. B., Dong, S., Ren, Z. F., Yuan, F., Yu, T., Zou, Z. G., and Liu, J.-M. J. M. J.-M. (2007). "Visible-Light Photocatalytic Properties of Weak Magnetic BiFeO$_3$ Nanoparticles." *Adv. Mater.*, 19(19), 2889–2892.

Gao, F., Yuan, Y., Wang, K. F., Chen, X. Y., Chen, F., Liu, J. M., and Ren, Z. F. (2006). "Preparation and photoabsorption characterization BiFeO$_3$ nanowires." *Appl. Phys. Lett.*, 89(10), 3–5.

Gao, J., Zhang, Q., Su, K., Chen, R., and Peng, Y. (2010). "Biosorption of Acid Yellow 17 from aqueous solution by non-living aerobic granular sludge." *J. Hazard. Mater.*, 174(1–3), 215–225.

Gao, J., Zhao, Y., Yang, W., Tian, J., Guan, F., Ma, Y., Hou, J., Kang, J., and Wang, Y. (2003). "Preparation of samarium oxide nanoparticles and its catalytic activity on the esterification." *Mater. Chem. Phys.*, 77(1), 65–69.

Gao, T., Chen, Z., Huang, Q., Niu, F., Huang, X., Qin, L., and Huang, Y. (2015a). "a Review : Preparation of Bismuth Ferrite Nanoparticles and Its Applications in Visible-Light Induced Photocatalyses." *Rev. Adv. Mater. Sci.*, 40, 97–109.

Gao, T., Chen, Z., Niu, F., Zhou, D., Huang, Q., Zhu, Y., Qin, L., Sun, X., and Huang, Y. (2015b). "Shape-controlled preparation of bismuth ferrite by hydrothermal method and their visible-light degradation properties." *J. Alloys Compd.*, 648, 564–570.

Gao, T., Chen, Z., Zhu, Y., Niu, F., Huang, Q., Qin, L., Sun, X., and Huang, Y. (2014). "Synthesis of BiFeo 3 nanoparticles for the visible-light induced photocatalytic property." *Mater. Res. Bull.*, 59, 6–12.

García-Montaño, J., Torrades, F., Pérez-Estrada, L. A., Oller, I., Malato, S., Maldonado, M. I., and Peral, J. (2008). "Degradation pathways of the commercial reactive azo dye Procion Red H-E7B under solar-assisted photo-fenton reaction." *Environ. Sci. Technol.*, 42(17), 6663–6670.

Garg, A., Sangal, V. K., and Bajpai, P. K. (2016). "Decolorization and degradation of Reactive Black 5 dye by photocatalysis: modeling, optimization and kinetic study." *Desalin. Water Treat.*, 57(38), 18003–18015.

Garg, A., Sangal, V. K., and Bajpai, P. K. (2017). "Photocatalytic Treatment of Binary Mixture of Dyes using UV/TiO$_2$ Process: Calibration, Modeling, Optimization and Mineralization Study." *Int. J. Chem. React. Eng.*, 15(2).

Gautam, A., Kshirsagar, A., Biswas, R., Banerjee, S., and Khanna, P. K. (2016). "Photodegradation of organic dyes based on anatase and rutile TiO$_2$ nanoparticles." *RSC Adv.*, 6(4), 2746–2759.

Gawande, M. B., Goswami, A., Asefa, T., Guo, H., Biradar, A. V., Peng, D.-L., Zboril, R., and Varma, R. S. (2015). "Core–shell nanoparticles: synthesis and applications in catalysis and electrocatalysis." *Chem. Soc. Rev.*, 44(21), 7540–7590.

Geng, L., Zhao, Y., Huang, X., Wang, S., Zhang, S., and Wu, S. (2007). "Characterization and gas sensitivity study of polyaniline/SnO$_2$ hybrid material prepared by hydrothermal route." *Sensors Actuators B Chem.*, 120(2), 568–572.

Ghadami, F., and Rouh Aghdam, A. S. (2020). "Preparation of NiCrAlY/nano-CeO$_2$ powder with the core-shell structure using high-velocity oxy-fuel spraying process." *Mater. Chem. Phys.*, 243, 122551.

Ghaly, H. A., El-Kalliny, A. S., Gad-Allah, T. A., Abd El-Sattar, N. E. A., and Souaya, E. R. (2017). "Stable plasmonic Ag/AgCl–polyaniline photoactive composite for degradation of organic contaminants under solar light." *RSC Adv.*, 7(21), 12726–12736.

Gharagozlou, M. (2011). "Influence of calcination temperature on structural and magnetic properties of nanocomposites formed by Co-ferrite dispersed in sol-gel silica matrix using tetrakis(2-hydroxyethyl) orthosilicate as precursor." *Chem. Cent. J.*, 5(1), 19.

Gheorghiu, F., Tanasa, R., Buscaglia, M. T., Buscaglia, V., Pastravanu, C. G., Popovici, E., and Mitoseriu, L. (2013). "Preparation of Bi$_2$Fe$_4$O$_9$ particles by hydrothermal synthesis and functional properties." *Phase Transitions*, 86(7), 726–736.

Ghosh Chaudhuri, R., and Paria, S. (2012). "Core/Shell Nanoparticles: Classes, Properties,

Synthesis Mechanisms, Characterization, and Applications." *Chem. Rev.*, 112(4), 2373–2433.

Gilja, V., Novaković, K., Travas-Sejdic, J., Hrnjak-Murgić, Z., Kraljić Roković, M., Žic, M., Gilja, V., Novaković, K., Travas-Sejdic, J., Kraljić Roković, M., and Hrnjak-Murgić, Z. (2017). "Stability and Synergistic Effect of Polyaniline/TiO$_2$ Photocatalysts in Degradation of Azo Dye in Wastewater." *Nanomaterials*, 7(12), 412.

Gilja, V., Vrban, I., Mandić, V., Žic, M., and Hrnjak-Murgić, Z. (2018). "Preparation of a PANI/ZnO Composite for Efficient Photocatalytic Degradation of Acid Blue." *Polymers (Basel).*, 10(9), 940.

Giwa, A. (2012). "Photocatalytic Decolourization and Degradation of C. I. Basic Blue 41 Using TiO$_2$ Nanoparticles." *J. Environ. Prot. (Irvine,. Calif).*, 03(09), 1063–1069.

Glaze, W. H., Kenneke, J. F., and Ferry, J. L. (1993). "Chlorinated byproducts from the titanium oxide-mediated photodegradation of trichloroethylene and tetrachloroethylene in water." *Environ. Sci. Technol.*, 27(1), 177–184.

Glimcher, P. W., and Sparks, D. L. (1992). "Movement selection in advance of action in the superior colliculus." *Nature*, 355(6360), 542–545.

Gnanaprakasam, A., Sivakumar, V. M., and Thirumarimurugan, M. (2015). "Influencing Parameters in the Photocatalytic Degradation of Organic Effluent via Nanometal Oxide Catalyst : A Review." *Indian J. Mater. Sci.*, 2015, 1–16.

Gogate, P. R., and Pandit, A. B. (2004). "A review of imperative technologies for wastewater treatment I: oxidation technologies at ambient conditions." *Adv. Environ. Res.*, 8(3–4), 501–551.

Golsheikh, A. M., Lim, H. N., Zakaria, R., and Huang, N. M. (2015). "Sonochemical synthesis of reduced graphene oxide uniformly decorated with hierarchical ZnS nanospheres and its enhanced photocatalytic activities." *RSC Adv.*, 5(17), 12726–12735.

Gomathi, T., Rajeshwari, K., Kanchana, V., Sudha, P. N., and Parthasarathy, K. (2019). "Impact of Nanoparticle Shape, Size, and Properties of the Sustainable Nanocomposites." *Sustain. Polym. Compos. Nanocomposites*, Cham: Springer International Publishing, 313–336.

Goncalves, M., Pinto, E., Nkeonye, P., and Oliveiracampos, A. (2005). "Degradation of and its simulated dyebath wastewater by heterogeneous photocatalysis." *Dye. Pigment.*, 64(2), 135–139.

Gong, L., Zhou, Z., Wang, S., and Wang, B. (2013). "Preparation and characterization of BiFeO$_3$@Ce-doped TiO$_2$ core-shell structured nanocomposites." *Mater. Sci. Semicond. Process.*, 16(2), 288–294.

Gözmen, B., Turabik, M., and Hesenov, A. (2009). "Photocatalytic degradation of Basic Red 46 and Basic Yellow 28 in single and binary mixture by UV/TiO$_2$/periodate system." *J. Hazard. Mater.*, 164(2–3), 1487–1495.

Grzechulska, J., and Morawski, A. W. (2002). "Photocatalytic decomposition of azo-dye acid black 1 in water over modified titanium dioxide." *Appl. Catal. B Environ.*, 36(1), 45–51.

Guillard, C., Disdier, J., Monnet, C., Dussaud, J., Malato, S., Blanco, J., Maldonado, M. I., and Herrmann, J.-M. (2003). "Solar efficiency of a new deposited titania photocatalyst: chlorophenol, pesticide and dye removal applications." *Appl. Catal. B Environ.*, 46(2), 319–332.

Guimard, N. K., Gomez, N., and Schmidt, C. E. (2007). "Conducting polymers in biomedical engineering." *Prog. Polym. Sci.*, 32(8–9), 876–921.

Gülce, H., Eskizeybek, V., Haspulat, B., Sarı, F., Gülce, A., and Avcı, A. (2013). "Preparation of a New Polyaniline/CdO Nanocomposite and Investigation of Its Photocatalytic Activity: Comparative Study under UV Light and Natural Sunlight Irradiation." *Ind. Eng. Chem. Res.*, 52(32), 10924–10934.

Gunture, Singh, A., Bhati, A., Khare, P., Tripathi, K. M., and Sonkar, S. K. (2019). "Soluble Graphene Nanosheets for the Sunlight-Induced Photodegradation of the Mixture of Dyes and its Environmental Assessment." *Sci. Rep.*, 9(1), 2522.

Guo, C., Xu, J., He, Y., Zhang, Y., and Wang, Y. (2011). "Photodegradation of rhodamine B and MO over one-dimensional TiO$_2$ catalysts under simulated solar irradiation." *Appl. Surf. Sci.*, 257(8), 3798–3803.

Guo, H., Yin, H., Yan, X., Shi, S., Yu, Q., Cao, Z., and Li, J. (2016). "Pt-Bi decorated nanoporous gold for high performance direct glucose fuel cell." *Sci. Rep.*, 6(1), 39162.

Gupta, A. K., Pal, A., and Sahoo, C. (2006). "Photocatalytic degradation of a mixture of Crystal Violet (Basic Violet 3) and Methyl Red dye in aqueous suspensions using Ag+ doped TiO$_2$." *Dye. Pigment.*, 69(3), 224–232.

Gupta, K. K., Singh, N. L., Pandey, A., Shukla, S. K., Upadayay, S. N., Mishra, V., Srivastava, P., Lalla, N. P., and Mishra, P. K. (2013). "Effect of Anatase/Rutile TiO$_2$ Phase Composition

on Arsenic Adsorption." *J. Dispers. Sci. Technol.*, 34(8), 1043–1052.

Gupta, V. K., Saravanan, R., Agarwal, S., Gracia, F., Khan, M. M., Qin, J., and Mangalaraja, R. V. (2017). "Degradation of azo dyes under different wavelengths of UV light with chitosan-SnO_2 nanocomposites." *J. Mol. Liq.*, 232, 423–430.

Gupta, V. K., Suhas, Nayak, A., Agarwal, S., Chaudhary, M., and Tyagi, I. (2014). "Removal of Ni (II) ions from water using scrap tire." *J. Mol. Liq.*, 190, 215–222.

Habibi-Yangjeh, A., Pirhashemi, M., and Ghosh, S. (2020). "$ZnO/ZnBi_2O_4$ nanocomposites with p-n heterojunction as durable visible-light-activated photocatalysts for efficient removal of organic pollutants." *J. Alloys Compd.*, 826, 154229.

Habibi-Yangjeh, A., and Shekofteh-Gohari, M. (2019). "Synthesis of magnetically recoverable visible-light-induced photocatalysts by combination of Fe_3O_4/ZnO with BiOI and polyaniline." *Prog. Nat. Sci. Mater. Int.*, 29(2), 145–155.

Habibi, M. H., and Vosooghian, H. (2005). "Photocatalytic degradation of some organic sulfides as environmental pollutants using titanium dioxide suspension." *J. Photochem. Photobiol. A Chem.*, 174(1), 45–52.

Haldar, S., Dixit, V. K., Vashisht, G., Khamari, S. K., Porwal, S., Sharma, T. K., and Oak, S. M. (2017). "Effect of carrier confinement on effective mass of excitons and estimation of ultralow disorder in Al x Ga1−x As/GaAs quantum wells by magneto-photoluminescence." *Sci. Rep.*, 7(1), 4905.

Hamadanian, M., Reisi-Vanani, a., and Majedi, a. (2010). "Sol-gel preparation and characterization of Co/TiO_2 nanoparticles: Application to the degradation of MO." *J. Iran. Chem. Soc.*, 7(S2), S52–S58.

Handayani, W., Ningrum, A. S., and Imawan, C. (2020). "The Role of pH in Synthesis Silver Nanoparticles Using Pometia pinnata (Matoa) Leaves Extract as Bioreductor." *J. Phys. Conf. Ser.*, 1428, 012021.

Hao, X., Gong, J., Ren, L., Zhang, D., Xiao, X., Jiang, Y., Zhang, F., and Tong, Z. (2017). "Preparation of polyaniline modified BiOBr with enhanced photocatalytic activities." *Funct. Mater. Lett.*, 10(04), 1750040.

Hardy, A., Gielis, S., Rul, H. Van den, D'Haen, J., Bael, M. K. Van, and Mullens, J. (2009). "Effects of precursor chemistry and thermal treatment conditions on obtaining phase pure bismuth ferrite from aqueous gel precursors." *J. Eur. Ceram. Soc.*, 29(14), 3007–3013.

Haruna, A., Abdulkadir, I., and Idris, S. O. (2020). "Photocatalytic activity and doping effects of BiFeO$_3$ nanoparticles in model organic dyes." *Heliyon*, 6(1), e03237.

Hassan Zaki, A., and Mohamed Ali. El Rouby, W. (2019). "Selective Photodegradation Using Titanate Nanostructures." *Photocatal. - Appl. Attrib.*, IntechOpen.

Hatchett, D. W., and Josowicz, M. (2008). "Composites of Intrinsically Conducting Polymers as Sensing Nanomaterials." *Chem. Rev.*, 108(2), 746–769.

He, X., and Zhang, C. (2019). "Recent advances in structure design for enhancing photocatalysis." *J. Mater. Sci.*, 54(12), 8831–8851.

Hengky, C. (2013). "Synthesis and Characterisation of Nanostructured BiFeO$_3$ for Photodecolourisation of Azo Dyes Using Visible Light." Cranfield University.

Hengky, C., Moya, X., Mathur, N. D., and Dunn, S. (2012). "Evidence of high rate visible light photochemical decolourisation of Rhodamine B with BiFeO$_3$ nanoparticles associated with BiFeO$_3$ photocorrosion." *RSC Adv.*, 2(31), 11843.

Herrmann, J.-M. (1999). "Heterogeneous photocatalysis: fundamentals and applications to the removal of various types of aqueous pollutants." *Catal. Today*, 53(1), 115–129.

Hiragond, C. B., Khanna, P. K., and More, P. V. (2018). "Probing the real-time photocatalytic activity of CdS QDs sensitized conducting polymers: Featured PTh, PPy and PANI." *Vacuum*, 155, 159–168.

Hirakawa, T., and Kamat, P. V. (2005). "Charge Separation and Catalytic Activity of Ag@TiO$_2$ Core−Shell Composite Clusters under UV−Irradiation." *J. Am. Chem. Soc.*, 127(11), 3928–3934.

Hoffmann, M. R., Martin, S. T., Choi, W., Bahnemannt, D. W., and Bahnemann, D. W. (1995). "Environmental Applications of Semiconductor Photocatalysis." *Chem. Rev.*, 95(1), 69–96.

Homaeigohar, S. (2020). "The Nanosized Dye Adsorbents for Water Treatment." *Nanomaterials*, 10(2), 295.

Hu, R., Xiao, X., Tu, S., Zuo, X., and Nan, J. (2015a). "Synthesis of flower-like heterostructured β-Bi2O$_3$/Bi2O$_2$CO$_3$ microspheres using Bi2O$_2$CO$_3$ self-sacrifice precursor and its visible-light-induced photocatalytic degradation of o-phenylphenol." *Appl. Catal. B Environ.*, 163, 510–519.

Hu, W., Liu, Y., Withers, R. L., Frankcombe, T. J., Norén, L., Snashall, A., Kitchin, M., Smith,

P., Gong, B., Chen, H., Schiemer, J., Brink, F., and Wong-Leung, J. (2013). "Electron-pinned defect-dipoles for high-performance colossal permittivity materials." *Nat. Mater.*, 12(9), 821–826.

Hu, Z., Zu, L., Jiang, Y., Lian, H., Liu, Y., Li, Z., Chen, F., Wang, X., and Cui, X. (2015b). "High Specific Capacitance of Polyaniline/Mesoporous Manganese Dioxide Composite Using KI-H2SO4 Electrolyte." *Polymers (Basel).*, 7(10), 1939–1953.

Huang, J., Virji, S., Weiller, B. H., and Kaner, R. B. (2003). "Polyaniline Nanofibers: Facile Synthesis and Chemical Sensors." *J. Am. Chem. Soc.*, 125(2), 314–315.

Huang, K., and Wan, M. (2002). "Self-Assembled Polyaniline Nanostructures with Photoisomerization Function." *Chem. Mater.*, 14(8), 3486–3492.

Humayun, M., Zada, A., Li, Z., Xie, M., Zhang, X., Qu, Y., Raziq, F., and Jing, L. (2016). "Enhanced visible-light activities of porous BiFeO$_3$ by coupling with nanocrystalline TiO$_2$ and mechanism." *Appl. Catal. B Environ.*, 180(July 2015), 219–226.

Huo, Y., Jin, Y., and Zhang, Y. (2010). "Citric acid assisted solvothermal synthesis of BiFeO$_3$ microspheres with high visible-light photocatalytic activity." *J. Mol. Catal. A Chem.*, 331(1–2), 15–20.

Huo, Y., Miao, M., Zhang, Y., Zhu, J., and Li, H. (2011). "Aerosol-spraying preparation of a mesoporous hollow spherical BiFeO$_3$ visible photocatalyst with enhanced activity and durability." *Chem. Commun.*, 47(7), 2089–2091.

Ikeda, S., Sugiyama, N., Pal, B., Marcí, G., Palmisano, L., Noguchi, H., Uosaki, K., and Ohtani, B. (2001). "Photocatalytic activity of transition-metal-loaded titanium(IV) oxide powders suspended in aqueous solutions: Correlation with electron–hole recombination kinetics." *Phys. Chem. Chem. Phys.*, 3(2), 267–273.

Ishihara, T., Baik, N. S., Ono, N., Nishiguchi, H., and Takita, Y. (2004). "Effects of crystal structure on photolysis of H$_2$O on K–Ta mixed oxide." *J. Photochem. Photobiol. A Chem.*, 167(2–3), 149–157.

Ishii, M., Kato, H., Hashimoto, I., and Homma, Y. (2013). "Graphite-encapsulated alumina nanoparticles fabricated by hot-filament chemical vapor deposition." *Mater. Express*, 3(4), 355–359.

Islam, M. R., Zubair, M. A., Bashar, M. S., and Rashid, A. K. M. B. (2019). "Bi$_{0.9}$HO$_{0.1}$FeO$_3$/TiO$_2$ Composite Thin Films: Synthesis and Study of Optical, Electrical and

Magnetic Properties." *Sci. Rep.*, 1–13.

Jang, S. H., Han, M. G., and Im, S. S. (2000). "Preparation and characterization of conductive polyaniline/silica hybrid composites prepared by sol–gel process." *Synth. Met.*, 110(1), 17–23.

Jantawasu, P., Sreethawong, T., and Chavadej, S. (2009). "Photocatalytic activity of nanocrystalline mesoporous-assembled TiO2 photocatalyst for degradation of MO monoazo dye in aqueous wastewater." *Chem. Eng. J.*, 155(1–2), 223–233.

Jiang, H. L., Akita, T., Ishida, T., Haruta, M., and Xu, Q. (2011a). "Synergistic catalysis of Au@Ag core-shell nanoparticles stabilized on metal-organic framework." *J. Am. Chem. Soc.*, 133(5), 1304–1306.

Jiang, J., Zou, J., Anjum, M. N., Yan, J., Huang, L., Zhang, Y., and Chen, J. (2011b). "Synthesis and characterization of wafer-like BiFeO3 with efficient catalytic activity." *Solid State Sci.*, (9), 1779–1785.

Jiang, K., Zhu, J. J., Wu, J. D., Sun, J., Hu, Z. G., and Chu, J. H. (2011c). "Influences of Oxygen Pressure on Optical Properties and Interband Electronic Transitions in Multiferroic Bismuth Ferrite Nanocrystalline Films Grown by Pulsed Laser Deposition." *ACS Appl. Mater. Interfaces*, 3(12), 4844–4852.

Jing, J., Feng, J., Li, W., and Yu, W. W. (2013). "Low-temperature synthesis of water-dispersible anatase titanium dioxide nanoparticles for photocatalysis." *J. Colloid Interface Sci.*, 396, 90–94.

Jones, P. M., Gallardo, D. E., and Dunn, S. (2008). "Photochemical investigation of a polarizable semiconductor, lead-zirconate-titanate." *Chem. Mater.*, 20(18), 5901–5906.

Ju, L., Chen, Z., Fang, L., Dong, W., Zheng, F., and Shen, M. (2011). "Sol-Gel Synthesis and Photo-Fenton-Like Catalytic Activity of EuFeO 3 Nanoparticles." *J. Am. Ceram. Soc.*, 94(10), 3418–3424.

Ju, M.-G., Wang, X., Liang, W., Zhao, Y., and Li, C. (2014). "Tuning the energy band-gap of crystalline gallium oxide to enhance photocatalytic water splitting: mixed-phase junctions." *J. Mater. Chem. A*, 2(40), 17005–17014.

Juang, R.-S., Lin, S.-H., and Hsueh, P.-Y. (2010). "Removal of binary azo dyes from water by UV-irradiated degradation in TiO2 suspensions." *J. Hazard. Mater.*, 182(1–3), 820–826.

Kabra, K., Chaudhary, R., and Sawhney, R. L. (2004). "Treatment of Hazardous Organic and

Inorganic Compounds through Aqueous-Phase Photocatalysis: A Review." *Ind. Eng. Chem. Res.*, 43(24), 7683–7696.

Kalikeri, S., Kamath, N., Gadgil, D. J., and Shetty Kodialbail, V. (2018). "Visible light-induced photocatalytic degradation of Reactive Blue-19 over highly efficient polyaniline-TiO$_2$ nanocomposite: a comparative study with solar and UV photocatalysis." *Environ. Sci. Pollut. Res.*, 25(4), 3731–3744.

Kalikeri, S., and Shetty Kodialbail, V. (2018). "Solar light-driven photocatalysis using mixed-phase bismuth ferrite (BiFeO$_3$/Bi$_{25}$FeO$_{40}$) nanoparticles for remediation of dye-contaminated water: kinetics and comparison with artificial UV and visible light-mediated photocatalysis." *Environ. Sci. Pollut. Res.*, 25(14), 13881–13893.

Kalpaklı, Y., Toygun, Ş., Köneçoğlu, G., and Akgün, M. (2014). "Equilibrium and kinetic study on the adsorption of basic dye (BY28) onto raw Ca-bentonite." *Desalin. Water Treat.*, 52(37–39), 7389–7399.

Kaneco, S., Rahman, M. A., Suzuki, T., Katsumata, H., and Ohta, K. (2004). "Optimization of solar photocatalytic degradation conditions of bisphenol A in water using titanium dioxide." *J. Photochem. Photobiol. A Chem.*, 163(3), 419–424.

Kapoor, N., Khandavilli, S., and Panchagnula, R. (2006). "Simultaneous determination of lamivudine and stavudine in antiretroviral fixed dose combinations by first derivative spectrophotometry and high performance liquid chromatography." *J. Pharm. Biomed. Anal.*, 41(3), 761–765.

Karim, M. R., Lee, H. W., Cheong, I. W., Park, S. M., Oh, W., and Yeum, J. H. (2009). "Conducting polyaniline-titanium dioxide nanocomposites prepared by inverted emulsion polymerization." *Polym. Compos.*, 31(1), 83-88.

Karpińska, J. (2004). "Derivative spectrophotometry - Recent applications and directions of developments." *Talanta*.4, 801-822.

Karthikeyan, K. T., Karthikeyan, S., and Jothivenkatachalam, K. (2014). "Removal of reactive blue 2 dye from aqueous solution using turmeric industrial waste activated carbon." *J. Chem. Pharm. Sci.*, 2115.

Kaur, M., Yadav, K. L., and Uniyal, P. (2015). "Investigations on multiferroic, optical and photocatalytic properties of lanthanum doped bismuth ferrite nanoparticles." *Adv. Mater. Lett.*, 6(10), 895–901.

Kayani, Z. N., Saleemi, F., and Batool, I. (2015). "Effect of calcination temperature on the properties of ZnO nanoparticles." *Appl. Phys. A*, 119(2), 713–720.

Ke, H., Wang, W., Wang, Y., Xu, J., Jia, D., Lu, Z., and Zhou, Y. (2011). "Factors controlling pure-phase multiferroic $BiFeO_3$ powders synthesized by chemical co-precipitation." *J. Alloys Compd.*, 509(5), 2192–2197.

Kee, M. W., and Wei, K. M. (2017). *Enhanced photodegradation of dye mixtures (MO and methyl green) and real textile wastewater by ZnO micro/nanoflowers.*

Kelly, J., and Kelly, P. (1995). "Nanofiltration of whey: quality, environmental and economic aspects." *Int. J. Dairy Technol.*, 48(1), 20–24.

Khan, J., Sayed, M., Ali, F., and Khan, H. M. (2018). "Removal of Acid Yellow 17 Dye by Fenton Oxidation Process." *Zeitschrift für Phys. Chemie*, 232(4), 507.

Khan, M. M., Ansari, S. A., Pradhan, D., Ansari, M. O., Han, D. H., Lee, J., and Cho, M. H. (2014). "Band gap engineered TiO_2 nanoparticles for visible light induced photoelectrochemical and photocatalytic studies." *J. Mater. Chem. A*, 2(3), 637–644.

Khanna, A., and Shetty K, V. (2013). "Solar photocatalysis for treatment of Acid Yellow-17 (AY-17) dye contaminated water using $Ag@TiO_2$ core-shell structured nanoparticles." *Environ. Sci. Pollut. Res.*, 20(8), 5692–5707.

Khanna, A., and Shetty K, V. (2014). "Solar light-driven photocatalytic degradation of Anthraquinone dye-contaminated water by engineered $Ag@TiO_2$ core–shell nanoparticles." *Desalin. Water Treat.*, 54(3), 744–757.

Khataee, A. R., Safarpour, M., Naseri, A., and Zarei, M. (2012). "Photoelectro-Fenton/nanophotocatalysis decolorization of three textile dyes mixture: Response surface modeling and multivariate calibration procedure for simultaneous determination." *J. Electroanal. Chem.*, 672(February), 53–62.

Khataee, A. R., and Zarei, M. (2011). "Photoelectrocatalytic decolorization of diazo dye by zinc oxide nanophotocatalyst and carbon nanotube based cathode: Determination of the degradation products." *Desalination*, 278(1–3), 117–125.

Kim, J. K., Kim, S. S., and Kim, W.-J. (2005). "Sol–gel synthesis and properties of multiferroic $BiFeO_3$." *Mater. Lett.*, 59(29–30), 4006–4009.

Kiriakidou, F., Kondarides, D. I., and Verykios, X. E. (1999). "The effect of operational

parameters and TiO₂-doping on the photocatalytic degradation of azo-dyes." *Catal. Today*, 54(1), 119–130.

Kisku, M. (2009). "Surfactant Assisted Autocombustion Synthesis Of Bismuth Ferrite." (10508014), 1–18.

Kitchin, J. R., Nørskov, J. K., Barteau, M. A., and Chen, J. G. (2004). "Role of Strain and Ligand Effects in the Modification of the Electronic and Chemical Properties of Bimetallic Surfaces." *Phys. Rev. Lett.*, 93(15), 156801.

Kiwaan, H. A., Atwee, T. M., Azab, E. A., and El-Bindary, A. A. (2020). "Photocatalytic degradation of organic dyes in the presence of nanostructured titanium dioxide." *J. Mol. Struct.*, 1200, 127115.

Konstantinou, I. K., and Albanis, T. A. (2004). "TiO₂-assisted photocatalytic degradation of azo dyes in aqueous solution: kinetic and mechanistic investigations." *Appl. Catal. B Environ.*, 49(1), 1–14.

Kornbrust, D., and Barfknecht, T. (1985). "Testing of 24 food, drug, cosmetic, and fabric dyes in the in vitro and the in vivo/in vitro rat hepatocyte primary culture DNA repair assays." *Environ. Mutagen.*, 7(1), 101–120.

Koutavarapu, R., Lee, G., Babu, B., Yoo, K., and Shim, J. (2019). "Visible-light-driven photocatalytic activity of tiny ZnO nanosheets anchored on NaBiS2 nanoribbons via hydrothermal synthesis." *J. Mater. Sci. Mater. Electron.*, 30(11), 10990–10911.

Kroemer, H. (2001). "Quasi-Electric Fields and Band Offsets: Teaching Electrons New Tricks (Nobel Lecture)." *ChemPhysChem*, 2(8–9), 490–499.

Ku, Y., and Hsieh, C.-B. (1992). "Photocatalytic decomposition of 2,4-dichlorophenol in aqueous TiO₂ suspensions." *Water Res.*, 26(11), 1451–1456.

Kubel, F., and Schmid, H. (1990). "Structure of a ferroelectric and ferroelastic monodomain crystal of the perovskite BiFeO₃." *Acta Crystallogr. Sect. B*, 46(6), 698–702.

Kuchibhatla, S. V. N. T., Karakoti, A. S., Baer, D. R., Samudrala, S., Engelhard, M. H., Amonette, J. E., Thevuthasan, S., and Seal, S. (2012). "Influence of Aging and Environment on Nanoparticle Chemistry: Implication to Confinement Effects in Nanoceria." *J. Phys. Chem. C*, 116(26), 14108–14114.

Kudo, A., and Miseki, Y. (2009). "Heterogeneous photocatalyst materials for water splitting."

Chem. Soc. Rev., 38(1), 253–278.

Kumar, S. G., and Rao, K. S. R. K. (2017). "Comparison of modification strategies towards enhanced charge carrier separation and photocatalytic degradation activity of metal oxide semiconductors (TiO$_2$, WO$_3$ and ZnO)." *Appl. Surf. Sci.*, 391, 124–148.

Kumari, A., Yadav, S. K., and Yadav, S. C. (2010). "Biodegradable polymeric nanoparticles based drug delivery systems." *Colloids Surfaces B Biointerfaces*, 75(1), 1–18.

Kusuma, M., and Chandrappa, G. T. (2019). "Effect of calcination temperature on characteristic properties of CaMoO4 nanoparticles." *J. Sci. Adv. Mater. Devices*, 4(1), 150–157.

Lathasree, S., Rao, A. N., SivaSankar, B., Sadasivam, V., and Rengaraj, K. (2004). "Heterogeneous photocatalytic mineralisation of phenols in aqueous solutions." *J. Mol. Catal. A Chem.*, 223(1–2), 101–105.

Lauhon, L. J., Gudiksen, M. S., Wang, D., and Lieber, C. M. (2002). "Epitaxial core–shell and core–multishell nanowire heterostructures." *Nature*, 420(6911), 57–61.

Lee, K. Y., Park, S. M., Kim, J. B., Saliby, I. El, Shahid, M., Kim, G.-J., Shon, H. K., and Kim, J.-H. (2016a). "Synthesis and Characterisation of Porous Titania-Silica Composite Aerogel for NOx and Acetaldehyde Removal." *J. Nanosci. Nanotechnol.*, 16(5), 4505–4511.

Lee, S., Lee, J., Nam, K., Shin, W., and Sohn, Y. (2016b). "Application of Ni-Oxide@TiO$_2$ Core-Shell Structures to Photocatalytic Mixed Dye Degradation, CO Oxidation, and Supercapacitors." *Materials (Basel).*, 9(12), 1024.

Leghari, S. A. K., Sajjad, S., Chen, F., and Zhang, J. (2011). "WO$_3$/TiO$_2$ composite with morphology change via hydrothermal template-free route as an efficient visible light photocatalyst." *Chem. Eng. J.*, 166(3), 906–915.

Li, D., Haneda, H., Hishita, S., and Ohashi, N. (2005). "Visible-light-driven nitrogen-doped TiO$_2$ photocatalysts: Effect of nitrogen precursors on their photocatalysis for decomposition of gas-phase organic pollutants." *Mater. Sci. Eng. B Solid-State Mater. Adv. Technol.*, 117(1), 67–75.

Li, G., and Gray, K. A. (2007). "The solid–solid interface: Explaining the high and unique photocatalytic reactivity of TiO$_2$-based nanocomposite materials." *Chem. Phys.*, 339(1–3), 173–187.

Li, H., Cao, X., Zhang, C., Yu, Q., Zhao, Z., Niu, X., Sun, X., Liu, Y., Ma, L., and Li, Z. (2017). "Enhanced adsorptive removal of anionic and cationic dyes from single or mixed dye solutions using MOF PCN-222." *RSC Adv.*, 7(27), 16273–16281.

Li, H., Zhu, L., Ma, C., and Zhang, H. (2014). "TiO$_2$ hollow microspheres: synthesis, photocatalytic activity, and selectivity for a mixture of organic dyes." *Monatshefte fur Chemie*, 29–37.

Li, L., Liu, X., Zhang, Y., Salvador, P. A., and Rohrer, G. S. (2013a). "Heterostructured (Ba,Sr)TiO$_3$/TiO$_2$ core/shell photocatalysts: Influence of processing and structure on hydrogen production." *Int. J. Hydrogen Energy*, 38(17), 6948–6959.

Li Puma, G., and Yue, P. L. (2002). "Effect of the Radiation Wavelength on the Rate of Photocatalytic Oxidation of Organic Pollutants." *Ind. Eng. Chem. Res.*, 41(23), 5594–5600.

Li, S., Lin, Y.-H., Zhang, B.-P., Li, J.-F., and Nan, C.-W. (2009a). "BiFeO$_3$/TiO$_2$ core-shell structured nanocomposites as visible-active photocatalysts and their optical response mechanism." *J. Appl. Phys.*, 105(5), 054310.

Li, S., Lin, Y.-H., Zhang, B.-P., Nan, C.-W., and Wang, Y. (2009b). "Photocatalytic and magnetic behaviors observed in nanostructured BiFeO$_3$ particles." *J. Appl. Phys.*, 105(5), 056105.

Li, W., and Zhao, D. (2013). "Extension of the Stöber Method to Construct Mesoporous SiO$_2$ and TiO$_2$ Shells for Uniform Multifunctional Core-Shell Structures." *Adv. Mater.*, 25(1), 142–149.

Li, X., Li, Q., and Wang, L. (2013b). "The effects of NaNbO$_3$ particle size on the photocatalytic activity for 2-propanol photodegradation." *Phys. Chem. Chem. Phys.*, 15(34), 14282.

Li, X., Wang, D., Cheng, G., Luo, Q., An, J., and Wang, Y. (2008). "Preparation of polyaniline-modified TiO$_2$ nanoparticles and their photocatalytic activity under visible light illumination." *Appl. Catal. B Environ.*, 81(3–4), 267–273.

Li, Y., Yang, Q., Wang, Z., Wang, G., Zhang, B., Zhang, Q., and Yang, D. (2018). "Rapid fabrication of SnO$_2$ nanoparticle photocatalyst: computational understanding and photocatalytic degradation of organic dye." *Inorg. Chem. Front.*, 5(12), 3005–3014.

Li, Z., Jia, L., Li, Y., He, T., and Li, X. M. (2015). "Ammonia-free preparation of Ag@SiO$_2$ core/shell nanoparticles." *Appl. Surf. Sci.*, 134, 122–126.

Liang, C.-H., Hou, M.-F., Zhou, S.-G., Li, F.-B., Liu, C.-S., Liu, T.-X., Gao, Y.-X., Wang, X.-G., and Lü, J.-L. (2006). "The effect of erbium on the adsorption and photodegradation of orange I in aqueous Er_3^+-TiO_2 suspension." *J. Hazard. Mater.*, 138(3), 471–478.

Liao, D. L., and Liao, B. Q. (2007). "Shape, size and photocatalytic activity control of TiO_2 nanoparticles with surfactants." *J. Photochem. Photobiol. A Chem.*, 187(2–3), 363–369.

Liao, G., Fang, J., Li, Q., Li, S., Xu, Z., and Fang, B. (2019). "Ag-Based nanocomposites: synthesis and applications in catalysis." *Nanoscale*, 11(15), 7062–7096.

Lin, H., Chen, Y., and Chen, Y. (2007). "Water splitting reaction on $NiO/InVO_4$ under visible light irradiation." *Int. J. Hydrogen Energy*, 32(1), 86–92.

Lin, S. H., and Chen, M. L. (1997). "Treatment of textile wastewater by chemical methods for reuse." *Water Res.*, 31(4), 868–876.

Lin, Y., Li, D., Hu, J., Xiao, G., Wang, J., Li, W., and Fu, X. (2012). "Highly Efficient Photocatalytic Degradation of Organic Pollutants by PANI-Modified TiO_2 Composite." *J. Phys. Chem. C*, 116(9), 5764–5772.

Liu, C., Hsieh, Y., Lai, P., Li, C., and Kao, C. (2006). "Photodegradation treatment of azo dye wastewater by UV/TiO process." *Dye. Pigment.*, 68(2–3), 191–195.

Liu, L., Ding, L., Liu, Y., An, W., Lin, S., Liang, Y., and Cui, W. (2017a). "A stable $Ag_3 PO_4$ @PANI core@shell hybrid: Enrichment photocatalytic degradation with π-π conjugation." *Appl. Catal. B Environ.*, 201, 92–104.

Liu, X. M., Fu, S. Y., and Huang, C. J. (2005). "Synthesis and magnetic characterization of novel $CoFe_2O_4$-$BiFeO_3$ nanocomposites." *Mater. Sci. Eng. B-Solid State Mater. Adv. Technol.*, 121(3), 255–260.

Liu, Y.-L., and Wu, J. M. (2019). "Synergistically catalytic activities of $BiFeO_3/TiO_2$ core-shell nanocomposites for degradation of organic dye molecule through piezophototronic effect." *Nano Energy*, 56, 74–81.

Liu, Y., Ding, S., Xu, J., Zhang, H., Yang, S., Duan, X., Sun, H., and Wang, S. (2017b). "Preparation of a p-n heterojunction $BiFeO_3$@TiO_2 photocatalyst with a core-shell structure for visible-light photocatalytic degradation." *Cuihua Xuebao/Chinese J. Catal.*, 38(6), 1052–1062.

Liu, Y., Ohko, Y., Zhang, R., Yang, Y., and Zhang, Z. (2010a). "Degradation of malachite

green on Pd/WO$_3$ photocatalysts under simulated solar light." *J. Hazard. Mater.*, 184(1–3), 386–391.

Liu, Y. Y., Yang, L., and Li, J. Y. (2013). "Strain-engineered orthorhombic-rhombohedral phase boundary in epitaxial bismuth ferrite films." *J. Appl. Phys.*, 113(18), 183524.

Liu, Y., Yao, W., Liu, D., Zong, R., Zhang, M., Ma, X., and Zhu, Y. (2015). "Enhancement of visible light mineralization ability and photocatalytic activity of BiPO$_4$/BiOI." *Appl. Catal. B Environ.*, 163, 547–553.

Liu, Z., and Davis, R. J. (1994). "Investigation of the Structure of Microporous Ti-Si Mixed Oxides by X-ray, UV Reflectance, FT-Raman, and FT-IR Spectroscopies." *J. Phys. Chem.*, 98(4), 1253–1261.

Liu, Z., Qi, Y., and Lu, C. (2010b). "High efficient ultraviolet photocatalytic activity of BiFeO 3 nanoparticles synthesized by a chemical coprecipitation process." *J. Mater. Sci. Mater. Electron.*, 21(4), 380–384.

Lu, F., Cai, W., and Zhang, Y. (2008). "ZnO Hierarchical Micro/Nanoarchitectures: Solvothermal Synthesis and Structurally Enhanced Photocatalytic Performance." *Adv. Funct. Mater.*, 18(7), 1047–1056.

Lu, H., Du, Z., Wang, J., and Liu, Y. (2015). "Enhanced photocatalytic performance of Ag-decorated BiFeO$_3$ in visible light region." *J. Sol-Gel Sci. Technol.*, 76(1), 50–57.

Lu, X., Zhang, W., Wang, C., Wen, T.-C., and Wei, Y. (2011). "One-dimensional conducting polymer nanocomposites: Synthesis, properties and applications." *Prog. Polym. Sci.*, 36(5), 671–712.

Lu, Y., Yu, M., Drechsler, M., and Ballauff, M. (2007). "Ag Nanocomposite Particles: Preparation, Characterization and Application." *Macromol. Symp.*, 254(1), 97–102.

Luan, J., Shen, Y., Wang, S., and Guo, N. (2017). "Synthesis, Property Characterization and Photocatalytic Activity of the Polyaniline/BiYTi$_2$O$_7$ Polymer Composite." *Polymers (Basel).*, 9(12), 69.

Luna, M. D. G. de, Laciste, M. T., Tolosa, N. C., and Lu, M.-C. (2018). "Effect of catalyst calcination temperature in the visible light photocatalytic oxidation of gaseous formaldehyde by multi-element doped titanium dioxide." *Environ. Sci. Pollut. Res.*, 25(15), 15216–15225.

Luo, J., and Maggard, P. A. (2006). "Hydrothermal Synthesis and Photocatalytic Activities of

SrTiO$_3$-Coated Fe$_2$O$_3$ and BiFeO$_3$." *Adv. Mater.*, 18(4), 514–517.

Luo, W., Zhu, L., Wang, N., Tang, H., Cao, M., and She, Y. (2010). "Efficient removal of organic pollutants with magnetic Nanoscaled BiFeO$_3$ as a reusable heterogeneous fenton-like catalyst." *Environ. Sci. Technol.*, 44(5), 1786–91.

Luzzati, S., Basso, M., Catellani, M., Brabec, C. ., Gebeyehu, D., and Sariciftci, N. . (2002). "Photo-induced electron transfer from a dithieno thiophene-based polymer to TiO$_2$." *Thin Solid Films*, 403–404, 52–56.

Lv, H., Zhao, H., Cao, T., Qian, L., Wang, Y., and Zhao, G. (2015). "Efficient degradation of high concentration azo-dye wastewater by heterogeneous Fenton process with iron-based metal-organic framework." *J. Mol. Catal. A Chem.*, 400, 81–89.

M. Emran, K. (2018). "The Electrocatalytic Activity of Polyaniline/TiO$_2$ Nanocomposite for Congo Red Degradation in Aqueous Solutions." *Int. J. Electrochem. Sci.*, 5085–5095.

Ma, H. C., Zhang, Y., Fu, Y. H., Yu, C. L., Song, Y., Ma, C., and Dong, X. L. (2011). "Preparation of Polyaniline–ZnO Photocatalyst and its Photocatalytic Property." *Adv. Mater. Res.*, 356–360, 519–523.

Ma, Y., Zhang, J., Tian, B., Chen, F., and Wang, L. (2010). "Synthesis and characterization of thermally stable Sm,N co-doped TiO$_2$ with highly visible light activity." *J. Hazard. Mater.*

MacDiarmid, A. G. (2001). "'Synthetic Metals': A Novel Role for Organic Polymers (Nobel Lecture)." *Angew. Chemie Int. Ed.*, 40(14), 2581–2590.

Macdiarmid, A. G., Chiang, J. C., Richter, A. F., and Epstein, A. J. (1987). "Polyaniline: a new concept in conducting polymers." *Synth. Met.*, 18(1–3), 285–290.

Madamwar, D., Tiwari, O., and Jain, K. (2019). *Mapping of Research Outcome on Remediation of Dyes, Dye Intermediates and Textile Industrial Waste A Research Compendium*. New Delhi.

Mahalingam, S., and Ahn, Y.-H. (2018). "Improved visible light photocatalytic activity of rGO-Fe$_3$O$_4$-NiO hybrid nanocomposites synthesized by in situ facile method for industrial wastewater treatment applications." *New J. Chem.*, 42(6), 4372–4383.

Mai, B. D., Nguyen, H. T., Nguyen, T. K. A., Ta, D. H., and Luu, T. N. (2019). "Effects of composition ratio on structure and phase transition of ferroelectric nanocomposites from silicon dioxide nanoparticles and triglycine sulfate." *Phase Transitions*, 92(6), 563–570.

Maity, D., Zoppellaro, G., Sedenkova, V., Tucek, J., Safarova, K., Polakova, K., Tomankova,

K., Diwoky, C., Stollberger, R., MacHala, L., and Zboril, R. (2012). "Surface design of core-shell superparamagnetic iron oxide nanoparticles drives record relaxivity values in functional MRI contrast agents." *Chem. Commun.*, 48(93), 11398.

Malato, S., Blanco, J., Vidal, A., and Richter, C. (2002). "Photocatalysis with solar energy at a pilot-plant scale: an overview." *Appl. Catal. B Environ.*, 37(1), 1–15.

Mali, S. S., Betty, C. A., Bhosale, P. N., and Patil, P. S. (2012). "Synthesis, Characterization of Hydrothermally Grown MWCNT–TiO_2 Photoelectrodes and Their Visible Light Absorption Properties." *ECS J. Solid State Sci. Technol.*, 1(2), M15–M23.

Manivannan, S., and Ramaraj, R. (2009). "Core-shell Au/Ag nanoparticles embedded in silicate sol-gel network for sensor application towards hydrogen peroxide." *J. Chem. Sci.*, 121(5), 735–743.

Manjunatha, M., Kumar, R., Anupama, A. V., Khopkar, V. B., Damle, R., Ramesh, K. P., and Sahoo, B. (2019). "XRD, internal field-NMR and Mössbauer spectroscopy study of composition, structure and magnetic properties of iron oxide phases in iron ores." *J. Mater. Res. Technol.*, 8(2), 2192–2200.

Marcì, G., Augugliaro, V., López-Muñoz, M. J., Martín, C., Palmisano, L., Rives, V., Schiavello, M., Tilley, R. J. D., and Venezia, A. M. (2001). "Preparation Characterization and Photocatalytic Activity of Polycrystalline ZnO/TiO_2 Systems. 1. Surface and Bulk Characterization." *J. Phys. Chem. B*, 105(5), 1026–1032.

Markad, G. B., Kapoor, S., Haram, S. K., and Thakur, P. (2017). "Metal free, carbon-TiO_2 based composites for the visible light photocatalysis." *Sol. Energy*, 144, 127–133.

Marmagne, O., and C. Coste. (1996). "Color removal from textile plant effluents." *Am. Dyest. Report.*, (April), 15–21.

Masoudpanah, S. M., Mirkazemi, S. M., Bagheriyeh, R., Jabbari, F., and Bayat, F. (2017). "Structural, magnetic and photocatalytic characterization of $Bi_{1-x}La_xFeO_3$ nanoparticles synthesized by thermal decomposition method." *Bull. Mater. Sci.*, 40(1), 93–100.

Medien, H. A. A. A., and Khalil, S. M. E. E. (2010). "Kinetics of the oxidative decolorization of some organic dyes utilizing Fenton-like reaction in water." *J. King Saud Univ. - Sci.*, 22(3), 147–153.

Mengyue, Z., Shifu, C., and Yaowu, T. (1995). "Photocatalytic degradation of organophosphorus pesticides using thin films of TiO_2." *J. Chem. Technol. Biotechnol.*, 64(4),

339–344.

Menon, N. G., Tatiparti, S. S. V., and Mukherji, S. (2018). "Effect of calcination temperature on the microstructure and electronic properties of TiO_2–ZnO nanocomposites and implications on photocatalytic activity." *Appl. Nanosci.*, 8(5), 915–930.

Merka, O., Yarovyi, V., Bahnemann, D. W., and Wark, M. (2011). "pH-Control of the Photocatalytic Degradation Mechanism of Rhodamine B over $Pb_3Nb_4O_{13}$." *J. Phys. Chem. C*, 115(16), 8014–8023.

Miao, J., Xie, A., Li, S., Huang, F., Cao, J., and Shen, Y. (2016). "A novel reducing graphene/polyaniline/cuprous oxide composite hydrogel with unexpected photocatalytic activity for the degradation of Congo red." *Appl. Surf. Sci.*, 360, 594–600.

Mioduska, J., Zielińska-Jurek, A., Janczarek, M., and Hupka, J. (2016). "The Effect of Calcination Temperature on Structure and Photocatalytic Properties of WO_3/TiO_2 Nanocomposites." *J. Nanomater.*, 2016, 1–8.

Mirmohseni, A., Rastgar, M., and Olad, A. (2019). "PANI-chitosan-TiO_2 ternary nanocomposite and its effectiveness on antibacterial and antistatic behavior of epoxy coating." *J. Appl. Polym. Sci.*, 136(23), 47629.

Mirzadeh, A., and Kokabi, M. (2007). "The effect of composition and draw-down ratio on morphology and oxygen permeability of polypropylene nanocomposite blown films." *Eur. Polym. J.*, 43(9), 3757–3765.

Mitra, M., Ahamed, S. T., Ghosh, A., Mondal, A., Kargupta, K., Ganguly, S., and Banerjee, D. (2019). "Polyaniline/Reduced Graphene Oxide Composite-Enhanced Visible-Light-Driven Photocatalytic Activity for the Degradation of Organic Dyes." *ACS Omega*, 4(1), 1623–1635.

Mohamed, A., Salama, A., Nasser, W. S., and Uheida, A. (2018). "Photodegradation of Ibuprofen, Cetirizine, and Naproxen by PAN-MWCNT/TiO_2–NH_2 nanofiber membrane under UV light irradiation." *Environ. Sci. Eur.*, 30(1), 47.

Mohamed, M. M., Reda, S. M., and Amer, A. A. (2020). "Enhanced performance of $BiFeO_3$@nitrogen doped TiO_2 core-shell structured nanocomposites: Synergistic effect towards solar cell amplification." *Arab. J. Chem.*, 13(1), 2611–2619.

Mohamed, R. M., Mkhalid, I. A., Baeissa, E. S., and Al-Rayyani, M. A. (2012). "Photocatalytic Degradation of Methylene Blue by Fe/ZnO/SiO_2 Nanoparticles under Visiblelight." *J. Nanotechnol.*, 2012, 1–5.

Mohammed, M. A., Uday, M. B., and Izman, S. (2020). "Effects of calcination temperature and time on the $Ca_3Co_4O_9$ purity when synthesized using starch-assisted sol-gel combustion method." *J. Adv. Ceram.*, 9(2), 162–172.

Mohan, D., and Pittman Jr., C. U. (2006). "Activated carbons and low cost adsorbents for remediation of tri- and hexavalent chromium from water." *J. Hazard. Mater.*, 137(2), 762–811.

Mohan, L., Durgalakshmi, D., Geetha, M., Sankara Narayanan, T. S. N. N., and Asokamani, R. (2012). "Electrophoretic deposition of nanocomposite (HAp + TiO_2) on titanium alloy for biomedical applications." *Ceram. Int.*, 38(4), 3435–3443.

Mohd Azmy, H. A., Razuki, N. A., Aziz, A. W., Abdul Satar, N. S., and Mohd Kaus, N. H. (2017). "Visible Light Photocatalytic Activity of $BiFeO_3$ Nanoparticles for Degradation of Methylene Blue." *J. Phys. Sci.*, 28(2), 85–103.

Moniz, S. J. A., Shevlin, S. A., Martin, D. J., Guo, Z.-X., and Tang, J. (2015). "Visible-light driven heterojunction photocatalysts for water splitting – a critical review." *Energy Environ. Sci.*, 8(3), 731–759.

Mornani, E. G., Mosayebian, P., Dorranian, D., and Behzad, K. (2016). "Effect of calcination temperature on the size and optical properties of synthesized ZnO nanoparticles." *J. Ovonic Res.*, 12(2), 75–80.

Mortazavian, S., Saber, A., and James, D. E. (2019). "Optimization of Photocatalytic Degradation of Acid Blue 113 and Acid Red 88 Textile Dyes in a UV-C/TiO_2 Suspension System: Application of Response Surface Methodology (RSM)." *Catalysts*, 9(4), 360.

Mudunkotuwa, I. A., Pettibone, J. M., and Grassian, V. H. (2012). "Environmental Implications of Nanoparticle Aging in the Processing and Fate of Copper-Based Nanomaterials." *Environ. Sci. Technol.*, 46(13), 7001–7010.

Muhd Julkapli, N., Bagheri, S., and Bee Abd Hamid, S. (2014). "Recent advances in heterogeneous photocatalytic decolorization of synthetic dyes." *Sci. World J.*, 2014(2014), 1–25.

Mukherjee, A., Chakrabarty, S., Kumari, N., Su, W.-N., and Basu, S. (2018). "Visible-Light-Mediated Electrocatalytic Activity in Reduced Graphene Oxide-Supported Bismuth Ferrite." *ACS Omega*, 3(6), 5946–5957.

Mukherjee, A., Hossain, S. M., Pal, M., and Basu, S. (2012). "Effect of Y-doping on optical properties of multiferroics $BiFeO_3$ nanoparticles." *Appl. Nanosci.*, 2(3), 305–310.

Muruganandham, M. (2004). "Photochemical oxidation of reactive azo dye with UV–H_2O_2 process." *Dye. Pigment.*, 62(3), 269–275.

Nagaraja, R., Kottam, N., Girija, C. R., and Nagabhushana, B. M. (2012). "Photocatalytic degradation of Rhodamine B dye under UV/solar light using ZnO nanopowder synthesized by solution combustion route." *Powder Technol.*, 215–216, 91–97.

Nair, V. R., and Shetty Kodialbail, V. (2020). "Floating bed reactor for visible light induced photocatalytic degradation of Acid Yellow 17 using polyaniline-TiO_2 nanocomposites immobilized on polystyrene cubes." *Environ. Sci. Pollut. Res.*, 27(13), 14441–14453.

Nasiri Azad, F., Ghaedi, M., Dashtian, K., Hajati, S., Goudarzi, A., and Jamshidi, M. (2015). "Enhanced simultaneous removal of malachite green and safranin O by ZnO nanorod-loaded activated carbon: modeling, optimization and adsorption isotherms." *New J. Chem.*, 39(10), 7998–8005.

Nasreen, S., Sundarrajan, S., Nizar, S., Balamurugan, R., and Ramakrishna, S. (2013). "Advancement in Electrospun Nanofibrous Membranes Modification and Their Application in Water Treatment." *Membranes (Basel).*, 3(4), 266–284.

National Center for Biotechnology Information. (2020). "PubChem Compound Summary for CID 22842, C.I. Acid Yellow 17, disodium salt." *PubChem*, <https://pubchem.ncbi.nlm.nih.gov/compound/22842#section=Structures> (Aug. 16, 2020).

Naumczyk, J., Szpyrkowicz, L., and Zilio-Grandi, F. (1996). "Electrochemical treatment of textile wastewater." *Water Sci. Technol.*, 17–24.

Neelgund, G. M., Bliznyuk, V. N., and Oki, A. (2016). "Photocatalytic activity and NIR laser response of polyaniline conjugated graphene nanocomposite prepared by a novel acid-less method." *Appl. Catal. B Environ.*, 187, 357–366.

Neethu, N., and Choudhury, T. (2018). "Treatment of Methylene Blue and MO Dyes in Wastewater by Grafted Titania Pillared Clay Membranes." *Recent Pat. Nanotechnol.*, 12(3), 200–207.

Neppolian, B. (2002). "Solar/UV-induced photocatalytic degradation of three commercial textile dyes." *J. Hazard. Mater.*, 89(2–3), 303–317.

Nerkar, N. V., Kondawar, S. B., Brahme, S. K., and Kim, Y. H. (2018). "Polyaniline/ZnO nanocomposites for the removal of MO dye from waste water." *Int. J. Mod. Phys. B*, 32(19), 1840085.

Nezamzadeh-Ejhieh, A., and Karimi-Shamsabadi, M. (2013). "Decolorization of a binary azo dyes mixture using CuO incorporated nanozeolite-X as a heterogeneous catalyst and solar irradiation." *Chem. Eng. J.*, 228(May), 631–641.

Nezamzadeh-Ejhieh, A., and Moazzeni, N. (2013). "Sunlight photodecolorization of a mixture of MO and Bromocresol Green by CuS incorporated in a clinoptilolite zeolite as a heterogeneous catalyst." *J. Ind. Eng. Chem.*, 19(5), 1433–1442.

Nezamzadeh-Ejhieh, A., and Zabihi-Mobarakeh, H. (2014). "Heterogeneous photodecolorization of mixture of methylene blue and bromophenol blue using CuO-nano-clinoptilolite." *J. Ind. Eng. Chem.*, 20(4), 1421–1431.

Nguyen, V.-H., Lin, S. D., Wu, J. C.-S., and Bai, H. (2014). "Artificial sunlight and ultraviolet light induced photo-epoxidation of propylene over V-Ti/MCM-41 photocatalyst." *Beilstein J. Nanotechnol.*, 5, 566–576.

Nomoev, A. V., Bardakhanov, S. P., Schreiber, M., Bazarova, D. G., Romanov, N. A., Baldanov, B. B., Radnaev, B. R., and Syzrantsev, V. V. (2015). "Structure and mechanism of the formation of core–shell nanoparticles obtained through a one-step gas-phase synthesis by electron beam evaporation." *Beilstein J. Nanotechnol.*, 6, 874–880.

O'Haver, T. C., Fell, A. F., Smith, G., Gans, P., Sneddon, J., Bezur, L., Michel, R. G., Ottaway, J. M., Miller, J. N., Ahmad, T. A., Fell, A. F., Chadburn, B. P., and Cottrell, C. T. (1982). "Derivative spectroscopy and its applications in analysis." *Anal. Proc.*, 19(1), 22.

O'Neill, C., Hawkes, F. R., Hawkes, D. L., Esteves, S., and Wilcox, S. J. (2000). "Anaerobic-aerobic biotreatment of simulated textile effluent containing varied ratios of starch and azo dye." *Water Res.*, 34(8), 2355–2361.

Ohno, K., Hoh, K., Tsuji, Y., and Fukuda, T. (2002). "Synthesis of Gold Nanoparticles Coated with Well-Defined, High-Density Polymer Brushes by Surface-Initiated Living Radical Polymerization." *Macromolecules*, 35, 8989.

Okitsu, K., Sharyo, K., and Nishimura, R. (2009). "One-Pot Synthesis of Gold Nanorods by Ultrasonic Irradiation: The Effect of pH on the Shape of the Gold Nanorods and Nanoparticles." *Langmuir*, 25(14), 7786–7790.

Olad, A., Behboudi, S., and Entezami, A. A. (2012). "Preparation , characterization and photocatalytic activity of TiO_2/ polyaniline core-shell nanocomposite." *Bull. Mater. Sci.*, 35(5), 801–809.

Olad, A., and Nosrati, R. (2012). "Preparation, characterization, and photocatalytic activity of polyaniline/ZnO nanocomposite." *Res. Chem. Intermed.*, 38(2), 323–336.

Ollis, D. F., Pelizzetti, E., and Serpone, N. (1991). "Photocatalyzed destruction of water contaminants." *Environ. Sci. Technol.*, 25(9), 1522–1529.

Pala, A., and Tokat, E. (2002). "Color removal from cotton textile industry wastewater in an activated sludge system with various additives." *Water Res.*, 36(11), 2920–2925.

Palácio, S. M., Espinoza-Quiñones, F. R., Módenes, A. N., Manenti, D. R., Oliveira, C. C., and Garcia, J. C. (2012). "Optimised photocatalytic degradation of a mixture of azo dyes using a $TiO_2/H_2O_2/UV$ process." *Water Sci. Technol.*, 65(8), 1392–1398.

Paliwal, A., Ameta, R., and Ameta, S. C. (2017). "Enhancing photocatalytic activity of bismuth ferrite by doping with cobalt and its use for degradation of Evans Blue." *Eur. Chem. Bull.*, 6(3), 120.

Palkar, V. R., Kundaliya, D. C., and Malik, S. K. (2003). "Effect of Mn substitution on magnetoelectric properties of bismuth ferrite system." *J. Appl. Phys.*, 93(7), 4337–4339.

Pamidimukkala, K. M. (2006). "X-ray Photoelectron Spectroscopy, Paper Surface Analysis By." *Encycl. Anal. Chem.*, Chichester, UK: John Wiley & Sons, Ltd.

Pan, J., Liu, G., Lu, G. Q. M., and Cheng, H.-M. (2011). "On the True Photoreactivity Order of {001}, {010}, and {101} Facets of Anatase TiO_2 Crystals." *Angew. Chemie Int. Ed.*, 50(9), 2133–2137.

Pandiselvi, K., and Thambidurai, S. (2016). "Synthesis of adsorption cum photocatalytic nature of polyaniline-ZnO/chitosan composite for removal of textile dyes." *Desalin. Water Treat.*, 57(18), 8843–8357.

Pang, X., Zhao, L., Akinc, M., Kim, J. K., and Lin, Z. (2011). "Novel Amphiphilic Multi-Arm, Star-Like Block Copolymers as Unimolecular Micelles." *Macromolecules*, 44(10), 3746–3752.

Pang, X., Zhao, L., Han, W., Xin, X., and Lin, Z. (2013). "A general and robust strategy for the synthesis of nearly monodisperse colloidal nanocrystals." *Nat. Nanotechnol.*, 8(6), 426–431.

Pant, H. C., Patra, M. K., Negi, S. C., Bhatia, A., Vadera, S. R., and Kumar, N. (2006). "Studies on conductivity and dielectric properties of polyaniline-zinc sulphide composites." *Bull. Mater. Sci.*, 29(4), 379–384.

Pare, B., and Singh, P. (2009). "Reduction in Chemical Oxygen Demand and Color Intensity of Dye-Contaminated Wastewaster Using Visible Irradiation and ZnO-Assisted Advanced Oxidation Process: A Green Laboratory Experiment for Wastewater Treatment." *Chem. Educ. ICT Age*, Dordrecht: Springer Netherlands, 225–234.

Pareek, V., Chong, S., Tadé, M., Adesina, A. A., Vishnu, P., Siewhui, C., Moses, T., and A., A. A. (2008). "Light intensity distribution in heterogenous photocatalytic reactors." *Asia-Pacific J. Chem. Eng.*, 3(2), 171–201.

Park, H. H., Woo, K., and Ahn, J.-P. (2013). "Core–Shell Bimetallic Nanoparticles Robustly Fixed on the Outermost Surface of Magnetic Silica Microspheres." *Sci. Rep.*, 3(1), 1497.

Patete, J. M., Peng, X., Koenigsmann, C., Xu, Y., Karn, B., and Wong, S. S. (2011). "Viable methodologies for the synthesis of high-quality nanostructures." *Green Chem.*, 13(3), 482.

Pathak, A., and Pramanik, P. (2001). "Nano-particles of oxides through chemical methods." *proceedings-indian Natl. Sci. Acad. part a*, 67(1), 47–70.

Patil, M. R., Khairnar, S. D., and Shrivastava, V. S. (2016). "Synthesis, characterisation of polyaniline–Fe$_3$O$_4$ magnetic nanocomposite and its application for removal of an acid violet 19 dye." *Appl. Nanosci.*, 6(4), 495–502.

Patil, S. H., Gaikwad, A. P., Sathaye, S. D., and Patil, K. R. (2018). "To form layer by layer composite film in view of its application as supercapacitor electrode by exploiting the techniques of thin films formation just around the corner." *Electrochim. Acta*, 265, 556–568.

Patra, J. K., and Baek, K.-H. (2014). "Green Nanobiotechnology: Factors Affecting Synthesis and Characterization Techniques." *J. Nanomater.*, 2014, 1–12.

Paul, D. R., Sharma, R., Nehra, S. P., and Sharma, A. (2019). "Effect of calcination temperature, pH and catalyst loading on photodegradation efficiency of urea derived graphitic carbon nitride towards methylene blue dye solution." *RSC Adv.*, 9(27), 15381–15391.

Pawar, S. G., Patil, S. L., Chougule, M. A., Mane, A. T., Jundale, D. M., and Patil, V. B. (2010). "Synthesis and Characterization of Polyaniline:TiO$_2$ Nanocomposites." *Int. J. Polym. Mater.*, 59(10), 777–785.

Peralta-Zamora, P., Kunz, A., Moraes, S. G. de, Pelegrini, R., Campos Moleiro, P. de, Reyes, J., and Duran, N. (1999). "Degradation of reactive dyes I. A comparative study of ozonation, enzymatic and photochemical processes." *Chemosphere*, 38(4), 835–852.

Pirhashemi, M., Habibi-Yangjeh, A., and Rahim Pouran, S. (2018). "Review on the criteria anticipated for the fabrication of highly efficient ZnO-based visible-light-driven photocatalysts." *J. Ind. Eng. Chem.*, 62, 1–25.

Poulios, I., Avranas, A., Rekliti, E., and Zouboulis, A. (2000). "Photocatalytic oxidation of Auramine O in the presence of semiconducting oxides." *J. Chem. Technol. Biotechnol.*, 75(3), 205–212.

Pourahmad, A., Sohrabnezhad, S., and Kashefian, E. (2010). "AgBr/nanoAlMCM-41 visible light photocatalyst for degradation of methylene blue dye." *Spectrochim. Acta Part A Mol. Biomol. Spectrosc.*, 77(5), 1108–1114.

Prabhakaran, T., and Hemalatha, J. (2008). "Synthesis and characterization of magnetoelectric polymer nanocomposites." *J. Polym. Sci. Part B Polym. Phys.*, 46(22), 2418–2422.

Prabhakaran, T., and Hemalatha, J. (2012). "Negative giant magnetoresistance effect in single layered superparamagnetic polymer nanocomposite structures of poly(vinyl alcohol)–polyaniline/bismuth ferrite." *Smart Mater. Struct.*, 21(8), 085012.

Pradhan, A. C., Sahoo, M. K., Bellamkonda, S., Parida, K. M., and Rao, G. R. (2016). "Enhanced photodegradation of dyes and mixed dyes by heterogeneous mesoporous Co–Fe/Al$_2$O$_3$ –MCM-41 nanocomposites: nanoparticles formation, semiconductor behavior and mesoporosity." *RSC Adv.*, 6(96), 94263–94277.

Pranwadee Kaewmuang, Thongtem, T., Thongtem, S., Kittiwachana, S., and Kaowphong, S. (2018). "Influence of Calcination Temperature on Particle Size and Photocatalytic Activity of Nanosized NiO Powder." *Russ. J. Phys. Chem. A*, 92(9), 1777–1781.

Prasannalakshmi, P., and Shanmugam, N. (2017). "Fabrication of TiO$_2$/ZnO nanocomposites for solar energy driven photocatalysis." *Mater. Sci. Semicond. Process.*, 61, 114–124.

Praserthdam, P., Phungphadung, J., and Tanakulrungsank, W. (2003). "Effect of crystallite size and calcination temperature on the thermal stability of single nanocrystalline chromium oxide: expressed by novel correlation." *Mater. Res. Innov.*, 7(2), 118–123.

Pron, A., and Rannou, P. (2002). "Processible conjugated polymers: from organic semiconductors to organic metals and superconductors." *Prog. Polym. Sci.*, 27(1), 135–190.

PS, H., Joseph, L., and A, D. (2013). "Photocatalytic degradation of textile dyes by hydrogel supported titanium dioxide nanoparticles." *J. Environ. Eng. Ecol. Sci.*, 2(1), 2.

Pugazhvadivu, K. S., Balakrishnan, L., Mohan Rao, G., and Tamilarasan, K. (2014). "Room temperature ferromagnetic and ferroelectric properties of $Bi_{1-x}Ca_xMnO_3$ thin films." *AIP Adv.*, 4(11), 117105.

Purkait, M. K., Maiti, A., DasGupta, S., and De, S. (2007). "Removal of congo red using activated carbon and its regeneration." *J. Hazard. Mater.*, 145(1–2), 287–295.

Qin, R., Hao, L., Liu, Y., and Zhang, Y. (2018). "Polyaniline-ZnO Hybrid Nanocomposites with Enhanced Photocatalytic and Electrochemical Performance." *ChemistrySelect*, 3(23), 6286–6293.

Qiu, Y., Liu, Y., Wang, L., Xu, L., Bai, R., Ji, Y., Wu, X., Zhao, Y., Li, Y., and Chen, C. (2010). "Surface chemistry and aspect ratio mediated cellular uptake of Au nanorods." *Biomaterials*, 31(30), 7606–7619.

Quickel, T. E., Schelhas, L. T., Farrell, R. A., Petkov, N., Le, V. H., and Tolbert, S. H. (2015). "Mesoporous bismuth ferrite with amplified magnetoelectric coupling and electric field-induced ferrimagnetism." *Nat. Commun.*, 6(1), 6562.

Radoičić, M., Šaponjić, Z., Janković, I. A., Ćirić-Marjanović, G., Ahrenkiel, S. P., and Čomor, M. I. (2013). "Improvements to the photocatalytic efficiency of polyaniline modified TiO_2 nanoparticles." *Appl. Catal. B Environ.*, 136, 133–139.

Rai, A., Singh, A., Ahmad, A., and Sastry, M. (2006). "Role of Halide Ions and Temperature on the Morphology of Biologically Synthesized Gold Nanotriangles." *Langmuir*, 22(2), 736–741.

Rajabi, H. R., Khani, O., Shamsipur, M., and Vatanpour, V. (2013). "High-performance pure and Fe_3^+-ion doped ZnS quantum dots as green nanophotocatalysts for the removal of malachite green under UV-light irradiation." *J. Hazard. Mater.*, 250–251, 370–378.

Rajesh, K. M., Ajitha, B., Ashok Kumar Reddy, Y., Suneetha, Y., and Sreedhara Reddy, P. (2016). "Synthesis of copper nanoparticles and role of pH on particle size control." *Mater. Today Proc.*, 3(6), 1985–1991.

Ramírez-Aparicio, J., Samaniego-Benítez, J. E., and Ramírez-Bon, R. (2016). "TiO_2-chabazite semiconductor composites for photocatalytic degradation of rhodamine under sunlight irradiation." *Sol. Energy*, 139, 258–265.

Rao, K. V. S., Subrahmanyam, M., and Boule, P. (2004). "Immobilized TiO_2 photocatalyst during long-term use: decrease of its activity." *Appl. Catal. B Environ.*, 49(4), 239–249.

Ratnawulan, Fauzi, A., and AE, S. H. (2017). "Effect of calcination temperature on phase transformation and crystallite size of copper oxide (CuO) powders." *AIP Conf. Proc.*, 060009.

Ratova, M., Kelly, P., West, G., and Tosheva, L. (2016). "A Novel Technique for the Deposition of Bismuth Tungstate onto Titania Nanoparticulates for Enhancing the Visible Light Photocatalytic Activity." *Coatings*, 6(3), 29.

Rauf, A., Sher Shah, M. S. A., Choi, G. H., Humayoun, U. Bin, Yoon, D. H., Bae, J. W., Park, J., Kim, W.-J., and Yoo, P. J. (2015). "Facile Synthesis of Hierarchically Structured Bi_2S_3/Bi_2WO_6 Photocatalysts for Highly Efficient Reduction of Cr(VI)." *ACS Sustain. Chem. Eng.*, 3(11), 2847–2855.

Razalli, R. L., Abdi, M. M., Tahir, P. M., Moradbak, A., Sulaiman, Y., and Heng, L. Y. (2017). "Polyaniline-modified nanocellulose prepared from Semantan bamboo by chemical polymerization: preparation and characterization." *RSC Adv.*, 7(41), 25191–25198.

Reddy, K. R., Karthik, K. V., Prasad, S. B. B., Soni, S. K., Jeong, H. M., and Raghu, A. V. (2016). "Enhanced photocatalytic activity of nanostructured titanium dioxide/polyaniline hybrid photocatalysts." *Polyhedron*, 120, 169–174.

Reddy, K. R., Nakata, K., Ochiai, T., Murakami, T., Tryk, D. A., and Fujishima, A. (2010). "Nanofibrous TiO_2 Core/Conjugated Polymer-Sheath Composites: Synthesis, Structural Properties and Photocatalytic Activity." *J. Nanosci. Nanotechnol.*, 10(12), 7951–7957.

Regmi, C., Dhakal, D., and Lee, S. W. (2018). "Visible-light-induced $Ag/BiVO_4$ semiconductor with enhanced photocatalytic and antibacterial performance." *Nanotechnology*, 29(6), 064001.

Reli, M., Kočí, K., Matějka, V., Kovář, P., and Obalová, L. (2012). "Effect of calcination temperature and calcination time on the kaolinite/tiO$_2$ composite for photocatalytic reduction of CO_2." *Geosci. Eng.*, 58(4), 10–22.

Reneker, D. H., and Yarin, A. L. (2008). "Electrospinning jets and polymer nanofibers." *Polymer (Guildf).*, 49(10), 2387–2425.

Retamoso, C., Escalona, N., González, M., Barrientos, L., Allende-González, P., Stancovich, S., Serpell, R., Fierro, J. L. G., and Lopez, M. (2019). "Effect of particle size on the photocatalytic activity of modified rutile sand (TiO_2) for the discoloration of methylene blue in water." *J. Photochem. Photobiol. A Chem.*, 378, 136–141.

Reza, K. M., Kurny, A., and Gulshan, F. (2017). "Parameters affecting the photocatalytic

degradation of dyes using TiO$_2$: a review." *Appl. Water Sci.*, 7(4), 1569–1578.

Riaz, U., Nwaoha, C., and Ashraf, S. M. (2014). "Recent advances in corrosion protective composite coatings based on conducting polymers and natural resource derived polymers." *Prog. Org. Coatings*, 77(4), 743–756.

Richardson, S. D., Willson, C. S., and Rusch, K. A. (2004). "Use of Rhodamine Water Tracer in the Marshland Upwelling System." *Ground Water*, 42(5), 678–688.

Robert, D., and Malato, S. (2002). "Solar photocatalysis: a clean process for water detoxification." *Sci. Total Environ.*, 291(1–3), 85–97.

Rodríguez-González, V., Zanella, R., Angel, G. del, and Gómez, R. (2008). "MTBE visible-light photocatalytic decomposition over Au/TiO$_2$ and Au/TiO$_2$–Al$_2$O$_3$ sol–gel prepared catalysts." *J. Mol. Catal. A Chem.*, 281(1–2), 93–98.

Romão, J., and Mul, G. (2016). "Substrate Specificity in Photocatalytic Degradation of Mixtures of Organic Contaminants in Water." *ACS Catal.*, 6(2), 1254–1262.

Rossignol, N., Jaouen, P., Robert, J.-M., and Quéméneur, F. (2000). "Production of exocellular pigment by the marine diatom Haslea ostrearia Simonsen in a photobioreactor equipped with immersed ultrafiltration membranes." *Bioresour. Technol.*, 73(2), 197–200.

Royen, P., and Swars, K. (1957). "Das System Wismutoxyd-Eisenoxyd im Bereich von 0 bis 55 Mol% Eisenoxyd." *Angew. Chemie*, 69(24), 779–779.

Sabzehmeidani, M. M., Karimi, H., and Ghaedi, M. (2020). "Enhanced visible light-active CeO$_2$/CuO/Ag$_2$CrO$_4$ ternary heterostructures based on CeO$_2$ /CuO nanofiber heterojunctions for the simultaneous degradation of a binary mixture of dyes." *New J. Chem.*, 44(13), 5033–5048.

Sadek, A. Z., Wlodarski, W., Kalantar-Zadeh, K., Baker, C., and Kaner, R. B. (2007). "Doped and dedoped polyaniline nanofiber based conductometric hydrogen gas sensors." *Sensors Actuators A Phys.*, 139(1–2), 53–57.

Sadek, A. Z., Wlodarski, W., Shin, K., Kaner, R. B., and Kalantar-zadeh, K. (2008). "A polyaniline/WO$_3$ nanofiber composite-based ZnO/64 YX LiNbO$_3$ SAW hydrogen gas sensor." *Synth. Met.*, 158(1–2), 29–32.

Sadr Ghayeni, S. B., Beatson, P. J., Schneider, R. P., Fane, A. G., Ghayeni, S. B. S., Beatson, P. J., Schneider, R. P., and Fane, A. G. (1998). "Water reclamation from municipal wastewater

using combined microfiltration reverse osmosis (ME-RO): Preliminary performance data and microbiological aspects of system operation." *Desalination*, 116(1), 65–80.

Safizade, B., Masoudpanah, S. M., Hasheminiasari, M., and Ghasemi, A. (2018). "Photocatalytic activity of $BiFeO_3/ZnFe_2O_4$ nanocomposites under visible light irradiation." *RSC Adv.*, 8(13), 6988–6995.

Saggioro, E. M., Oliveira, A. S., Pavesi, T., Maia, C. G., Ferreira, L. F. V., and Moreira, J. C. (2011). "Use of Titanium Dioxide Photocatalysis on the Remediation of Model Textile Wastewaters Containing Azo Dyes." *Molecules*, 16(12), 10370–10386.

Saha, A. K., and Chaudhuri, M. (2003). "Solar photocatalytic degradation of metal complex azo dyes and treatment of dye house waste." *Indian J. Eng. Mater. Sci.*

Saha, S., Chaudhary, N., Mittal, H., Gupta, G., and Khanuja, M. (2019). "Inorganic–organic nanohybrid of MoS2-PANI for advanced photocatalytic application." *Int. Nano Lett.*, 9(2), 127–139.

Sahel, K., Perol, N., Dappozze, F., Bouhent, M., Derriche, Z., and Guillard, C. (2010). "Photocatalytic degradation of a mixture of two anionic dyes: Procion Red MX-5B and Remazol Black 5 (RB5)." *J. Photochem. Photobiol. A Chem.*, 212(2–3), 107–112.

Sahu, G., Wang, K., Gordon, S. W., Zhou, W., and Tarr, M. A. (2012). "Core-shell $Au–TiO_2$ nanoarchitectures formed by pulsed laser deposition for enhanced efficiency in dye sensitized solar cells." *RSC Adv.*, 2(9), 3791.

Sajid, M. M., Khan, S. B., Shad, N. A., and Amin, N. (2018). "Synthesis of $Zn_3(VO_4)_2/BiVO_4$ heterojunction composite for the photocatalytic degradation of methylene blue organic dye and electrochemical detection of H_2O_2." *RSC Adv.*, 8(62), 35403–35412.

Sakthivel, S., Geissen, S.-U., Bahnemann, D. W., Murugesan, V., and Vogelpohl, A. (2002). "Enhancement of photocatalytic activity by semiconductor heterojunctions: α-Fe_2O_3,WO_3 and CdS deposited on ZnO." *J. Photochem. Photobiol. A Chem.*, 148(1–3), 283–293.

Sakthivel, S., Neppolian, B., Shankar, M. V., Arabindoo, B., Palanichamy, M., and Murugesan, V. (2003). "Solar photocatalytic degradation of azo dye: Comparison of photocatalytic efficiency of ZnO and TiO_2." *Sol. Energy Mater. Sol. Cells*, 77(1), 65–82.

Salama, A., Mohamed, A., Aboamera, N. M., Osman, T. A., and Khattab, A. (2018). "Photocatalytic degradation of organic dyes using composite nanofibers under UV irradiation." *Appl. Nanosci.*, 8(1–2), 155–161.

San, N., Hatipoğlu, A., Koçtürk, G., Çınar, Z., and Çinar, Z. (2001). "Prediction of primary intermediates and the photodegradation kinetics of 3-aminophenol in aqueous TiO_2 suspensions." *J. Photochem. Photobiol. A Chem.*, 139(2–3), 225–232.

Sandhya, K. P., Haridas, S., and Sugunan, S. (2013). "Visible light induced photocatalytic activity of polyaniline modified TiO_2 and Clay-TiO_2 composites." *Bull. Chem. React. Eng. Catal.*, 8(2), 145–153.

Sanjinés, R., Tang, H., Berger, H., Gozzo, F., Margaritondo, G., and Lévy, F. (1994). "Electronic structure of anatase TiO_2 oxide." *J. Appl. Phys.*, 75(6), 2945–2951.

Saquib, M., Abu Tariq, M., Faisal, M., and Muneer, M. (2008). "Photocatalytic degradation of two selected dye derivatives in aqueous suspensions of titanium dioxide." *Desalination*, 219(1–3), 301–311.

Saquib, M., and Muneer, M. (2002). "Semiconductor mediated photocatalysed degradation of an anthraquinone dye, Remazol Brilliant Blue R under sunlight and artificial light source." *Dye. Pigment.*, 53(3), 237–249.

Saravanan, R., Sacari, E., Gracia, F., Khan, M. M., Mosquera, E., and Gupta, V. K. (2016). "Conducting PANI stimulated ZnO system for visible light photocatalytic degradation of coloured dyes." *J. Mol. Liq.*, 221, 1029–1033.

Sarkar, A., Singh, A. K., Sarkar, D., Khan, G. G., and Mandal, K. (2015). "Three-Dimensional Nanoarchitecture of $BiFeO_3$ Anchored TiO_2 Nanotube Arrays for Electrochemical Energy Storage and Solar Energy Conversion." *ACS Sustain. Chem. Eng.*, 3(9), 2254–2263.

Sarmah, S., and Kumar, A. (2011). "Photocatalytic activity of polyaniline-TiO_2 nanocomposites." *Indian J. Phys.*, 85(5), 713–726.

Satapathy, S., Ahlawat, A., Paliwal, A., Singh, R., Singh, M. K., and Gupta, P. K. (2014). "Effect of calcination temperature on nanoparticle morphology and its consequence on optical properties of Nd:Y_2O_3 transparent ceramics." *CrystEngComm*, 16(13), 2723–2731.

Sathish, M., Viswanathan, B., and Viswanath, R. P. (2007). "Characterization and photocatalytic activity of N-doped TiO_2 prepared by thermal decomposition of Ti-melamine complex." *Appl. Catal. B Environ.*, 74(3–4), 307–312.

Sayılkan, F., Asiltürk, M., Erdemoğlu, S., Akarsu, M., Sayılkan, H., Erdemoğlu, M., and Arpaç, E. (2006). "Characterization and photocatalytic properties of TiO_2-nanosols synthesized by hydrothermal process at low temperature." *Mater. Lett.*, 60(2), 230–235.

Scott, J. P., and Ollis, D. F. (1995). "Integration of chemical and biological oxidation processes for water treatment: Review and recommendations." *Environ. Prog.*, 14(2), 88–103.

Seema, H., Durrani, S., and Saeed, K. (2010). "Auto-combustion synthesis and characterization of multiferroic ($BiFeO_3$) materials." *JPMS Conf. Issue*.

Segne, T. (2011). "Studies on Characterization and Photocatalytic Activities of Visible Light Sensitive TiO_2 Nano Catalysts Co-doped with Magnesium and Copper." *Int. Res. J. Pure Appl. Chem.*, 1(3), 84–103.

Selbach, S. M., Tybell, T., Einarsrud, M. A., and Grande, T. (2008). "The ferroic phase transitions of $BiFeO_3$." *Adv. Mater.*, 20(19), 3692–3696.

Sengodu, P., and Deshmukh, A. D. (2015). "Conducting polymers and their inorganic composites for advanced Li-ion batteries: a review." *RSC Adv.*, 5(52), 42109–42130.

Senthilvelan, S., Chandraboss, V. L., Karthikeyan, B., Natanapatham, L., and Murugavelu, M. (2013). "TiO_2, ZnO and nanobimetallic silica catalyzed photodegradation of methyl green." *Mater. Sci. Semicond. Process.*, 16(1), 185–192.

Serpone, N., Lawless, D., and Khairutdinov, R. (1995). "Size Effects on the Photophysical Properties of Colloidal Anatase TiO_2 Particles: Size Quantization versus Direct Transitions in This Indirect Semiconductor?" *J. Phys. Chem.*, 99(45), 16646–16654.

Sevimli, M. F., and Kinaci, C. (2002). "Decolorization of textile wastewater by ozonation and Fenton's process." *Water Sci. Technol.*, 45(12) 279-286.

Shabbir, A., Gilani, Z. A., Nawaz, A., Warsi, M. F., Khan, M. A., Nazir, S., and Aboud, M. F. A. (2016). "Enhanced dielectric and photocatalytic behaviour of dy-co co-doped multiferroic $BiFeO_3$ nanoparticles." *Dig. J. Nanomater. Biostructures*, 11(4), 1189–1195.

Shah, T., Gul, T., and Saeed, K. (2019). "Photodegradation of bromophenol blue in aqueous medium using graphene nanoplates-supported TiO_2." *Appl. Water Sci.*, 9(4), 105.

Shahabuddin, S., Muhamad Sarih, N., Mohamad, S., and Joon Ching, J. (2016). "$SrTiO_3$ Nanocube-Doped Polyaniline Nanocomposites with Enhanced Photocatalytic Degradation of Methylene Blue under Visible Light." *Polymers (Basel).*, 8(2), 27.

Shahabuddin, S., Sarih, N. M., Ismail, F. H., Shahid, M. M., and Huang, N. M. (2015). "Synthesis of chitosan grafted-polyaniline/Co_3O_4 nanocube nanocomposites and their photocatalytic activity toward methylene blue dye degradation." *RSC Adv.*, 5(102), 83857–

83867.

Shaheen, S. E., Radspinner, R., Peyghambarian, N., and Jabbour, G. E. (2001). "Fabrication of bulk heterojunction plastic solar cells by screen printing." *Appl. Phys. Lett.*, 79(18), 2996–2998.

Shang, M., Wang, W., Sun, S., Ren, J., Zhou, L., and Zhang, L. (2009). "Efficient Visible Light-Induced Photocatalytic Degradation of Contaminant by Spindle-like PANI/BiVO$_4$." *J. Phys. Chem. C*, 113(47), 20228–20233.

Sharma, S., and Khare, N. (2018). "Sensitization of narrow band gap Bi$_2$S$_3$ hierarchical nanostructures with polyaniline for its enhanced visible-light photocatalytic performance." *Colloid Polym. Sci.*, 296(9), 1479–1489.

Shekofteh-Gohari, M., Habibi-Yangjeh, A., Abitorabi, M., and Rouhi, A. (2018). "Magnetically separable nanocomposites based on ZnO and their applications in photocatalytic processes: A review." *Crit. Rev. Environ. Sci. Technol.*, 48(10–12), 806–857.

Shetty, S., Palkar, V., and Pinto, R. (2002). "Size effect study in magnetoelectric BiFeO$_3$ system." *Pramana*, 58(5–6), 1027–1030.

Shi, J., Zheng, J., and Wu, P. (2009). "Preparation, characterization and photocatalytic activities of holmium-doped titanium dioxide nanoparticles." *J. Hazard. Mater.*, 161(1), 416–422.

Shifu, C., Wei, Z., Wei, L., Huaye, Z., Xiaoling, Y., and Yinghao, C. (2009). "Preparation, characterization and activity evaluation of p–n junction photocatalyst p-CaFe$_2$O$_4$/n-Ag$_3$VO$_4$ under visible light irradiation." *J. Hazard. Mater.*, 172(2–3), 1415–1423.

Shirmardi, A., Teridi, M. A. M., Azimi, H. R., Basirun, W. J., Jamali-Sheini, F., and Yousefi, R. (2018). "Enhanced photocatalytic performance of ZnSe/PANI nanocomposites for degradation of organic and inorganic pollutants." *Appl. Surf. Sci.*, 462, 730–738.

Shirota, Y., and Kageyama, H. (2007). "Charge carrier transporting molecular materials and their applications in devices." *Chem. Rev.*, 107(4), 953–1010.

Siddique, M., Khan, N. M., and Saeed, M. (2019). "Photocatalytic Activity of Bismuth Ferrite Nanoparticles Synthesized via Sol-Gel Route." *Zeitschrift für Phys. Chemie*, 233(5), 595–607.

Sifontes, A. B., Rosales, M., Méndez, F. J., Oviedo, O., and Zoltan, T. (2013). "Effect of Calcination Temperature on Structural Properties and Photocatalytic Activity of Ceria

Nanoparticles Synthesized Employing Chitosan as Template." *J. Nanomater.*, 2013, 1–9.

Silva, R. B. da, Pinto, R. A., Soares, J. M., Franco, A., Correa, M. A., Bohn, F., and Costa, J. A. P. da. (2019). "Effect of the synthesis method and calcination temperature on the formation of Ni–NiO nanocomposites." *J. Sol-Gel Sci. Technol.*, 91(2), 286–294.

Simões, A. Z., Stojanovic, B. D., Ramirez, M. A., Cavalheiro, A. A., Longo, E., and Varela, J. A. (2008). "Lanthanum-doped $Bi_4Ti_3O_{12}$ prepared by the soft chemical method: Rietveld analysis and piezoelectric properties." *Ceram. Int.*, 34(2), 257–261.

Singh, J., Kumari, P., and Basu, S. (2019). "Degradation of toxic industrial dyes using SnO_2/g-C_3N_4 nanocomposites: Role of mass ratio on photocatalytic activity." *J. Photochem. Photobiol. A Chem.*, 371, 136–143.

So, C. M., Cheng, M. Y., Yu, J. C., and Wong, P. K. (2002). "Degradation of azo dye Procion Red MX-5B by photocatalytic oxidation." *Chemosphere*, 46(6), 905–912.

Sobana, N., and Swaminathan, M. (2007). "The effect of operational parameters on the photocatalytic degradation of acid red 18 by ZnO." *Sep. Purif. Technol.*, 56(1), 101–107.

Sodeinde, O., and Eboreime, U. (2013). "Adsorption of Textile Wastes Containing Methylene Blue & Congo Red using Activated Carbon Produced from Coconut Shell." *Int. J. Comput. Eng. Manag.*, 16(5), 21–26.

Sohrabi, M., and Ghavami, M. (2008). "Photocatalytic degradation of Direct Red 23 dye using UV/TiO_2: Effect of operational parameters." *J. Hazard. Mater.*, 153(3), 1235–1239.

Soltani, T., and Entezari, M. H. (2013a). "Photolysis and photocatalysis of methylene blue by ferrite bismuth nanoparticles under sunlight irradiation." *J. Mol. Catal. A Chem.*, 377(3), 197–203.

Soltani, T., and Entezari, M. H. (2013b). "Sono-synthesis of bismuth ferrite nanoparticles with high photocatalytic activity in degradation of Rhodamine B under solar light irradiation." *Chem. Eng. J.*, 223(May 2013), 145–154.

Soltani, T., and Entezari, M. H. (2013c). "Solar photocatalytic degradation of RB5 by ferrite bismuth nanoparticles synthesized via ultrasound." *Ultrason. Sonochem.*, 20(5), 1245–1253.

Soni, N., and Prakash, S. (2015). "Antimicrobial and mosquitocidal activity of microbial synthesized silver nanoparticles." *Parasitol. Res.*, 114(3), 1023–1030.

Soram, B. S., Ngangom, B. S., and Sharma, H. B. (2012). "Effect of annealing temperatures

on the structural and optical properties of sol-gel processed nanocrystalline $BiFeO_3$ thin films." *Thin Solid Films*, 524, 57–61.

Specchia, V., and Gianetto, A. (1984). "Powdered activated carbon in an activated sludge treatment plant." *Water Res.*, 18(2), 133–137.

Srdic, V., Mojic, B., Nikolic, M., and Ognjanovic, S. (2013). "Recent progress on synthesis of ceramics core/shell nanostructures." *Process. Appl. Ceram.*, 7(2), 45–62.

Steplin Paul Selvin, S., Ganesh Kumar, A., Sarala, L., Rajaram, R., Sathiyan, A., Princy Merlin, J., and Sharmila Lydia, I. (2018). "Photocatalytic Degradation of Rhodamine B Using Zinc Oxide Activated Charcoal Polyaniline Nanocomposite and Its Survival Assessment Using Aquatic Animal Model." *ACS Sustain. Chem. Eng.*, 6(1), 258–267.

Sugihartono, I., Retnoningtyas, A., Rustana, C., Umiatin, Yudasari, N., Isnaeni, Imawan, C., and Kurniadewi, F. (2019). "The influence of calcination temperature on optical properties of ZnO nanoparticles." *AIP Conf. Proc.*, 060010.

Sun, H., Li, J., Zhang, G., and Li, N. (2016). "Microtetrahedronal $Bi_{12}TiO_{20}$/g-C_3N_4 composite with enhanced visible light photocatalytic activity toward gaseous formaldehyde degradation: Facet coupling effect and mechanism study." *J. Mol. Catal. A Chem.*, 424, 311–322.

Sun, P., Zhang, J., Liu, W., Wang, Q., and Cao, W. (2018). "Modification to L-H Kinetics Model and Its Application in the Investigation on Photodegradation of Gaseous Benzene by Nitrogen-Doped TiO_2." *Catalysts*, 8(8), 326.

Sun, Q., Hu, X., Zheng, S., Zhang, J., and Sheng, J. (2019). "Effect of calcination on structure and photocatalytic property of N-TiO_2/g-C3N4@diatomite hybrid photocatalyst for improving reduction of Cr(VI)." *Environ. Pollut.*, 245, 53–62.

Sun, Y., Xiong, X., Xia, Z., Liu, H., Zhou, Y., Luo, M., and Wang, C. (2013). "Study on visible light response and magnetism of bismuth ferrites synthesized by a low temperature hydrothermal method." *Ceram. Int.*, 39(4), 4651–4656.

Sundarrajan, M., Jeelani, A., Santhanam, V., Durgadevi, S., and Abirami, S. (2018). "Effect of Concentration, pH and Time on the Morphology of Silver Nanoparticles Synthesized by Green Method using Phyllanthus Niruri and Solanum Nigrum Leaf Extracts." *Int. J. Curr. Res. Rev.*, 10(21), 25–29.

Sutar, R. S., Barkul, R. P., Delekar, S. D., and Patil, M. K. (2020). "Sunlight assisted photocatalytic degradation of organic pollutants using g-C_3N_4-TiO_2 nanocomposites." *Arab. J.*

Chem., 13(4), 4966–4977.

Sydulu Singu, B., Srinivasan, P., and Pabba, S. (2011). "Benzoyl Peroxide Oxidation Route to Nano Form Polyaniline Salt Containing Dual Dopants for Pseudocapacitor." *J. Electrochem. Soc.*, 159(1), A6–A13.

Szafraniak, I., Połomska, M., Hilczer, B., Pietraszko, A., and Kępiński, L. (2007). "Characterization of BiFeO$_3$ nanopowder obtained by mechanochemical synthesis." *J. Eur. Ceram. Soc.*, 27(13–15), 4399–4402.

Szymczyk, M., El-Shafei, A., and Freeman, H. S. (2007). "Design, synthesis, and characterization of new iron-complexed azo dyes." *Dye. Pigment.*, 72(1), 8–15.

Tae Kwon, Y., Yong Song, K., In Lee, W., Jin Choi, G., and Rag Do, Y. (2000). "Photocatalytic Behavior of WO$_3$-Loaded TiO$_2$ in an Oxidation Reaction." *J. Catal.*, 191(1), 192–199.

Taghdiri, M. (2017). "Selective Adsorption and Photocatalytic Degradation of Dyes Using Polyoxometalate Hybrid Supported on Magnetic Activated Carbon Nanoparticles under Sunlight, Visible, and UV Irradiation." *Int. J. Photoenergy*, 2017, 1–15.

Talsky, G. (1994). *Derivative Spectrophotometry. Deriv. Spectrophotometry*, Wiley.

Tamboli, M. S., Palei, P. K., Patil, S. S., Kulkarni, M. V., Maldar, N. N., and Kale, B. B. (2014). "Polymethyl methacrylate (PMMA)–bismuth ferrite (BFO) nanocomposite: low loss and high dielectric constant materials with perceptible magnetic properties." *Dalt. Trans.*, 43(35), 13232–13241.

Tan, S., Zhai, J., Xue, B., Wan, M., Meng, Q., Li, Y., Jiang, L., and Zhu, D. (2004). "Property Influence of Polyanilines on Photovoltaic Behaviors of Dye-Sensitized Solar Cells." *Langmuir*, 20(7), 2934–2937.

Teng Ong, S., Yee Gan, H., and Eau Leow, L. (2017). "Utilization of Corn Cob and TiO$_2$ Photocatalyst Thin Films for Dyes Removal." *Acta Chim. Slov.*, 144–158.

Tinghui, L., Matsuura, T., and Sourirajan, S. (1983). "Effect of membrane materials and average pore sizes on reverse osmosis separation of dyes." *Ind. Eng. Chem. Prod. Res. Dev.*, 22(1), 77–85.

Tiwari, D., and Dunn, S. (2009). "Photochemistry on a polarisable semi-conductor: what do we understand today?" *J. Mater. Sci.*, 44(19), 5063–5079.

Treffry-Goatley, K., Buckley, C. A., and Groves, G. R. (1983). "Reverse osmosis treatment

and reuse of textile dyehouse effluents." *Desalination*, 47(1–3), 313–320.

Turabik, M. (2008). "Adsorption of basic dyes from single and binary component systems onto bentonite: simultaneous analysis of Basic Red 46 and Basic Yellow 28 by first order derivative spectrophotometric analysis method." *J. Hazard. Mater.*, 158(1), 52–64.

Umrao, S., Abraham, S., Theil, F., Pandey, S., Ciobota, V., Shukla, P. K., Rupp, C. J., Chakraborty, S., Ahuja, R., Popp, J., Dietzek, B., and Srivastava, A. (2014). "A possible mechanism for the emergence of an additional band gap due to a Ti–O–C bond in the TiO_2 – graphene hybrid system for enhanced photodegradation of methylene blue under visible light." *RSC Adv.*, 4(104), 59890–59901.

Veldurthi, N. K., Palla, S., Velchuri, R., Guduru, P., and Muga, V. (2015). "Degradation of mixed dyes in aqueous wastewater using a novel visible light driven $LiMg_{0.5}Mn_{0.5}O_2$ photocatalyst." *Mater. Express*, 5(5), 445–450.

Venkatachalam, N., Palanichamy, M., Arabindoo, B., and Murugesan, V. (2007). "Enhanced photocatalytic degradation of 4-chlorophenol by Zr4+ doped nano TiO_2." *J. Mol. Catal. A Chem.*, 266(1–2), 158–165.

Venkatesh, D., Pavalamalar, S., and Anbalagan, K. (2019). "Selective Photodegradation on Dual Dye System by Recoverable Nano SnO_2 Photocatalyst." *J. Inorg. Organomet. Polym. Mater.*, 29(3), 939–953.

Vineetha, M. N., Matheswaran, M., and Sheeba, K. N. (2013). "Photocatalytic colour and COD removal in the distillery effluent by solar radiation." *Sol. Energy*, 91, 368–373.

Vinet, L., and Zhedanov, A. (2011). "A 'missing' family of classical orthogonal polynomials." *J. Phys. A Math. Theor.*, 44(8), 085201.

Vinu, R., and Madras, G. (2010). "Environmental remediation by photocatalysis." *J. Indian Inst. Sci.*, 90(2), 189–230.

Virji, S., Kaner, R. B., and Weiller, B. H. (2006). "Hydrogen Sensors Based on Conductivity Changes in Polyaniline Nanofibers †." *J. Phys. Chem. B*, 110(44), 22266–22270.

Vohra, M. S., and Tanaka, K. (2001). "Enhanced Photocatalytic Activity of Nafion-Coated TiO_2." *Environ. Sci. Technol.*, 35(2), 411–415.

Wang, B., Li, C., Pang, J., Qing, X., Zhai, J., and Li, Q. (2012a). "Novel polypyrrole-sensitized hollow TiO_2/fly ash cenospheres: Synthesis, characterization, and photocatalytic ability under

visible light." *Appl. Surf. Sci.*, 258(24), 9989–9996.

Wang, C., Xu, B.-Q., Wang, X., and Zhao, J. (2005). "Preparation and photocatalytic activity of ZnO/TiO$_2$/SnO$_2$ mixture." *J. Solid State Chem.*, 178(11), 3500–3506.

Wang, D., and Li, Y. (2011). "Bimetallic nanocrystals: Liquid-phase synthesis and catalytic applications." *Adv. Mater.*, 23(9), 1044–1060.

Wang, D., Zhao, P., and Li, Y. (2011a). "General preparation for Pt-based alloy nanoporous nanoparticles as potential nanocatalysts." *Sci. Rep.*, 1(1), 37.

Wang, F., Min, S., Han, Y., and Feng, L. (2010). "Visible-light-induced photocatalytic degradation of methylene blue with polyaniline-sensitized TiO$_2$ composite photocatalysts." *Superlattices Microstruct.*, 48(2), 170–180.

Wang, F., and Zhang, K. (2011). "Reduced graphene oxide–TiO$_2$ nanocomposite with high photocatalystic activity for the degradation of rhodamine B." *J. Mol. Catal. A Chem.*, 345(1–2), 101–107.

Wang, J., Neaton, J. B., Zheng, H., Nagarajan, V., Ogale, S. B., Liu, B., Viehland, D., Vaithyanathan, V., Schlom, D. G., Waghmare, U. V., Spaldin, N. A., Rabe, K. M., Wuttig, M., and Ramesh, R. (2003). "Epitaxial BiFeO$_3$ multiferroic thin film heterostructures." *Science (80-.).*, 299(5613), 1719–1722.

Wang, J., Wang, Z., Huang, B., Ma, Y., Liu, Y., Qin, X., Zhang, X., and Dai, Y. (2012b). "Oxygen Vacancy Induced Band-Gap Narrowing and Enhanced Visible Light Photocatalytic Activity of ZnO." *ACS Appl. Mater. Interfaces*, 4(8), 4024–4030.

Wang, L., Fu, X., Han, Y., Chang, E., Wu, H., Wang, H., Li, K., and Qi, X. (2013a). "Preparation, Characterization, and Photocatalytic Activity of TiO$_2$ /ZnO Nanocomposites." *J. Nanomater.*, 2013, 1–6.

Wang, M., Han, J., Guo, P., Sun, M., Zhang, Y., Tong, Z., You, M., and Lv, C. (2018). "Hydrothermal synthesis of B-doped Bi2MoO6 and its high photocatalytic performance for the degradation of Rhodamine B." *J. Phys. Chem. Solids*, 113, 86–93.

Wang, W., Li, N., Chi, Y., Li, Y., Yan, W., Li, X., and Shao, C. (2013b). "Electrospinning of magnetical bismuth ferrite nanofibers with photocatalytic activity." *Ceram. Int.*, 39(4), 3511–3518.

Wang, W., Xu, J., Zhang, L., and Sun, S. (2014). "Bi$_2$WO$_6$/PANI: An efficient visible-light-

induced photocatalytic composite." *Catal. Today*, 224, 147–153.

Wang, X., Lin, Y., Ding, X., and Jiang, J. (2011b). "Enhanced visible-light-response photocatalytic activity of bismuth ferrite nanoparticles." *J. Alloys Compd.*, 509(23), 6585–6588.

Wang, X., Lin, Y., Zhang, Z. C., and Bian, J. Y. (2011c). "Photocatalytic activities of multiferroic bismuth ferrite nanoparticles prepared by glycol-based sol–gel process." *J. Sol-Gel Sci. Technol.*, 60(1), 1–5.

Wang, Y., Wang, Q., Zhan, X., Wang, F., Safdar, M., and He, J. (2013c). "Visible light driven type II heterostructures and their enhanced photocatalysis properties: a review." *Nanoscale*, 5(18), 8326.

Wang, Z. L. (2003). "New Developments in Transmission Electron Microscopy for Nanotechnology." *Adv. Mater.*, 15(18), 1497–1514.

Wang, Z., Xue, M., Huang, K., and Liu, Z. (2011d). "Textile Dyeing Wastewater Treatment." *Adv. Treat. Text. Effl.*, InTech, 91–116.

Watters, J. C., Biagtan, E., and Senler, O. (1991). "Ultrafiltration of a Textile Plant Effluent." *Sep. Sci. Technol.*, 26(10–11), 1295–1313.

Weber, P., and Knauf, R. (1998). "Ultrafiltration of surface water with ®MOLPURE FW50 hollow fibre module." *Desalination*, 119(1–3), 335–339.

Wei, J., and Xue, D. (2008). "Low-temperature synthesis of $BiFeO_3$ nanoparticles by ethylenediaminetetraacetic acid complexing sol-gel process." *Mater. Res. Bull.*, 43(12), 3368–3373.

Wei, X., Jiao, L., Sun, J., Liu, S., and Yuan, H. (2010). "Synthesis, electrochemical, and gas sensitivity performance of polyaniline/MoO_3 hybrid materials." *J. Solid State Electrochem.*, 14(2), 197–202.

Wetchakun, N., Chaiwichain, S., Inceesungvorn, B., Pingmuang, K., Phanichphant, S., Minett, A. I., and Chen, J. (2012a). "$BiVO_4$ /CeO_2 Nanocomposites with High Visible-Light-Induced Photocatalytic Activity." *ACS Appl. Mater. Interfaces*, 4(7), 3718–3723.

Wetchakun, N., Incessungvorn, B., Wetchakun, K., and Phanichphant, S. (2012b). "Influence of calcination temperature on anatase to rutile phase transformation in TiO_2 nanoparticles synthesized by the modified sol–gel method." *Mater. Lett.*, 82, 195–198.

Wijannarong, S., Aroonsrimorakot, S., Thavipoke, P., Kumsopa, C., and Sangjan, S. (2013). "Removal of Reactive Dyes from Textile Dyeing Industrial Effluent by Ozonation Process." *APCBEE Procedia*, 5, 279–282.

Wong, C. C., and Chu, W. (2003). "The direct photolysis and photocatalytic degradation of alachlor at different TiO_2 and UV sources." *Chemosphere*, 50(8), 981–987.

Wongkalasin, P., Chavadej, S., and Sreethawong, T. (2011). "Photocatalytic degradation of mixed azo dyes in aqueous wastewater using mesoporous-assembled TiO\n2 nanocrystal synthesized by a modified sol-gel process." *Colloids Surfaces A Physicochem. Eng. Asp.*, 384(1–3), 519–528.

Wu, H., and Zhang, Z. (2011). "High photoelectrochemical water splitting performance on nitrogen doped double-wall TiO_2 nanotube array electrodes." *Int. J. Hydrogen Energy*, 36(21), 13481–13487.

Wu, N., Wang, J., Tafen, D. N., Wang, H., Zheng, J.-G., Lewis, J. P., Liu, X., Leonard, S. S., and Manivannan, A. (2010a). "Shape-Enhanced Photocatalytic Activity of Single-Crystalline Anatase TiO_2 (101) Nanobelts." *J. Am. Chem. Soc.*, 132(19), 6679–6685.

Wu, W., Liang, S., Shen, L., Ding, Z., Zheng, H., Su, W., and Wu, L. (2012). "Preparation, characterization and enhanced visible light photocatalytic activities of polyaniline/Bi3NbO7 nanocomposites." *J. Alloys Compd.*, 520, 213–219.

Wu, Y., Xing, M., Tian, B., Zhang, J., and Chen, F. (2010b). "Preparation of nitrogen and fluorine co-doped mesoporous TiO_2 microsphere and photodegradation of acid orange 7 under visible light." *Chem. Eng. J.*, 162(2), 710–717.

Xia, Y., He, Z., Su, J., Liu, Y., Tang, B., and Li, X. (2018). "Fabrication of Novel n-$SrTiO_3$ /p-BiOI Heterojunction for Degradation of Crystal Violet Under Simulated Solar Light Irradiation." *Nano*, 13(06), 1850070.

Xia, Y., and Yin, L. (2013). "Core–shell structured α-Fe_2O_3@TiO_2 nanocomposites with improved photocatalytic activity in the visible light region." *Phys. Chem. Chem. Phys.*, 15(42), 18627.

Xian, T., Yang, H., Dai, J. F., Wei, Z. Q., Ma, J. Y., and Feng, W. J. (2011a). "Photocatalytic properties of BiFeO3 nanoparticles with different sizes." *Mater. Lett.*, 65(11), 1573–1575.

Xian, T., Yang, H., Dai, J. F., Wei, Z. Q., Ma, J. Y., and Feng, W. J. (2011b). "Photocatalytic properties of $SrTiO_3$ nanoparticles prepared by a polyacrylamide gel route." *Mater. Lett.*,

65(21–22), 3254–3257.

Xie, H., Wang, K., Jiang, Y., Zhao, Y., and Wang, X. (2014). "An improved co-precipitation method to synthesize three bismuth ferrites." *Synth. React. Inorganic, Met. Nano-Metal Chem.*, 44(9), 1363–1367.

Xie, J., He, Y., Wang, H., Duan, M., Tang, J., Wang, Y., Chamas, M., and Wang, H. (2018). "Photocatalytic Degradation of Binary Dyes Mixture over $SrTiO_3$ Synthesized Using Sodium Carboxymethylcellulose Additive." *Russ. J. Phys. Chem. A*, 92(4), 809–815.

Xiong, P., Chen, Q., He, M., Sun, X., and Wang, X. (2012). "Cobalt ferrite–polyaniline heteroarchitecture: a magnetically recyclable photocatalyst with highly enhanced performances." *J. Mater. Chem.*, 22(34), 17485.

Xuan, S., Wang, Y.-X. J., Yu, J. C., and Leung, K. C.-F. (2009). "Preparation, Characterization, and Catalytic Activity of Core/Shell Fe_3O_4@Polyaniline@Au Nanocomposites." *Langmuir*, 25(19), 11835–11843.

Xue, Z., Wang, T., Chen, B., Malkoske, T., Yu, S., and Tang, Y. (2015). "Degradation of tetracycline with $BiFeO_3$ prepared by a simple hydrothermal method." *Materials (Basel).*, 8(9), 6360–6378.

Yacamán, M. J., Ascencio, J. A., Liu, H. B., and Gardea-Torresdey, J. (2001). "Structure shape and stability of nanometric sized particles." *J. Vac. Sci. Technol. B Microelectron. Nanom. Struct.*, 19(4), 1091.

Yaghoubi-berijani, M., and Bahramian, B. (2020). "Synthesis, and New Design into Enhanced Photocatalytic Activity of Porphyrin Immobilization on the Surface of Bismuth Oxyhalides Modified with Polyaniline." *J. Inorg. Organomet. Polym. Mater.*, 1–18.

Yamashita, T., and Hayes, P. (2009). "Erratum to 'Analysis of XPS spectra of Fe_{2+} and Fe_{3+} ions in oxide materials' [Appl. Surf. Sci. 254 (2008) 2441–2449]." *Appl. Surf. Sci.*, 255(18), 8194.

Yang, C., Dong, W., Cui, G., Zhao, Y., Shi, X., Xia, X., Tang, B., and Wang, W. (2017). "Enhanced photocatalytic activity of $PANI/TiO_2$ due to their photosensitization-synergetic effect." *Electrochim. Acta*, 247, 486–495.

Yang, L., Si, Z., Weng, D., and Yao, Y. (2014). "Synthesis, characterization and photocatalytic activity of porous WO_3/TiO_2 hollow microspheres." *Appl. Surf. Sci.*, 313, 470–478.

Yang, Q., Chen, F., Li, X., Wang, D., Zhong, Y., and Zeng, G. (2016). "Self-assembly Z-scheme heterostructured photocatalyst of Ag_2O@Ag-modified bismuth vanadate for efficient photocatalytic degradation of single and dual organic pollutants under visible light irradiation." *RSC Adv.*, 6(65), 60291–60307.

Yang, S. Y., Seidel, J., Byrnes, S. J., Shafer, P., Yang, C. H., Rossell, M. D., Yu, P., Chu, Y. H., Scott, J. F., Ager, J. W., Martin, L. W., and Ramesh, R. (2010). "Above-bandgap voltages from ferroelectric photovoltaic devices." *Nat. Nanotechnol.*, 5(2), 143–147.

Ye, A., Fan, W., Zhang, Q., Deng, W., and Wang, Y. (2012). "CdS–graphene and CdS–CNT nanocomposites as visible-light photocatalysts for hydrogen evolution and organic dye degradation." *Catal. Sci. Technol.*, 2(5), 969.

Yu, F. (2006). "From molecular clusters to nanoparticles: second-generation ion-mediated nucleation model." *Atmos. Chem. Phys.*, 6(12), 5193–5211.

Yu, J., Yu, H., Cheng, B., and Trapalis, C. (2006). "Effects of calcination temperature on the microstructures and photocatalytic activity of titanate nanotubes." *J. Mol. Catal. A Chem.*, 249(1–2), 135–142.

Zaleska, A. (2008). "Doped-TiO_2: A Review." *Recent Patents Eng.*, 2(3), 157–164.

Zalesskii, A. V., Frolov, A. A., Khimich, T. A., and Bush, A. A. (2003). "Composition-induced transition of spin-modulated structure into a uniform antiferromagnetic state in a $Bi_{1-x}La_xFeO_3$ system studied using 57Fe NMR." *Phys. Solid State*, 45(1), 141–145.

Zalfani, M., Schueren, B. van der, Hu, Z.-Y., Rooke, J. C., Bourguiga, R., Wu, M., Li, Y., Tendeloo, G. Van, and Su, B.-L. (2015). "Novel 3DOM $BiVO_4$ /TiO_2 nanocomposites for highly enhanced photocatalytic activity." *J. Mater. Chem. A*, 3(42), 21244–21256.

Zang, L. (2008). "Enhanced Photocatalytic Degradation of Dye Pollutants under Visible Irradiation on Al (III) -Modified TiO_2 : Structure , Interaction , and Interfacial Electron Transfer." 42(1), 308–314.

Zhang, H., Chen, B., and Banfield, J. F. (2010). "Particle Size and pH Effects on Nanoparticle Dissolution." *J. Phys. Chem. C*, 114(35), 14876–14884.

Zhang, H., Han, J., Niu, X., Han, X., Wei, G., and Han, W. (2011a). "Study of synthesis and catalytic property of WO_3/TiO_2 catalysts for NO reduction at high temperatures." *J. Mol. Catal. A Chem.*, 350(1–2), 35–39.

Zhang, H., Sun, S., Ding, H., Deng, T., and Wang, J. (2020). "Effect of calcination temperature on the structure and properties of SiO_2 microspheres/nano-TiO_2 composites." *Mater. Sci. Semicond. Process.*, 115, 105099.

Zhang, J., Ayusawa, T., Minagawa, M., Kinugawa, K., Yamashita, H., Matsuoka, M., and Anpo, M. (2001). "Investigations of TiO_2 Photocatalysts for the Decomposition of NO in the Flow System." *J. Catal.*, 198(1), 1–8.

Zhang, J., Li, M., Feng, Z., Chen, J., and Li, C. (2006a). "UV Raman Spectroscopic Study on TiO_2 . I. Phase Transformation at the Surface and in the Bulk." *J. Phys. Chem. B*, 110(2), 927–935.

Zhang, J., Zhang, Z., Zhang, Y., Li, C., Sun, X., Si, H., Peng, Z., and Li, Y. (2015a). "Preparation of novel $YBiO_3$/Bi_2O_3 heterostructured composite with high visible light photocatalytic activity." *Mater. Express*, 5(4), 336–342.

Zhang, L., Liu, P., and Su, Z. (2006b). "Preparation of PANI–TiO_2 nanocomposites and their solid-phase photocatalytic degradation." *Polym. Degrad. Stab.*, 91(9), 2213–2219.

Zhang, L., Zhang, X., Zou, Y., Xu, Y.-H., Pan, C.-L., Hu, J.-S., and Hou, C.-M. (2015b). "Hydrothermal synthesis, influencing factors and excellent photocatalytic performance of novel nanoparticle-assembled $Bi_{25}FeO_{40}$ tetrahedrons." *CrystEngComm*, 17(34), 6527–6537.

Zhang, L., Zou, Y., Song, J., Pan, C.-L., Sheng, S.-D., and Hou, C.-M. (2016a). "Enhanced photocatalytic activity of $Bi_{25}FeO_{40}$ –Bi_2WO_6 heterostructures based on the rational design of the heterojunction interface." *RSC Adv.*, 6(31), 26038–26044.

Zhang, M., Yang, H., Xian, T., Wei, Z., and Feng, W. (2011b). "Preparation of bismuth ferrite nanoparticles and their photocatalytic activity for MO degradation." *2011 Int. Conf. Remote Sensing, Environ. Transp. Eng. RSETE 2011 - Proc.*, 6177–6180.

Zhang, S., Chen, Q., Jing, D., Wang, Y., and Guo, L. (2012). "Visible photoactivity and antiphotocorrosion performance of PdS–CdS photocatalysts modified by polyaniline." *Int. J. Hydrogen Energy*, 37(1), 791–796.

Zhang, T., Oyama, T. ki, Horikoshi, S., Hidaka, H., Zhao, J., and Serpone, N. (2002). "Photocatalyzed N-demethylation and degradation of methylene blue in titania dispersions exposed to concentrated sunlight." *Sol. Energy Mater. Sol. Cells*, 73(3), 287–303.

Zhang, W. J., Yang, B., and He, H. B. (2011c). "Calcination Conditions Influencing the Preparation of Porous TiO_2 Film Using PEG1000 as Template." *Adv. Mater. Res.*, 382, 340–

343.

Zhang, W., Xin, H., Li, R., and He, H. (2013). "Effects of Calcination Time on Structure and Activity of Porous TiO$_2$-Al$_2$O$_3$ Photocatalyst." *Asian J. Chem.*, 25(7), 3769–3772.

Zhang, X., Wu, J., Meng, G., Guo, X., Liu, C., and Liu, Z. (2016b). "One-step synthesis of novel PANI–Fe$_3$O$_4$@ZnO core–shell microspheres: An efficient photocatalyst under visible light irradiation." *Appl. Surf. Sci.*, 366, 486–493.

Zhang, Y., Hsieh, Y.-C., Volkov, V., Su, D., An, W., Si, R., Zhu, Y., Liu, P., Wang, J. X., and Adzic, R. R. (2014). "High Performance Pt Monolayer Catalysts Produced via Core-Catalyzed Coating in Ethanol." *ACS Catal.*, 4(3), 738–742.

Zhang, Z., Wang, C. C., Zakaria, R., and Ying, J. Y. (1998). "Role of particle size in nanocrystalline TiOi-based photocatalysts." *J. Phys. Chem. B*, (52), 10871–10878.

Zhao, L., Ran, J., Shu, Z., Dai, G., Zhai, P., and Wang, S. (2012). "Effects of Calcination Temperatures on Photocatalytic Activity of Ordered Titanate Nanoribbon/SnO$_2$ Films Fabricated during an EPD Process." *Int. J. Photoenergy*, 2012, 1–7.

Zhao, W., Liu, Y., Wei, Z., Yang, S., He, H., and Sun, C. (2016). "Fabrication of a novel p-n heterojunction photocatalyst n-BiVO4@p-MoS2 with core-shell structure and its excellent visible-light photocatalytic reduction and oxidation activities." *Appl. Catal. B Environ.*, 185, 242–252.

Zheng, J., Chang, F., Jiao, M., Xu, Q., Deng, B., and Hu, X. (2018). "A visible-light-driven heterojuncted composite WO$_3$/Bi$_{12}$O$_{17}$Cl$_2$: Synthesis, characterization, and improved photocatalytic performance." *J. Colloid Interface Sci.*, 510, 20–31.

Zhu, A., Zhao, Q., Li, X., and Shi, Y. (2014). "BiFeO$_3$/TiO$_2$ Nanotube Arrays Composite Electrode: Construction, Characterization, and Enhanced Photoelectrochemical Properties." *ACS Appl. Mater. Interfaces*, 6(1), 671–679.

Zhu, J., Ye, M., and Han, A. (2017a). "Preparation and microwave absorption properties of BiFeO$_3$ and BiFeO$_3$/PANI composites." *J. Mater. Sci. Mater. Electron.*, 28(18), 13350–13359.

Zhu, L., Lu, Q., Lv, L., Wang, Y., Hu, Y., Deng, Z., Lou, Z., Hou, Y., and Teng, F. (2017b). "Ligand-free rutile and anatase TiO$_2$ nanocrystals as electron extraction layers for high performance inverted polymer solar cells." *RSC Adv.*, 7(33), 20084–20092.

Zuorro, A., Lavecchia, R., Monaco, M. M., Iervolino, G., and Vaiano, V. (2019). "Photocatalytic Degradation of Azo Dye Reactive Violet 5 on Fe-Doped Titania Catalysts under Visible Light Irradiation." *Catalysts*, 9(8), 645.

PUBLICATION BASED ON THE RESEARCH WORK

JOURNAL ARTICLES

1. Kalikeri, S., and Shetty Kodialbail, V. (2018). "Solar light-driven photocatalysis using mixed-phase bismuth ferrite ($BiFeO_3/Bi_{25}FeO_{40}$) nanoparticles for remediation of dye-contaminated water: kinetics and comparison with artificial UV and visible light-mediated photocatalysis." *Environ. Sci. Pollut. Res.*, 25(14), 13881–13893. **(IF-3.056)**

2. Kalikeri, S., and Shetty Kodialbail, V. (2020). "Auto combustion synthesis of narrow band-gap bismuth ferrite nanoparticles for solar photocatalysis to remediate azo dye containing water" Environ. *Sci. Pollut. Res.*, **(IF-3.056)**

3. Kalikeri, S., and Shetty Kodialbail, V. (2020). "Visible Light active Bismuth ferrite embedded TiO_2 nanocomposite structures for mixed dye mineralization by photocatalysis: A strategy to harness solar energy for wastewater remediation" Mat **Sci** Semicon Proc., (Under review)., **(IF-3.085)**

CONFERENCE PROCEEDINGS

1. Shankramma, K., and Vidya Shetty, K. (2020). "Effect of narrow band gap bismuth ferrite nanoparticles on the Photocatalytic degradation of azo dye in Aqueous Solution Under solar light irradiation." *Proceesings Int. Conf. Phys. Allied Sci.*, Bidar, India, 133.

2. Shankramma, K., and Vidya Shetty, K. (2019). "Auto Combustion Synthesis of Narrow Bandgap Bismuth Ferrite Nanoparticles for Solar Photocatalysis to Remediate Azo Dye Containing Water." *Proc. Natl. Symp. Environ. Pollut. Prev. Control -Future Perspect.*, Mangaluru, 49.

3. Shankramma, K., and Vidya Shetty, K. (2019). "Bismuth Ferrite Nanoparticle mediated Photocatalytic Degradation of Dye-contaminated Water under Solar, Visible and UV light." *Proc. Int. Conf. Recent Adv. Chem. Environ. Energy Eng.*, Chennai, 45.

4. Shankramma, K., and Vidya Shetty, K. (2018). "Solar Light Driven Photocatalysis for Treatment of Acid Yellow-17 (AY-17) Dye Contaminated Water Using Bismuth Ferrite Nanoparticles: Comparison with Artificial Visible Light-mediated Photocatalysis." *Proc. Int. Conf. Nano Sci. Eng. Appl.*, Hyderabad, 54.

5. Shankramma, K., and Vidya Shetty, K. (2018). "Photocatalytic Activity of Bismuth Ferrite Nanoparticles for Degradation of Dye; A Comparative Study." *Proc. Int. Conf. Recent Adv. Mater. Sci. Biophys.*, Mangaluru, 30.

6. Shankramma, K., and Vidya Shetty, K. (2017). "Photocatalytic Degradation of Acid Yellow-17 under Solar and Visible Light Irradiation using Bismuth Ferrite Nanoparticles." *Int. Conf. Nanotechnol. Appl. Chem. Energy Environ.*, Surat, 60–61.

7. Shankramma, K., and Vidya shetty, K. (2017). "Ultraviolet, Visible and Solar Photocatalytic Activity of Bismuth Ferrite Nanoparticles for Degradation of Dyes: An Aid to Environmental Remediation." *Proc. Int. Conf. Adv. Nanotechnol.*, Guwahati, 11–12.

8. Shankramma, K., and Vidya Shetty, K. (2015). "Photocatalytic Degradation of Organic Dyes under Visible light irradiation using Bismuth Ferrite Nanoparticles." *Int. Conf. Nano Sci. Nanotechnol. Adv. Mater.*, Visakhapatnam, 124.

OTHER RELATED PUBLICATIONS

JOURNAL ARTICLES

1. Kalikeri, S., Kamath, N., Gadgil, D. J., and Shetty Kodialbail, V. (2018). "Visible light-induced photocatalytic degradation of Reactive Blue-19 over highly efficient polyaniline-TiO_2 nanocomposite: a comparative study with solar and UV photocatalysis." *Environ. Sci. Pollut. Res.*, 25(4), 3731–3744. **(IF-3.056)**

CONFERENCE PROCEEDINGS

1. Shankramma, K., and Shetty K, V. (2015). "Application of Nano Biotechnology in wastewater treatment." *8th Natl. Women's Sci. Congr. (Matruvedike- Women Sci. Forum)*, Bengaluru: Vijnana Kannada, 114–117.

2. Shankramma, K., and Shetty K, V. (2014). "Application of nanotechnology in wastewater treatment." *10th Kannada Vijnana Sammelana (Swadeshi Vijnana Andolana-Karnataka)*, Mysore: Vijnana Kannada, 89–92.

BIO-DATA

SHANKRAMMA K

Email ID: shankrutk@gmail.com

Contact no: +91-9945877182

PERSONAL DETAILS:

Fathers Name: Channabasappa K

Mather Name: Gayatri K

Date of Birth: 01 August, 1987

Gender: Female

Nationality: Indian

Permanent Address: Shankramma K

D/O Channabasappa K

Ward-1, Near Kariyamma Devi Temple,

Talakallu, Hadagali (T),

Bellary (D) M.J. Halli (PO)- 583220

EDUCATIONAL QUALIFICATION:

Ph.D., Environmental Nanotechnology

Dept. of Chemical Engineering   2014-2020

National Institute of Technology, Surathkal, India

M.Tech., Nanoscience and Technology   2011-2013

Kuvempu University, Shimoga, India

M.Sc. Biotechnology   2009-2011

Kuvempu University, Shimoga, India

B.Sc. Chemistry, Botany, Zoology   2006-2009

Kuvempu University, Shimoga, India

DECLARATION:

I hereby declare that the above-written particulars are true to the best of my knowledge.

Place: Surathkal, India

Date:

SHANKRAMMA K